

# UC San Diego

## UC San Diego Electronic Theses and Dissertations

### Title

A study of saturated granular assemblages and its implications for transport, stress propagation and failure in marine sediments

### Permalink

<https://escholarship.org/uc/item/873359jz>

### Author

Le Dantec, Nicolas

### Publication Date

2009

Peer reviewed|Thesis/dissertation

UNIVERSITY OF CALIFORNIA, SAN DIEGO

A study of saturated granular assemblages  
and its implications for transport, stress propagation and failure in marine sediments

A dissertation submitted in partial satisfaction of the  
requirements for the degree Doctor of Philosophy

in

Oceanography

by

Nicolas Le Dantec

Committee in charge:

Grant B. Deane, Chair  
Scott A. Ashford  
Michael J. Buckingham  
Neal W. Driscoll  
Joe D. Goddard  
Robert T. Guza  
Michael Longuet-Higgins

2009

Copyright

Nicolas Le Dantec, 2009

All rights reserved.

The dissertation of Nicolas Le Dantec is approved, and it is acceptable  
in the quality and form for publication on microfilm:

---

---

---

---

---

---

---

Chair

University of California, San Diego

2009



## **DEDICATION**

I dedicate this dissertation to my parents, in recognition of their constant support, of the education they gave me, of their care and love. Thank you.

## EPIGRAPH

[...] who knows what the  
ostrich sees in the sand?  
*Samuel Becket*

# TABLE OF CONTENTS

<b>SIGNATURE PAGE .....</b>	<b>iii</b>
<b>DEDICATION.....</b>	<b>iv</b>
<b>EPIGRAPH.....</b>	<b>v</b>
<b>TABLE OF CONTENTS.....</b>	<b>vi</b>
<b>LIST OF FIGURES .....</b>	<b>x</b>
<b>LIST OF TABLES .....</b>	<b>xvi</b>
<b>ACKNOWLEDGMENTS.....</b>	<b>xvii</b>
MATERIAL SUBMITTED FOR PUBLICATION IN THE DISSERTATION .....	xxii
<b>VITA.....</b>	<b>xxiv</b>
<b>ABSTRACT OF THE DISSERTATION .....</b>	<b>xxv</b>
<b>CHAPTER 1: Introduction .....</b>	<b>1</b>
BACKGROUND AND RATIONALE.....	2
OVERVIEW OF PROJECTS.....	5
CORE STUDY ON SATURATED GRANULAR PILINGS.....	7
IMPLICATIONS FOR MARINE SEDIMENTS .....	9
OUTLINE OF THE DISSERTATION.....	10
<b>CHAPTER 2: Measurements of the Apparent Mass at the Base of Water-Saturated Granular Pilings .....</b>	<b>11</b>
ABSTRACT .....	12
INTRODUCTION .....	13
METHODS.....	21
Description of the column apparatus .....	21
Data acquisition protocol .....	24
Overview of the dataset.....	24
Sequence of events that occur during a run.....	25
Pilings with Overweight.....	27
Immersed pilings.....	28
Settled pilings.....	29
Data processing.....	30
Measurement of wall-to-grain friction coefficient and repose angle .....	31
LOAD CELL DESCENT .....	32
Overview of the three piling regimes for dry, free-surface pilings.....	33
Analysis of the load cell output slope .....	35
Analysis of the piling base displacement.....	36

Choice of the apparent mass .....	36
Applicability of the analysis to dry and saturated pilings with free-surface and overweight.....	38
Efficacy of the data analysis procedure .....	39
The effect of grain usage on apparent mass .....	41
<b>RESULTS FOR THE APPARENT MASS OF PILINGS.....</b>	<b>43</b>
Dry pilings results: free surface and overweight.....	44
Immersed piling results: free surface and overweight .....	45
Comparison of overshoot responses between dry and immersed pilings, and with previous studies ..	46
Consequences of saturating dry, free-surface pilings .....	47
Consequences of forming saturated pilings through settling versus immersion .....	48
<b>DISCUSSION.....</b>	<b>49</b>
Comparison of apparent mass measurements at the base of dry pilings with earlier studies .....	49
Comparison between dry and saturated pilings: qualitative similarities .....	53
Comparison between dry and saturated pilings: quantitative differences .....	55
Role of water.....	58
Limitations of the dataset.....	60
The interpretation of piling response to load cell base descent and some implications for modeling ..	63
About piling decompression: a new regime - progressive friction mobilization and choice of the apparent mass.....	63
The relaxation oscillations: a window on the heterogeneous distribution of stress within the pilings? .....	68
<b>CONCLUDING REMARKS .....</b>	<b>74</b>
 <b>CHAPTER 3: Modeling stress in saturated granular pilings using the Oriented Stress Linearity approach to quantify arching.....</b>	 <b>100</b>
ABSTRACT .....	101
INTRODUCTION .....	102
THEORETICAL ANALYSIS .....	110
Force balance .....	110
The OSL model.....	111
Texture tensor, arching and effective friction angles, and characteristics.....	111
The OSL relation.....	113
Analytical OSL solution in two dimensional configurations .....	114
Janssen and modified Janssen models .....	115
Comparison between Janssen model and the OSL model.....	117
Constitutive relations .....	117
Correspondence between model parameters from two-dimensional solutions .....	117
Stability analysis.....	119
METHODS.....	120
Implementation of numerical simulations.....	120
Discretization scheme .....	121
Boundary conditions .....	122
Integration of the vertical, normal stress to get the apparent mass.....	122
Numerical parameters .....	123
Experimental measurements and datasets.....	124
Regression procedure.....	128
DISCUSSION OF MODELING RESULTS .....	130
Comparison of apparent mass predictions .....	130
Free-surface pilings.....	130
Overweight pilings.....	133

Effect of saturation on overweight piling behavior.....	135
OSL model predictions for overweight pilings interchanging dry and immersed parameters .....	135
Shielding of overweight mass by granular pilings .....	136
Oscillations and influence of arching angle fluctuations .....	138
$\sigma_{zz}$ and $\sigma_{rz}$ within simulated pilings .....	138
Tentative mechanism for oscillation-damping.....	139
Changes in piling behavior within the OSL framework .....	141
Physical signification of the OSL parameters .....	141
Interpretation of the changes in piling behavior.....	142
Selectivity of the OSL model in its adjustable parameters.....	144
Correspondence between the Janssen and OSL model parameters.....	145
CONCLUDING REMARKS .....	147
Summary of main results .....	147
Comments on the oscillations .....	148
Lubrication effects and relevance of dry granular theories to saturated granular systems.....	149
Accounting for random fluctuations of the piling texture.....	150
About the OSL approach .....	151
APPENDIX .....	151
Alternate regression methods.....	151
Numerical instabilities .....	152
<b>CHAPTER 4: Tectonic Controls on Nearshore Sediment Accumulation and Submarine Canyon</b>	
<b>Morphology Offshore La Jolla, Southern California .....</b>	<b>175</b>
ABSTRACT .....	176
INTRODUCTION .....	178
METHODOLOGY .....	182
Data acquisition .....	182
Data Processing .....	184
RESULTS.....	185
Bathymetry .....	186
Canyon Morphology .....	186
Secondary incisions.....	187
Asymmetry between the north and south walls.....	188
Transgressive surface structure.....	189
Tectonic expressions on-land.....	191
Sedimentary Units Offshore La Jolla.....	192
Estuarine unit .....	192
Healing-phase deposits .....	192
Holocene sands .....	193
DISCUSSION.....	195
Structural controls on canyon location.....	196
Morphology of the La Jolla Canyon .....	197
Morphology of the Scripps Canyon.....	199
Topographic effect.....	201
Erosive processes at the canyon edges.....	202
Tectonic control on sediment distribution and thickness during the transgression.....	203
Hydrodynamic control on modern sediment accumulation during the highstand.....	207
CONCLUSION .....	211

APPENDIX: LONG-TERM TECTONIC CONTROL ON HOLOCENE SHELF SEDIMENTATION OFFSHORE LA JOLLA, CALIFORNIA .....	239
<b>CHAPTER 5: Sediment dynamics below the seabed .....</b>	<b>245</b>
FOREWORD .....	246
INSTRUMENTATION .....	247
Development, operation and performance characteristics of three sensors built for the project .....	247
Differential pressure sensor .....	247
Displacement sensor .....	248
Force sensor .....	250
Sensor outfitting .....	250
Calibration and laboratory tests .....	251
Field deployments .....	252
Video system to track individual granular displacements .....	253
PRELIMINARY FIELD OBSERVATIONS .....	255
Dataset overview .....	255
Preliminary analysis of selected features .....	256
Measurement strategy for the second deployment .....	258
COMMENTS .....	258
Other examples of dynamical behavior in the bulk of granular assemblies from laboratory studies .....	258
Experiments by Bagnold .....	259
Limitations to the interpretation of the dataset .....	261
Implications .....	262

# LIST OF FIGURES

- Figure 2-1: A schematic of the experiment setup. A. Diagrams of the apparatus used to measure the apparent mass at the base of the granular piling. The diagram on the left shows the piling before the descent of the load cell base. The diagram on the right shows the displacements of the piling and the load cell after descent of the load cell base. B.....77
- Figure 2-2: Run outputs. A. Change in mass measured at the base of the piling as a function of the load cell base downward displacement. Each black curve is the output of a single run. Three runs from the dry free-surface dataset for different piling heights are displayed and labeled by the corresponding apparent mass. The circles denote the.....78
- Figure 2-3: The average slope of the run output for each of the 3 regimes identified in Fig. 2-2B, showing the dry free-surface dataset. Absolute values of average slopes are expressed in mV per micrometer of load cell base displacement and plotted as a function of the average load cell voltage during each regime. Regime I is .....79
- Figure 2-4: Analysis of the piling base and load cell mechanical response. Piling base displacement and load cell expansion versus load cell base displacement for the run output in Fig. 2-2B. The thick solid line represents the displacement of the piling base (positive displacement corresponds to downward motion). The thick dashed line.....80
- Figure 2-5: The average slope of the run output for each of the 3 regimes identified in Fig. 2-2B, showing four datasets. See the caption of Fig. 2-3 for a description of the plot elements. The standard deviations of the ensemble means are not displayed. Each color represents a dataset. The dry free-surface is in black, the dry overweight in.....81
- Figure 2-6: Piling base displacement at the point at which the apparent mass is obtained. Each point along one of the thick lines is an ensemble mean of all repeated runs for a fixed piling height, plotted against the piling height. The same four datasets as in Fig. 2-5 are displayed. Light vertical lines are the standard deviations of the ensemble.....82
- Figure 2-7: Descent procedure and measurement fluctuations. A. Standard deviation of the mass at the piling base measured at different stages of load cell base descent, plotted as a function the mass of grains poured. Dotted and dashed lines respectively correspond to measurements at the beginning and end of regime I (see Fig. 2-2B). .....83
- Figure 2-8: Usage trend. A. Apparent mass versus grain usage number for a selected piling height. Circles represent data points and the line is a linear, least-mean-square fit to the data. B. Plot of the slope of the linear fit as a function of poured mass. Each data point corresponds to the trend in apparent mass versus usage number for a fixed .....84
- Figure 2-9: Apparent mass plotted as a function of poured mass. Each point corresponds to the ensemble mean of all the repeated runs for a fixed piling height. Squares and triangles respectively correspond to the free-surface and overweight datasets. The gray curve shows a Janssen model fit to the free-surface data. The oblique gray.....86
- Figure 2-10: Overshoot effect compared to data from previous literature. Apparent mass versus poured mass, both normalized by the asymptotic mass. Solid and dashed black lines correspond to the dry overweight and immersed overweight datasets collected by the authors for the present study. Each point corresponds to the.....87

- Figure 2-11: Effect of the addition of water. Squares and triangles respectively correspond to the dry and immersed free-surface datasets. Each point corresponds to the ensemble mean of all the repeated runs for a fixed piling height. The gray curves show a Janssen model fit to both datasets. The oblique gray line represents the lithostatic.....88
- Figure 2-12: Effect of the pouring procedure comparing both immersed free-surface datasets. Squares and triangles respectively correspond to the settling and immersion procedures. See Fig. 2-11 for a description of the additional lines. A. Apparent mass versus poured mass. B. Apparent piling height versus actual piling height.....89
- Figure 2-13: Measured piling heights versus poured mass for both immersed free-surface datasets. Each point corresponds to the ensemble means of the measured piling heights for a fixed expected piling height corresponding to a fixed poured mass. Squares and triangles respectively correspond to the settling and submersion procedures. The.....90
- Figure 3-1: Schematic of the small-scale stress propagation rule. Granular packing in a vertical plane  $(r, z)$ , showing the arching angle  $\tau$ , i.e. the major principal axis of the texture tensor at a point within the granular assembly. The thick, gray lines represent the characteristics along which stress is propagated. The darker grains symbolize a .....155
- Figure 3-2: Schematic illustrating the aspect ratio of a computational grid cell. For a given radial step  $\Delta r$ , the vertical step  $\Delta z$  is set by the largest of the two slopes  $c_{\pm}$  of the characteristics, which is  $c_{+}$  in this example.....155
- Figure 3-3: Model fits for free-surface datasets. Apparent mass versus poured mass. Each data point, represented by a triangle, corresponds to the ensemble mean of all the repeated runs for a fixed piling height. The dash-dot, dashed and solid curves show model fits to the data (see section 3-4.3 for a description of the regression method used to ..156
- Figure 3-4: Model fits for overweight datasets. Apparent mass versus poured mass, both normalized by the asymptotic mass. Triangles connected by a dotted line represent data, each point corresponding to the ensemble mean of all the repeated runs for a fixed piling height. The dash-dot and solid curves show model fits to the data (see .....158
- Figure 3-5: OSL model predictions. Apparent mass versus poured mass, both normalized by the asymptotic mass. Filled symbols connected by dotted lines are data points. Gray and black are used respectively for the dry and immersed cases. Solid curves show the OSL model fits to the data. Dashed curves show the OSL model prediction.....159
- Figure 3-6: Overweight datasets collapse. Contribution to the apparent mass of overweight pilings induced by the overweight, normalized by the overweight mass  $\left( \left( M_{app}^{overweight} - M_{app}^{free-surface} \right) / M_{over} \right)$ . Symbols are obtained from free-surface and overweight data points. Circles and squares respectively correspond to the dry...160
- Figure 3-7: Simulated stresses within pilings. Vertical cross-section of the color-coded stress intensity (in Pa) extending from the piling central axis to the wall. Pressure and shear stress obtained from the same simulation are shown respectively in the left and right panels in each subplot, with vertical axis labeled respectively as poured mass and ....161
- Figure 3-8: Model predictions with fluctuations of the arching angle. Apparent mass versus poured mass for the dry datasets. Squares and triangles correspond respectively to the



free-surface and overweight data points. There are three series of curves, each consisting of 10 thin, gray and 2 thick, black curves. Gray curves show OSL .....	163
Figure 3-9: Pair-wise comparisons of the OSL parameters estimated by fitting the data. Color-coded quadratic error arrays plotted in the $(\eta, \mu)$ parameter space. Each array is scaled by its minimum value and masked at twice its minimum value, so the unique color scale is relative to each error array, even within the same subplot. Black solid lines..	165
Figure 3-10: Different regression methods for OSL model fit to the free-surface, dry dataset. Apparent mass versus poured mass. Triangles are data points. The dash-dot, dashed and solid curves show model fits to the data, respectively with the Janssen, modified Janssen and OSL models. The oblique gray line represents the lithostatic behavior. ..	166
Figure 3-11: Suppression of numerical instabilities. Apparent mass versus poured mass for dry datasets. Squares and circles correspond respectively to the free-surface and overweight data points. The 2 gray curves show respectively OSL model fit to the free-surface data and OSL model prediction for overweight pilings using free- .....	167
Figure 3-12: Simulated stresses within pilings with numerical instabilities (see Fig. 3-7 for details on cross-sectional views of stress fields). Simulations correspond to the parameters estimated from the model fit to the free-surface, dry dataset $(\eta = 1.47, \mu = -0.9)$ with smoothing of horizontal stress profiles every 100.....	169
Figure 4-1: Location map showing expression of the structural high on the shelf, the left-lateral jogs on the right-lateral Rose Canyon Fault (arrows indicate sense of strike-slip motion), and the fault-induced scalloping where the Rose Canyon Fault coincides with the shelf edge north and south of the pop-up structure. Bathymetry modified .....	214
Figure 4-2: Survey coverage and bathymetry. A. Survey ship tracks shown in black lines and superimposed on high-resolution Submetrix bathymetry show data coverage as well as core locations with purple stars (push core near the La Jolla Canyon head and vibracore near the Scripps Pier south of the Scripps Canyon). Local faults .....	215
Figure 4-3: Perspective view of the submarine canyon heads. Submetrix bathymetry has a vertical exaggeration of 6:1 while land topography has none. Note the asymmetry in the canyon heads and in secondary canyon development and the longitudinal variability of the canyon edges. Features labeled as in Figure 4-2 .....	216
Figure 4-4: Perspective view of the seismic dataset. Selected seismic profiles showing the estuarine, healing-phase, and upper Holocene sand units are displayed with a vertical exaggeration of 6:1. Beds dip regionally to the south, but dip to the north just north of the Scripps Canyon. Note the thinning of the Holocene sands towards the ...	218
Figure 4-5: Transgressive surface roughness increases with water depth. A. The most offshore line, strike line 11, exhibits more roughness on the transgressive surface due to deformation on the Carmel Valley and Salk faults. B. Strike line 10 is slightly shallower and exhibits significant smoothing of the transgressive surface.....	220
Figure 4-6: Chirp profiles. A. Strike line 8 uninterpreted (top) and interpreted (bottom) shows estuarine, healing-phase, and Holocene sand units. Note that the Scripps Canyon is located within a high in the transgressive surface. B. Dip line 3 uninterpreted (top) and interpreted (bottom) shows healing-phase and upper Holocene sand.....	222

Figure 4-7: A. Bathymetry. B. Depth to the transgressive surface. C. Depth to the top of the healing-phase. D. Healing-phase and Holocene sand units cumulative isopach map. E. Healing-phase isopach map. F. Holocene sands isopach map. G. Estuarine sediments isopach map. H. Local bedding dips showing reversal with faults .....	223
Figure 4-8: Bathymetry with superimposed faults. Perspective view and photograph of the sea cliffs between La Jolla Shores and La Jolla Cove looking southeast and showing cuestas in the intertidal reefs as well as details of dipping beds.....	225
Figure 4-9: A. Perspective view that shows estuarine sediments outcropping at the seafloor. Bathymetry and seismic profile have vertical exaggeration of 6:1 while land topography has none. Inset shows line location and figure orientation. B. Dive picture showing estuarine sediments at seafloor along slope of canyon ridge. Push ...	226
Figure 4-10: A. Line 4 shows failure planes near the Scripps Canyon seen as faint, dipping reflectors within the transparent Holocene sand unit. The concave character of some of these reflectors is similar to the concave up features on the seafloor corresponding to secondary canyons in Figure 4-6A. B. Line 1_24 shows failure planes and convex ...	228
Figure 4-11: Perspective view of the head of the La Jolla Canyon looking southeast, with insets of selected seismic profiles, illustrating bedrock deformation in the RCFZ. A. Possible expression of the Scripps Fault. B. Submarine cuestas. C. Dipping bedding. Submetrix bathymetry and inset CHIRP seismic profiles have a vertical .....	229
Figure 4A-1: Survey ship track (black lines) superimposed on 2 m gridded bathymetry (data used in this study were acquired, processed, archived, and distributed by Seafloor Mapping Lab of California State University Monterey Bay: <a href="http://seafloor.csumb.edu/SFMLweb-DATA.htm">http://seafloor.csumb.edu/SFMLweb-DATA.htm</a> ). White lines on bathymetry are contours (10 m intervals) to 100 m.....	241
Figure 4A-2: CHIRP along-shelf strike lines. A: Profile S10 from offshore shows shoaling of transgressive surface (TS) to north of Scripps Canyon. At this depth, Holocene sediments mantle transgressive surface. B: Nearshore profile S4 shows truncation of underlying layers as consequence of wavebase erosion, which is interpreted to.....	241
Figure 4A-3: CHIRP cross-shelf dip lines. A: Profile D1 shows truncation along interpreted transgressive surface. Basal reflective package is interpreted as part of early transgression, and thickness of overlying acoustically transparent unit is greatest in mid-shelf, thinning both landward and seaward. B: Profile D2, farther to south.....	242
Figure 4A-4: Holocene sediment thickness above transgressive surface (contour interval = 5 m) superimposed on bathymetric contours (contour interval = 10 m). Extent of isopach map is limited to mid-shelf and shoreward by data density shown in Figure 1. Isopachs show depocenter of Holocene sediments directly north of Scripps Canyon, where...	242
Figure 4A-5: Two models of possible faulting mechanisms and expected bathymetry. A: Offset with more resistant Del Mar Formation exposed on upthrown block, along predominantly strike-slip fault, would cause bathymetry to step offshore. B: In case of left step on dextral strike-slip fault (e.g., Rose Canyon fault), we would expect.....	243
Figure 5-1: Differential pressure sensor. A. Waterproofed sensor potted in epoxy with accompanying circuit board and clamped to a deployment mount. B. Sensor alone showing diaphragm .....	264

Figure 5-2: Displacement sensor. A. Strain gauge alone. B. Compliant plastic sheet with waterproofed strain gauges at the base of the sheet and circuit board. C. Sensor potted in epoxy with accompanying circuit board and clamped to a deployment mount. D. Schematic of the deformation of the compliant sheet of area <i>A</i> . The deformation is...	264
Figure 5-3: Force sensor. A. Sensor alone showing the notch in the bending beam and wires attached to the strain gauge that is bonded on the back side. B. Waterproofed sensor potted in epoxy with accompanying circuit board and clamped to a deployment mount. The strain gauge and notch are covered with a protective jacket.....	265
Figure 5-4: Calibration of the displacement sensors. A. Linearity. Sensor output in Volts plotted against load in grams. Each point represents one measurement. B. Symmetry. Measured deformation in millimeters of displacement of the extremity of the compliant sheet plotted against load in grams. The blue and green curves.....	266
Figure 5-5: Geometry of the tank set-up for preliminary laboratory experiments. Three sensors are simultaneously used to measure differential pressure (blue), displacement (green) and force (red). The colored dots represent a top view of the sensor layout. The photograph shows an example of controlled modification of the environment .....	267
Figure 5-6: Time series of sensor outputs for measurements acquired in the configuration shown in Fig. 5-5. Steps in the experimental procedure are indicated below the plots, together with the identified phases of relaxation of the displacement sensor and relevant data filtering information. For the differential pressure sensor, 5 mV .....	268
Figure 5-7: Enlarged view of a portion of the time series shown in Fig. 6. The same correspondences between the voltage output of the sensors and the associated physical variables apply .....	269
Figure 5-8: First deployment. The sensor package is shown before burial to illustrate the sensor configuration, with two displacement sensors in the foreground, one differential pressure sensor in the middle and two force sensors in the background. Note that the two right-most sensors are lower than the pair of left-most sensors. All sensors...	270
Figure 5-9: Second deployment configuration. Note the pair of nearby differential pressure sensors in the middle aimed at investigating arching effects and stress heterogeneities, the almost collocated displacement and force sensors meant to identify stick-slip dynamics and the video system in the black housing, with a displacement sensor.....	271
Figure 5-10: Burial of the sensor package. The photograph shows suspended sediments settling over the instruments.....	272
Figure 5-11: Deployment location. For both measurements campaigns, the sensor package was set-up in the surf zone by the Scripps Pier, which is shown in the photograph. The inset is a photograph of the computer set-up on the Scripps Pier .....	273
Figure 5-12: Video system. A. Front view of the high speed and high resolution camera in its waterproof housing used for deployment, showing the transparent optical face plate and the light head. In the photograph a force sensor is set-up right in front of camera. The monitor displays the image of two orthogonal rulers indicating the .....	274
Figure 5-13: Analysis of images from the video system used to track individual grain displacements. All axes are labeled in pixels (1 pixel = 40 microns) A. Grayscale image from the	

video system. B. Color-coded difference between two images taken 3 seconds apart. The color scale is chosen to obtain a convenient contrast and has no.....	275
Figure 5-14: Heterogeneity and localization of granular motion. Three difference images from laboratory experiments on bedform displacement with a push-plate (see Fig. 5-5). The images are color-coded with arbitrary scales and each image was obtained from still frames 3 seconds apart (see the caption of Fig. 5-13). Panels A, B and C ...	276
Figure 5-15: Experiment overview. Plot of the significant wave height at the Scripps Pier at the time of the first deployment. One of the displacement sensors failed during a large wave event where the compliant sheet was exposed.....	277
Figure 5-16: A 22 hour summary time series from the differential pressure sensor (top plot) and the deeper and shallower displacement sensors (middle and bottom plot respectively). Annotations provide information on the sensors operation. Note the 3 mm displacement measured at approximately 9 cm depth at around 850 minutes on the...	278
Figure 5-17: Expanded view of 100 minutes of data taken from Fig. 5-15. Note the difference in the nature of motion between both sensors, with single event displacements at a depth of approximately 9 cm below the seabed (middle plot) and creep at approximately 3 cm below the seabed (lower plot) .....	279

## LIST OF TABLES

Table 3-1: Piling characteristics for all 5 datasets: packing ratio, bulk density and number of data points.....	127
Table 3-2: Measured angles of repose and wall friction in dry and saturated conditions.....	127
Table 3-3: Performance of Janssen, modified Janssen and OSL model fits to free-surface datasets: asymptotic mass, distance $E$ and $Q_c$ .....	133
Table 3-4: Performance of OSL model fits to all 5 datasets: $E$ and $Q_c$ .....	135
Table 3-5: Estimated OSL parameters and derived arching angle and yield angle along arches for OSL model fits to all 5 datasets.....	144
Table 3-6: Summary of estimated (bold) and derived (regular, see section 3-5.5) parameters for Janssen, modified Janssen and OSL model fits to free-surface datasets .....	147
Table 5-1: List of the variables involved in the mathematical model for the analysis of the differential pressure sensor output.....	248
Table 5-2: List of the variables involved in the mathematical model for the analysis of the displacement sensor output.....	250

## **ACKNOWLEDGMENTS**

I am grateful for all the help, advice and support I have received during the course of my graduate studies at Scripps Institution of Oceanography (SIO). Beyond the dissertation that materializes the accomplished work, and gets filed in the library, a PhD is a journey of learning. I have been fortunate enough to have great teachers accompanying me along this challenging path, whether they were professors, researchers, technicians, colleagues or friends.

I'll start with my committee chair, Grant Deane, who has been my advisor since I arrived at SIO. Grant is at the same time my mentor and my best supporter. I am thankful for the long discussions about the theoretical and experimental aspects of my work, as well as the conversations about his own research. Grant is attached both to the success of my PhD project and to my personal development as a scientist. He has always cared that I get the most out of my graduate studies, which I very much value.

Grant has devoted a lot of his time and resources from his laboratory to the accomplishment of my PhD project. I am thankful that he let me conduct research according to my personal interests, allowing me to focus on areas away from his research goals and encouraging me to develop my own thinking. Throughout my PhD he achieved a great balance between letting me work out solutions by myself so I own my research and providing the necessary help when I was stumbling to pass hurdles. I appreciate that he has always been available to help me at all the stages of my PhD, from the first year when I was starting the process of identifying a suitable research project until the last

stretch when I was writing this dissertation, and every step in between, in the lab, on the Scripps Pier, scuba diving off the Pier.

While the SIO community as a whole has contributed to my education as an oceanographer, I owe Grant my education as a physicist. Starting from the will to understand fundamental mechanisms in geophysical problems, I have learnt with Grant how to exploit novel ideas for designing effective experiments in order to collect reliable data that can be tested against models. I believe the wide range of expertise I have acquired, from theory to laboratory experiments and field measurements, is a highly valuable asset.

Finally, what I appreciate most about Grant is his dedication. In science as in other activities and projects he takes up, he sets very high standards and is committed to getting the work done. In addition, I value that he always acknowledges when the job is well done.

When I arrived at SIO, I intended to work on coastal processes. Grant made it possible for me to approach the question under different angles. He approved of my wish to address the problem at different scales and with various scientific tools. Neal Driscoll gave me the opportunity to explore the large scale context. He trained me in marine geology, sedimentary stratigraphy and tectonics. I am thankful for the field experience I gained with him, through cruises and field trips, including a memorable circumnavigation of Iceland. The time spent in the field, when Neal is at his best, has always been very enriching. I appreciate his positive energy and motivation.

Neal has provided me with a broader education, giving me chance to expand my skill set. I am thankful for his advice on the research project I undertook under his

guidance and for his perspective on more general science questions. I appreciate the genuine interest Neal shows for my work on a field somewhat distant from his main focus, consistent with his personal curiosity and desire to understand earth processes. Neal is keen to teach people who are willing to learn and generous with his scientific ideas. I am pleased to have him as a mentor as well.

I thank Mike Buckingham and Scott Ashford, who have both been very interested in my research project. Mike first oriented me toward the field of granular matter as he was familiar with the concept of force chains. Scott has provided valuable insight on the protocol for the laboratory measurements, and agreed to remain on my committee after he moved to Oregon State University. I appreciate the support they gave me throughout my PhD.

I also thank Michael Longuet-Higgins and Bob Guza for the attention they took to the definition and the realization of my PhD project. I appreciate the feedback they provided. I thank Joe Goddard who accepted to join my committee recently. I enjoyed insightful discussions which have led to significant improvements to my dissertation.

I have undertaken a computer simulation project under the guidance of Lev Tsimring and Dmitri Volfson. The work involved coupling direct numerical, soft molecular dynamics simulations with two-phase fluid dynamics simulations. It was not continued because I needed to focus on the core study of my PhD. Yet, I am thankful that they readily accepted to advise me on this complementary project. Thanks to John Taylor for his help with this enterprise.

I also acknowledge the guidance from Dale Stokes and the support from James Uyloan and Cary Humphries, in Grant's laboratory. Dale has provided much advice on



the design of experimental set-ups, which always revealed very effective. James has provided help any time I needed his expertise on electronics, hardware and software. Cary has spent a lot of his time and effort on my various projects: building equipment, deploying the instruments in the surf zone, training me on machining and other shop skills. Thanks for being a great group to work with and for bearing with the disturbances from my laboratory experiments. The noise from the vacuum cleaner every time I emptied the beads out of the granular column was probably the most annoying of all. I know you'll remember me every time you discover beads hidden in a corner of the laboratory throughout the next few years.

If Grant's lab was my primary residence at SIO, Neal's lab was my second home. I have had a great time with everyone in his large team: Leah, Liz, Jessica, Dany, Jeff, Becca, Mike, John, Justin, Kurt, Christie, Jen, Jenna, and many more I haven't had enough chance to interact with. Thanks as well to Jeff Babcock and Graham Kent who are part of the same team. Of course, special thanks to Leah. Our collaboration on the La Jolla Geology project has been a great experience, at the same time fun and enriching. I have very much enjoyed working with you.

I would like to thank all my professors from the first and second year classes. I understand that teaching is a demanding commitment. It is important to me to acknowledge that the course work was a significant part of my education at SIO. I appreciate the benefits in acquiring a wide knowledge base at the contact of the diverse SIO faculty.

An additional strength of SIO is the resources available on campus. I want to thanks the staff from the Marine Science Development Shop, and especially Ken Duff

and Dave Malmberg, who built my granular column. I also want to acknowledge the help from the Staff Shop and the Hydraulics Laboratory crews. In addition, thanks to Christian McDonald, Rich Walsh and Wayne Pawelek. Without you, all the diving for the field deployments of my surf zone project, to collect the push core from the La Jolla Canyon and for other projects with Grant's laboratory, would not have been possible. I am thankful as well for the support from the SIO Library, in particular Peter Brueggeman, who put together an impressive bibliography on the Scripps and La Jolla canyons and help me go through the literature on the La Jolla Submarine Canyon in great details.

I am thankful for the support from the SIO administrative staff. First I want to thank the Marine Physical Laboratory staff, and especially Evelyn Doudera, who is in charge on the 4<sup>th</sup> floor of Spiess Hall. I also appreciate the great work from the Graduate Department. In particular, I have always been able to count on Alice Zheng, Dawn Huffmann, Denise Darling and Josh Reeves, from the Graduate Office.

I want to acknowledge support from the Wyer Fellowship during first year. It was always a pleasure to interact with Mrs Wyer and her husband John who are both very interesting and kind.

Now, I would like to mention the support from a large and diverse group of friends. I have had the chance to meet truly amazing people during my time in La Jolla. To begin with, there is the great group of the International House of Robbins Street in first year, continued in the second year at Florey Street. Then there are the many groups at SIO: the AOS kids, the Geology kids and significant others, the PO group, the French contingent, and the Spanish gang from MAE. Interacting with you was fun and stimulating. I enjoyed many wonderful trips, hikes and parties in your company. It was

awesome to have you around. Thank you all very much. I can only hope there are more fun outings and travels together in store. Thank you also to the friends from sailing and soccer.

Thank you Flavia. You are my inspiration and my guardian angel. Meeting you was certainly the best of all the benefits of doing my PhD at SIO. I am grateful for your kindness and understanding. I admire your strength and commitment. I learn everyday by your side. Getting through the PhD program together was a challenging and rewarding experience, which contributed to tie strong bonds together. That we share a keen interest in nature and care for the oceans makes our work more satisfying and our life more complete. Whatever happens, I hope we will always be as proud of each other as we are now.

## **MATERIAL SUBMITTED FOR PUBLICATION IN THE DISSERTATION**

Chapter 2 is currently being prepared for submission for publication in Granular Matter as: Le Dantec, Nicolas; Deane, Grant B. “Measurements of the Apparent Mass at the Base of Water-Saturated Granular Pilings”. The dissertation author was the primary investigator and author of this paper.

Chapter 3, in part is currently being prepared for submission for publication as: Le Dantec, Nicolas; Deane, Grant B. “Modeling stress in saturated granular pilings using the OSL approach to quantify arching”. The dissertation author was the primary investigator and author of this paper.

Chapter 4 was submitted for publication in *Marine Geology*, 2009 as: Le Dantec Nicolas; Hogarth Leah J.; Driscoll, Neal W.; Babcock Jeff. “Tectonic controls on nearshore sediment accumulation and submarine canyon morphology offshore La Jolla, Southern California”. The dissertation author was the primary investigator and author of this paper.

The appendix to Chapter 4, in full, is a reprint of the material as it appears in: *Geology*, 2007, Hogarth Leah J.; Babcock Jeff; Driscoll, Neal W.; Le Dantec Nicolas; Hass, Jennifer K.; Inman, Douglas L.; Masters, Patricia M. “Long-term tectonic control on Holocene shelf sedimentation offshore La Jolla, California”. The dissertation author was a co-author on this paper.

# VITA

## Education

- 2004            Master of Science in Oceanography  
University of California, San Diego, CA
- 2002            Master of Science in Engineering  
Institut National des Télécommunications, Evry, France
- 1996 – 1999    Classes Préparatoires de Mathématiques  
Lycée Louis-Le-Grand, Paris, France

## Publications

**Le Dantec N.**, Deane, G.B., Modeling stress in saturated granular pilings using the OSL approach to quantify arching, *in preparation*.

**Le Dantec N.**, Deane, G.B., Measurements of the Apparent Mass at the Base of Water-Saturated Granular Pilings, Granular Matter, 2009, *in preparation*.

**Le Dantec N.**, Hogarth L.J., Driscoll N.W., Babcock J., Tectonic controls on nearshore sediment accumulation and submarine canyon morphology offshore La Jolla, Southern California, Marine Geology, *accepted with revisions*.

Hogarth L.J., Babcock J., Driscoll N.W., **Le Dantec N.**, Haas J.K., Inman D.L., Masters P.M., 2007, Long-term tectonic control on Holocene shelf sedimentation offshore La Jolla, California. Geology, v. 35 (3), p. 275-278.

## Fields of Study

Mechanics of saturated granular matter  
Marine sediment dynamics  
Coastal sediment processes

# **ABSTRACT OF THE DISSERTATION**

A study of saturated granular assemblages and its implications for transport, stress  
propagation and failure in marine sediments

by

Nicolas Le Dantec

Doctor of Philosophy in Oceanography

University of California, San Diego, 2009

Grant B. Deane, Chair

The subject of small-scale marine sediment mechanics is an area of active research, motivated by its key role in beach and shelf processes. Much of the existing small-scale work has focused on two-phase flows and particle behavior at the sediment interface, and their role in sediment transport and shaping seabed morphology. The study presented here considers the behavior of unconsolidated sediments below the seabed, 100 to 1000 grain diameters deep. Motivated by field observations off La Jolla Shores Beach that suggest dynamical behavior at such depths, a series of laboratory experiments were conducted to study the behavior of unconsolidated, saturated granular assemblies. Careful measurements of the apparent mass at the base of dry and saturated, glass beads pilings were acquired to examine stress redirection effects. The experiment protocol included

slowly lowering the piling base to achieve reproducible piling configurations through wall friction mobilization. Results are analyzed using the Janssen and Oriented Stress Linearity (OSL) models, the latter allowing interpretation of the arching behavior in terms of arch direction and friction angle along arches. The data show qualitative similarities between dry and saturated granular assemblies, suggesting a commonality in their underlying physics, but quantitative differences in the intensity of the arching mechanism, probably associated with lubrication effects. Analysis of the piling quasistatic descent shows evidence of a progressive upward decompression punctuated with dynamic piling reconfigurations interpreted as relaxation oscillations. Both features are associated with spatial and temporal stress heterogeneities and have implications for modeling the mechanics of granular assemblies. Granular matter theories are expected to reproduce such observations occurring under minute deformations in these laboratory experiments.

This work also describes a study of nearshore sediment accumulation and submarine canyon morphology offshore La Jolla, using new seismic data and bathymetry. Isopach maps of the sedimentary sequences overlying the bedrock reveal the critical role of the tectonic landscape on the spatial distribution of modern stratigraphic units. A detailed examination of the morphological characteristics of the Scripps and La Jolla canyons refines the relationship between canyon location and development and regional tectonic deformation, and provides insight on the stability of unconsolidated, saturated marine sediments.

## **CHAPTER 1: Introduction**



## **BACKGROUND AND RATIONALE**

This thesis is motivated by the study of marine sediment mechanics. The mechanics of marine sediments impacts nearshore and shelf processes from beach erosion and ripple formation to submarine slope failure and turbidity currents. Surf zone and swash zone dynamics, cross-shore and alongshore transport, changes in beach profile, long term dispersal and accumulation are all examples of processes that are closely related to the mechanics of marine sediments throughout their life cycle on the shelf, between input from river discharge, cliff erosion or offshore supply, and transport off the shelf. The small-scale physics controlling the behavior of marine sediments is an element common to all of these processes, and is thus of central importance for understanding coastal and shelf processes.

The field of sediment dynamics has a long history, extending back well over half a century. A significant body of work consisting of laboratory flume and field studies, theoretical work and modeling, has been undertaken to better understand the complex relationships between hydrodynamic forcing, sediment transport and seabed topography. Much of this work has focused on the characterization of the bottom boundary layer through which fluid flow influences the seabed, the determination of the conditions of deposition or erosion, the description of the modes of entrainment, the detailed resolution of the overlying hydrodynamics and the assessment of transport rates and morphological changes in the seabed. Results obtained thus far underline the need to account for the small-scale variability of the hydrodynamics, sediment properties and granular effects

like particle sorting, and feedbacks between flow pattern and bed morphology. Due to the great spatial and temporal variability of the processes involved, a comprehensive, deterministic description of sediment transport is not available at this time. In addition, the required level of resolution goes beyond current capabilities of computer simulations.

Taking a broader perspective, the mechanics of marine sediments involves a delicate equilibrium constantly adjusting in response to the interactions between a number of processes: geological, physical, chemical, biological. For example, geological processes acting over long time-scales affect the regional morphology and stratigraphy of the nearshore environment, such as the evolution of the shoreline and sediment accumulation patterns. At smaller scales, studying sediment mechanics requires knowledge about the microscopic physics of grains that compose beach sediments, thus leading to the research subject of granular matter.

The degree of understanding of the sedimentary processes that contribute to making and shaping the nearshore environment is variable. For instance, much is known about the physical oceanography and hydrodynamics of the shallow water area. But if marine sediments mechanics can be described as the study of the interaction between fluid and sediment particles, a question comes to mind: What do we know about unconsolidated, saturated granular matter?

Granular systems are very familiar to many people, from sandcastles on the beach to pictures of desert dunes or headlines about devastating landslides. Yet, there are many poorly understood and even unexplored behaviors, which makes the field of granular matter be the subject of intense theoretical and experimental research efforts, both in the engineering and physics communities. The complexity of granular media originates in

physics at the scale of individual grains, including contact friction, intergranular forces and packing geometry. Because of their intrinsic spatial and temporal heterogeneities, which stem from spatial disorder, and of the ineffectiveness of Brownian diffusion, microscopic properties of granular systems give rise to collective behaviors that affect their macroscopic response. As a consequence, granular matter exhibits hysteresis in several respects, such as the internal structure resulting from their formation, memory effects affecting their response to subsequent perturbations and the co-existence of solid-like and fluidized phases. The coupling and distribution of jammed and fluidized regimes, the effects of geometrical properties of individual grains, such as shape or roughness, the role of intergranular forces, like adhesion, cohesion and interlocking, relationships between static and dynamic heterogeneities and arching mechanisms are open issues. Several theoretical descriptions of granular matter mechanics exist, some using classical approaches and others, more recent, based on more unconventional views, but none is entirely satisfactory. In addition, most of the research effort has been concentrated on dry granular systems, with limited attention to saturated granular materials. Little is known about the effect of saturating granular assemblies on the typical behavior of dry granular matter and few experimental observations are available.

Note that throughout the dissertation the term arching is used to refer both to the concave, arch-like granular formations that have been identified within the internal structure of small-scale granular systems and to the redirection of the stress transmitted through a granular assembly, i.e. their anisotropy, which may be associated with such arches. As defined in soil mechanics, arching normally involves localized yielding, i.e. plastic behavior, in addition to stress transfer. In other words, the standard denotation of

arching relates to heterogeneity or localization of load transfer around yielded zones, thus possibly making my usage of arching *a priori* improper. However, notwithstanding the fact that there is no conclusive evidence that granular arches play a role in stress deflection within the bulk of granular systems (more generally, the related question of the transition between microscopic and macroscopic properties of granular materials remains unclear), it is possible that they correspond to loci where the material is at the limit of plastic yielding. Experimental observations supporting this possibility are presented (see the discussion at the end of chapter 2) and a theoretical approach that relies on this hypothesis is examined (see chapter 3), both motivating the perhaps bold choice for the meaning of arching adopted here. Admittedly, the experimental set-up used to conduct the core, laboratory study of the dissertation (see chapter 2) does not allow direct observation of granular arches. However, they have been consistently reported in other studies using various observation methods. In addition, high-speed, high-resolution photographic data acquired during both tank and field experiments confirm the presence of granular arches (see in chapter 5 the difference-images showing individual grain motion on video frames that contain approximately 100 grains across the field of view).

## **OVERVIEW OF PROJECTS**

For my Ph.D. dissertation, I have undertaken a study of saturated granular matter in a marine context. Consistent with the afore-mentioned complexity of granular systems and broad variety of marine sedimentary processes that it is relevant to, I have completed a number of projects. My work includes field and laboratory experiments, analytical and

numerical modeling, and interpretation of bathymetry and stratigraphic data. I started with an observational study of sediment dynamics at shallow depths (about ten centimeters) below the seabed near the Scripps Pier. I designed multiple sensors for mechanical measurements in saturated sediments, tested and calibrated them in the laboratory, and planned and executed field deployments of the integrated sensor package. Motivated by the observation of dynamic sediment behavior 100 to 1000 grain diameters below the seabed, I then conducted a series of laboratory experiments with the objective of studying stress redirection effects in saturated, unconsolidated, granular assemblies. This project required designing an original laboratory apparatus, testing and refining the set-up and measurement protocols to achieve the sensitivity and reproducibility necessary for meaningful conclusions, and carrying out a detailed analysis of the mechanical response of the entire system to accurately define the piling behavior. The results of these experiments have been interpreted within selected existing theoretical frameworks.

In addition to the work focusing on the small-scale behavior of saturated sediment, I also participated in a study on nearshore sediment accumulation and submarine canyon morphology offshore La Jolla. The analysis and interpretation of Compressed High Intensity Radar Pulse (CHIRP) seismic data and high-resolution swath bathymetry revealed the role of tectonic deformation in defining and shaping the nearshore environment, including the distribution of modern sedimentary units overlying the bedrock and the location and development of the Scripps and La Jolla canyons. This study confirms the need for a detailed understanding of the geologic framework when examining long-term sediment distribution on the shelf.

## CORE STUDY ON SATURATED GRANULAR PILINGS

The experiments on granular pilings, consisting in measuring the apparent mass at the base of a granular assembly confined in a cylindrical container, constitute the central component of this thesis. Here, the term apparent mass is used for consistency with most recent studies. The purpose was to identify a granular system that could provide convincing evidence that the observations and concepts developed in the study of dry granular matter are relevant and applicable to saturated granular assemblies. In particular, the occurrence of arching effects associated with the existence of force chains has been tested using models that quantify arching intensity, thus allowing direct comparisons between dry and saturated granular piling mechanics.

The choice of the piling configuration was motivated by the fact that it is a well-known example of a granular system in which spatial heterogeneities and arching significantly affect macroscopic behavior. The silo is a conventional geometry that has a long history of study, primarily because of its application to industry. This problem has received much attention, starting with the Janssen model (the first to describe the mass shielding effect more than a century ago), pursued with numerical models of stress distribution aimed at improving silo design, and continuing with recent laboratory experiments, performed with carefully controlled protocols providing repeatable data and insight into granular mechanics.

The piling configuration offers some advantages over other commonly investigated geometries, such as the sandpile or the response of a granular layer to a point load. Because of the obvious need for saturated granular assemblies to be studied in

immersed conditions, the requirement of a single macroscopic measurement of the mass over the entire piling base seemed more practical than smaller scale, higher resolution pressure measurements needed in the other two cases. An additional advantage is that, for the scenario where an overweight of appropriate mass is added at the top of the piling, the variation of apparent mass at the base of the piling with piling height provides a stringent test for candidate models of granular behavior.

The theoretical analysis uses the Janssen and the Oriented Stress Linearity (OSL) models. The Janssen model, which is retained both for its wide utilization and its simplicity, serves as a basis for a preliminary interpretation of the measurements. The Oriented Stress Linearity (OSL) model is chosen for further analysis on the grounds that its proposed approach provides a quantitative assessment of the stress propagation properties at a granular scale and also because of its ability to predict the overshoot observed for overweight pilings. The limitations of these two models are discussed. Other standard soil mechanics models exist that use the framework of elastoplasticity with selected yield criteria. Such theoretical approaches, among the most basic examples of which are the Coulomb method of wedges and the method of characteristics, are not pursued in this dissertation.

The piling experiments show that saturated granular assemblies exhibit essentially the same physics as dry assemblies, i.e. in the case of pilings the physics includes stress redirection effects, dynamical rearrangements under forcing, and the influence of the packing ratio of pilings on arching intensity. However, observed quantitative differences between dry and saturated assemblies suggest that lubrication effects have an impact on arching mechanisms. In addition, the results presented here confirm the need to

characterize the internal friction angle, which is associated with the rheology of the material, as it is not equivalent to the repose angle, at least in the unconsolidated assemblies studied here. Finally, the experiments have implications for modeling granular systems, as they show significant departure from elastic regime behavior.

### **IMPLICATIONS FOR MARINE SEDIMENTS**

The experiments on saturated granular pilings have implications for the small-scale mechanics of marine sediments, where one would expect arching mechanisms and stress fluctuations to occur at least in non-cohesive sediments. The commonality of behavior between dry and saturated pilings suggests that some of the same processes identified in laboratory studies of granular materials could be inferred to impact small-scale, marine sediments mechanics, consistent with the preliminary field observations of dynamic sediment behavior below the seabed. This thesis study prompts to examine possible coupling effects between interstitial seawater and the granular phase in upper seabed sediments, such as dynamic rearrangement of the heterogeneous structure of the sediment assembly due to its interaction with pore fluid flow.

Additionally, the work on the small-scale mechanical behavior of unconsolidated, saturated granular assemblies may have relevance for large scale sediment dynamics. A better understanding of mechanisms for microscopic yield phenomena associated with dynamical rearrangements at the granular scale may provide insight on precursors and triggering factors in larger sliding events such as submarine slumps or avalanches. The idea of an effective internal friction related to arching mechanisms, and thereby failure



mechanisms, may shed light on the development of incisions into modern unconsolidated sediments at the edge of the Scripps canyon, the shape of which indicates that slope stability is not primarily governed by repose angle. Also, if there is a relationship between the mechanical behavior of marine sediments at the seabed interface and the small-scale physical processes inferred to occur in the upper seabed, then knowledge of the geological landscape, i.e. specifically the sub-bottom lithology, may be central to certain nearshore processes. For example, the occurrence of bedrock or consolidated substrate at shallow depth below the seabed may affect the response of overlying sediments to hydrodynamic forcing, while their presence may not be advertised in the sole topography unless they are outcropping. This effect may have significance for scouring mechanisms as well.

## **OUTLINE OF THE DISSERTATION**

The organization of my dissertation is as follows. The second and third chapters respectively consist of the laboratory measurements of the apparent mass at the base of dry and saturated pilings, and their interpretation using models for stress propagation and arching mechanisms. In the fourth chapter, I present the results of the seismics study offshore La Jolla showing tectonic controls on nearshore sediment accumulation and submarine canyon morphology. The last chapter is a brief account of the field measurements of shallow sediments dynamics with a description of the developed sensors and preliminary observations.

## **CHAPTER 2: Measurements of the Apparent Mass at the Base of Water-Saturated Granular Pilings**

## ABSTRACT

Stress redirection effects within dry and saturated granular pilings are investigated through measurements of the apparent mass at the base of the piling. Pilings were formed from 1 mm diameter spherical glass beads confined in an acrylic column 100 grain diameters across and 500 grain diameters tall. Mobilization of the wall-to-grain friction was controlled by slowly lowering a plate attached to a load cell at the base of piling. The mass shielding observed in confined pilings and the mass overshoot observed in pilings supporting an overweight were reproduced in this study in both dry and saturated pilings, suggesting that the physical processes underlying the mechanical behavior of non-cohesive, dense granular pilings are essentially the same whether or not they are saturated. These results support the relevance of the theoretical framework and conceptual tools developed for dry granular systems to the study of liquid-saturated granular media, which are important for geophysical problems such as sediment transport and slope failure. Saturating a dry piling was found to increase the mass shielding length. The shielding length of saturated pilings was also found to be dependant on the grain packing ratio, which was sensitive to the piling formation procedure. Analysis of the relaxation response of the load-cell and piling system shows evidence of a progressive upward decompression of the piling associated with wall friction mobilization and punctuated with dynamic piling reconfigurations that I interpret as relaxation oscillations.

## INTRODUCTION

Granular matter, also referred to as particulate or divided media, is ubiquitous, from sand grains and snow flakes in the natural environment to powders and granulates in the food, pharmaceutical and chemical industries, and is relevant to the fields of civil engineering, materials science, and geophysics (Brown and Richards 1970; Bagnold 1988; Jaeger *et al.* 1996; de Gennes 1999; Duran 2000; Hutter and Pudasaini 2005). The storage, transport and processing of granular materials represents a significant cost (Jaeger *et al.* 1996; Duran 2000). Gains in efficiency concerning the filling, storage and discharge of granular materials in silos and other vessels, based on a better understanding of granular pilings, would provide significant economic benefits. The behavior of saturated granular matter, such as marine sediments, also has important applications. Avalanches and the erosion, transport and deposition of sediments have high societal impacts (Beatley *et al.* 2002). Slope failures and landslides, whether aerial or submarine, are a danger for large populations (Masson *et al.* 2006; Lykousis *et al.* 2007). The shoreline evolution, driven by littoral zone processes, is of considerable interest given that roughly a third of the world population lives within 100 km of a coastline (Cohen *et al.* 1997). However, current models do not adequately account for the wide range of the macroscopic behaviors observed in dry and saturated granular systems, and improvements would benefit engineering practices and policies.

Granular systems exhibit a broad range of complex features. They show hysteresis phenomena, including stick-slip dynamics, shear zones, and instabilities, which occur because fluidized or solid states can co-exist with a jamming transition between the two

phases (Jaeger and Nagel 1992; Albert *et al.* 2000; Mueth *et al.* 2000; O'Hern *et al.* 2003). Granular systems also show memory in that they are sensitive to their formation history (Vanel *et al.* 1999; Duran 2000; Josserand *et al.* 2000; Toiya *et al.* 2004), and arching effects (Duran *et al.* 1994; Bouchaud *et al.* 1995; Duran *et al.* 1998; Claudin 1999; Duran 2000; Ogale *et al.* 2005). All these behaviors arise from the microscopic physics of grain-to-grain contacts, such as the indeterminacy of frictional contacts, the heterogeneity of intergranular forces, and the role of the coordination number, or number of touching neighbors per grain (Mueth *et al.* 1998; Radjai *et al.* 1998; Behringer *et al.* 1999; Longhi *et al.* 2002; Silbert *et al.* 2002; Kolb and Clement 2005). Constitutive equations remain to be found that can account for microscopic granular physics and, at this time, granular matter modeling is a topic of major debate.

Granular matter theories developed in the classical field of soil mechanics using the mathematical framework of elasticity and plasticity generally rely on complex closure equations relating the stress ( $\sigma_{ij}$ ) and strain ( $\varepsilon_{ij}$ ) fields (Feda 1982; Wu *et al.* 1996; Lubarda 2002). The lack of a physical basis for the multiple parameters involved hinders the interpretation of numerical solutions. Alternative models have been developed for the rheology of slow, dense granular flows, topic which motivates vast, on-going research efforts (Clement 1999; Pouliquen and Chevoir 2002; Volfson *et al.* 2003; MiDi 2004; Jop *et al.* 2006; Goyon *et al.* 2008; Jiang and Liu 2009). In the case of static granular systems, models for the stress distribution within assemblies that are based on the discrete and fragile nature of granular matter have been proposed recently (Bouchaud *et al.* 1995; Coppersmith *et al.* 1996; Cates *et al.* 1998b,a; Otto *et al.* 2003), resulting in some controversy. Questions regarding the range of scales over which such models are relevant

and the pertinence of the approach consisting in modeling the propagation of stress within granular assemblies are not yet settled (Savage 1998; Geng *et al.* 2001; Luding 2005; Atman *et al.* 2009).

The main focus of this work is the behavior of saturated granular pilings, a subject that has received relatively little attention. The consequences of water saturation are not always intuitive (Hansen *et al.* 2001; Daerr *et al.* 2003; Rousseaux *et al.* 2004). The presence of water in the pore medium modifies intergranular friction and cohesion forces, resulting in particular effects that are the subject of recent studies (Geminard *et al.* 1999; Lesaffre *et al.* 2000; Losert *et al.* 2000; Samadani and Kudrolli 2001; Bocquet *et al.* 2002; Gayvallet and Geminard 2002; Van Damme *et al.* 2002; Duong *et al.* 2004; Jain *et al.* 2004; Cassar *et al.* 2005; Loiseleux *et al.* 2005; Divoux and Geminard 2007; Philippe and Richard 2008). The grain-to-grain friction is affected by water at intergranular contacts, through lubrication and, in dynamic conditions, viscosity and fluid-particle interactions. Although liquid bridges create cohesion in partially saturated assemblies (Bocquet *et al.* 2002), causing dramatic changes in properties such as the repose angle (Samadani and Kudrolli 2001), fully immersed granular matter generally has weak cohesion unless particles are sufficiently fine.

The apparent mass (Vanel and Clement 1999; Vanel *et al.* 2000; Bertho *et al.* 2003b; Ovarlez *et al.* 2003; Bertho *et al.* 2004; Tixier *et al.* 2004; Ovarlez and Clement 2005; Liu *et al.* 2009) at the base of a confined granular piling is a conventional measurement, which shows shielding of the mass after a certain depth of material poured in the column, i.e. the apparent mass reaches an asymptote for tall pilings. The deviation from lithostatic behavior, first reported by Roberts, Janssen and Lord Rayleigh (Duran

2000; Sperl 2006), is caused by the redirection of the vertical stress within the granular bulk, in the direction normal to the sidewalls, and the static friction at the walls, which support an increasingly large fraction of the piling mass. Grains at the piling base are subject to the mass of overlying grains only within the shielding length, also called the screening length.

Despite the significant number of existing theoretical and experimental studies on the subject (Cowin 1977; Nedderman 1992; Boutreux *et al.* 1997; Claudin and Bouchaud 1997; Evesque and de Gennes 1998; Wood *et al.* 1998; Vanel and Clement 1999; Masson and Martinez 2000; Vanel *et al.* 2000; Bertho *et al.* 2003b; Landry *et al.* 2003; Ovarlez *et al.* 2003; Bertho *et al.* 2004; Landry and Grest 2004; Tixier *et al.* 2004; Ovarlez and Clement 2005; Abdel-Fattah *et al.* 2006; Brauer *et al.* 2006; Matchett 2006; Niedostatkiwicz and Tejchman 2007; Rahmoun *et al.* 2008; Liu *et al.* 2009), the silo is an example of a granular system for which the behavior has been long-known, but for which there is no model providing an exact description of the granular piling response. On one hand, the pioneering work by Janssen resulted in an *ad-hoc* model for the stress redirection effect, model which is also called the method of differential slices (Nedderman 1992). Although the Janssen model is based on a simplified view of the piling mechanical response (de Gennes 1999; Duran 2000) and only provides a lower bound for the apparent mass (Cowin 1977), its robust reproduction of the shielding effect has contributed to its long-lasting success. One of the limitations of the Janssen model is the lack of a strain-stress relationship since, although the stress field is considered continuous, deformation is not incorporated into the model. The recent OSL model, which involves a refined constitutive equation, derived from the concept of force lines as

preferred directions of yield and stress propagation, is an improvement over the performance of the Janssen model, even though it also lacks a stress-strain relationship (Bouchaud *et al.* 1995; Claudin 1999; Vanel *et al.* 2000). On the other hand, continuum models based on the theory of isotropic linear elasticity have been applied to the geometry of the silo. They provide a description for the piling deformation but the solution is incompatible with the rigid plate at the base of pilings encountered in laboratory experiments and full size silos, and the derivation is valid only in the limit of tall pilings (Evesque and de Gennes 1998; Ovarlez and Clement 2005). Although these approaches are fundamentally different, yielding a system of equations that is hyperbolic for the former and elliptic for the latter, they result in the same equation for the apparent mass as a function of the poured mass. In fact, the Janssen model is designed to encode stress redirection in a fashion similar to basic treatments of the load on retaining walls using the earth-at-rest coefficient, while an elastic cylindrical body confined in a column of the exact appropriate size will show stress redirection as vertical compression results in lateral expansion against the walls of the fitted column. Since granular pilings exhibit lateral stress deflection, both models are equally able to reproduce the measurements, each expressing the shielding length in function of parameters specific to their respective modeling framework. Both models are unable to predict the piling behavior in the conditions of yield, i.e. failures.

Two refinements of the typical silo experiment have been introduced over the last decade. First, the mechanical response of the piling when an overweight is placed at the top surface has been identified as a strong test for granular matter theories (Vanel *et al.* 2000). In particular, when the overweight mass is approximately equal to the free-surface



asymptotic mass, the apparent mass at the base of the overweight piling exhibits an overshoot (Ovarlez *et al.* 2003). Candidate models for granular matter can be assessed by their ability to reproduce the peak, which is especially useful when other features like mass shielding and even other conventional experiment configurations are not sufficiently discriminatory to make model comparisons (Geng *et al.* 2001). The Janssen model does not predict the overshoot (Nedderman 1992; Vanel *et al.* 2000). The OSL theory captures the peak but as the first of a series of oscillations arising from the propagative nature of the model and which are not observed in measurements, possibly because they are diffusively damped (Bouchaud *et al.* 1995; Claudin 1999). Elastic theory predicts an overshoot but with an error over 10-fold on its amplitude, unless an *ad-hoc* piling division separating two sections with different anisotropies is introduced (Ovarlez and Clement 2005).

The second improvement consists in displacing the piling relative to the column walls to mobilize wall friction, which is central to the apparent mass measurement at the piling base because the degree of mass shielding resulting from lateral stress deflection within the granular bulk is contingent upon wall friction mobilization. Experiment procedures allowing the application of boundary conditions, whether by lowering the load cell base or by lifting the walls, were introduced in a few recent studies, yielding a more uniform, better-determined wall-to-grain friction mobilization (Vanel and Clement 1999; Bertho *et al.* 2003b; Ovarlez *et al.* 2003; Bertho *et al.* 2004; Liu *et al.* 2009). For a sufficiently slow boundary velocity, the piling can be regarded as quasistatic, i.e. changes in the piling state, reflected in the mass measured at the base of the piling, occur on sufficiently long time scales that they can be resolved by the load cell. Such protocols,

together with careful data analysis procedures (Claudin 1999; Vanel *et al.* 2000), provide an opportunity to acquire reproducible measurements in the column configuration. Obtaining reproducible data is particularly difficult in the case of granular matter experiments because the properties and behavior of assemblies are related to their construction history. Numerous studies on granular silos conducted with different protocols and over a range of environment conditions illustrate the importance of the method adopted for piling formation and the influence of external constraints exerted on the granular assemblage (Vanel *et al.* 1998; Vanel and Clement 1999; Ovarlez and Clement 2003; Tixier *et al.* 2004). In the absence of consensus on theoretical approaches for modeling the mechanical behavior of granular materials, the reliability and significance of some of the existing datasets has been questioned (Cowin 1977; Brauer *et al.* 2006).

The objective of this study is to investigate the effect of saturation of granular pilings. The apparatus and protocol were validated by acquiring a dataset for dry grains, taking the opportunity to reproduce prior results from existing literature, including the shielding effect as well as the overshoot feature. Water saturated pilings were formed following two different immersion protocols. The organization of the paper is as follows. First the set-up and protocols are described, detailing some technical solutions required to obtain satisfactory measurement resolution and ensure consistency of the pilings. Then the piling response to the load cell base descent is analyzed in details to define the conditions of the measurement of the apparent mass. Results for the piling apparent mass are presented, including the shielding behavior, the influence of the packing ratio and the occurrence of an overshoot in the case of saturated columns. The effect of the pore water

on intergranular contacts and stress distribution in the piling is discussed, with a focus on the stress redirection effect within the granular bulk, which is quantitatively analyzed using the Janssen model. Final thoughts are given on the mechanical behavior of the piling during the descent.

Concerning the terminology, it is useful to mention that the phenomenon of stress redirection or lateral deflection has been referred to as arching in recent studies on the stress state of granular systems (Bouchaud *et al.* 1995; Claudin 1999; Ogale *et al.* 2005; Garcia and Medina 2008). Yet, such usage of the term arching is not entirely in conformity with the typical meaning of arching in soil mechanics, which involves localized yielding, i.e. plasticity, in addition to stress transfer, the transfer being from the yielding mass of soil onto adjoining stationary parts (Terzaghi 1943; Didwania *et al.* 2000). The theoretical approach used in this chapter only assumes the granular material to be at the limit of slippage along the sidewalls, without further constraint other than stability on the stress state within the bulk (see section 2-6.1). Therefore, the term arching will only be used when discussing the formation of granular arches and their role in the mechanical response of the piling to the load cell base descent (see section 2-6.6.2 on a tentative interpretation of the observed relaxation-oscillations). For completeness, it is interesting to note that the only theory of arching to be reproduced in Terzaghi's treatise on soil mechanics (Terzaghi 1943) is in fact based on the method of differential slices. His selected example, the yield of a section of horizontal support, is solved with the assumptions of vertical sliding surfaces above the yielding strip and constant ratio of horizontal to vertical, normal stresses within the in-between fill. The problem at hand in his chapter dedicated to arching therefore becomes virtually the same as that of the

vertical stress at the bottom of a silo. Admittedly, ample cautionary remarks are provided regarding the erroneous assumptions on which such a solution relies.

## METHODS

### Description of the column apparatus

The experiment consists in measuring the weight at the base of a granular piling in a configuration similar to silos or bins. The grains were poured into a laterally-confining cylindrical column (Fig. 2-1). The top of the granular assembly was either left as a free-surface boundary or loaded with a cylindrical overweight placed after the grains were poured. The bottom of the piling was supported by a piston that fits inside, but is not mechanically connected to, the column (Fig. 2-1A). The aluminum piston was anodized to avoid corrosion problems. The force exerted on the piston was measured with a submersible load cell (LC, jr S-beam model QLA150 by Futek) attached to the bottom of the piston. The base of the load cell was attached to a nut that was vertically driven by a brass, micrometric screw (MS). The screw was connected to a computer-controlled, optically-encoded stepper motor through a gear box (MG). Dampers were installed on the gear train so that the piston was decoupled from motor vibrations.

The choice of the piling base descent velocity is known to have a strong influence on the piling behavior, at least for dry pilings (Vanel and Clement 1999; Bertho *et al.* 2003b; Ovarlez *et al.* 2003), especially at extreme levels of humidity (Bertho *et al.* 2004), and thus impacts the interpretation of the mechanical response of the piling. The descent velocity was set at 1.7 micrometers/s, corresponding to a steady, quasistatic regime. No

significant velocity-sensitivity is expected at the prevailing relative humidity range (37%-43%). The initial acceleration was slow, about  $7.65 \text{ micrometer/sec}^2$ , to avoid major piling rearrangement when starting the descent. A steady descent velocity was reached after 0.22 sec, corresponding to a displacement of about 0.2 micrometers. The load cell stiffness needs to be chosen with care (Tixier *et al.* 2004). With a stiffness of  $8.8 \cdot 10^5 \text{ N/m}$ , the load cell was notably more compliant than the piston and the screw, significantly less compliant than the piling, and sufficiently compliant to distinguish the different phases of the piling response to the load cell base descent (see section 2-4.1).

The grains used are non-cohesive, non-coated, 1 mm diameter soda-lime glass beads (manufactured by GlennMills), with a density of  $2.53 \text{ g/cm}^3$  and 95% sphericity. They are slightly polydisperse with an actual size distribution ranging from 0.8 mm to 1.2 mm (Fig. 2-1B). The finite size and the shape dispersion of the grains tend to create disorder in the packings, avoiding ordered piling configurations that can have different mechanical properties (Geng *et al.* 2001).

The column is a transparent cast acrylic tube of approximately 6.5 mm wall thickness and 10 cm inside diameter. The ratio of grain to column diameter was 1:100, which is much smaller than in actual granular systems such as grain silos for instance, but also larger than in recent laboratory studies on confined piling (see (Vanel and Clement 1999; Ovarlez *et al.* 2003; Liu *et al.* 2009) for example). The use of cast acrylic ensured sufficient tensile strength to keep mechanical deformations small (about 2 nm of radial deformation at the exerted pressure). The column inside wall was machined to a round section within 25 micrometers. The inner wall was sanded in order to remove the machine-induced grooves and obtain a homogeneous roughness. The working height of

the column above the piston is about 1 m. Three rods connected the top of the column to the base of the apparatus to provide mechanical stabilization. A self-lubricating Teflon ring (TR) was attached around the top of the piston (Fig. 2-1), leaving a 200 micrometer gap between the edge of the ring and the inner wall of the column, which provided sufficient space to allow the piston to self-adjust for vertical movement while preventing grains from slipping past the ring.

The whole apparatus is water-tight owing to an o-ring (O-R) seal between the seat and the flange at the bottom of the column (Fig. 2-1A). The water was transferred in and out of the column through a 3 mm hole (H) located at the very bottom of the column, below the load cell. Hence, for experiments on liquid-saturated pilings, the entire column was immersed, including the load cell. The measured mass at the base of liquid-saturated pilings corresponds to buoyant conditions, i.e. not accounting for the contribution from hydrostatic pressure. Fresh water was used in all liquid-saturated runs.

All mechanical parts were free of metal polish or a finishing coat to avoid contamination of grains with surfactants or chemical compounds. This point is critical as grain-to-grain friction directly depends on surface properties. During initial experiments, not shown in this paper, a very large drift, up to 50%, was observed in the measured mass. Precise measurements of the surface tension of water in which samples of grains used in experiments had been stirred showed a reduction in surface tension, which was getting more significant with grain usage. Values around 60 mN/m were measured, compared 72 mN/m for the control water sample. This suggested a progressive contamination of the grains. The source of the surfactants was identified as the metal

finish of the pail used to pour grains, which was then eliminated and the experiment started over.

The apparatus was tested and, when required, improved to ensure that its sensitivity was sufficient to resolve the characteristic features of the measured mass at the piling base. System properties, such as static friction between the self-adjusting piston and the column wall in the dry case, electric noise induced for example by random phase lags in the position of the poles of the coil in the motor at rest, and load cell drift were investigated and mitigated. In order to obtain a baseline voltage characteristic of the column without a piling but otherwise in the same conditions as when measuring the piling mass, the load cell output was recorded at the beginning of each run before pouring the grains and while lowering the load cell base. Subsequent readings were taken in reference to this value. The final linearity and repeatability of the measurement system were respectively within 2 g over the 1 kg experiment range, and between 2 g at the 50 g low end and 10 g at the 1 kg high end of the experiment range. These measurement errors are significantly less than the measurement fluctuations caused by random realizations of pilings from run to run (see Fig. 2-8A and section 3.6) and of the same order as the weight of a horizontal slice of dry piling with a thickness of 1 grain diameter (13 g). Other sources of measurement error, wear and electrostatic charges on grains, are discussed in section 2.2.2.

## **Data acquisition protocol**

### *Overview of the dataset*

A data point consists of ensemble measurements, which improves the reproducibility of the experiment results by reducing the run-dependant variability of piling configuration. One run corresponds to pouring a known mass of grains in the column and measuring the mass at the base of the piling formed, which yields a single measurement. Each data point consists of an average of 10 measurements, corresponding to 10 piling realizations for a fixed poured mass. Finally, a dataset consists of the collection of data points for a specified piling type. Datasets were acquired for 5 piling types: 1) dry piling without overweight, 2) dry piling with overweight, 3) immersed piling without overweight, 4) immersed piling with overweight and 5) settled piling without overweight. The last 3 datasets concern liquid-saturated pilings with two different methods of piling formation. For the 5<sup>th</sup> dataset, the data points consist of averages over only 5 measurements at each fixed piling height. Measurements are plotted in terms of apparent mass versus poured mass or apparent height versus poured height. The apparent and poured heights are obtained from  $h = m/(A\rho)$ , where  $m$  is the apparent or poured mass,  $A$  the cross section of the piling inside the column and  $\rho$  the bulk density of the granular assembly. In the case of liquid-saturated pilings, since the load cell records differential pressure when it is submerged, the bulk density, the apparent mass and the poured mass are reduced by buoyancy effects.

#### *Sequence of events that occur during a run*

Here, the general sequence of a run is described in the case of dry, free-surface pilings. Additions to the sequence specific to overweight or liquid-saturated pilings are discussed later. The experiment protocol was designed with the primary objective of



obtaining reproducible piling states. At the beginning of each run, a reference baseline for the load cell output voltage was collected before any grains were poured into the column (see section 2-3.1.3). Then, a pre-determined mass of grains, known to within 2 g, was poured through a funnel to form a piling. A short interval after piling formation ( $< 10$  s), the load cell base was lowered to mobilize the grain friction at the column wall and allow an estimate of the apparent mass at the base of the piling. A typical descent was recorded for 45 s, although full mobilization of the wall friction was always established within 7 s (see section 2-4.1).

The piling structure and texture (Radjai *et al.* 1998; de Gennes 1999) are influenced by its formation history (Vanel and Clement 1999). Here, the funnel was not filled so that the granular outflow was not a typical funnel discharge. The grains exited the funnel spout as a wide beam and fell in a rain-like, distributed fashion, hitting the side wall before reaching the free surface and impacting the free surface at random angles and locations over the inside column cross-section. There was probably no preferred avalanche direction as the grains came to rest on the free-surface and were subsequently covered by other grains, yielding a homogeneous piling. The free-surface boundary was near-horizontal, which made it possible to read the piling height with 1 mm accuracy. The resulting dry piling had a packing ratio of about 63%, near the random close packing fraction, consistent with energetic conditions of piling formation.

After each run the grains were vacuumed out of column, so that every run corresponded to a unique piling realization where the entire piling was only subject to load cell base descent once. A given batch of grains was reused about ten times. Multiple runs were performed in random order at each single usage of a given batch. The usage

number (one cycle of pouring and vacuuming) associated with a batch was recorded to investigate possible effects associated with reusing grains. The piston was readjusted after a run so that its descent always started from the same position in the column.

The glass beads and the acrylic column both had a tendency to accumulate electrostatic charge. Vacuuming the grains aggravated the phenomenon. Accumulation of electrostatic charge is associated with small-scale modifications of the grain surface properties. The resulting effects on the frictional properties of intergranular contacts could not be measured here. So, to keep the build-up of electrostatic charge to a minimum, all containers used to handle, weigh, store and pour the grains were metallic and the entire experiment apparatus was grounded. The inside wall of the column was wiped with a slightly damp cloth after each run, leaving sufficient time for residual moisture to dry before the next run. After the vacuuming step, the grains collected were sieved through a grounded wire mesh with an opening of about 2 grain diameters to remove most surface charges before reusing them. In addition, the column and piston were periodically taken apart to be thoroughly rinsed in order to remove potential contaminants or dust.

#### *Pilings with Overweight*

For the overweight datasets, an aluminum cylinder, a little smaller in cross-sectional diameter than the inner column, was lowered and gently placed on top of the piling before starting the load cell base descent. The overweight rested horizontally on the leveled piling surface without touching the inner wall of column. Although the surficial layers of grains were affected by this change in boundary conditions, as some

grains were displaced into the gap between the overweight and the column wall, there were probably no major rearrangements below the upper section of the piling since the piling height, and thus the packing ratio, did not change between dry, free-surface and dry, overweight runs. Time intervals between end of piling formation and overweight positioning as well as between overweight positioning and start of load cell base descent were short ( $< 10$  s). The mass of the overweight was similar to the asymptotic apparent mass of free-surface pilings.

### *Immersed pilings*

The protocol for immersed piling runs consisted of pouring grains to form a dry piling, slowly raising the water level inside the column to avoid major piling disturbances, and then starting the load cell base descent. Piling immersion began shortly after piling was formed ( $< 10$  s). The flow of water into the column was driven by a pressure head on the order of a meter and stopped at a 5 cm water depth over the piling free-surface. In the case of overweight pilings, the water depth was sufficient to fully submerge the overweight that was placed after piling immersion. No grain motion was observed during immersion, even at the base of the piling where the water flows in through the narrow gap between the Teflon ring around the piston and the column wall. The behavior of the piling during immersion is further discussed in section 5.5.

The time interval between the end of the immersion and the next step in the protocol, either load cell base descent for free-surface pilings or positioning of the overweight for overweight pilings, was short ( $< 10$  s). At the end of a run, the grains were laid on plastic mesh and oven dried at 40 degrees C, and residual water was dried

off the column inside wall so the piling of the following run was formed in dry conditions.

Since the packing ratio has a large influence on the shielding intensity (Ovarlez *et al.* 2003), a key objective in using the same piling construction method until submersion was to obtain comparable packing ratios in the dry and immersed cases in order to investigate the role of water as pore medium. The resulting packing ratios are smaller for immersed pilings than for dry pilings by only about 1%, which is comparable to the packing ratio resolution caused by piling height reading error. As for dry pilings, the packing ratio for immersed pilings did not change between free-surface and overweight runs.

### Settled pilings

The experimental procedure for settled pilings was meant to reproduce conditions corresponding to settling of particles through a liquid, such as marine sediments deposition, and test the influence of the piling formation and the packing ratio. The column was filled with sufficient water at the beginning of a run so that the piling surface remained at least 5 cm below the water surface. The water depth was such that falling grains almost always attained terminal velocity, which was significantly lower than for the dry and immersed pilings, before reaching the top of the piling. The reduction in energy associated with settled piling formation caused a significant decrease in the packing ratio, which was estimated to be 59%.

In general, the free-surface of settled pilings was tilted by up to 15 degrees from the horizontal. As the grains were settling, re-circulating eddies of a few centimeters in

height were observed just above the piling free-surface. The eddies were axially asymmetric with respect to the vertical axis at the center of the column and a majority of the grains were deflected away from the larger eddy as they settled. I believe these vortices caused the piling free-surface to be slanted. Piling height reading was only accurate to within 2 mm, i.e. 2 grain diameters, because of the increased difficulty in determining the mean level of the free-surface. However, the corresponding absolute error on packing ratio was 1%, which is 4 times smaller than the difference in packing ratio between the immersed and settled pilings.

Shortly after the piling was formed ( $< 10$  s), the water level in the column was lowered to about 2 cm above the piling free-surface and subsequently raised to 5 cm above it, with the intention of reproducing the same final flow conditions as for the immersed pilings. The effect of dynamic forcing of the pore fluid on the internal piling structure is unknown, but may be significant even at the low fluid velocities typical of the experiments. Additional questions regarding the saturation procedure used for settled pilings are discussed in section 5.5.

### **Data processing**

In order to obtain a run output, the load cell output is amplified, low-pass filtered with a 2 pole 10 Hz analog filter, sampled at 1 kHz with a 16 bit analog to digital converter and then passed through an additional 5 Hz finite impulse response equi-ripple filter. The start of the load cell base descent is precisely identified for each run by detecting a local minimum in the voltage output derivative within a narrow window around the time of descent start recorded during the experiment. Then, the run baseline is

subtracted from a 35 second-long record starting at the beginning of the load cell base descent to constitute the output of a single run.

### **Measurement of wall-to-grain friction coefficient and repose angle**

The wall-to-grain dynamic friction coefficient was measured for the experiment set-up with a device resembling the leaf spring slider used in (Ovarlez *et al.* 2001). Measurements were done on the column section occupied by the bottom of the piling to obtain a friction measurement typical of the wall surface where shielding occurs for all piling heights. A bore gauge (T-shaped device used to measure a bore's inside diameter and which horizontal head consists of two telescopic rods enclosing a coil, compression spring) was attached to the top of the piston and applied a 1.5 N normal force on grains glued on two tapered extensions fitted over the extremities of the bore gauge's rods. This system was in a steady-sliding regime during load cell descent, when the tangential wall-to-grain friction force was evaluated. Measurements were acquired both in dry and immersed conditions, yielding wall-to-grain friction angles of  $\theta_{dry} = 20$  degrees and  $\theta_{saturated} = 21.5$  degrees, with a precision of 4 degrees. The penetration depth at the wall-to-grain contact interface, determined from the normal contact force using Hertz theory, was about 40 times larger during the friction measurements than during piling experiments. The difference in loading regime may affect the frictional properties of the wall-to-grain contact (Abou-Chakra and Tuzun 1999).

To measure the repose angle of the glass beads, a conical pile was poured on a dish from a gradually raised source kept at a constant, very small distance ( $< 1$  cm) from

the apex of the pile. The saturated pile was formed underwater from already immersed grains. The measurement process was repeated 5 times. The repose angles obtained are  $\phi_{dry} = 23.5$  degrees and  $\phi_{saturated} = 23$  degrees, with a precision of 2 degrees. Samadani and Kudrolli (Samadani and Kudrolli 2001) also found little difference in the repose angle of dry and underwater piles formed with glass beads.

### LOAD CELL DESCENT

As discussed in the introduction, a key objective of the experiment approach must be to establish boundary conditions at the piling wall that are both reproducible and known. Understanding the behavior of the piling during the descent phase of the load cell base is central to this goal, and discussed in detail here. Fig. 2-2A shows the general structure of three run outputs, each corresponding to a different piling height for a dry, free-surface run. The vertical axis is effective mass at the piston and the horizontal axis is displacement of the load cell base calculated from time and knowledge of the load cell base velocity. As the load cell base is lowered, the measured mass decreases by about 25% to 50% until it approaches an approximately constant value. The decrease in measured mass is not monotonic, and temporary increases can be observed, superposed on the overall trend. Overall, the mean trend can be approximated by an exponential decay starting shortly after the beginning of the load cell base descent. Analysis of many such runs has shown that the variation in measured mass as the load cell base is lowered can be divided into three successive regimes, discussed below.

### **Overview of the three piling regimes for dry, free-surface pilings**

The three distinct regimes that occur during the descent of the load cell base have been annotated in Fig. 2-2B, which shows an expended view of the middle curve in Fig. 2-2A. The first regime is characterized by a linear decrease in measured mass with load cell base displacement. During the second regime, the measured mass continues to decrease, but at a slower and decreasing rate. Finally, the third regime occurs when the measured mass has stabilized near a minimum value (Fig. 2-2B). The run outputs present a definitive change in slope between the first two regimes, while the transition between the last two regimes is more difficult to determine (Fig. 2-2B).

The measured mass in the third regime is not constant because of events characterized by a sudden increase in measured mass immediately followed by a return to about the same minimum value (Fig. 2-2A). I interpret these features as relaxation oscillations. They sometimes occur during the second regime as well, and in general start after less than about 10 micrometers of load cell base displacement. The interpretation and significance of the relaxation oscillations and their variations in amplitude and frequency from run to run are discussed later (see section 2-6.6.2).

The three regimes identified in Fig. 2-2B correspond to successive phases of the mechanical response of the confined piling during the load cell base descent, and each has a specific physical significance for the piling state. The first regime corresponds to expansion of the load cell while the piling, at least at its base, is jammed upwards due to load cell over-compression induced by the kinetic energy transferred from the falling grains. The piling response is then purely elastic. Since the jammed lower piling is stiffer than the load cell, the load cell base descent is accommodated by expansion of the load



cell while the piling remains essentially stationary. If non-zero, the piling base displacement is smaller than 25 nm, which is the resolution of our system for the load cell expansion (see section 2-4.3). The change in measured mass of the piling over time during this regime is given by  $m(t) = m_o(k/g)Vt$ , with  $m_o$  the measured mass before the start of the load cell base descent,  $V$  the descent velocity,  $k$  the spring constant of the load cell,  $g$  the gravity constant and  $t$  the time. I label this phase as the elastic regime.

The second regime corresponds to the mobilization of grain friction at the column wall, starting as the piling base descent begins. In the second regime, the upward force exerted by the expanding load cell on the piling has decreased sufficiently that the wall-to-grain friction at the base of the piling changes orientation from downward to upward. Reversal and full mobilization of wall friction is extended beyond the bottom section of the piling by progressive loosening of the underlying sections that are displaced downwards. Therefore, the duration of this regime is related to the piling height, and ranges from 1 to 7 seconds, i.e. about 1.5 to 12 micrometers (Fig. 2-6). A 10 micrometers piling base displacement corresponds to 1% of a grain diameter. I label this phase as the decompression regime.

Finally, the third regime starts after the full friction mobilization has been progressively achieved over the entire piling length. Except during relaxation oscillations, the measured mass remains close to a minimum corresponding to the situation where the wall friction is everywhere at the dynamic limit of slippage, the fraction of the piling mass supported by the lateral wall is maximum and the piling is slipping at the descent velocity of the load cell. Hence, this regime consists of a steady descent of the piling with relaxation oscillations. I label this phase as the relaxed regime.

### **Analysis of the load cell output slope**

Each of the three regimes exhibits a distinct mean slope of measured mass versus load cell base descent. This is illustrated in Fig. 2-3, which shows the ensemble averages of the mean output slopes for all piling heights for dry, free-surface pilings. The slope for the first regime represents an average across the regime. The slope for the second regime represents an average from the start of the regime to a single e-folding distance determined from a least-mean-square exponential fit to the run output. The slope for the third regime represents an average taken from 17 micrometers to 59.5 micrometers load cell base descent, which was always well within the third regime.

The average output slopes in the elastic regime fall right along the load cell stiffness obtained from independent calibration measurements over the whole range of the experiments. The stiffening of load cell with compression is well-matched by the increase of average slope of the run outputs with increasing output voltage, in the elastic regime (Fig. 2-3). In the decompression regime, the average output slope is non-zero and smaller than the load cell stiffness, which corresponds to the diminishing rate of decrease of the measured mass as it approaches its minimum value. Average slopes during the decompression regime are larger for taller pilings than for shorter pilings: as the change in measured mass during the decompression regime increases with piling height, so does the rate of change in measured mass near the beginning of the decompression regime. This confirms that the decrease in the measured mass during the decompression regime is dependant on the piling height. Not only does the regime duration increase with piling height, but so does the residual stiffness of the piling at the beginning of the regime. The

output slope in the relaxed regime averages to zero for all piling heights, independent of the expansion state of the load cell. This is consistent with the steady descent of the piling without overall change in measured mass, except for the transient relaxation oscillations.

### **Analysis of the piling base displacement**

The analysis of the piling base displacement, derived from the available parameters and outputs of the experimental system, confirms our interpretation of the physical significance of the three regimes observed (Fig. 2-4). The deformation of the load cell can be directly derived from its output voltage and the load cell stiffness determined by calibration experiments. The displacement of the piling base is then obtained by subtracting the measured load cell expansion from the load cell base displacement ( $D_p = D_{LC} - e$ ). Fig. 2-4 indicates that the elastic regime corresponds to load cell expansion while the piling is immobile and that the well-defined transition to the decompression regime corresponds exactly to the beginning of the piling base descent. In the decompression regime the load cell continues to expand while the piling base moves downward. Approaching the relaxed regime, the load cell stops expanding overall and the piling base displacement follows the load cell base displacement.

### **Choice of the apparent mass**

Drawing from these observations, a systematic procedure is defined and applied to all run outputs to detect the termination of the elastic regime as the beginning of the piling base displacement. In practice, it is the point when the ratio of the piling base displacement to load cell base displacement, which varies from 0 to 1, reaches the

threshold of  $1/3$ . The load cell expansion is not derived from the load cell stiffness observed in calibration experiments because the stiffness response of the load cell is not exactly reproducible (see the variance in the stiffness in Fig. 2-3). Instead, an initial output slope representative of the elastic regime is used to ensure a more accurate determination of the beginning of the decompression regime. The initial slope is evaluated well within the elastic regime very near the maximum slope. Because the load cell stiffness depends on its deformation state, i.e. it decreases with decreasing output voltage (Fig. 2-3), this initial slope is not exactly adequate to assess the load cell expansion beyond the elastic regime. The resulting over-evaluation of the piling base displacement amounts to less than 1% error at the end of the decompression regime, and does not increase during the relaxed regime owing to the overall non-expansion of the load cell.

The choice of the apparent mass at the base of the piling from the measured mass record corresponds to conditions of full mobilization of the wall-to-grain friction over the entire piling height, while keeping the piling displacement small enough to prevent major piling rearrangements. The apparent mass is chosen during the decompression regime that constitutes an intermediate phase between the elastic and relaxed regimes, neither of which strictly satisfies the above requirements (see sections 3.1 and 5.6.2). In practice, the best exponential fit to the second regime of the run output is estimated from a least-mean-square regression. Then the apparent mass is taken as one e-folding distance on the exponential fit. This regression method is global as it uses all of the available data from the relevant regime. The fixed parameters used in the fit are the point where the piling descent starts, as the origin, and the measured mass characteristic of the relaxed regime,

as the asymptote. The asymptotic value is calculated from the filtered data after suppressing fluctuations more than one standard deviation away from the mean to exclude most of the relaxation oscillations, as they do not characterize the conditions of fully mobilized wall friction right before slippage. This procedure keeps the piling base displacement at the point chosen as the apparent mass within about 10 micrometers for all run outputs (Fig. 2-6).

### **Applicability of the analysis to dry and saturated pilings with free-surface and overweight**

Although the data analysis procedure was primarily based on the interpretation of the dry free-surface dataset corresponding to the conventional silo experiment, it is supported by observations that are common to all the acquired run outputs and is therefore applicable to the entire dataset. In particular, overweight and immersed pilings consistently show the three regimes that characterize the response of the entire mechanical system during the load cell base descent. Subtleties in some characteristics of these regimes are discussed below.

For all three regimes, the average output slopes are similar between dry and immersed pilings of the same height and same boundary conditions at the top of the piling. Piling immersion causes a reduction of the load cell voltage output due to buoyancy effects while leaving the load cell output slope unchanged, therefore shifting the data points for immersed runs to the right on Fig. 2-5. A noticeable consequence is that the average output slopes for the elastic regime in the immersed case lie over the calibrated load cell stiffness while they are systematically below the calibration curve in

the dry case (Fig. 2-5). The difference arises from the piling response to the load cell descent, since immersion does not affect the load cell stiffness. The piling behavior, and in particular its stiffness, appears to be closely related to the formation procedure, whether or not the piling is subsequently immersed. In addition, as expected from the overshoot amplitude (see (Ovarlez *et al.* 2003) and Figs. 2-9A, B), the range in average output voltage over all piling heights is smaller for each of the three regimes when comparing overweight runs to free-surface runs (Fig. 2-5).

The piling displacement at the point chosen as the apparent mass is significantly smaller for shorter piling compared with medium and tall pilings (Fig. 2-6), confirming that the friction mobilization is very rapidly achieved over the entire piling height when the piling is short enough. Piling displacements corresponding to the apparent mass are also systematically larger in the overweight cases than in the free surface cases for a fixed piling height (Fig. 2-6), suggesting that the mobilization of wall-to-grain friction is affected by presence of the overweight. Tallest pilings constitute an exception to this last observation, indicating that for sufficiently tall pilings the mechanical response of the granular assembly near the top of the piling does not affect the wall friction mobilization of the lower piling, which determines the measured mass at the piling base. In addition, piling base displacements corresponding to the apparent mass measurement are about twice as large in the immersed case than in the dry case (Fig. 2-6). The presence of water at the wall-to-grain contact may increase the anchoring length (see (de Gennes 1997) and section 5.6.1).

### **Efficacy of the data analysis procedure**

The analysis of the standard deviation of the measured mass reinforces our interpretation of the mechanical behavior of the confined piling during the load cell descent and our choice for the apparent mass. Except for short pilings, standard deviations of the measured mass evaluated at the beginning and end of the elastic regime are very similar and double the standard deviation of the apparent mass (Fig. 2-7A). The piling state is more reproducible at the chosen apparent mass than at the beginning and the end of the elastic regime, consistent with wall friction mobilization occurring during the decompression regime. Short pilings do not exhibit a marked decrease in standard deviation of measured mass during the decompression regime because piling state variability affects measured mass through shielding, which only occurs beyond a certain piling height.

The standard deviations of the apparent mass ensemble values are on the order of 20 g for most data points (Fig. 2-7B), ensuring that the experiment set-up has sufficient resolution to test the Janssen-like behavior and the overshoot effect in immersed conditions. Such fluctuations between piling realizations for a fixed piling height are caused by the random character of granular assemblies and should not be confused with the measurement error related to the performance of the apparatus. They range from 5 g for short pilings to about 50 g for taller pilings (Fig. 2-7B) and increase at a steady rate that does not appear to be exactly proportional either to poured mass or to apparent mass. The effect of run-to-run variability in piling configuration, which plays a role in the mass shielding mechanism, is more significant for taller pilings where shielding is most intense.

Overweight runs corresponding to the range of piling heights where the apparent mass is expected to decrease from the overshoot peak to the asymptotic level (Ovarlez *et al.* 2003) have larger standard deviations, almost double that of free surface runs with the same piling height. The shielding intensity is evidently even more dependant on small changes in piling configuration at such piling heights that are near the shielding length (see section 2-6.1). Standard deviations for immersed pilings are a little larger than but comparable with those of dry pilings, except in the case of short immersed overweight pilings where they are five times larger than for short dry overweight pilings. Other than increased sensitivity of shielding intensity on piling configuration, the authors are not aware of a particular cause for such high standard deviations, up to 70 g, for short immersed overweight pilings. However, even these larger standard deviations are well below the expected amplitude of the overshoot peak relative to the asymptotic level.

### **The effect of grain usage on apparent mass**

The run-to-run fluctuations in the apparent mass measurements for a fixed piling height show a positive trend with grain usage (Fig. 2-8A) for dry pilings, interpreted as an alteration of the surface properties of the grains. This systematic part of the standard deviation is of the same order of magnitude as the remaining fluctuations that are random. The positive slope of the linear fit for dry pilings consistently increases with piling height (Fig. 2-8B), without showing direct proportionality between the effect of grain usage and the poured nor the apparent mass. The drift is interpreted as a result of alterations of the surface properties of the grains while handling them, including the



introduction of contaminants from contact with other materials, physical wear and changes in the chemical properties linked with electrostatic charge issues and mitigations.

In the case of immersed pilings, the dependence of the apparent mass on the usage number of the grains is not as pronounced (Fig. 2-8B). The usage trend is not increasing with piling height, and is even negative for some piling heights. The presence of interstitial water may be responsible for the absence of a marked dependence on grain usage, for example by removing contaminants or dust particles eroded from the surface of the grains, hence suppressing some of the consequences of usage. The large positive trend for short immersed pilings with overweight is probably related to the high standard deviations observed for such pilings (see Fig. 2-7B and section 3.6). In addition, the analysis of the standard deviation of the apparent mass shows that while detrending the data would improve the reproducibility by a factor of two in the dry case, it would leave the standard deviation almost unchanged in the immersed case (Fig. 2-8C), which confirms that grain usage does not have a systematic effect on the apparent mass of immersed pilings.

Given the relatively small magnitude of the observed trend with usage, the lack of strong evidence to identify its cause for dry pilings and its inconsistency for immersed pilings, the data was left as is in all cases. Removing the trend would not have changed any of the results of this paper, besides a small reduction of the asymptotic mass and the shielding length (see section 2-6.1) in the dry case.

Although the grains showed evidence of changes in surface properties with usage, modifications in the surface properties of the column inside wall were not significant. At the end of the data acquisition, a series of 10 runs was performed to repeat one data point

for dry, free-surface pilings. The difference in the ensemble average of the apparent mass between the original and newly acquired data points was 1g, which is well within the error of the experiment apparatus. The standard deviations of the two ensemble measurements were comparable, indicating that the range in piling configurations was also preserved. Alteration of the inside wall surface through wear or contamination while using the apparatus is possible but had no measurable effect on the apparent mass. Surface preparation (sanding) of the column inside wall and regular maintenance of the set-up probably contributed to preserving consistent experiment conditions and were therefore beneficial to measurement reproducibility.

## **RESULTS FOR THE APPARENT MASS OF PILINGS**

In the following, data are plotted as apparent mass versus poured mass, which is the convention most commonly encountered in the literature. However, I will often refer to piling heights in terms of either meters or grain diameters. Given the changes in bulk density between pilings, whether they are dry, immersed or settled, a good rule of thumb is that a poured mass of 1 kg corresponds to a piling height of 77 grain diameters in the dry case, 129 grain diameters in the immersed case and 139 grain diameters in the settled case.

The Janssen model, which has been fitted to all the free-surface curves, has one free parameter amounting to a shielding length. Estimates of this length for the free-surface datasets respectively are  $\lambda = 6.1$  cm,  $\lambda = 8.2$  cm and  $\lambda = 14.5$  cm for the dry, immersed and settled free-surface pilings. Standard deviations for a selected data point

are shown as a reference for the measurement dispersion (Figs. 2-9A, B, 2-11A, and 2-12A), and a complete plot of the standard deviations can be found in Fig. 2-7B.

### **Dry pilings results: free surface and overweight**

The apparent mass of dry, free-surface and dry, overweight pilings is plotted against poured mass in Fig. 2-9A. The curves show that the evolution of the apparent mass is smooth in both cases, but monotonic for free-surface pilings only. The overweight pilings are characterized by an overshoot followed by a decay for increasing poured mass.

The apparent mass of free-surface pilings initially increases linearly with the poured mass. However, measurements deviate very rapidly from lithostatic behavior, starting at pilings about 20 grain diameters high. Then, the rate of increase in apparent mass decreases regularly with the poured mass. The apparent mass, measured at the base of the piling, of grains poured in the column is progressively shielded as the piling is built-up. After a piling height of about 200 grain diameters, corresponding to four times the piling radius, the free-surface apparent mass reaches an asymptote. The asymptotic apparent mass is equivalent to the poured mass of a piling of about 55 grain diameters, corresponding to 1.1 times the piling radius.

For overweight pilings, the mass applied on top of the piling is a little smaller than the free-surface asymptote (Fig. 2-9A). The apparent mass of very short pilings, up to 10 grains high, also follows a lithostatic response. Then, the rate of increase in apparent mass with poured mass also decreases, but more rapidly than in the case of free-surface pilings. The apparent mass becomes quasi-stationary for piling heights ranging

from 35 to 70 grain diameters, constituting a broad maximum. Beyond this height, the piling apparent mass decreases towards roughly the same asymptote as the free-surface case. The decay from the wide peak observed for tall pilings is somewhat slower than the increase to the overshoot observed for short pilings.

Close observation of the overweight case reveals small variations, equivalent to the poured mass of one grain layer, occurring in the densely sampled range of data corresponding to short pilings. Perhaps such variations, which could be interpreted as small oscillations, are not observed in the rest of the curve because there are too few data points.

### **Immersed piling results: free surface and overweight**

The apparent mass of immersed, free-surface and immersed, overweight pilings is plotted against poured mass in Fig. 2-9B. The overall shapes of the curves are somewhat similar to the dry case, and show a convergence to an asymptote for free-surface pilings and an overshoot for overweight pilings. However, the apparent mass of immersed pilings is less smooth than in the dry case. The overweight pilings exhibit slow variations, equivalent to the poured mass of 2.5 grain layers, that could be interpreted as oscillations on the downward side of the peak.

For free-surface pilings, the lithostatic behavior lasts up to piling heights of about 20 grain diameters, as in the dry case. The asymptote is reached for pilings around 200 to 250 grain diameters, which is slightly taller than in the dry case. The asymptotic apparent mass is equivalent to the poured mass of a piling of about 75 grain diameters, corresponding to 1.5 times the piling radius.

For overweight pilings, the lithostatic phase is limited to short pilings, less than 10 grain diameters. The peak is not as broad as in the dry case and occurs for shorter pilings, spanning the 15-30 grain diameters range.

### **Comparison of overshoot responses between dry and immersed pilings, and with previous studies**

The dry, overweight and immersed, overweight datasets normalized by the corresponding free-surface apparent mass asymptote are plotted in Fig. 2-10. Three normalized datasets from two previous studies (Vanel *et al.* 2000; Ovarlez *et al.* 2003) are included for comparison. Although the datasets were acquired with different set-ups, grains and experiment protocols, making direct comparison problematic, the similarity in piling behavior between the datasets is encouraging. The three dry, overweight datasets (shown in gray in Fig. 2-10) exhibit the same overall pattern of rapid overshoot for short pilings followed by a slow asymptotic decay to the free-surface asymptotic mass.

The Ovarlez *et al.* data, plotted as a solid gray line in Fig. 2-10, was acquired following a procedure similar but not identical to this study (see (Ovarlez *et al.* 2003) and section 5.6.1), which makes a comparison particularly relevant. The main difference is that the Ovarlez *et al.* overweight mass was equal to the asymptotic free-surface mass, whereas it was 0.94 times the asymptotic free-surface mass in the present study. The overshoot and decay of the apparent mass curve are comparable to the present study. Although the normalized amplitudes of the peaks are comparable, the peak observed in their dataset is significantly narrower.

The other two datasets were acquired following a procedure where the load cell descent velocity was 10 times larger than used here, and data was collected with only one run for each data point. The values for their overweight normalized mass are 0.93 and 1.33, i.e. either a little smaller or significantly larger than the asymptote. The oscillations in the curves and the width of the peaks are likely caused by the random character of piling configurations. These two datasets are shown to illustrate the influence of the mass of the overweight on the overshoot response. As the overweight normalized mass increases, the peak occurs at smaller piling heights and reaches a larger normalized apparent mass (Vanel *et al.* 2000). This is consistent with observations from the present study, looking at the evolution of the overshoot response between the dry case where the normalized overweight mass is 0.94 and the immersed case where the normalized overweight mass is 1.22. Obviously, water may also contribute to the difference in the observed overshoot response.

### **Consequences of saturating dry, free-surface pilings**

The apparent mass and apparent piling height at the base of dry, free-surface and immersed, free-surface pilings are plotted in Figs. 2-11A, B. Fig. 2-11A shows apparent mass versus poured mass, which is the usual presentation for this data on confined pilings. In the immersed case, the presence of water decreases the bulk density of the piling by a factor of 0.61. The change in the bulk density can be accommodated in the data presentation by plotting the apparent piling height versus poured height, as shown in Fig 11B. All other factors being equal, we would expect curves of apparent piling height made with grains of variable density to collapse.

Least-mean-square fits of the Janssen model to the data are plotted as gray, solid lines in the figures. Both dry and immersed pilings show Janssen-like behavior, although quantitative agreement is better in the dry case than the immersed case. The RMS error of the best least-mean-square fit to the dry, free-surface pilings is 9 g, or 1.1% of the asymptotic apparent mass, whereas the RMS error in the immersed case is 18 g, or 2.7% of the asymptotic apparent mass.

Fig. 2-11A shows that saturating the dry, free-surface piling decreases the asymptotic apparent mass by approximately 20%, whereas the reduction in bulk density accompanying saturation would result in an expected reduction of approximately 40%, other factors being equal. Evidently, saturating the piling has also increased the shielding length, partially offsetting the reduction in mass due to buoyancy. Fig. 2-11B shows the increase in shielding length accompanying saturation more clearly, from 6.1 cm to 8.2 cm. This weakened shielding behavior reflects changes in the mechanical response of the piling induced by saturation.

### **Consequences of forming saturated pilings through settling versus immersion**

In the above section, I examined the different responses of dry versus immersed pilings. Here, the comparison is between two different piling formation procedures, both pilings being saturated. The procedures, described in sections 2.2.4 and 2.2.5, result in different packing ratios (0.63 for the immersed piling and 0.59 for the settled piling: see Fig. 2-13) and, presumably, other changes in piling configuration. The immersed, free-surface and settled, free-surface curves are plotted in Figs. 2-12A (apparent mass versus poured mass) and 2-12B (apparent piling height versus piling height).

Least-mean-square fits of the Janssen model to the immersed and settled pilings are plotted as gray, solid lines in the figures. The immersed piling shows behavior consistent with the Janssen model, whereas the agreement between the model and data for the settled case is rather poor by comparison. The RMS error of the best least-mean-square fit to the settled piling is 54 g, or 5.2% of the asymptotic apparent mass, and the discrepancy between the model and data can be as high as 85 g at individual points on the curve.

Figs. 2-12A and 2-12B show that the shielding length is quite sensitive to the method used to form the piling. The reduced packing ratio for the settled piling results in a 6% reduction in the piling bulk density, whereas Fig 12A shows a 66% increase in the asymptotic apparent mass. Fig. 2-12B shows that the screening length has increased from 8.2 cm for the immersed piling to 14.5 cm for the settled piling.

## DISCUSSION

### **Comparison of apparent mass measurements at the base of dry pilings with earlier studies**

From earlier studies, it is known that dry pilings exhibit a number of common and reproducible features. The first of these is generally referred to as Janssen behavior, consisting in a gradual reduction in the increase of apparent mass to an asymptotic limit (Nedderman 1992; Duran 2000; Sperl 2006). The initial regime corresponds to a lithostatic response and the final regime to shielding of the piling mass. They are separated by a transition zone of progressive mass shielding that arises from vertical to horizontal stress redirection within the granular bulk and wall-to-grain friction, altogether



resulting in partial support of the piling mass by the column wall. In cylindrical coordinates  $(r, \varphi, z)$ , with depth increasing downward from the piling free-surface (Fig. 2-1A), the stress redirection equation is  $\sigma_{rr} = K\sigma_{zz}$  and the relation between shear stress and horizontal stress at the wall, assuming friction is fully mobilized, is  $\sigma_{rz} = \mu_w \sigma_{rr}$  at  $r = R$ , where  $\mu_w$  is the Coulomb friction coefficient and  $R$  is the radius of the piling. The Janssen parameter,  $K$ , quantifies a mechanical property of the assembly and corresponds to the earth-at-rest coefficient used in soil mechanics (Terzaghi *et al.* 1996; Michalowski 2005). The lower and upper limits of the earth-at-rest coefficient, respectively the active and passive Rankine states, are

$$(1 - \sin(\phi')) / (1 + \sin(\phi')) \leq K \leq (1 + \sin(\phi')) / (1 - \sin(\phi')),$$

where the internal friction angle  $\phi'$  is determined from tri-axial or direct shear tests (Terzaghi *et al.* 1996). The Janssen parameter can be expressed in terms of the internal friction angle, which is often considered equal to the repose angle (Terzaghi *et al.* 1996; Claudin 1999; Michalowski 2005), or elastic coefficients (Ovarlez and Clement 2005). The Jaky formula  $K = 1 - \sin(\phi)$  is often used in engineering applications.

The resulting functional relationship between the apparent mass and the poured mass

$$M_{app} = M_{asym} \left( 1 - \exp(-M_{pour} / M_{asym}) \right), \text{ with } M_{asym} = \rho \pi R^3 / 2K\mu_w$$

has a unique parameter  $\lambda = R / 2K\mu_w$ , known as the shielding length, which accounts for both the bulk and wall behaviors and determines the asymptotic apparent mass and the rate of gradual shielding. Typical shielding lengths range from 1 to 5 times the piling radius. As stated earlier, the equations underlying the Janssen model relate averaged

quantities, rely on simplifying assumptions and correspond to specific boundary conditions, and yet the model has proven very successful at predicting the apparent mass as a function of the poured mass in various column and silo set-ups. However, in general, Janssen model predictions are not in complete agreement with measurements as they tend to slightly underestimate the apparent mass of short pilings and overestimate the apparent mass of tall pilings.

A second characteristic of the apparent mass at the base of dry pilings is the very large measurement fluctuations between pilings realizations. The apparent mass is extremely sensitive to changes in the configuration of the granular assembly reflected by changes in  $K$ . Small temperature variations and tapping are examples of small perturbations reported to cause large variations in apparent mass (Claudin and Bouchaud 1997; Vanel *et al.* 1998). The reported increase of the variance in the ensemble apparent mass with increasing piling height, until the asymptotic regime, is also attributed to the dependence of the apparent mass on piling configuration (Vanel *et al.* 2000), and can be explained as follows. Changes in shielding intensity with piling configuration are only observable for pilings taller than the height beyond which gradual shielding of piling mass occurs. Therefore the standard deviation in the ensemble mass is small for short pilings. The variability in the configuration of piling layers at heights within the asymptotic regime has a limited effect on the variance in the apparent mass at the piling base since the grains at the bottom are mechanically shielded from such layers. Consequently, the variance in the apparent mass does not further increase once the asymptotic regime has been attained.

A third characteristic observed in previous studies is an overshoot in apparent mass for pilings that support at their top surface an overweight of mass roughly similar to the free-surface piling asymptotic mass (Ovarlez *et al.* 2003). Overweight pilings respond like free-surface pilings in that they begin with a lithostatic response and gradually shield both the poured and overweight mass with increasing piling height. The asymptotic apparent mass of free-surface and overweight pilings are similar because the vertical stress exerted by the overweight on the piling is laterally redirected through the piling to the wall, which then supports the overweight-induced stress. When the overweight mass is roughly the same as the asymptotic mass, the apparent mass shows a pronounced peak or overshoot between the initial and final regimes. The value of the peak increases with increasing overweight mass. When the overweight mass is chosen equal to the free-surface asymptotic mass (Ovarlez *et al.* 2003), the overshoot occurs when the piling height is a little smaller than the shielding length of the piling and shows a maximum of 15% to 20% of the free-surface asymptotic mass. Systematic study of dry, overweight pilings is recent (Ovarlez *et al.* 2003) and the overshoot feature, which is not predicted by Janssen model, is poorly understood.

Here, Janssen-like behavior is observed in the free-surface case (Fig. 2-9A). The Janssen parameter  $K$  can be derived from the fitted shielding length and the dynamic wall-to-grain friction coefficient ( $\mu_w = \tan(\theta)$ ) measured with the bore gauge device (see section 2-3.4), which is probably adequate since the apparent mass is chosen during the piling descent, i.e. in quasistatic conditions. The obtained Janssen parameter ( $K_{dry} = 1.14$ ) is similar to  $K$ -values reported in previous laboratory studies on pilings of glass beads

with high packing ratios, and within the stability bounds ( $0.43 \leq K_{dry} \leq 2.33$ ). The change in standard deviation with piling height (Fig. 2-7B) is also consistent with previous observations, despite the continued increase in variance within the asymptotic regime, which precludes a scaling with apparent mass. Finally, the apparent mass at the base of the piling with overweight does exhibit an overshoot before gradually approaching the same asymptote as in the free-surface case (Fig. 2-9A). The peak value is consistent with that expected from previous studies (Vanel *et al.* 2000; Ovarlez *et al.* 2003). Differences in the shape of the peak, which is not as sharp as in (Ovarlez *et al.* 2003) may arise from differences in experiment set-up. In particular, a higher column diameter to grain diameter ratio may hinder the occurrence of the peak at a consistent piling height owing to the variability in the shielding intensity across the piling in the radial direction. The agreement between the measurements presented here and known results from prior studies lends confidence that the experiment set-up, protocol and analysis procedures are valid, i.e. that the datasets obtained actually reflect the apparent mass at the base of a granular piling.

### **Comparison between dry and saturated pilings: qualitative similarities**

One of the main results of this study is to demonstrate that saturated pilings exhibit the same fundamental characteristics as dry pilings. The gradual shielding of the piling mass from an initial lithostatic behavior to an asymptotic regime in the free-surface case (Fig. 2-9B), the large sensitivity of the measurements to the piling configuration that causes an increase of variance in ensemble apparent mass with increasing apparent mass

(Fig. 2-7B) and the overshoot in the overweight case (Fig. 2-9B) are all observed in the case of saturated pilings formed by immersion of dry pilings.

Our interpretation of the results is that essentially the same microscopic physics governing inter-granular contacts defines the macroscopic mechanical response of dry and saturated pilings. The Janssen model reproduces the apparent mass of the immersed, free-surface piling (Fig. 2-11A) with a similar goodness-of-fit as the dry case. Given that piling saturation does not qualitatively affect wall-to-grain friction (see section 2-3.4), observing a Janssen-like behavior in saturated pilings demonstrates that lateral stress deflection, the other mechanism underlying the mass shielding typical of dry pilings, also occurs in saturated pilings. The measurement fluctuations are comparable in dry and immersed cases, except for short, immersed pilings with overweight. Observing a similar level of sensitivity to piling configuration in dry and immersed conditions suggests that the mechanism by which piling configuration affects stress distribution through the piling is similar. The variance in apparent mass is a little larger in the immersed than in the dry case for the same poured mass but so is the corresponding piling height. The overshoot effect for pilings supporting an overweight of mass roughly similar to the asymptotic mass is clearly observed in the immersed case.

Finally, the settled pilings experiments show that, as for dry pilings, the packing ratio is a central parameter influencing the intensity of mass shielding in saturated pilings. A small reduction in packing ratio, and thus a reduction in bulk density, does not yield a reduction but a significant increase in the asymptotic apparent mass of free-surface pilings, demonstrating the sensitivity of the shielding effect to piling configuration.

### Comparison between dry and saturated pilings: quantitative differences

Although dry and saturated pilings exhibit similar qualitative behavior, there are quantitative differences. Here I discuss changes in the stress redirection efficacy and its sensitivity to packing ratio using estimates of the Janssen parameter  $K$  obtained from the fitted shielding length and the measured wall-to-grain friction coefficient.

Piling saturation reduces the Janssen parameter from  $K_{dry} = 1.14$  to  $K_{immersed} = 0.79$ . It is generally admitted that the total stress in saturated soils is the sum of the pore pressure and an effective stress corresponding to that of the solid matrix with a reduced density (Terzaghi 1943). The results presented here challenge the idea that the effective stress is the same for dry and saturated pilings under quasistatic conditions, as they indicate a change in the mechanical behavior of the granular assembly due to water saturation. The difference in stress redirection efficacy between dry and immersed pilings is an unambiguous feature of our measurements of the apparent mass at the base of slowly lowered pilings. First, there is a 30% change in  $K$ , which is well above the measurement fluctuations. The variability in piling configuration reflected in the variance in apparent mass is equivalent to only a 5% change in stress redirection efficacy. Furthermore, the possibility that the difference between  $K_{dry}$  and  $K_{immersed}$  is an artifact solely caused by measurement error in the wall friction angle can reasonably be ruled out. The measured wall friction values are accurate to within 2 degrees, and a wall-to-grain friction angle of 15.5 degrees in saturated conditions, instead of the measured 21.5 degrees, is required to keep the product  $\mu_w \lambda$ , and therefore  $K$ , constant. Obtaining such different estimates of the Janssen parameter for dry and immersed pilings indicates that

using the repose angle, which is not significantly modified by saturation (see section 2-3.4), as an equivalent for the internal friction angle in expressions for  $K$  is not appropriate for all pilings.

In addition to reducing  $K$ , piling saturation seems to enhance the attenuation in the lateral stress deflection typically associated with a reduction in packing ratio. The reduction in stress redirection efficacy between the settled and immersed pilings is larger than what is reported for dry pilings with the same change in packing ratios. The Janssen parameter is reduced by 46% from  $K_{\text{immersed}} = 0.79$  to  $K_{\text{settled}} = 0.45$  between the immersed and settled pilings, packing ratios of which respectively are 0.63 and 0.59. A previous study (Ovarlez *et al.* 2003) investigating the variations in estimated  $K$  parameter with changes in the packing ratio of dry, free-surface granular pilings can be used as a reference for comparison. Because I discuss relative changes between datasets acquired with the same equipment, it is realistic to assume that differences in the set-ups may have only a limited impact in our comparison. Interpolation from their measurement yields a 24% reduction of  $K$  from approximately 1.08 to 0.80 accompanying a change in packing ratio from 0.63 to 0.59. All other factors being equal, the same change in packing ratio results in more weakening of the mass shielding in the saturated case than in the dry case. Alternatively, besides their packing ratio, other aspects of the configuration of granular assemblies that influence the stress redirection mechanism may be affected by the piling formation procedure. Again, differences in estimates of the Janssen parameter for two saturated pilings, constituted of the same grains but formed following different protocols, suggests that the Janssen parameter cannot solely be obtained from the repose angle of the granular material confined in the piling (Claudin 1999).

Settled pilings exhibit a Janssen-like behavior, but with significant quantitative disagreement between model and data. This suggests that there may be limitations on the applicability of the Janssen model to the response of some saturated pilings, depending on their formation procedure. With a single parameter to capture both the asymptotic apparent mass and the rate of gradual shielding, the Janssen model usually underestimates the apparent mass of short pilings and overestimates the asymptotic mass (Vanel and Clement 1999; Landry *et al.* 2003; Ovarlez and Clement 2005; Liu *et al.* 2009). For settled pilings however, the discrepancy is much larger than typical errors reported in previous studies. In particular, the model fails to reproduce the response of short pilings, which actually follow a lithostatic behavior for piling heights up to 40 grain diameters (Fig. 2-12B). The Janssen parameter of settled pilings,  $K_{settled}$ , is very low compared to values reported for column experiments I know, but still within the stability bounds ( $0.44 \leq K_{saturated} \leq 2.29$ ), while  $K_{immersed}$  is similar to typical values of the Janssen parameters.

Most of the output runs for settled pilings show a curious overshoot feature at the transition between the decompression regime and the relaxed regime. Instead of an overall smooth, monotonic stabilization of the measured mass near a minimum value, a sudden and brief decrease followed by an increase to approach a plateau is observed. This behavior might correspond to piling recompaction after the first rearrangement of the piling. Given the relatively low initial compaction of the piling at the beginning of the decompression regime, the first rearrangement may lead to a more compacted configuration, which could explain the observed overshoot at the end of the piling decompression. The shielding of the piling mass would then intensify. This specific



piling response during descent demonstrates the importance of the procedure used to form the piling and suggests that the role of water in the physics of intergranular contacts may be augmented when pilings are formed by settling.

### **Role of water**

The changes in the estimated Janssen parameters for the dry and immersed pilings suggest that water-induced modifications of intergranular contact forces affect stress redirection within the piling. The reduction in stress deflection observed for immersed pilings presumably originates in water acting as a lubricant. Lubrication is known to have a large effect on the frictional properties of intergranular contacts over a wide range of dynamic regimes, including quasistatic conditions (Lesaffre *et al.* 2000). The thin water film covering asperities on granular surfaces will tend to reduce the effective roughness scale, and consequently the resistance of the intergranular contacts to sliding. Under the same loading conditions, lubricated contacts will yield for a smaller value of the tangential stress than dry contacts (Geminard *et al.* 1999; Losert *et al.* 2000), resulting in a reduced ability for stress redirection within lowered pilings. At least some of the reduction in the intensity of the stress redirection must occur during piling base descent through piling readjustment occurring at the scale of intergranular contacts. Whether or not a reduced stress redirection would occur if a piling was immersed but not lowered is unclear.

In addition to lubrication, there are other effects associated with liquid saturation, including fluid viscosity and cohesive interactions originating in chemical reactions. Previous studies on saturated granular assemblies suggest that the role of fluid viscosity

is not significant here, given the very slow descent velocity (Ancey 2001; Divoux and Geminard 2007). Capillary bridges are known to play a role in partially saturated granular assemblies, but are not relevant in this study (Gayvallet and Geminard 2002). Cohesive interactions resulting from chemical reactions and causing an ageing behavior have been reported even in the case of fully-saturated granular systems, but are not pertinent here given the use of fresh water, the relatively large grain diameter and short duration of experiment runs (Gayvallet and Geminard 2002). Dynamic forces exerted by the interstitial liquid on the grains, including drag or non-uniform pore water pressure, are most likely not relevant since the system is in a quasistatic regime.

As mentioned above (see sections 5.1 and 5.3), although current models for dry pilings assume the internal friction angle can be replaced by the granular assembly repose angle in the expression of the Janssen parameter, the saturated assemblies studied here have essentially the same repose angle as the dry assembly and yet, they exhibit a significant reduction in the Janssen parameter. Recent studies (Cassar *et al.* 2005; Jop *et al.* 2006; Chevoir *et al.* 2009) have proposed that the rheology of saturated granular layers under shear can be described by an effective friction. Results from numerical simulations of the weak and strong force networks of granular packs during loading-unloading cycle suggest the emergence of a macroscopic friction angle (Garcia and Medina 2008). The effective or macroscopic, internal friction angle of the piling is affected by saturation and packing ratio changes (Lesaffre *et al.* 2000) and therefore accounts for differences in the mechanical response of dry, immersed and saturated pilings.

### **Limitations of the dataset**

This section is a discussion of the limitations of the measurements, considering the resolution of small features in the apparent mass at the piling base, the characterization of the piling configuration, and the procedure chosen to saturate the pilings.

There are constraints limiting the resolution of small amplitude variations in the apparent mass. Oscillations of the apparent mass with piling height can only be detected if their amplitude is larger than the variance in the ensemble mean, which is associated with differences in piling configuration arising both between pilings of the same height and between pilings of different heights. At initial consideration, it might seem that investigating fluctuations in the apparent mass with height would be better achieved by keeping the same piling and incrementally increasing its height, rather than by emptying out the column between runs as in the current procedure. However, the interpretation of the mechanical response of the piling to the load cell base descent procedure and the subsequent choice of apparent mass would require re-examination under the incremental pouring scenario. Pilings would be subjected to the base descent and associated wall friction mobilization multiple times, which could induce piling inhomogeneity in the vertical direction. In addition, the density of data points for tall pilings is insufficient to observe small variations in the apparent mass superposed over the overall curve, i.e. any oscillations occurring over small changes in piling height would be aliased in our measurements. The data presented in a recent study (Liu *et al.* 2009) exhibit oscillations in the apparent mass during the asymptotic regime, with an amplitude of 5% of the

asymptotic apparent mass. This observation constitutes interesting experimental evidence of qualitative agreement with the predictions of the OSL model (Vanel *et al.* 2000).

Although the apparent mass at the piling base depends on the properties of the intergranular contacts in the piling bulk and at the wall, the experiment does not collect any direct information about the internal structure of the piling, such as the stress distribution throughout the piling and at the walls, the intergranular contact angle distribution and the coordination number. Besides, there is no assessment of the changes in these internal properties as a consequence of usage-induced modifications of the grain surface, nor when the overweight is applied. The absence of measurable differences in the packing ratio between free-surface and overweight pilings (see section 2-3.2.3 and 2.2.4) does not preclude subtle changes in piling configuration, which could modify the stiffness of the upper layers of the piling and the mobilization of wall friction during the piling descent. The stiffness of the overweight does affect the piling behavior, which is completely different when the overweight has the same mechanical properties as the piling itself, as can be observed when the equivalent mass of grains is poured instead of applying the overweight. The overweight does not exhibit by itself a shielding effect, i.e. its mass is fully supported by the top layer of the piling.

Finally, the effects of the saturation procedures on the piling configuration are not well characterized. Intergranular contacts created underwater may be different from those created in air and then immersed because of differences in the kinetic energy of falling grains between both formation methods. The viscosity of the thinning liquid layer as grains come to close contact (Yang and Hunt 2008) could affect the mechanical properties of the intergranular contacts for settled pilings. In addition, in the case of

immersed pilings most grains are wetted before they get fully immersed as a result of surface tension that acts in the pore space as in capillary tubes. At a given time, the grains get wet on the few granular layers ahead of the raising water level, in a pattern similar to percolation. The mechanical behavior of granular assemblies formed from wet grains is known to be very different from that of dry or fully saturated assemblies and the percolation-wetting process prior to immersion could induce temporary changes in the stress distribution throughout the piling, leading to small readjustments.

Another issue with saturated pilings is the possibility that small air bubbles remained trapped on the surface of grains, leaving regions of the intergranular contact areas dry. Slowly raising the water level in immersed pilings helped prevent bubble entrapment. Bubbles trapped between intergranular contacts increase grain buoyancy, but I am confident that this effect is less than 0.1%. Root-mean-square roughness of the grain surface is on the order of 100 nm, so any air trapped within intergranular contact regions must lie within convex-shaped asperities – bubbles on this scale would be very rapidly dissolved because of the Laplace pressure. However, observations of the damaged surfaces of grains used during the experiments under a microscope with a magnification factor of 200 did not reveal any convex asperities, suggesting that the contact regions were free of air. Settled piling formation was accompanied by distinctly visible plumes of small bubbles entrained by grains as they broke the water surface, but they were confined to the upper 10 cm of the water column, which provided sufficient isolation from the piling surface to prevent them being trapped in the piling.

There may be dynamic variations in the stress distribution within saturated pilings associated with changes in the pore pressure. In the immersed case, although the flow rate

was small and the piling geometry was not observed to be disturbed, adding water may lead to temporary excess in the pore pressure in some parts of the assembly. Changes in the stress distribution throughout the piling may also occur as the vertical gradient in pore pressure is modified when stopping, or reversing in the case of settled pilings (see section 2-3.2.5), the water flow. Self-compaction, in the case of settled pilings, is another mechanism that could create small, temporary pore pressure gradients in the vertical direction. Numerical simulations on the filling of silos with saturated sand suggest that the dissipation of the excess pore pressure occurs over several minutes (Abdel-Fattah *et al.* 2006), so that pore pressure-induced changes in the stress distribution within the piling may be relevant here.

### **The interpretation of piling response to load cell base descent and some implications for modeling**

The mechanical behavior of the piling during the descent of the load cell base is important for a number of reasons. Firstly, it has consequences for the choice of apparent mass, which is a fundamental metric for granular piling experiments. Secondly, it provides clues to the heterogeneous distribution of stress within the column, which depends on its formation procedure. Finally, constraints can be placed on the range of displacements over which elastic behavior occurs, which has implications for modeling the behavior of granular pilings during quasistatic base descent.

*About piling decompression: a new regime - progressive friction mobilization and choice of the apparent mass*

The analysis of the degree of mobilization of the wall-to-grain friction along the lateral piling boundary, which will also be referred to as the friction configuration, serves as a basis for the choice of apparent mass. The friction configuration is a consequence of the granular displacements during piling formation and in response to the time-varying bottom boundary condition. Before the load cell base descent, the friction configuration is heterogeneous. The friction mobilization for grains in contact with the wall depends on the path they followed before coming to rest on the piling free-surface (de Gennes 1997) and on modifications of the initial friction state due to compaction of the confined piling. Upon formation, the piling compacts both under its own weight and under the weight of the overlying granular matter subsequently poured. Since the displacement required to achieve full friction mobilization, called the anchoring length, is estimated to be on the order of 1 micrometer (Evesque and de Gennes 1998), the small downward displacement due to compaction is central to the mobilization of wall-to-grain friction in the upward orientation. Boundary conditions impose a negligible displacement at the bottom and top of the piling, and the vertical displacement is maximal at mid-height, exceeding 1 micrometer for piling heights of a few centimeters or more. Because of the deformation of the compliant load cell during piling formation, the upward force exerted by the load cell tends to orient friction downward near the piling base, having an effect on wall-to-grain friction opposite to compaction. Incidentally, the vertical displacements due to self-compaction are smaller near the walls than at the center of the silo, due to lateral boundary conditions. The difference is small but qualitatively crucial since it is responsible for the shear stresses within the granular bulk.

The initial friction configuration is modified by lowering the load cell base. Here, the interpretation of the fluctuations in the measured mass during the load cell base descent shows evidence of a decompression regime that had not been previously identified as such. The reduction in measured mass between the start of piling base motion and the stabilization of the measured mass near the minimum value of the relaxed regime is not instantaneous, which is why I have interpreted this transition as a progressive mobilization of the wall-to-grain friction. Numerical, discrete element molecular dynamics simulations of confined granular pilings with moving walls also exhibit upward propagation of the wall friction mobilization (Landry and Grest 2004). I propose that the piling displacement in the system studied here is not simultaneous along the piling height, as if the accommodation space made available by the piling base descent was utilized to anchor the grains in contact with the wall and to loosen layers of the piling little by little, from the bottom upward. The displacement required to fully mobilize wall-to-grain friction for upper layers would be the sum of the typical anchoring length and of the cumulative displacements necessary to the decompression and full friction mobilization of the underlying layers. The apparent mass reduction could arise not only from an increase of the lateral wall support owing to wall-to-grain friction mobilization, but also from the formation of concave downward arches with a higher stress-bearing capacity. In fact, at least in the lower section of the piling, the orientation of the arches is likely to reverse from concave upward to concave downward, effectively increasing the parameter  $K$  used in the Janssen model.

The choice of the apparent mass one e-folding scale after the beginning of the decompression regime in the current study is appropriate to ensure a more homogeneous



friction configuration at least over a height exceeding the shielding length. Since the friction configuration is heterogeneous before the load cell base descent and is unchanged during the elastic regime, it is not uniform over the piling height before the piling base descent either, so that choosing the apparent mass at the end of the elastic regime would not be adequate. As already mentioned (see section 2-4.6), a large reduction of the variance in the measured mass is observed during the first e-folding scale of the decompression regime, supporting the analysis of the changes in friction configuration.

The identification of a decompression regime constitutes the main difference between our dry piling study and the work of Ovarlez *et al.* (2003). They do identify a region of slow measured mass decrease lasting for 50  $\mu\text{m}$  or more after their linear expansion regime (Ovarlez *et al.* 2003). Differences in aspects of the experiment set-up, such as the stiffness of the load cell compared to other elements of the system, the ratio of piling to grain diameters or specific properties of the column and granular materials used, may explain the somewhat different piling responses.

Notwithstanding differences in piling base descent behavior, the main results reported here are independent of the exact choice of the apparent mass. This was verified by checking for a Janssen-like behavior when the apparent mass was chosen as the measured mass either at the beginning or at the end of the load cell base descent. Of course, these alternate choices result in an increase of the estimated shielding length because of the lesser friction mobilization. But the overall effects of liquid-saturation and of packing ratio modifications, assessed from their influence on the shielding length, are the same. Previous studies on dynamic pilings with kinematic boundary conditions have also shown evidence of a Janssen-like behavior (Vanel and Clement 1999; Bertho *et al.*

2003b). The velocities were 10 to  $10^4$  times larger than our study and the experiment procedures different from our study. Their results showed a large and instantaneous reduction in the measured mass owing to friction mobilization, as expected, followed by a relatively smaller increase in apparent mass occurring over a finite displacement. The piling response they obtained after displacements  $10^3$  times larger than our study was characteristic of a different regime, probably involving the dilatancy of the granular piling. Dilatancy, in the sense first described by Reynolds (Reynolds 1885; Rowe 1969), may be understood as the tendency of a dense assembly to expand in order to overcome packing interlocking or imbrication when accommodating for shear strain. Although dilatancy effects may influence the piling response even in the case of small displacements, it seems unlikely that they are significant in our study (Ovarlez *et al.* 2003).

The displacement of the piling base during the load cell base descent almost certainly exceeds the range of elastic deformation immediately after initiation of piling motion and well before full friction mobilization. So does the total vertical strain of the piling during the decompression regime, and probably during each relaxation oscillations as well. Using the Hertz theory for the mechanics of solid contact interactions to estimate the penetration depths, the change in the deformation of the grains at the piling base associated with the decrease in measured mass during the decompression regime is on the order of 5 nm, i.e. less than 1/3% of the load cell base descent in one second. Similarly, the vertical asymptotic displacement of a confined elastic material of 10 cm in height is about 10 nm, according to a solution derived within the framework of isotropic elasticity and assuming stress and displacements are depth-independent in the limit of high depths

(Ovarlez and Clement 2005). Plastic deformation of the granular piling presumably occurs at the very beginning of the decompression regime. As a consequence, accounting for plasticity, i.e. changes in the piling configuration, may be required for modeling the change in measured mass under the time-varying bottom boundary condition. This is consistent with recent observations of deviation from elasticity in high precision tri-axial tests of granular assemblies at very low stress levels (30-400 kPa), where particle crushing is unlikely to be significant (Kuwano and Jardine 2002a,b,2007).

The implication is that neither the Janssen model, which is an *ad hoc* model for static pilings, nor elastic theory, which is not valid over the range of strains encountered during load cell base descent, are adequate to predict the measured mass at the base of granular pilings during the load cell base descent. However, as stated earlier, both of these theories do encapsulate the effects of stress redirection, and therefore reproduce the mass shielding behavior of free-surface granular pilings.

*The relaxation oscillations: a window on the heterogeneous distribution of stress within the pilings?*

The relaxation oscillations observed during the load cell base descent, discussed in section 3.1, consist in a brief, temporary increase in the apparent mass of the piling. They are superposed on the background response of the piling to the load cell base descent, which consists of a progressive friction mobilization followed by a steady sliding or creeping behavior. The relaxation oscillations were observed in all of the pilings, regardless of height and formation procedure. Occurring after the beginning of the piling descent, i.e. during both the decompression and relaxed regimes, they show how the intensity of the shielding mechanism adjusts to the slow downward displacement

of the piling base. As such, they could probe the internal structure of the granular assembly and provide information about the heterogeneous distribution of stress within the pilings.

Although there is no definitive evidence whether the relaxation oscillations are caused by changes in wall-to-grain friction, rearrangements within the piling, or both, interpreting some of the characteristics of the relaxation oscillations, analyzing their variability, and comparing them to similar features in other studies suggests that they are associated with internal piling rearrangements. Firstly, the relaxation oscillations occur roughly every 10 sec, i.e. every 15 to 20 micrometers of displacement, which is much larger than the anchoring length (see section 2-6.6.1). In any case, the existence of a regular pattern in the column wall asperities that could cause the regular spacing of the relaxation oscillations is not expected given the wall surface preparation (see section 2-3.1.1). Additionally, the relaxation oscillations occurring during the decompression regime result in a net reduction in measured mass, but usually fall short of reaching the minimum measured mass. If they were only reflecting wall friction mobilization, the measured mass at the end of the relaxation oscillations would be expected to approach the minimum measured mass, as is observed of relaxation oscillations occurring during the relaxed regime.

Secondly, the amplitude of the relaxation oscillations varies by up to a factor of 4 between runs of fixed piling height and same piling formation procedure. Such differences seem more likely to be caused by differences in piling configuration than by run-to-run differences in the wall-to-grain contact interactions. Overall, the amplitude of the relaxation oscillations increases with piling height, and so does mass shielding,

consistent with an association of the relaxation oscillations with instabilities in the piling configuration, which in turn are related to the intensity of the arching mechanism. Similarly, the amplitude of the relaxation oscillations in the response of pilings of intermediate heights is larger in the overweight case than in the free surface case, consistent with a relationship between relaxation oscillations and arching, which both increase in magnitude as the stress on the piling increases. In addition, the relaxation oscillations have much smaller amplitudes in the settled case than in the immersed case but the same frequency, while the wall friction is essentially unchanged (see section 2-3.4). If relaxation oscillations were solely caused by changes in wall friction, the smaller wall normal stress in the settled case compared to the immersed case should result in a reduced oscillation frequency.

Finally, the relaxation oscillations follow a pattern different from the stick-slip oscillations observed in a slightly different context in previous studies and associated with wall friction (Ovarlez and Clement 2003). In their study, the base of the force sensor was pushed upward through relatively large displacements (multiple grain diameters) before lowering it, and the ratio of piling to grain diameters was smaller. Stick-slip behavior consisting of a two-phase cycle, one of slow stress build-up without displacement and one of sudden stress release with finite displacement, was observed when the piling was pushed upward at slow velocities, up to around 2 micrometer/sec, at which point a transition occurred to steady sliding. They also observed stick-slip oscillations when the piling was lowered so that the vertical stress supported by the wall showed a slow build-up while mobilizing wall friction followed by a sudden reduction upon slippage, and the corresponding cycle on the measured mass consisted of a slow

decrease followed by a sudden increase. In our study, the relaxation oscillations do not show the dissymmetric pattern typical of stick-slip oscillations. The rate of change in measured mass, augmentation and reduction, are very similar during the two phases of a relaxation oscillation, which occupy only a portion, one half to one third, of the interval separating two events. The nature of the relaxation oscillations provide some additional support to the idea that they originate not only from wall friction but also from internal piling rearrangements.

In the remainder of the section, I assume that the relaxation oscillations are associated with modifications of the jammed piling configuration through adjustments to the arching structure maintaining the piling stability. The rearrangements of the stress distribution in the granular bulk may occur as the micrometric piling displacements change the degree of anchoring of some grains at the wall or the mobilization of some intergranular contacts. As a comparison, in the context of guided chutes corresponding to emptying a silo by opening its base, the initiation of fractures within the piling has been tentatively attributed to changes in the wall friction mobilization due to defects in packing or to wall roughness fluctuations (Duran 2000). Here, for relaxation oscillations occurring during the relaxed regime, the release of compression energy as sections of the granular assembly loosen up is balanced by the storage of energy in the intergranular contact network immediately reformed. The variations in mechanical energy could be associated with local plastic yield accompanying piling rearrangements (Evesque and Stefani 1991). Micrometric granular displacements involved in the partial readjustment of the contact network into a new configuration result in large variations in the stress observed at the scale of the entire assembly. Analogous features have been observed in

different experiment conditions, either avalanches within the piling under temperature fluctuations (Claudin and Bouchaud 1997), intermittent compact flow in hoppers (Bertho *et al.* 2003a), and associated with large stress fluctuations. In a study on weakly vibrated granular pilings, significant force fluctuations without appreciable grain motion have been reported and attributed to activation of force networks (Umbanhowar and van Hecke 2005). Similarly, the relaxation oscillations could be interpreted as arch failures followed by the transfer of out of balance stresses to other arches. Arches collapse when the stress locally exceeds their threshold, because of changes either in the stress they carry or in their failure threshold. Successive formation and destruction of arches was observed in studies of size segregation (Duran *et al.* 1994) and drag force fluctuations (Geng and Behringer 2005) in two-dimensional granular assemblies. A comparable process involving breaking and reforming of force chains has been invoked to explain observations of creep during loading of confined granular media at low stress levels (Kuwano and Jardine 2002a). Thus, our measurements indicate that the adjustment of the piling to a time-varying bottom boundary condition involves non-uniform, plastic deformation associated with changes in piling stiffness. This preliminary interpretation may be of interest for modeling considerations, as it suggests that non-elastic components of strain may play a large role in determining the stress distribution in granular assemblies. Accordingly, previous studies have proposed that rare events, where piling rearrangements involve large displacements of individual grains relative to neighboring grains, may play a central role in the relaxation of granular materials (Ribiere *et al.* 2005).

Although a detailed analysis of the variability in the relaxation oscillations is beyond the scope of this article, some qualitative comments on the piling mechanical behavior can be made from additional features observed in their amplitude variations and their frequency. Relaxation oscillations of larger amplitudes are observed for dry run outputs compared to immersed runs, suggesting that saturating the pilings affects some of the dynamic features of their mechanical response, i.e. the internal piling rearrangements, in addition to modifying the overall piling behavior, i.e. the change in apparent mass with poured mass (see sections 5.3 and 5.4). The effect of saturation on the dynamical response of granular assemblies has been observed previously. The occurrence of the transition between the stick-slip and sliding regimes at a slower shear velocity in immersed granular layers than in dry layers was attributed to the reduction in intergranular contact friction induced by lubrication (Geminard *et al.* 1999). Incidentally, the relaxation oscillations are very often paired in the dry case. The occurrence of double peaks probably reflects a particular mechanism related to dry wall-to-grain contacts or to dry intergranular contacts involved in bulk piling rearrangements. In addition, the amplitude of the relaxation oscillations is larger in the immersed case than in the settled case, reinforcing the idea that changes in the packing ratio or maybe in the intergranular contact properties due to the piling formation procedure result in changes in the mechanical response of the piling. Another interesting feature of the relaxation oscillations is their periodicity, which is rather consistent throughout the entire dataset, and may be interpreted in terms of a length scale characteristic of the heterogeneity in the stress distribution within the piling. The typical length scale associated with stress gradients within granular assemblies, such as the length or the spacing of force lines, or



the width of shear zones, is on the order of 10 grain diameters (de Gennes 1999; Pouliquen and Chevoir 2002). Although the scale of our laboratory set-up may not be sufficient to exactly reproduce the behavior of real-size granular systems, the size of the pilings investigated here is about 5 to 10 times this sub-system length scale, which lends a particular significance to our results, especially in the perspective of their relevance for modeling granular assemblies using continuum theories.

### **CONCLUDING REMARKS**

Column experiments have been done for dry and saturated granular assemblies of glass spheres. The change in the mass measured at the base of the pilings during the descent was analyzed in detail to define the choice of the apparent mass, yielding a reduction in the variance in the ensemble piling mass. The results for the piling apparent mass were analyzed in the framework of the Janssen model. Experiments on dry pilings confirmed the results obtained in prior studies, consistent with the shielding effect arising from stress redirection within the piling and wall friction. Experiments on liquid-saturated granular pilings showed commonality of behavior, suggesting that similar physics are relevant in dry and immersed assemblies, at the scale of intergranular contacts. The stress redirection effect was less efficient in liquid-saturated pilings, possibly due to a reduction of the grain-to-grain friction by lubrication of the intergranular contacts. In addition, a regime of progressive decompression of the piling was identified during the quasistatic descent of the piling, together with transient features interpreted as relaxation-oscillations, both of which have implications for modeling the

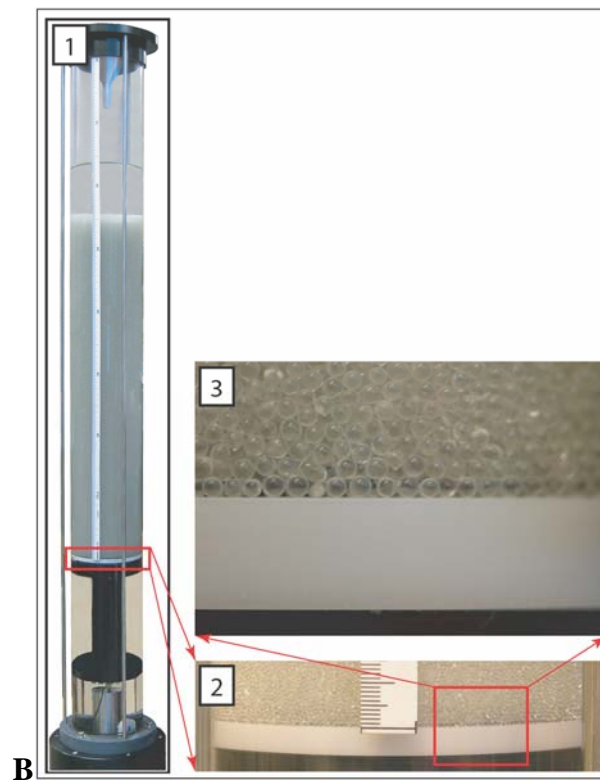
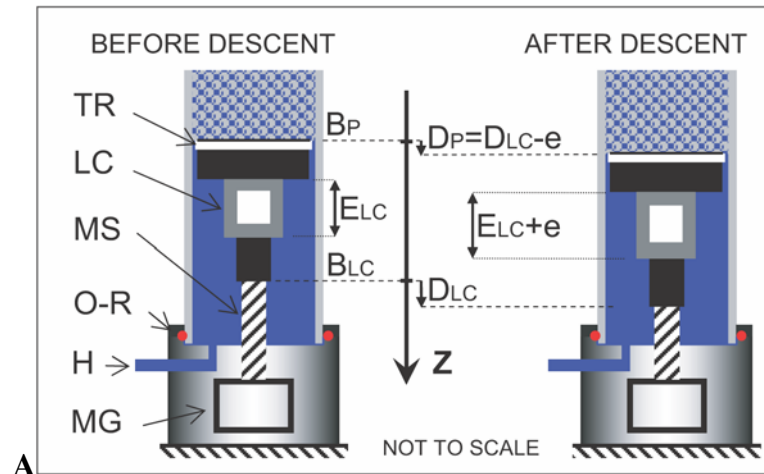
mechanical response of granular assemblies. Theories for granular matter are expected to reproduce the stress heterogeneities and the large stress fluctuations associated with minute deformations that are observed at least at scales typical of laboratory experiments.

This work has a number of implications, including application to geophysical problems such as sediment transport. In the study of beach and nearshore processes, measurements of sediment fluxes are generally concerned with the suspended and bedload contributions, considering the seabed below the bedload layer as immobile (Fredsoe and Deigaard 1992; Nielsen 1992). Yet the hydrodynamic forcing from wave and currents and the seafloor morphology may affect the stress distribution within the upper layer of the seabed, at depths of a few hundred grain diameters (see Chapter 5 of the dissertation). Granular scale displacements and changes in the packing arrangement may influence the stability and erodability of sediments much below the bedload layer, giving rise to an active layer. In addition, theories for the rheology of saturated granular materials could be applied to modeling submarine canyon formation, slope failure and landslide motion (Iverson and Vallance 2001; Friedmann *et al.* 2003; Mangeney *et al.* 2007; Abrams *et al.* 2009). Proper assessment of slope stability is critical to mitigate the risks associated with submarine failures and avalanches, which constitute a threat for underwater infrastructures like oil rigs, and have the potential to trigger tsunamis. Finally, better understanding of the mechanical behavior of saturated granular materials, for example in the case of loading on structures, settlement and scouring, will benefit the design of underwater constructions.

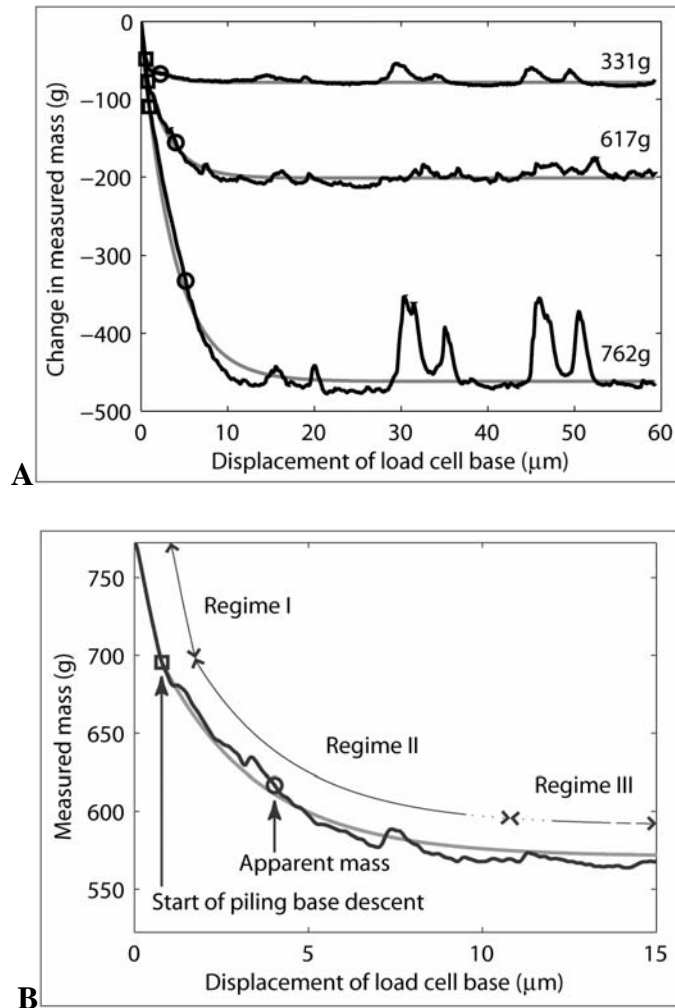
The effect of the interstitial water on the stress redirection mechanism evidenced in this work deserves further investigation by experimental studies of the influence of the

liquid properties, such as lubrication (Cain *et al.* 2000), pH (Gayvallet and Geminard 2002) and viscosity (Lesaffre *et al.* 2000), on the stress redirection effect in saturated pilings. More precise measurements of the packing ratio and the stress distribution within the piling would be a critical step forward in understanding the relationship between the stress redirection effect, the piling density and the heterogeneity of the force distribution at intergranular contacts. The piling to grain diameter ratio may affect the mechanisms of stress propagation, which calls for studies of scaling effects, bearing in mind that doubling the piling size amounts to handling 8 times as many grains. In the context of underwater sediment dynamics, more complex experiments studying the piling response to hydrodynamic forcing, such as periodic wave loading, may uncover features in the mechanical response of saturated granular matter involving a coupling between the granular and liquid phases.

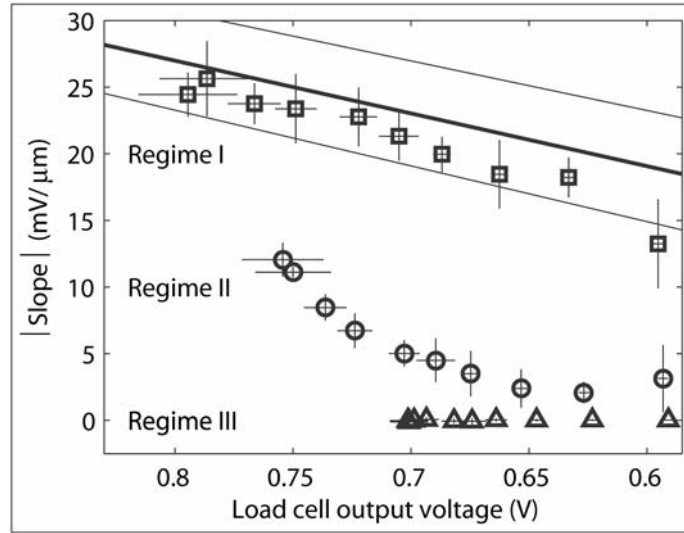
**Acknowledgements:** I thank Dale Stokes, James Uyloan, Cary Humphries and Dylan Hatt for technical assistance. Financial support was provided by the U.S National Science Foundation.



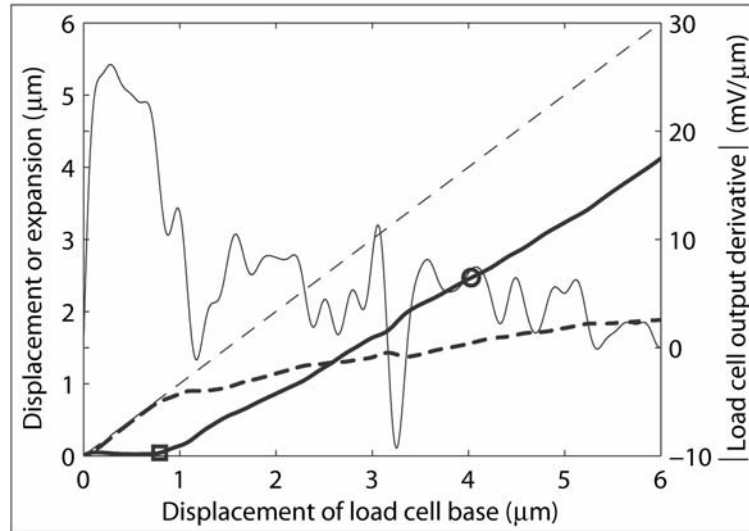
**Figure 2-1: A schematic of the experiment setup. A. Diagrams of the apparatus used to measure the apparent mass at the base of the granular piling. The diagram on the left shows the piling before the descent of the load cell base. The diagram on the right shows the displacements of the piling and the load cell after descent of the load cell base. B. Pictures of the apparatus showing: 1. the entire column, 2. an expansion of the base of the piling and 3. an expansion of the glass beads**



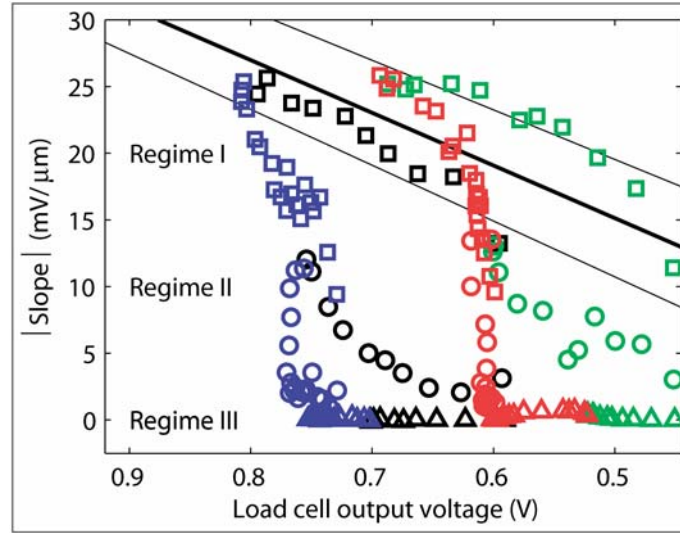
**Figure 2-2: Run outputs. A. Change in mass measured at the base of the piling as a function of the load cell base downward displacement. Each black curve is the output of a single run. Three runs from the dry free-surface dataset for different piling heights are displayed and labeled by the corresponding apparent mass. The circles denote the point during the run corresponding to the apparent mass at the base of the piling. The squares in the upper, left corner denote the point at which the piling base begins to move (see Fig. 2-2B). The gray lines show an exponential fit to each of the three runs. B. An expanded view of the middle run in Fig. 2-2A, showing the mass measured at the base of the piling as a function of the load cell base downward displacement. The three annotated regimes are discussed in the text**



**Figure 2-3:** The average slope of the run output for each of the 3 regimes identified in Fig. 2-2B, showing the dry free-surface dataset. Absolute values of average slopes are expressed in mV per micrometer of load cell base displacement and plotted as a function of the average load cell voltage during each regime. Regime I is displayed with squares, regime II with circles and regime III with triangles. Each point corresponds to the ensemble mean of all the repeated runs for a fixed piling height of the dry free-surface dataset. The thick black line shows the load cell stiffness obtained from calibration of the load cell response. The pair of thin black lines represents the standard deviation of the load cell stiffness. The thin lines crossing over each data point correspond to the standard deviations of the ensemble means

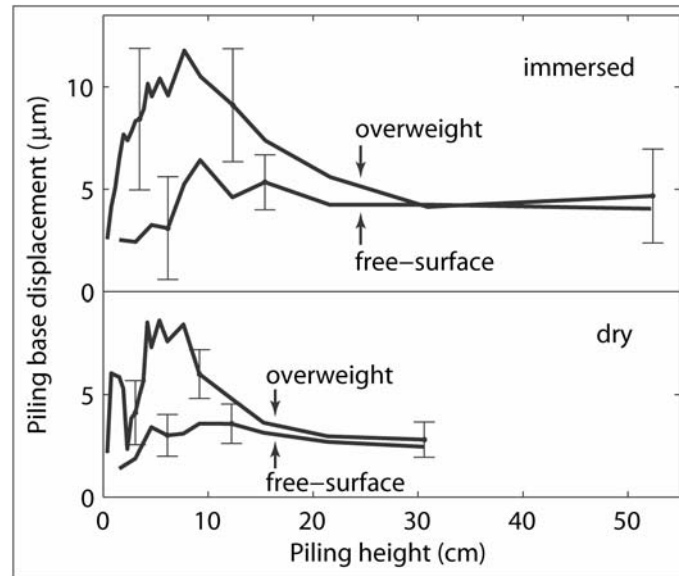


**Figure 2-4: Analysis of the piling base and load cell mechanical response.** Piling base displacement and load cell expansion versus load cell base displacement for the run output in Fig. 2-2B. The thick solid line represents the displacement of the piling base (positive displacement corresponds to downward motion). The thick dashed line represents the expansion of the load cell. The thin dotted line is the sum of the previous two curves, showing the displacement that would be observed for the piling base if the load cell had no compliance. The circle denotes the displacement of the load cell base at which the apparent mass is obtained. The square marks the point at which the piling base begins to descend. The thin solid curve is the absolute value of the slope of the run output expressed in mV per micrometer of load cell base displacement and corresponding to the vertical axis in the right

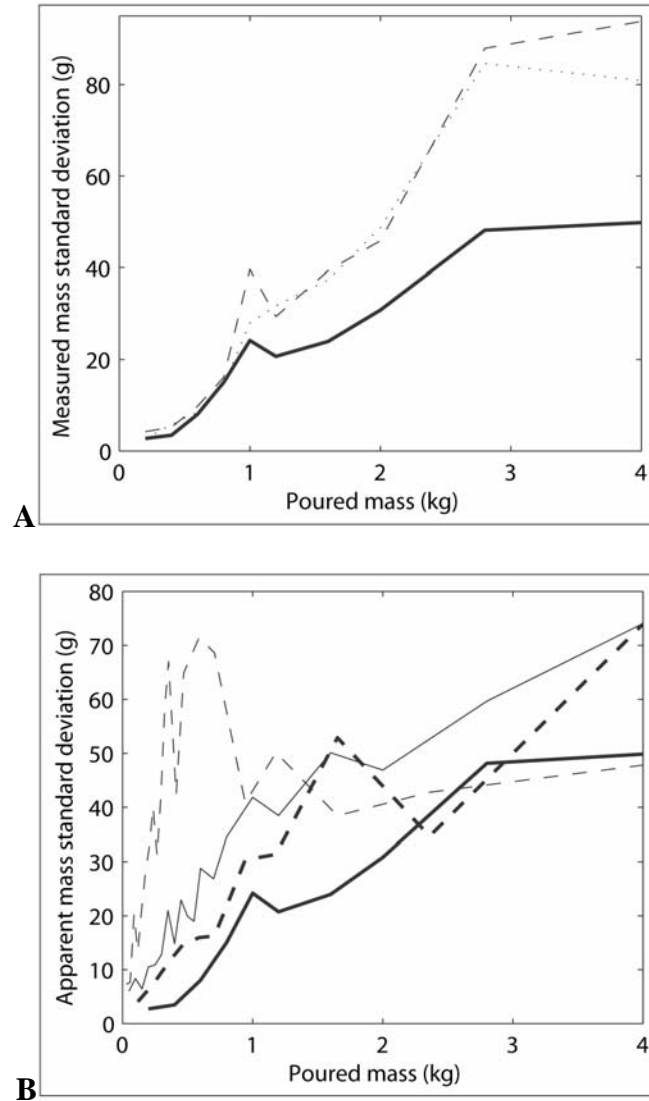


**Figure 2-5:** The average slope of the run output for each of the 3 regimes identified in Fig. 2-2B, showing four datasets. See the caption of Fig. 2-3 for a description of the plot elements. The standard deviations of the ensemble means are not displayed. Each color represents a dataset. The dry free-surface is in black, the dry overweight in blue, the immersed free-surface in green and the immersed overweight in red



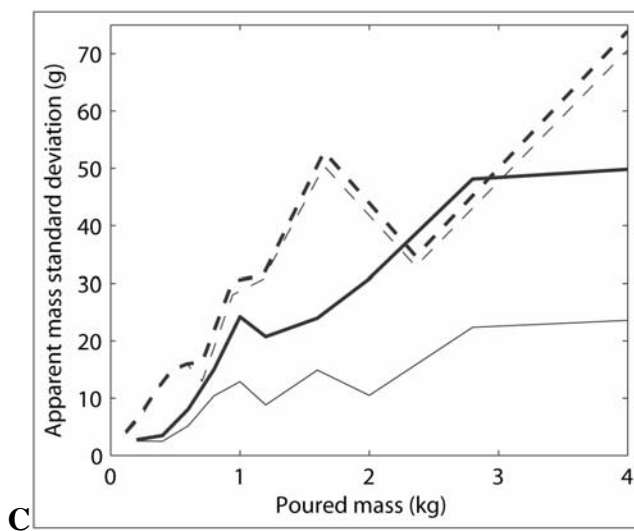
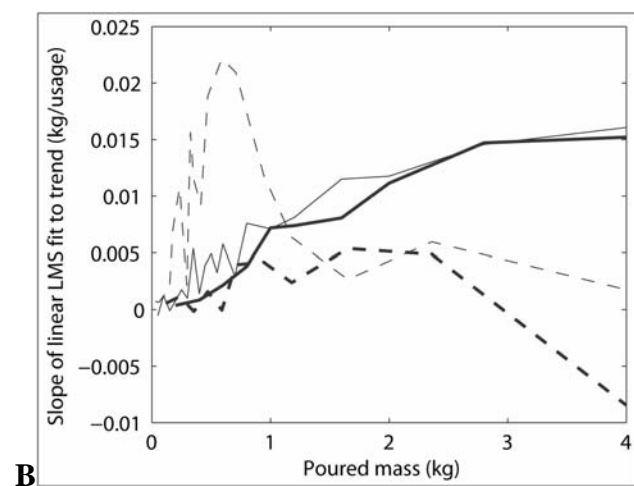
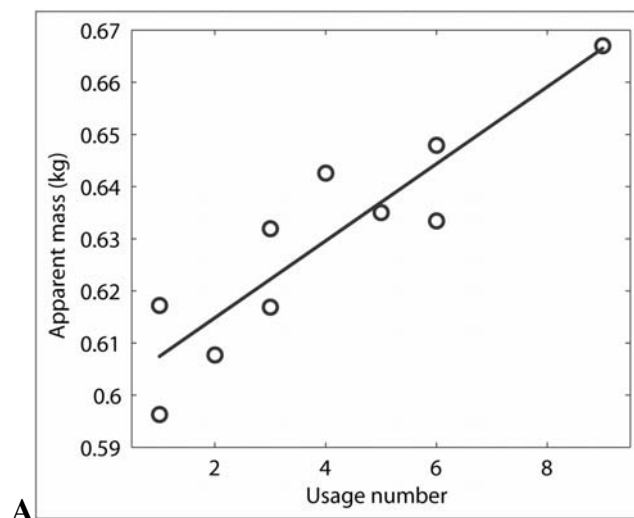


**Figure 2-6: Piling base displacement at the point at which the apparent mass is obtained. Each point along one of the thick lines is an ensemble mean of all repeated runs for a fixed piling height, plotted against the piling height. The same four datasets as in Fig. 2-5 are displayed. Light vertical lines are the standard deviations of the ensemble means for selected points**



**Figure 2-7: Descent procedure and measurement fluctuations. A. Standard deviation of the mass at the piling base measured at different stages of load cell base descent, plotted as a function the mass of grains poured. Dotted and dashed lines respectively correspond to measurements at the beginning and end of regime I (see Fig. 2-2B). The thick solid line corresponds to the apparent mass obtained within regime II (see Fig. 2-2B). B. Plot of the standard deviation of the apparent mass against the poured mass. Thick and thin solid lines correspond respectively to the dry free-surface and dry overweight datasets. Thick and thin dashed lines correspond respectively to the immersed free-surface and immersed overweight datasets**

**Figure 2-8: Usage trend. A. Apparent mass versus grain usage number for a selected piling height. Circles represent data points and the line is a linear, least-mean-square fit to the data. B. Plot of the slope of the linear fit as a function of poured mass. Each data point corresponds to the trend in apparent mass versus usage number for a fixed piling height. See the caption of Fig. 2-7B for an explanation of the correspondence between line types and datasets. C. Influence of the trend on the standard deviation of the apparent mass, plotted against poured mass. The two solid lines correspond to the dry free-surface dataset and the two dashed lines to the free-surface immersed dataset. In both cases, the thick and thin lines respectively correspond to apparent mass without and with detrending of the change in mass associated with usage number (see Fig. 2-8A, B)**



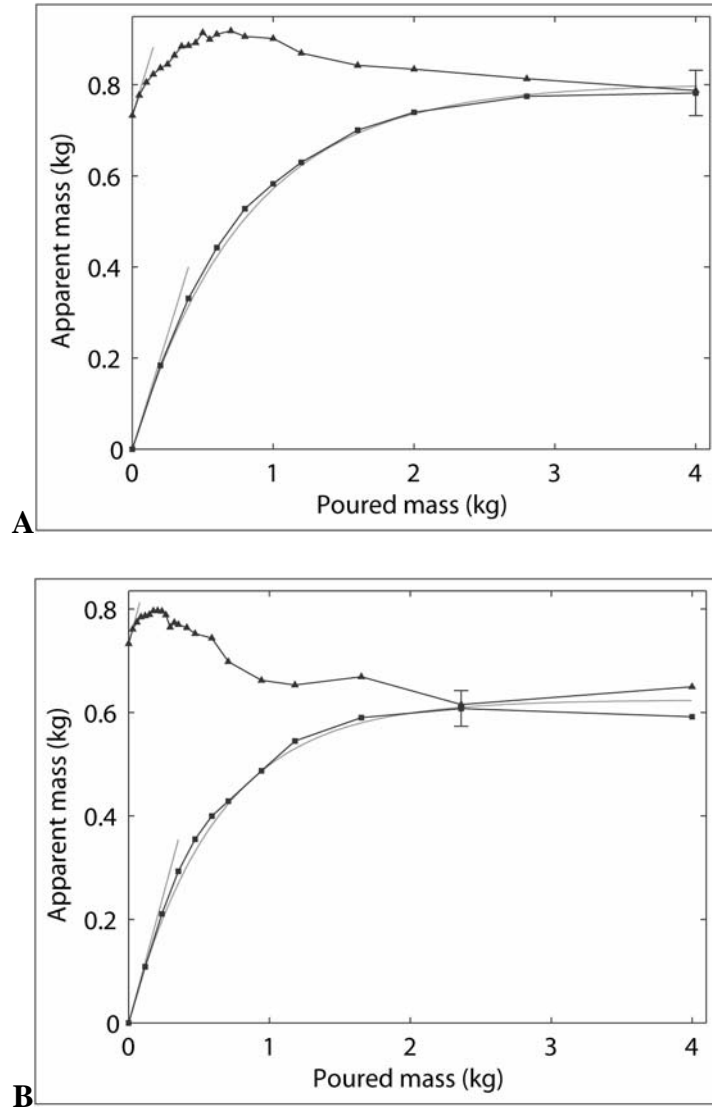


**Figure 2-9: Apparent mass plotted as a function of poured mass. Each point corresponds to the ensemble mean of all the repeated runs for a fixed piling height. Squares and triangles respectively correspond to the free-surface and overweight datasets. The gray curve shows a Janssen model fit to the free-surface data. The oblique gray lines represent the lithostatic behavior. The vertical line corresponds to the standard deviation of one point selected from the free-surface dataset and representative of the asymptotic regime. A. Dry datasets. B. Immersed datasets**

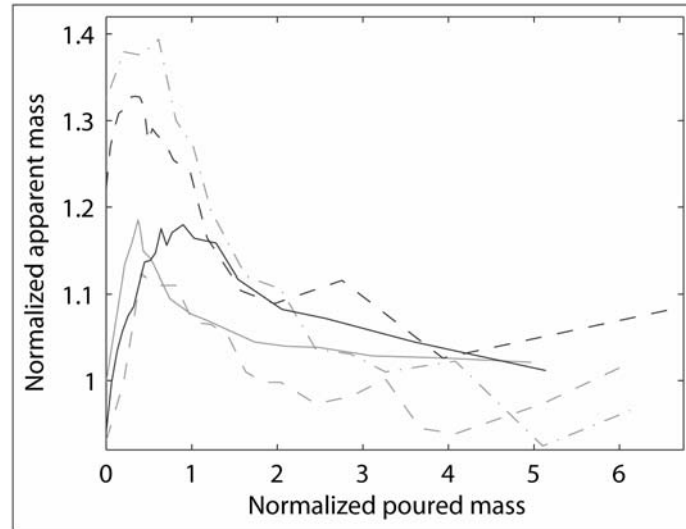


**Figure 2-10: Overshoot effect compared to data from previous literature. Apparent mass versus poured mass, both normalized by the asymptotic mass. Solid and dashed black lines correspond to the dry overweight and immersed overweight datasets collected by the authors for the present study. Each point corresponds to the ensemble mean of all the repeated runs for a fixed piling height. Gray curves are data published by other researchers using slightly different experiment and data analysis procedures. The solid gray line comes from (Ovarlez *et al.* 2003) and the dashed and dash-dot lines from (Vanel *et al.* 2000)**

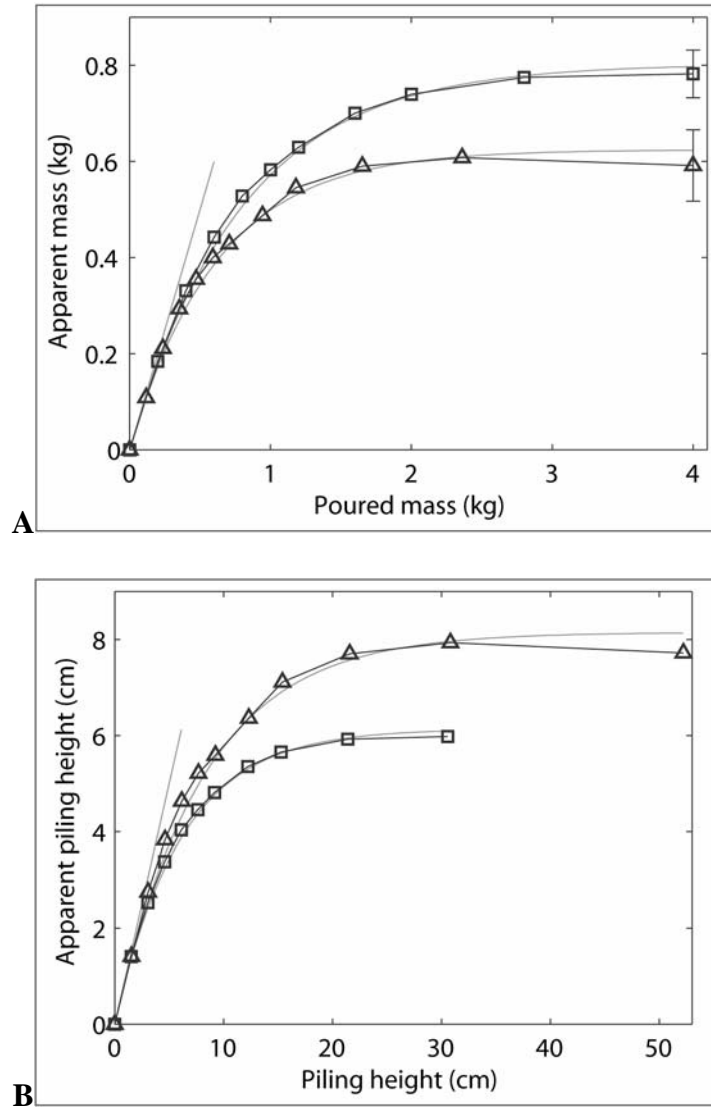


**Figure 2-11: Effect of the addition of water. Squares and triangles respectively correspond to the dry and immersed free-surface datasets. Each point corresponds to the ensemble mean of all the repeated runs for a fixed piling height. The gray curves show a Janssen model fit to both datasets. The oblique gray line represents the lithostatic behavior. A. Apparent mass versus poured mass. The vertical lines correspond to the standard deviation of one point selected from each dataset and representative of the asymptotic regime. B. Apparent piling height versus actual piling height**

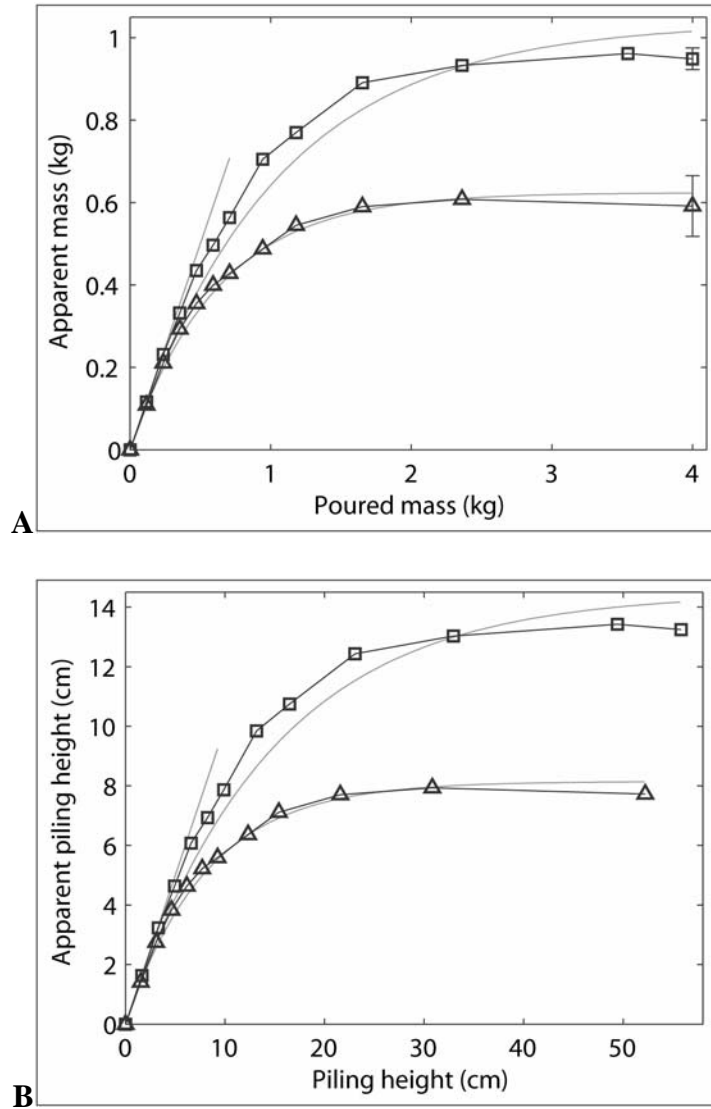


**Figure 2-12: Effect of the pouring procedure comparing both immersed free-surface datasets. Squares and triangles respectively correspond to the settling and immersion procedures. See Fig. 2-11 for a description of the additional lines. A. Apparent mass versus poured mass. B. Apparent piling height versus actual piling height**



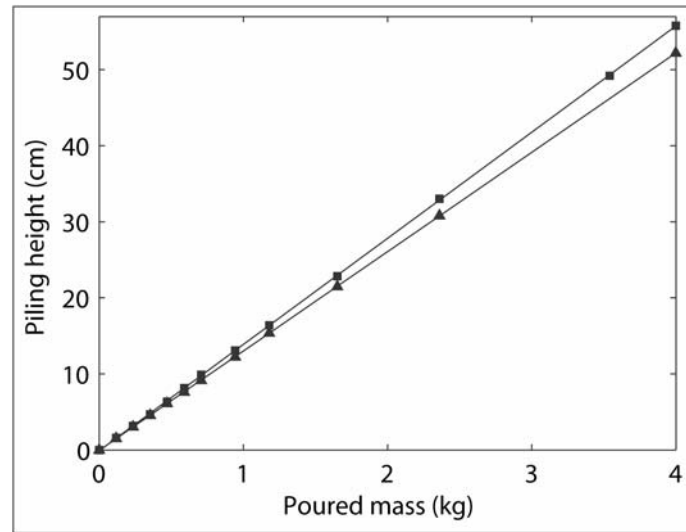


**Figure 2-13: Measured piling heights versus poured mass for both immersed free-surface datasets. Each point corresponds to the ensemble means of the measured piling heights for a fixed expected piling height corresponding to a fixed poured mass. Squares and triangles respectively correspond to the settling and submersion procedures. The two lines are a first order fit to each dataset**

## References

- Abdel-Fattah MT, Moore ID, Abdel-Fattah TT (2006) Behaviour of elevated concrete silos filled with saturated solids. *Canadian Journal of Civil Engineering* 33:227-239
- Abou-Chakra H, Tuzun U (1999) Coefficient of friction of binary granular mixtures in contact with a smooth wall PART I: Direct shear bore measurements of the effects of particle size ratio and particle surface roughness. *Chemical Engineering Science* 54:5901-5912
- Abrams DM, Lobkovsky AE, Petroff AP, Straub KM, McElroy B, Mohrig DC, Kudrolli A, Rothman DH (2009) Growth laws for channel networks incised by groundwater flow. *Nature Geoscience* 2:193-196
- Albert I, Tegzes P, Kahng B, Albert R, Sample JG, Pfeifer M, Barabasi AL, Vicsek T, Schiffer P (2000) Jamming and fluctuations in granular drag. *Physical Review Letters* 84:5122-5125
- Ancey C (2001) Role of lubricated contacts in concentrated polydisperse suspensions. *Journal of Rheology* 45:1421-1439
- Atman APF, Claudin P, Combe G (2009) Departure from elasticity in granular layers: Investigation of a crossover overload force. *Computer Physics Communications* 180:612-615
- Bagnold R (1988) The physics of sediment transport by wind and water: a collection of hallmark papers. American Society of Civil Engineers, New York
- Beatley T, Brower D, Schwab A (2002) An introduction to coastal zone management. Island Press, Washington DC
- Behringer RP, Howell D, Kondic L, Tennakoon S, Veje C (1999) Predictability and granular materials. *Physica D* 133:1-17
- Bertho Y, Giorgiutti-Dauphine F, Hulin JP (2003a) Intermittent dry granular flow in a vertical pipe. *Physics of Fluids* 15:3358-3369
- Bertho Y, Giorgiutti-Dauphine F, Hulin JP (2003b) Dynamical Janssen effect on granular packing with moving walls. *Physical Review Letters* 90
- Bertho Y, Brunet T, Giorgiutti-Dauphine F, Hulin JP (2004) Influence of humidity on granular packings with moving walls. *Europhysics Letters* 67:955-961
- Bocquet L, Charlaix E, Restagno F (2002) Physics of humid granular media. *Comptes Rendus Physique* 3:207-215

Bouchaud JP, Cates ME, Claudin P (1995) Stress-Distribution in Granular Media and Nonlinear-Wave Equation. *Journal De Physique I* 5:639-656

Boutreux T, Raphael E, deGennes PG (1997) Propagation of a pressure step in a granular material: The role of wall friction. *Physical Review E* 55:5759-5773

Brauer K, Pfitzner M, Krimer DO, Mayer M, Jiang YM, Liu M (2006) Granular elasticity: Stress distributions in silos and under point loads. *Physical Review E* 74

Brown R, Richards J (1970) principles of powder mechanics. Pergamon Press, Oxford

Cain RG, Page NW, Biggs S (2000) Microscopic and macroscopic effects of surface lubricant films in granular shear. *Physical Review E* 62:8369-8379

Cassar C, Nicolas M, Pouliquen O (2005) Submarine granular flows down inclined planes. *Physics of Fluids* 17

Cates ME, Wittmer JP, Bouchaud JP, Claudin P (1998a) Jamming, force chains, and fragile matter. *Physical Review Letters* 81:1841-1844

Cates ME, Wittmer JP, Bouchaud JP, Claudin P (1998b) Development of stresses in cohesionless poured sand:2535-2560

Chevoir F, Roux JN, da Cruz F, Rognon PG, Koval G (2009) Friction law in dense granular flows. *Powder Technology* 190:264-268

Claudin P (1999) Sandpile physics - A phenomenological description of stress propagation in granular materials. *EDP sciences*

Claudin P, Bouchaud JP (1997) Static avalanches and giant stress fluctuations in silos. *Physical Review Letters* 78:231-234

Clement E (1999) Rheology of granular media. *Current Opinion in Colloid & Interface Science* 4:294-299

Cohen JE, Small C, Mellinger A, Gallup J, Sachs, J, Vitousek PM, Mooney, HA (1997) Estimates of Coastal Populations 10.1126/science.278.5341.1209c. *Science* 278:1209c-1213

Coppersmith SN, Liu C, Majumdar S, Narayan O, Witten TA (1996) Model for force fluctuations in bead packs. *Physical Review E* 53:4673-4685

Cowin SC (1977) Theory of Static Loads in Bins. *Journal of Applied Mechanics-Transactions of the Asme* 44:409-412

Daerr A, Lee P, Lanuza J, Clement E (2003) Erosion patterns in a sediment layer. *Physical Review E* 67

de Gennes PG (1997) Friction forces on a solid experiencing more than one contact. *Comptes Rendus De L Academie Des Sciences Serie Ii Fascicule B-Mecanique Physique Chimie Astronomie* 325:7-14

de Gennes PG (1999) Granular matter: a tentative view. *Reviews of Modern Physics* 71:S374-S382

Didwania AK, Cantelaube F, Goddard JD (2000) Static multiplicity of stress states in granular heaps. *Proceedings of the Royal Society a-Mathematical Physical and Engineering Sciences* 456:2569-2588

Divoux T, Geminard JC (2007) Friction and dilatancy in immersed granular matter. *Physical Review Letters* 99

Duong NHP, Hosoi AE, Shinbrot T (2004) Periodic knolls and valleys: Coexistence of solid and liquid states in granular suspensions. *Physical Review Letters* 92

Duran J (2000) *Sand, powders, and grains: An introduction to the physics of granular materials*. Springer-Verlag, New York

Duran J, Kolb E, Vanel L (1998) Static friction and arch formation in granular materials. *Physical Review E* 58:805-812

Duran J, Mazozi T, Clement E, Rajchenbach J (1994) Size Segregation in a 2-Dimensional Sandpile - Convection and Arching Effects. *Physical Review E* 50:5138-5141

Evesque P, Stefani C (1991) Relationship between Dilatancy, Stresses and Plastic Dissipation in a Granular Material with Rigid Grains. *Journal De Physique Ii* 1:1337-1347

Evesque P, de Gennes PG (1998) On the statics of silos. *Comptes Rendus De L Academie Des Sciences Serie Ii Fascicule B-Mecanique Physique Astronomie* 326:761-766

Feda J (1982) *Mechanics of particulate materials: the principles*. Elsevier Science & Technology

Fredsøe J, Deigaard R (1992) *Mechanics of coastal sediment transport*. World Scientific

- Friedmann SJ, Kwon G, Losert W (2003) Granular memory and its effect on the triggering and distribution of rock avalanche events. *Journal of Geophysical Research-Solid Earth* 108
- Garcia X, Medina E (2008) Strong-weak network anisotropy switching and hysteresis in three-dimensional granular materials. *Physical Review E* 78
- Gayvallet H, Geminard JC (2002) Ageing of the avalanche angle in immersed granular matter. *European Physical Journal B* 30:369-375
- Geminard JC, Losert W, Gollub JP (1999) Frictional mechanics of wet granular material. *Physical Review E* 59:5881-5890
- Geng JF, Behringer RR (2005) Slow drag in two-dimensional granular media. *Physical Review E* 71
- Geng JF, Howell D, Longhi E, Behringer RP, Reydellet G, Vanel L, Clement E, Luding S (2001) Footprints in sand: The response of a granular material to local perturbations. *Physical Review Letters* 87
- Goyon J, Colin A, Ovarlez G, Ajdari A, Bocquet L (2008) Spatial cooperativity in soft glassy flows. *Nature* 454:84-87
- Hansen JL, van Hecke M, Haaning A, Ellegaard C, Andersen KH, Bohr T, Sams T (2001) Pattern formation - Instabilities in sand ripples. *Nature* 410:324-324
- Hutter K, Pudasaini S (2005) Geophysical granular and particle-laden flows. *Philosophical Transactions: Mathematical, Physical and Engineering Sciences* 363:1495-1700
- Iverson RM, Vallance JW (2001) New views of granular mass flows. *Geology* 29:115-118
- Jaeger HM, Nagel SR (1992) Physics of the Granular State. *Science* 255:1523-1531
- Jaeger HM, Nagel SR, Behringer RP (1996) Granular solids, liquids, and gases. *Reviews of Modern Physics* 68:1259-1273
- Jain N, Ottino JM, Lueptow RM (2004) Effect of interstitial fluid on a granular flowing layer. *Journal of Fluid Mechanics* 508:23-44
- Jiang YM, Liu M (2009) Granular solid hydrodynamics. *Granular Matter* 11:139-156
- Jop P, Forterre Y, Pouliquen O (2006) A constitutive law for dense granular flows. *Nature* 441:727-730

- Josserand C, Tkachenko AV, Mueh DM, Jaeger HM (2000) Memory effects in granular materials. *Physical Review Letters* 85:3632-3635
- Kolb E, Clement E (2005) Experimental response function of a 2D granular media around the jamming transition. *Powders and Grains 2005: Proceedings of the 5th International Conference on Micromechanics of Granular Media*:373-376
- Kuwano R, Jardine RJ (2002a) On measuring creep behaviour in granular materials through triaxial testing. *Canadian Geotechnical Journal* 39:1061-1074
- Kuwano R, Jardine RJ (2002b) On the applicability of cross-anisotropic elasticity to granular materials at very small strains. *Geotechnique* 52:727-749
- Kuwano R, Jardine RJ (2007) A triaxial investigation of kinematic yielding in sand. *Geotechnique* 57:563-579
- Landry JW, Grest GS (2004) Granular packings with moving side walls. *Physical Review E* 69
- Landry JW, Grest GS, Silbert LE, Plimpton SJ (2003) Confined granular packings: Structure, stress, and forces. *Physical Review E* 67
- Lesaffre C, Mineau V, Picart D, Van Damme H (2000) Densification under vibration of a saturated granular packing. *Comptes Rendus De L Academie Des Sciences Serie Iv Physique Astrophysique* 1:647-653
- Liu J, Shi QF, Liang XW, Yang L, Sun G (2009) Size dependence of effective mass in granular columns. *Physica a-Statistical Mechanics and Its Applications* 388:379-384
- Loiseleux T, Gondret P, Rabaud M, Doppler D (2005) Onset of erosion and avalanche for an inclined granular bed sheared by a continuous laminar flow. *Physics of Fluids* 17
- Longhi E, Easwar N, Menon N (2002) Large force fluctuations in a flowing granular medium. *Physical Review Letters* 89
- Losert W, Geminard JC, Nasuno S, Gollub JP (2000) Mechanisms for slow strengthening in granular materials. *Physical Review E* 61:4060-4068
- Lubarda V (2002) *Elastoplasticity theory*. CRC Press, Boca Raton
- Luding S (2005) Granular media - Information propagation. *Nature* 435:159-160
- Lykousis V, Locat J, Sakellariou D (2007) Submarine mass movements and their consequences: 3rd international symposium. Springer Verlag, Dordrecht

- Mangeney A, Tsimring LS, Volfson D, Aranson IS, Bouchut F (2007) Avalanche mobility induced by the presence of an erodible bed and associated entrainment. *Geophysical Research Letters* 34
- Masson DG, Harbitz CB, Wynn RB, Pedersen G, Lovholt F (2006) Submarine landslides: processes, triggers and hazard prediction. *Philosophical Transactions of the Royal Society a-Mathematical Physical and Engineering Sciences* 364:2009-2039
- Masson S, Martinez J (2000) Effect of particle mechanical properties on silo flow and stresses from distinct element simulations. *Powder Technology* 109:164-178
- Matchett AJ (2006) Stresses in a bulk solid in a cylindrical silo, including an analysis of ratholes and an interpretation of rathole stability criteria. *Chemical Engineering Science* 61:2035-2047
- Michalowski RL (2005) Coefficient of earth pressure at rest. *Journal of Geotechnical and Geoenvironmental Engineering* 131:1429-1433
- MiDi GDR (2004) On dense granular flows. *European Physical Journal E* 14:341-365
- Mueth DM, Jaeger HM, Nagel SR (1998) Force distribution in a granular medium. *Physical Review E* 57:3164-3169
- Mueth DM, Debregeas GF, Karczmar GS, Eng PJ, Nagel SR, Jaeger HM (2000) Signatures of granular microstructure in dense shear flows. *Nature* 406:385-389
- Nedderman R (1992) *Statics and kinematics of granular materials*. Cambridge University Press
- Niedostatkiewicz M, Tejchman J (2007) Investigations of porosity changes during granular silo flow using electrical capacitance tomography (ECT) and particle image velocimetry (PIV). *Particle & Particle Systems Characterization* 24:304-312
- Nielsen P (1992) *Coastal bottom boundary layers and sediment transport*. World Scientific
- O'Hern CS, Silbert LE, Liu AJ, Nagel SR (2003) Jamming at zero temperature and zero applied stress: The epitome of disorder. *Physical Review E* 68
- Ogale SB, Bathe RN, Choudhary RJ, Kale SN, Ogale AS, Banpurkar AG, Limaye AV (2005) Boundary effects on the stability of thin submerged granular piles. *Physica a-Statistical Mechanics and Its Applications* 354:49-58

- Otto M, Bouchaud JP, Claudin P, Socolar JES (2003) Anisotropy in granular media: Classical elasticity and directed-force chain network. *Physical Review E* 67
- Ovarlez G, Clement E (2003) Slow dynamics and aging of a confined granular flow. *Physical Review E* 68
- Ovarlez G, Clement E (2005) Elastic medium confined in a column versus the Janssen experiment. *European Physical Journal E* 16:421-438
- Ovarlez G, Kolb E, Clement E (2001) Rheology of a confined granular material. *Physical Review E* 64
- Ovarlez G, Fond C, Clement E (2003) Overshoot effect in the Janssen granular column: A crucial test for granular mechanics. *Physical Review E* 67
- Philippe P, Richard T (2008) Start and stop of an avalanche in a granular medium subjected to an inner water flow. *Physical Review E* 77
- Pouliquen O, Chevoir F (2002) Dense flows of dry granular material. *Comptes Rendus Physique* 3:163-175
- Radjai F, Wolf DE, Jean M, Moreau JJ (1998) Bimodal character of stress transmission in granular packings. *Physical Review Letters* 80:61-64
- Rahmoun J, Millet O, de Saxce G (2008) A continuous media approach to modeling the stress saturation effect in granular silos. *Journal of Statistical Mechanics-Theory and Experiment*
- Reynolds O (1885) On the dilatancy of media composed of rigid particles in contact. *Philosophical Magazine* 20:469-481
- Ribiere P, Richard P, Delannay R, Bideau D, Toiya M, Losert W (2005) Effect of rare events on out-of-equilibrium relaxation. *Physical Review Letters* 95
- Rousseaux G, Caps H, Wesfreid JE (2004) Granular size segregation in underwater sand ripples. *European Physical Journal E* 13:213-219
- Rowe PW (1969) Osborne Reynolds and Dilatancy. *Geotechnique* 19:1-&
- Samadani A, Kudrolli A (2001) Angle of repose and segregation in cohesive granular matter. *Physical Review E* 64
- Savage S (1998) Modeling and granular material boundary value problems. In: Herrmann H, Hovi J, Luding S (eds) *Physics of dry granular media*. Kluwer Academic Publishers, Dordrecht, pp25-96



- Silbert LE, Ertas D, Grest GS, Halsey TC, Levine D (2002) Geometry of frictionless and frictional sphere packings. *Physical Review E* 65
- Sperl M (2006) Experiments on corn pressure in silo cells - translation and comment of Janssen's paper from 1895. *Granular Matter* 8:59-65
- Terzaghi K (1943) *Theoretical soil mechanics*. Wiley & Sons, New York
- Terzaghi K, Peck R, Mesri G (1996) *Soil mechanics in engineering practice*. Wiley and Sons, New York
- Tixier M, Pitois O, Mills P (2004) Experimental impact of the history of packing on the mean pressure in silos. *European Physical Journal E* 14:241-247
- Toiya M, Stambaugh J, Losert W (2004) Transient and oscillatory granular shear flow. *Physical Review Letters* 93
- Umbanhowar P, van Hecke M (2005) Force dynamics in weakly vibrated granular packings. *Physical Review E* 72
- Van Damme H, Mansoutre S, Colombet P, Lesaffre C, Picart D (2002) Pastes: lubricated and cohesive granular media. *Comptes Rendus Physique* 3:229-238
- Vanel L, Clement E (1999) Pressure screening and fluctuations at the bottom of a granular column. *European Physical Journal B* 11:525-533
- Vanel L, Clement E, Lanuza J, Duran J (1998) Pressure fluctuations in a granular column *Physics of Dry Granular Media*. Kluwer Academic Publishers, pp249-254
- Vanel L, Howell D, Clark D, Behringer RP, Clement E (1999) Memories in sand: Experimental tests of construction history on stress distributions under sandpiles. *Physical Review E* 60:R5040-R5043
- Vanel L, Claudin P, Bouchaud JP, Cates ME, Clement E, Wittmer JP (2000) Stresses in silos: Comparison between theoretical models and new experiments. *Physical Review Letters* 84:1439-1442
- Volfson D, Tsimring LS, Aranson IS (2003) Partially fluidized shear granular flows: Continuum theory and molecular dynamics simulations. *Physical Review E* 68
- Wood DR, Boulton GS, Rotter JM (1998) Mechanics of granular materials in engineering and Earth sciences - A discussion meeting held 28 and 29 January 1998. *Philosophical Transactions of the Royal Society of London Series A-Mathematical Physical and Engineering Sciences* 356:2451-2782

Wu W, Bauer E, Kolymbas D (1996) Hypoplastic constitutive model with critical state for granular materials. *Mechanics of Materials* 23:45-69

Yang FL, Hunt ML (2008) A mixed contact model for an immersed collision between two solid surfaces. *Philosophical Transactions of the Royal Society a-Mathematical Physical and Engineering Sciences* 366:2205-2218

Chapter 2 is currently being prepared for submission for publication in *Granular Matter* as: Le Dantec, Nicolas; Deane, Grant B. “Measurements of the Apparent Mass at the Base of Water-Saturated Granular Pilings”. The dissertation author was the primary investigator and author of this paper.

**CHAPTER 3: Modeling stress in saturated granular pilings  
using the Oriented Stress Linearity approach to  
quantify arching**

## ABSTRACT

Measurements of the apparent mass at the base of dry and saturated granular pilings, without and with overweight, are compared with predictions for stresses in static, confined pilings, which are obtained from numerical implementation of the Oriented Stress Linearity (OSL) model. The OSL model provides a better description of free-surface data than Janssen model and performs equally well as a modified Janssen model involving a lithostatic base layer. The OSL model is capable of predicting the overshoot observed for overweight pilings but also shows intrinsic oscillations that are not observed in the experimental data. The efficacy of mass shielding is observed to decrease for saturated pilings and for pilings with decreasing packing ratios. This result is discussed in the light of changes in the OSL model parameters estimated from the data. Despite limitations in both its conceptual foundation and its predictive power, the OSL model allows interpretation of the arching behavior of granular pilings in terms of arch direction and friction angle along arches. The oscillations predicted by the OSL model, which are most prominent in the fit to overweight datasets, could not be damped by allowing random fluctuations of the arching angle about its mean.

## INTRODUCTION

Granular systems reveal a variety of complex responses to forcing and the description of their mechanical behavior by existing theories can sometimes be inadequate, thus leaving the research field of granular matter still quite open for theoretical and experimental studies (Jaeger *et al.* 1996; Duran 2000; Mehta 2007). Even in configurations that may seem simple, the spatial and temporal heterogeneity intrinsic to granular assemblies hinders the understanding and prediction of their macroscopic properties, which are determined by the collective behavior of individual grains (Mehta 2007). Heterogeneities in the internal structure of granular materials and in their subsequent response to excitation or perturbations are associated with heterogeneities in the displacements of grains (Dauchot *et al.* 2005). The existence of long-range correlations and non-local behavior raises the question of the role of discontinuities in the strain and stress fields and their significance in the characterization of a mesoscopic homogeneous scale (Luding 2005). Along with the difficulty in defining and measuring displacements within granular media (Cates *et al.* 1998a; Savage 1998; de Gennes 1999), the afore-mentioned characteristics constitute a major hurdle in devising a comprehensive theory of granular matter. At this time, the expression of a macroscopic closure relation from microscopic granular physics is a widely debated topic.

A classic approach based on the framework of elasticity and plasticity theories adopts an incremental description of stress-strain relationships with a decomposition of deformation into elastic and plastic parts (Lubarda 2002; Rao *et al.* 2008). The stress field is maintained by reversible, elastic displacements that store granular energy while

irreversible, plastic displacements involving sliding and rolling of grains are dissipative. Closure relations in the form of yield conditions and flow rules require introducing rheological parameters based on granular effects, such as dilatancy or Mohr-Coulomb plasticity, and which are determined from tri-axial tests. Memory effects accounting for the dependence on the preparation history can be encoded by the compaction of the system (Brauer *et al.* 2006).

Hypoelastic or hypoplastic theories (Kolymbas 2000) do not require yield conditions nor flow rules and assume that the stress rate tensor is a function of the stress tensor, strain rate tensor and the packing ratio, with the dependence in the strain rate tensor being linear or incrementally non-linear, respectively (Rao *et al.* 2008). Such models, which show dilatancy effects and stress-level dependence, can also describe the scale effects associated with shear bands, provided a characteristic length is introduced. This is done in the micro-polar hypoplastic model by accounting for rotations, which are observed in granular materials under shear, and couple stresses (Tejchman and Wu 2008) following the Cosserat model. The dependence on the preparation history is considered through the effect of the direction of deformation rate. Although the model parameters can be related to the granulometric properties of the materials (Tejchman and Wu 2008), these models lack an appealing physical basis in particular regarding the significance of the choice of the Jaumann derivative of the stress as the frame indifferent stress rate tensor (Rao *et al.* 2008).

The recently proposed OSL model (Bouchaud *et al.* 1995; Wittmer *et al.* 1997; Cates *et al.* 1998a; Claudin 1999) is also developed as a continuum model but its closure equation is derived by assuming a local propagation rule for stresses which depends on

the construction history rather than on the strain. Based on the concept of fragile matter (Cates *et al.* 1998b), where the material responds linearly to loads compatible with its internal structure and reorganizes plastically for others, the OSL approach consists in a physical model of force chains. A preferred direction of yield is assumed, along which the shear strength of the material is reduced. The resulting stress-only constitutive relation renders the existence of long range structures associated with the disordered, anisotropic contact force network. Combining the above closure with the stress continuity equations gives hyperbolic equations for the stress field, in contrast with elliptic-hyperbolic equations in the case of elastoplastic theories. The equivalent of a wave equation for stress propagation is obtained in two dimensional configurations, with the vertical direction replacing the temporal coordinate, and where physical force chains or stress paths become mathematic characteristics of the hyperbolic equations (Bouchaud *et al.* 1995; Claudin 1999).

The validity of the OSL approach is controversial. That the strain tensor is not considered when modeling stresses within granular materials using the framework of continuum mechanics is seen as major shortcoming of the OSL model by a large part of the research community (Savage 1997; Savage 1998; Didwania *et al.* 2000). The idea that, within a range of compatible loads, the stress response of granular systems can be determined solely from a stress propagation rule and without further specifying the configuration, is rejected by some, on the basis that a such approach mixes macroscopic and microscopic arguments without establishing a proper transition between scales. Conversely, leaving strain aside obviates questions associated with the significance of a displacement field for granular materials and lifts the inconsistency between the

reproducibility of some experimental observations on granular systems and their unpredictability by theories that require strain to be specified (Cates *et al.* 1998a; Savage 1998). In any case, keeping in mind the above reservations, the OSL successfully reproduces several observations typical of granular materials and captures at least some of the physics of force chains (Wittmer *et al.* 1996). As such, it most likely provides valid insights that are not offered by more conventional theories of granular mechanics.

Force chains, which play a central role in the OSL model, consist of chainlike groups of particles with above average contact force (Cates *et al.* 1998b). Their main orientation appears to correspond with the direction of the most compressive principal stress exerted on the material (Peters *et al.* 2005). Spatially organized into a force network, the grains aligned along force chains bear the majority of the load of the granular assembly. Also called arches, or granular bridges, they are a manifestation of the heterogeneity of granular systems. The existence of force chains is confirmed by direct observations (Majmudar and Behringer 2005; Sanfratello *et al.* 2009), indirect inference from fluctuations in experimental measurements (Geng and Behringer 2005) and numerical simulations (Fortin *et al.* 2005; Peters *et al.* 2005; Tordesillas *et al.* 2009). Their presence is equally well recognized among the engineering, soil mechanics and physics communities (Kuwano and Jardine 2002; Fortin *et al.* 2005; Majmudar and Behringer 2005). Yet, at present there is no consensus on the modeling of the effects induced by force chains on the mechanical behavior of granular materials (Socolar *et al.* 2002; Tordesillas *et al.* 2009). Further, despite many investigations on force chains and discussions on their role, quantitative methods to characterize and determine force chains have been proposed only recently (Peters *et al.* 2005).



The focus of this work is on the determination of the stress at the base of dry and saturated granular pilings confined in columns for the analysis of experimental data on the apparent mass measured at the base of such pilings (Le Dantec and Deane 2009). The silo is a classic example of a granular system where spatial heterogeneities in the material have long been known to have significant mechanical effects, but where such effects are still incompletely understood and modeled at this point (Duran 2000). Obviously, stress redirection has been identified, together with wall friction, as responsible for the observed, progressive shielding of the piling mass with increasing height (Nedderman 1992; Duran 2000). Janssen model, although imperfect in many ways (Le Dantec and Deane 2009), reproduces the shielding effect with reasonable accuracy and is generally recommended for its simplicity (Nedderman 1992). However, it does not capture other effects, including the lithostatic behavior observed in the lower region of the piling and the non-monotonic response observed when an overweight is applied on top of the piling. It is also unable to predict the large scatter in the measurements of the mass at the base of pilings, the strong dependence of the measured mass on the filling procedure and the stress fluctuations and jamming effects observed during discharge. These features, some of which are not so subtle, are related to granular arches and the heterogeneities within the piling.

Numerous refinements on the Janssen model have been proposed (Nedderman 1992). There are also other analyses based on the framework of elastoplasticity (Nedderman 1992), which is the theoretical approach generally used in soil mechanics, or, less frequently, hypoplasticity, and rarely hybrid models with viscosity (Tejchman 1998; Rao *et al.* 2008). They often propose numerical solutions obtained through Discrete

or Finite Element Methods, which are more practical and reveal more realistic than simplified analytical solutions. Results are usually confronted with the predictions of Janssen model. The most common models of such type are the Coulomb method of wedges and the method of characteristics (Nedderman 1992), both of which appear to share some features with the OSL model (see section 3-3.2 for a description of the OSL model). The Coulomb method of wedges assumes a constant angle for yield surfaces and is essentially a 2-dimensional solution which can yet be applied to the case of a cylindrical geometry (Bagster and Nedderman 1985; Nedderman 1992). The method of characteristics exhibits oscillations in the predicted apparent mass, which arise from discontinuities in the boundary conditions that are reflected downward at the sidewalls and centerline (Horne and Nedderman 1976).

The lack of reproducible, trusted data and benchmark scenarios that would be more selective or ambitious than the sole mass shielding effect prevents from testing and comparatively differentiating such theories (Rotter *et al.* 1998). Overall, it is not clear that they provide significant improvement over Janssen model (Nedderman 1992). Furthermore, comparisons of recent experimental measurements on dry granular pilings with the predictions obtained from the method of characteristics under the hypothesis that the material is everywhere at the threshold of Coulomb failure show rather large discrepancies, indicating that this assumption is too constraining and inadequate (Claudin 1999). It can be expected that a refined analysis consisting in a full elastoplastic treatment where only certain parts of the assembly are at the threshold of yield, as it has been done in the case of sand piles using the method characteristics (Didwania *et al.* 2000), would improve this result. In any case, among conventional models following a continuum

mechanics approach, the authors are not aware of an exact analysis focusing specifically on granular arches and heterogeneities within the piling, and explicitly considering the aforementioned effects associated with force chains.

Recent experiments on granular pilings at the laboratory scale have motivated interesting contributions to the topic of the mechanical response of confined granular pilings (Le Dantec and Deane 2009). In particular, a simple yet effective modification to Janssen model has been proposed, consisting in introducing a lithostatic layer, devoid of stress redirection effect, at the bottom of the piling (Vanel and Clement 1999). Another *ad-hoc* decomposition of the piling in two layers has been suggested as an extension of Janssen model in order to accommodate for the stiffening of the upper region of the piling when an overweight is placed on its free-surface (Ovarlez and Clement 2005). The stress fluctuations observed in the measured mass at the piling base have been investigated by adapting the q-model, a scalar model for stress propagation, to allow the formation of arches (Claudin and Bouchaud 1997). Note that the scaling of the predictions of the q-model with the piling size was subsequently shown to be inconsistent with measurements (Ovarlez *et al.* 2003). Finally, the OSL model, initially developed to study arching in sandpiles, has also been applied to the configuration of confined granular pilings (Claudin 1999; Vanel *et al.* 2000). It outperforms Janssen model and is equivalent to the modified Janssen model in the case of free-surface pilings. More importantly, it is the only model able to reproduce the response observed when an overweight is applied on top of the piling, with the notable weakness of also predicting resonant oscillations. Such oscillations are not observed experimentally and, if they exist, have a much smaller amplitude than their counterparts in the OSL model.

The usage of the term arching to denote stress redirection as well as the formation of granular arches, a definition which differs from the normal meaning of arching in soil mechanics, as already mentioned earlier in the dissertation, can perhaps be supported by the following comment. According to the stress propagation rule proposed in the OSL model (see section 3-3.2.1), the material is assumed to be at the limit of slippage along certain directions that are determined by the internal structure of the assembly. i.e. lateral stress deflection occurs through stress transmission along force chains. (Bouchaud *et al.* 1995; Claudin 1999). The approach is consistent with (but not equivalent to) the usual concept of arching since stress transfer is accompanied by localized yielding.

The objective of this paper is to interpret the effect of saturation of granular pilings on arching mechanisms in the light of the OSL model, notwithstanding the deficiencies of the latter. Measurements have been acquired on dry and saturated pilings, without and with an overweight. Experiments and data analysis were carefully conducted to guarantee the reproducibility of the data (Le Dantec and Deane 2009). Rather than evaluating the performance of the OSL model, the purpose here is to exploit the correspondence between physical arches and characteristics along which stress is propagated in the model. With the exception of the modified Janssen model in the free-surface case and the Janssen model for reference, other available theories mentioned above will not be used. Given that their performance is usually assessed by comparison with Janssen model, the latter can serve as a proxy for them. In addition, they do not readily apply to the overweight case nor offer the possibility of inverting variables characterizing the internal structure of the material from model parameters. The organization of the paper is as follows. First the theory and its numerical implementation

are described, then the experimental methods are recalled and the data regression procedure is explained. Model fits are presented and the results of parameter estimations are discussed. The effects of saturation, packing ratio and overweight loading on the arching mechanism are interpreted using the OSL model metrics: the arching angle and the internal friction angle along arches (Claudin 1999; Vanel *et al.* 2000). Finally, a simple, vain attempt at introducing fluctuations in the arching angle to damp the oscillations predicted by the model is reported.

## THEORETICAL ANALYSIS

### Force balance

Stress continuity follows from the force balance on a continuum body in static equilibrium,

$$\nabla_i \sigma_{ij} = F_j, \quad (1)$$

where  $\sigma_{ij}$  is the stress tensor, which is symmetric ( $\sigma_{ij} = \sigma_{ji}$ ) due to the balance of moments, and  $F_j$  represents the body forces (in this case,  $F_j = \rho g_j$ , where  $\rho$  is the bulk density of the granular material and  $g_j$  is the acceleration of gravity). The cylindrical polar coordinates  $(r, \varphi, z)$  are a natural choice for the piling geometry, with  $z$  the vertical axis oriented downward. The stress continuity can be rewritten as

$$\partial_z \sigma_{zz} + \partial_r \sigma_{rz} = \rho g - \sigma_{rz}/r, \text{ and} \quad (2)$$

$$\partial_z \sigma_{rz} + \partial_r \sigma_{rr} = -(\sigma_{rr} - \sigma_{\varphi\varphi})/r, \quad (3)$$

since  $\partial_\varphi \sigma_{ij} = 0$  and  $\sigma_{r\varphi} = \sigma_{z\varphi} = 0$  follow from exploiting the axial symmetry around the vertical axis taken to coincide with the central axis of the piling  $r = 0$ . Four components of the stress tensor are left to be determined so that 2 closure equations are required.

## The OSL model

### Texture tensor, arching and effective friction angles, and characteristics

Here the OSL approach is described, following the presentation of the model given in (Bouchaud *et al.* 1995; Wittmer *et al.* 1997; Cates *et al.* 1998a; Claudin 1999; Vanel *et al.* 2000), to which the reader is referred for further details. To obtain the additional equations required to close the system of equations (2-3), the OSL model assumes that the internal structure of a granular assembly yields definite relations between components of the stress tensor (see section 3-2). The choice for the stress-only relationships is then motivated by the objective of capturing the microscopic physics of grain-to-grain contacts. This is done by taking into account the spatial arrangement of the grains within the material, which is known to strongly affect its mechanical behavior, for example its stiffness. The geometrical configuration of the grains is encoded in a texture tensor characterizing the orientation of the contacts between a grain and its neighbors. The observed anisotropy of the texture tensor reflects the existence of preferred direction of alignment between grains. The principal axes of the texture tensor can be associated with the force chains observed in granular materials. Such collective, chain-like structures that take the form of arches, are thought to play the role of preferred paths for stress propagation within the assembly. In a  $(r, z)$  plane, a local set of normal axes  $(m, n)$  can be defined from the contact orientation, with the local arch direction defined by its

angle  $\tau$  measured counterclockwise from the downward vertical axis, as shown in Fig. 3-1.

The OSL model assumes that the friction between parallel arches or force chains is fully mobilized with an effective friction angle  $\psi$ , which can be written as

$$\sigma_{nm} = \tan \psi \sigma_{nn} . \quad (4)$$

The angle  $\psi$  can be positive or negative, depending on the direction of the tangential force along the arch, respectively either outward or inward, which corresponds to a situation of active or passive failure, when filling or emptying a silo. Obviously,  $|\psi| < \phi'$ , where  $\phi'$  is the internal friction angle of the material. Practically, equation (4) means that the granular material will yield under a shear stress exceeding  $\tan \phi$  times the normal stress, except along the direction  $\tau$  of the arches where yield will occur for a smaller shear stress in excess of  $\tan \psi$  times the normal stress. This effect can be described as an anisotropic frictional behavior:  $\phi'(\tau) = \psi$  and  $\phi'(\tilde{\tau}) = \phi'$  if  $\tilde{\tau} \neq \tau$ , with  $\tilde{\tau}$  spanning orientations in the  $(r, z)$  plane.

The system of equations (2-4) is hyperbolic, i.e. takes a simplified form along curves that are called characteristics, and along which the variables, here the stresses, are propagated. In two-dimensional coordinates, an anisotropic wave equation is recovered (see section 3-3.2.3). The characteristics of the stress propagation equations respectively make an angle  $\tau$  and  $\tau - \psi - \pi/2$  with the vertical axis (see Fig. 3-1), noting that the second angle is negative. An important property of the closure equation (4) is that the characteristics coincide with the granular force chains, which suggests that the constitutive relation successfully mimics the internal arching structure of the material.

The OSL relation

In order to simplify the resolution of the equations (2-4), the OSL model assumes constant arching and effective friction angles throughout the material. Then equation (4) can be rewritten, in cylindrical polar coordinates, as

$$\sigma_{rr} = \eta \sigma_{zz} + \mu \sigma_{rz}, \quad (5)$$

which is the OSL equation, where

$$\eta = -\tan \tau \tan(\tau - \psi - \pi/2), \text{ and} \quad (6)$$

$$\mu = \tan \tau + \tan(\tau - \psi - \pi/2). \quad (7)$$

The strong constraint of constant  $\tau$  and  $\psi$  may be justified in some systems such as the confined pilings studied in this work. In general, unless a system is perturbed, the internal structure is believed to be determined by the formation history of the material for grains are expected to keep their configuration once buried, as a memory effect. The texture of granular materials prepared following a consistent protocol is likely to be uniform since most grains will probably have similar orientations of their contacts with neighbors when they come to rest.

A second relation is required to obtain a closed equation system.  $\sigma_{\varphi\varphi} = \sigma_{rr}$  is assumed, on the basis that it is consistent with the symmetry of the piling configuration which imposes this relation at  $r = 0$  and that the particular form of the second relation has been shown to have little influence on the numerical simulations. In addition, this choice further simplifies the equation system, which is now

$$\partial_z \sigma_{zz} + \partial_r \sigma_{rz} = \rho g - \sigma_{rz}/r \quad (2)$$



$$\partial_z \sigma_{rz} + \partial_r \sigma_{rr} = 0 \quad (8)$$

$$\sigma_{rr} = \eta \sigma_{zz} + \mu \sigma_{rz}, \quad (5)$$

and will be solved numerically (see section 3-4.1).

Analytical OSL solution in two dimensional configurations

In this section, the preliminary steps of a geometric solution for a two dimensional configuration are outlined to illustrate the propagative nature of the equation system. In a Cartesian coordinate system  $(x, z)$ , still with a downward vertical axis, the above equations become

$$\partial_z \sigma_{zz} + \partial_x \sigma_{xz} = \rho g \quad (9)$$

$$\partial_z \sigma_{xz} + \partial_x \sigma_{xx} = 0 \quad (10)$$

$$\sigma_{xx} = \eta \sigma_{zz} + \mu |\sigma_{xz}|, \quad (11)$$

where the OSL relation has been slightly modified to satisfy the symmetry constraint. By defining two propagation velocities

$$c_{\pm} = \frac{1}{2} \left( \mu \pm \sqrt{\mu^2 + 4\eta} \right), \quad (12)$$

the equation system (9-11) can be transformed into

$$\partial_u (\sigma_{xz} - c_+ \sigma_{zz}) = (c_+ / (c_+ - c_-)) \rho g \quad (13)$$

$$\partial_v (\sigma_{xz} - c_- \sigma_{zz}) = (-c_- / (c_+ - c_-)) \rho g, \quad (14)$$

with the change of variables  $u = x - c_+ z$  and  $v = x - c_- z$ .

The hybrid variables  $\sigma_{xz} - c_{\pm} \sigma_{zz}$  are propagated in the  $(x, z)$  plane along lines of constant slopes  $c_{\pm}$  that are the characteristics of the equation system. This observation is

important for the numerical implementation of the solution in the three dimensional geometry of the piling, as it sets constraints on the vertical to horizontal grid size ratio.

In addition, as mentioned earlier and as a counterpart to the geometrical view of ray propagation, the equation system (9-11) can also be rewritten in the form of a wave propagation equation,

$$(\partial z - c_+ \partial x)(\partial z - c_- \partial x)\sigma_{ij} = 0. \quad (15)$$

This equation is satisfied by the components of the stress tensor and solutions take the general form

$$\sigma_{zz} = \rho g z + f_+(x - c_+ z) - f_-(x - c_- z) \quad (16)$$

$$\sigma_{xz} = c_+ f_+(x - c_+ z) - c_- f_-(x - c_- z). \quad (17)$$

The wave-like nature of the solutions to the equation system is evident in the numerical simulations shown below.

### Janssen and modified Janssen models

A presentation of Janssen analysis can found in (Nedderman 1992; de Gennes 1999; Duran 2000; Sperl 2006; Le Dantec and Deane 2009), including discussion on the limitations of the model, and only a brief outline is given here. Janssen model really is one dimensional as the stresses are only allowed to vary with depth. The force balance for a horizontal slab can be written as

$$\sigma_{rz} 2\pi R dz + \sigma_{zz}(z + dz)\pi R^2 = \rho g \pi R^2 dz + \sigma_{zz}(z)\pi R^2, \quad (18)$$

where  $R$  is the radius of the piling. Full mobilization of the Coulomb friction at the wall  $\sigma_{rz} = \mu_w \sigma_{rr}$  and the constitutive relation  $\sigma_{rr} = K \sigma_{zz}$  are assumed, with  $\mu_w$  the wall-

to-grain friction coefficient ( $\mu_w = \tan \theta$ , where  $\theta$  is the wall friction angle) and  $K$  the Janssen parameter (Le Dantec and Deane 2009). Then equation (18) becomes

$$d\sigma_{zz}/dz - \rho g + \sigma_{zz}/\lambda = 0, \text{ with} \quad (19)$$

$$\lambda = R/2K \tan \theta \quad (20)$$

and the boundary condition  $\sigma_{zz}(0) = Q$  at the top of the piling. The solution for the apparent mass at the base of the piling is

$$M_{app} = M_{asym} \left( 1 - \exp \left( -\frac{M_{pour}}{M_{asym}} \right) \right) + Q \exp \left( -\frac{M_{pour}}{M_{asym}} \right), \text{ with} \quad (21)$$

$$M_{asym} = \rho \pi R^3 / 2K \tan \theta. \quad (22)$$

The modified Janssen model (Vanel *et al.* 1998) is an *ad-hoc* elaboration on Janssen model including a layer with a lithostatic behavior at the base of the piling, consistent with experimental (Vanel *et al.* 1998), numerical (Landry *et al.* 2003) and theoretical (Evesque and de Gennes 1998) results. No mass shielding occurs below a height  $H_{litho}$ . The typical Janssen picture applies above this layer. The relation between apparent and poured masses in the free-surface case is

$$M_{app} = M_{pour}, \text{ if } z < H_{litho}, \text{ and otherwise}$$

$$M_{app} = M_{litho} + \left( M_{asym} - M_{litho} \right) \left( 1 - \exp \left( -\frac{M_{pour} - M_{litho}}{M_{asym} - M_{litho}} \right) \right), \quad (23)$$

with  $M_{litho} = \rho \pi R^2 H_{litho}$ . Such an extension cannot be derived as a rigorous solution of equation (19) with the appropriate change of vertical coordinate to account for the lithostatic layer. It is not readily applicable to the overweight scenario.

## Comparison between Janssen model and the OSL model

### Constitutive relations

In the particular case where  $\mu = 0$ , corresponding to a material with a property of local symmetry, i.e. where the force lines are symmetrical with respect to the vertical coordinate axis, the OSL constitutive relation becomes  $\sigma_{rr} = \eta \sigma_{zz}$ . The closure equation of Janssen model, which is global, is recovered locally. Thus the OSL model can be seen as a generalized Janssen theory taking into account shear stress within the piling and radial dependence of the stresses, with the notable difference that it is based on a conceptual analysis of stress propagation at the granular scale. While the Janssen model, where the granular assembly is described by the differential equation (18), does not account for some important properties of granular matter such as spatial heterogeneity (Mehta 2007) and dilatancy (Reynolds 1885), the OSL model incorporates at least some of the physics relevant to the behavior of the granular systems. As such, the OSL allows an interpretation of the parameters involved in the closure relation in terms of force chains orientation and strength.

### Correspondence between model parameters from two-dimensional solutions

The analytical OSL solution obtained for two dimensional, free-surface pilings using the method of characteristics takes the following form, after simplification in the limit of tall pilings,

$$M_{app} = M_{asym,OSL} \left( 1 - \left( \frac{1 - c_+ \tan \theta}{1 - c_- \tan \theta} \right)^n \right), \text{ with} \quad (24)$$

$$M_{asym,OSL} = (\rho DR / \eta \tan \theta) \left( 1 - \frac{1}{2} \mu \tan \theta \right), \text{ and} \quad (25)$$

$$n = \frac{M_{pour}}{M_{asym,OSL}} \frac{1}{(c_+ - c_-) \tan \theta} . \quad (26)$$

A detailed account of the derivation can be found in (Claudin 1999), up to the omission of the second term in the second factor on the right-hand side of equation (25) which is obtained at the final step when integrating the vertical, normal stress  $\sigma_{zz}$  to obtain the apparent mass at the piling base. Comparisons of the analytical solution with numerical simulations implemented in two dimensions confirm that the rectification is required. The correction is important since equation (25) is involved in the determination of the correspondence between the OSL parameters  $(\eta, \mu)$  and the Janssen parameter  $K$ , which is carried out below.

A Taylor series expansion of the analytical OSL solution, considering the wall friction coefficient to be small, yields, as a first order approximation, the solution derived from Janssen model for free-surface pilings

$$M_{app} = M_{asym,OSL} \left( 1 - \exp \left( - \frac{M_{pour}}{M_{asym,OSL}} \right) \right) . \quad (27)$$

Coming back to Janssen model (see section 3-3.3) and repeating the analysis for two dimensional, free-surface pilings yields the solution (21) with

$$\lambda_{2D} = R/K \tan \theta , \text{ and} \quad (28)$$

$$M_{asym,2D} = \rho D R / K \tan \theta , \quad (29)$$

instead of (20, 22). The differences are due to the geometry of the horizontal slab in a  $(x, z)$  plane, which modifies the force balance (18) into

$$\sigma_{rz} 2dz + \sigma_{zz} (z + dz) 2R = \rho g 2R dz + \sigma_{zz} (z) 2R . \quad (30)$$

Matching  $M_{asym,OSL}$  with  $M_{asym,2D}$  gives

$$K = \eta / \left(1 - \frac{1}{2} \mu \tan(\theta)\right). \quad (31)$$

Concerning the assumption of tall pilings limit made to get (24-26), the geometrical construction of the analytical solution involves reflections of the stress-propagating characteristics off the column wall and the central axis of symmetry. A piling can be considered as tall if its height spans a sufficient number of reflection cycles, the unit height of which is  $R(1/c_+ - 1/c_-)$ . As confirmed in figures displaying vertical cross sections of the stress fields obtained from numerical simulations (see section 3-5.3.1), the number of reflections turns out to be small, between 2 and 4. However, the simplification is probably justified since tall pilings in the experiments are well within the shielded regime where the apparent mass no longer increases with piling height (Le Dantec and Deane 2009) (see section 3-5.1.1 below).

### Stability analysis

The range of the OSL parameters  $(\eta, \mu)$ , or equivalently of the force chains and effective internal angles  $(\tau, \psi)$  is limited by stability bounds. The Mohr-Coulomb criterion, which determines stability constraints relating components of the stress tensor (Brown and Richards 1970; Nedderman 1992; Claudin 1999), allows setting the parameter bounds. In its general form, the Mohr-Coulomb criterion consists of applying the Coulomb friction law at the scale of intergranular contacts within the assembly. It is written as the yield condition under shear, using the internal friction angle

$$|\sigma_{nm}| \leq \tan \phi' \sigma_{nn}. \quad (32)$$

Applying this criterion, rewritten in the cylindrical polar coordinates, at the central axis of the piling  $r = 0$  and at the column wall  $r = R$  (where  $R$  is the piling radius) is sufficient to ensure that the stability is verified throughout the piling. These limit situations are extreme opposites where the shear stress is respectively zero, due to symmetry constraints, and maximum.

The internal stability, obtained for  $\sigma_{rz} = 0$ , is given by

$$(1 - \sin(\phi')) / (1 + \sin(\phi')) \leq \eta \leq (1 + \sin(\phi')) / (1 - \sin(\phi')), \quad (33)$$

which exactly amounts to the Rankine bounds (Terzaghi *et al.* 1996; Le Dantec and Deane 2009). The stability at the wall, obtained for  $\sigma_{rz} = \tan \theta_w \sigma_{rr}$ , is given by

$$\frac{\eta_0 (1 - \mu \tan \theta_w)}{1 + \sqrt{A}} \leq \eta \leq \frac{\eta_0 (1 - \mu \tan \theta_w)}{1 - \sqrt{A}}, \text{ with} \quad (34)$$

$$\eta_0 = 1 / (1 + 2 \tan^2 \phi'), \text{ and} \quad (35)$$

$$A = (1 - \eta_0^2) (1 - \tan^2 \theta_w / \tan^2 \phi'). \quad (36)$$

Additionally, in practice the wall friction angle cannot exceed the internal friction angle since the reverse would result in the occurrence of a sliding plane one grain diameter away from the wall. Note that the stability zone narrows as the wall and internal friction angles get closer (see section 3-5.4.3).

## METHODS

### Implementation of numerical simulations

The equation system (2, 8, 5) can be numerically solved on a  $(r, z)$  plane. The OSL relation (5) is inserted into (8) to replace the radial, normal stress. The simulation

consists in computing the vertical components of the stress tensor  $(\sigma_{zz}, \sigma_{rz})$  at a horizontal grid level using the known stresses from the level immediately above. As the simulation progresses downward from the specification of the upper boundary conditions, stresses are propagated through the piling. Discretized equations are not numbered in the paper.

### Discretization scheme

Partial derivatives along the vertical and radial directions are respectively evaluated as forward and centered, first order finite differences

$$\begin{aligned}\partial_z \sigma_{ij} &= \frac{1}{\Delta z} (\sigma_{ij}(r, z + \Delta z) - \sigma_{ij}(r, z)), \\ \partial_r \sigma_{ij} &= \frac{1}{\Delta r} (\sigma_{ij}(r + \frac{\Delta r}{2}, z) - \sigma_{ij}(r - \frac{\Delta r}{2}, z)),\end{aligned}$$

where  $\Delta r$  and  $\Delta z$  are the radial and vertical steps. The stress components from the level immediately above the currently computed level are discretized using at a first order, centered scheme with either a  $\Delta r$  step if evaluated on a radial bin or a  $\frac{\Delta r}{2}$  step if evaluated in the middle of two adjacent radial bins.

$$\begin{aligned}\sigma_{ij}(r, z) &= \frac{1}{2} (\sigma_{ij}(r + \Delta r, z) + \sigma_{ij}(r - \Delta r, z)), \\ \sigma_{ij}(r + \frac{\Delta r}{2}, z) &= \frac{1}{2} (\sigma_{ij}(r + \Delta r, z) + \sigma_{ij}(r, z)), \\ \sigma_{ij}(r - \frac{\Delta r}{2}, z) &= \frac{1}{2} (\sigma_{ij}(r, z) + \sigma_{ij}(r - \Delta r, z)).\end{aligned}$$

The discretized equation system is then

$$\sigma_{zz}(r, z + \Delta z) = \left( \rho g \Delta z + \frac{1}{2} (\sigma_{zz}(r + \Delta r, z) + \sigma_{zz}(r - \Delta r, z)) - \frac{\Delta z}{2 \Delta r} (\sigma_{rz}(r + \Delta r, z) + \sigma_{rz}(r - \Delta r, z)) - \frac{\Delta z}{r} \sigma_{rz}(r, z) \right),$$



$$\sigma_{rz}(r, z + \Delta z) = \left( \frac{1}{2} (\sigma_{rz}(r + \Delta r, z) + \sigma_{rz}(r - \Delta r, z)) - \frac{\Delta z}{2\Delta r} \left( \eta (\sigma_{zz}(r + \Delta r, z) + \sigma_{zz}(r - \Delta r, z)) + \mu (\sigma_{rz}(r + \Delta r, z) + \sigma_{rz}(r - \Delta r, z)) \right) \right).$$

### Boundary conditions

At the wall,  $\sigma_{rz}(R + \Delta r, z) = W_{rz}(z)$  and  $\sigma_{rr}(R + \Delta r, z) = W_{rr}(z)$ , where  $(W_{rz}, W_{rr})$  are stresses exerted by the wall on the piling. The wall-to-grain friction gives  $\sigma_{rz}(R, z + \Delta z) = \tan \theta \sigma_{rr}(R, z + \Delta z)$  and  $W_{rz}(z) = \tan \theta W_{rr}(z)$ . The resulting discretized equations at the wall are

$$\sigma_{zz}(R, z + \Delta z) = \left( \begin{aligned} &\rho g \Delta z + \sigma_{zz}(R, z) - \left( \tan \theta + \frac{\Delta z}{r} \right) \sigma_{rz}(R, z) \\ &- \eta \tan \theta \frac{\Delta z}{2\Delta r} \sigma_{zz}(R - \Delta r, z) \\ &+ (1 - \mu \tan \theta) \frac{\Delta z}{2\Delta r} \sigma_{rz}(R - \Delta r, z) \end{aligned} \right) / \left( 1 - \frac{\eta \tan^2 \theta}{1 - \mu \tan \theta} \right),$$

$$\sigma_{rz}(R, z + \Delta z) = \eta \tan \theta \sigma_{zz}(R, z + \Delta z) / (1 - \mu \tan \theta).$$

At the central axis boundary, the shear stress is set to zero by symmetry, and the normal stress is determined using a first order centered scheme and symmetry properties

$$\sigma_{rz}(z + \Delta z, 0) = 0$$

$$\sigma_{rz}(z + \Delta z, 0) = \rho g \Delta z + \sigma_{rz}(z, \Delta r).$$

Finally, to initiate the simulation, at the top of the piling the shear stress is set to zero and the normal stress is the pressure exerted by the mass of the overweight over the piling horizontal cross-section, if applicable.

### Integration of the vertical, normal stress to get the apparent mass

The apparent mass is evaluated at certain horizontal levels of the grid, corresponding either to the experimental piling heights when the simulation is used for

parameter estimation, or to a denser, regular spacing over the maximum piling height when the simulation results are plotted. The stresses on each grid cell along a given horizontal grid level are integrated over the area of the corresponding ring  $A_{ring}(r)$ , which is evaluated as

$$A_{ring}(r) = \pi \left( \left( r + \frac{\Delta r}{2} \right)^2 - \left( r - \frac{\Delta r}{2} \right)^2 \right), \text{ yielding}$$

$$A_{ring}(r) = 2\pi \cdot r \Delta r .$$

The areas of the first and last rings are

$$A_{ring}(0) = \pi \left( \frac{\Delta r}{2} \right)^2, \text{ and}$$

$$A_{ring}(R) = 2\pi \cdot \left( R - \frac{\Delta r}{4} \right) \frac{\Delta r}{2} .$$

The resulting concentric ring forces are then summed to cover the entire piling cross-section, and divided over by  $g$  to obtain the apparent mass.

### Numerical parameters

The geometrical and granular parameters, namely the piling radius  $R$  and height  $H$ , the wall-to-grain friction angle  $\theta$  and the internal friction angle  $\phi'$  are taken equal to the experiment parameters (see section 3-4.2). In the remainder of the paper, the repose angle  $\phi$  is used in replacement for the internal friction angle  $\phi'$  because no other direct measurement is available. Although it is common, such a simplification is questionable (Cates *et al.* 1998a; Claudin 1999) and reveals inappropriate in this case (Le Dantec and Deane 2009) (see section 3-5.4.3 below). The numerical simulations are not affected since the internal friction angle is used only to determine the stability bounds for the OSL parameters (see section 3-3.5).

The number of vertical grid cells is determined from  $R$ ,  $H$  and the number of radial grid cells because of the constraint on the aspect ratio of the grid cell arising from the propagative nature of the OSL model. As mentioned above, the equation system resolved here describes stress propagation within the piling along characteristics of constant slopes  $c_{\pm}$  (see section 3-3.2.3). In order to avoid distorting the solution, the spatial discretization needs to be consistent with the velocity at which information, i.e. the stress fields, is propagated. Compared with cells exactly adjusted so the slope is the cell diagonal, tall cells will cause loss of information about the stress field while short cell will give rise to an artificial length scale in the solution. The two slopes are not equal in general. In this study, the cell size is adjusted to the largest slope, yielding a cell somewhat too short for the second characteristic, as shown in Fig.2.

The number of grid cells in the radial direction was chosen to guarantee the numerical convergence of the solution. Simulations were performed at different grid densities, setting other numerical parameters to values typical of the experiment configuration. The asymptotic mass of the solution was found to converge exponentially to a limit value with increasing number of radial grid cells. While solutions with 20 radial cells or less showed over 10% difference with the limit solution, the difference was below 1% for grids containing 200 radial cells. This number was used for the numerical simulations presented in the paper. Thus, each grain spans about 4 cells in the radial direction, which is not inconsistent with the modeling approach since the OSL model has no knowledge of the grain diameter.

## **Experimental measurements and datasets**

The experimental methods are described in details in (Le Dantec and Deane 2009) and summarized here. The experimental set-up and protocol were thoroughly tested to ensure the reproducibility of the dataset and verify that the sensitivity of the apparatus was sufficient to resolve the characteristic features of the apparent mass at the piling base. Pilings were formed from 1 mm diameter spherical glass beads with a density of  $2.53 \text{ g/cm}^3$  and confined in an acrylic column 100 grain diameters across and 500 grain diameters tall. The grains were poured in a rain-like, distributed fashion. Fresh water was used for immersed runs. The whole apparatus was water-tight so that for experiments on saturated pilings, the entire column was immersed, including the load cell. Two protocols were used for saturated pilings, either pouring a dry piling and immersing it by slowly raising the water level inside the column, or pouring grains into a water-filled column where they settled.

Measurements were acquired using a procedure of slow (1.7 micrometers/s) descent of the base of a load cell that was connected to a self-adjusted piston supporting the piling. The objective was to allow full mobilization of the wall-to-grain friction, while keeping the piling displacement small enough to prevent major piling rearrangements. As the load cell base was lowered, the measured mass decreased by about 25% to 50% until it approached an approximately constant value. The decrease in measured mass was not monotonic and temporary increases were observed, superposed on the overall trend of exponential decay. A careful analysis of the piling behavior motivated the choice of the apparent mass one e-folding distance on the least-mean-square exponential fit to the decompression regime starting at the beginning of the piling base descent. Despite the

dynamic boundary conditions imposed, the piling is in a quasistatic regime, in the sense that changes in the piling state, reflected in the mass measured at the base of the piling, occur on sufficiently long time scales that they can be resolved by the load cell. Thus it is appropriate to compare the measurements to predictions from models describing stresses within static granular systems.

A total of 5 datasets were acquired, each of them being associated with a different piling type: 1) dry, without overweight, 2) dry, with overweight, 3) immersed, without overweight, 4) immersed, with overweight and 5) settled, without overweight. The last 3 datasets concern saturated pilings with two different methods of piling formation. The overweight mass in the second and fourth datasets was equal to 0.94 and 1.22 times the asymptotic mass of the corresponding free-surface piling, respectively. A dataset is composed of a collection of data points consisting of ensemble measurements averaging 10 piling realizations (5 in the case of the fifth dataset) for a fixed poured mass, which improves the reproducibility of the experiment results by reducing the run-dependant variability in piling configuration.

Measurements are plotted in terms of apparent mass versus poured mass or apparent height versus poured height. The apparent and poured heights are obtained from  $h = m/(A\rho)$ , where  $m$  is the apparent or poured mass,  $A$  the cross section of the piling inside the column and  $\rho$  the bulk density of the granular assembly. The density, and packing ratio, were determined by recording the piling heights. In the case of saturated pilings, since the load cell records differential pressure when it is submerged, the bulk density, the apparent mass and the poured mass are reduced by buoyancy effects.

A summary of some of the relevant properties of the datasets is given in Table 3-1. In particular, the packing ratio has a significant influence on the intensity of the shielding effect (Le Dantec and Deane 2009) (see sections 4.1.1 and 4.4.2 below) and the number of data points in each dataset  $N_d$ , i.e. the number of piling heights sampled, will be used when assessing the quality of the model fit to the data (see section 3-4.3). Additionally, the wall friction and repose angles of the dry and saturated granular material used in the experiments were measured and are reported in Table 3-2.

**Table 3-1: Piling characteristics for all 5 datasets: packing ratio, bulk density and number of data points**

Datasets	Packing Ratio	$\rho$ (g/cm <sup>3</sup> )	$N_d$
Dry, Free-surface	63.3%	1.601	11
Dry, Overweight	63.3%	1.601	21
Immersed, Free-surface	62.7%	0.959	12
Immersed, Overweight	62.6%	0.958	22
Settled Free-surface	58.7%	0.898	13

**Table 3-2: Measured angles of repose and wall friction in dry and saturated conditions**

Measured angles	Repose Angle $\phi$	Wall Friction angle $\theta$
Dry	23.5°	20°
Saturated	23°	21.5°

### Regression procedure

Experimental data were fitted to the Janssen, modified Janssen and OSL models, the modified Janssen model being adjusted to the free-surface datasets only. Model parameters were estimated by finding the minimum of a cost function used to evaluate the difference between measurements and model predictions. The normalized Euclidian distance  $E$ , amounting to a weighed least-mean-square function (Claudin 1999; Vanel *et al.* 2000), was chosen because it accounts for differences in the measurement dispersion between piling heights, which are typically significant in apparent mass measurements at the base of granular pilings (Claudin 1999; Le Dantec and Deane 2009).

$$E = \sqrt{\frac{1}{N_d} \sum_{i=1}^{N_d} \left( \frac{M_{app}^i - M_{pred}^i}{\Delta M_{app}^i} \right)^2}, \quad (37)$$

where  $M_{app}^i$  is the ensemble average apparent mass,  $M_{pred}^i$  the apparent mass predicted by the model with the set of tested model parameters, and  $\Delta M_{app}^i$  the empirical dispersion of the measurements, all three taken at a given height. The distance  $E$  is the reduced version of the Mahalanobis distance (Morrison 1967), or generalized squared interpoint distance, which is used in statistical analysis of multivariate data. A distance  $E$  of 1 means that the difference between measurements and model predictions is equal to the measurement dispersion.

Here, the empirical dispersion is

$$\Delta M_{app}^i = \sqrt{\frac{1}{N_r} \sum_{j=1}^{N_r} (M_{app}^{i,j} - M_{app}^i)^2}, \quad (38)$$

where  $N_r$  is the number of piling realizations at a given height,  $M_{app}^{i,j}$  is the apparent mass for a given piling realization (index j) at the height considered (index i) and  $M_{app}^i$  is the ensemble average of the apparent mass over all the piling realizations at the height considered ( $M_{app}^i = \langle M_{app}^{i,j} \rangle_j$ ). The empirical dispersion  $\Delta M_{app}^i$  is different from the standard deviation  $S^i$  shown in plots (see Figs. 3-1 and 3-8),  $S^i = \sqrt{N_r / (N_r - 1)} \Delta M_{app}^i$ , which is the best unbiased estimate of the variance, or corrected empirical dispersion. Note that the measurement fluctuations stem from the variability in piling configuration, and are not representative of the error due the sensitivity of the experiment apparatus, which is much smaller (Le Dantec and Deane 2009).

In addition, a coefficient was used to assess the quality of the regression, independent of the number of involved data points  $N_d$  and adjustable model parameters (Claudin 1999). The quality coefficient is obtained using the complementary of the incomplete  $\Gamma$  function, the number of degrees of freedom of the regression  $N_f$  and the  $\chi^2$  test.

$$Q_c = \Gamma_{inc}^{comp}(N_f/2, \chi^2/2), \text{ with} \quad (39)$$

$$\chi^2 = E^2 N_d, \text{ and} \quad (40)$$

$$N_f = N_d - N_p, \text{ so that} \quad (41)$$

$$Q_c = \frac{1}{\Gamma(N_f/2)} \int_{\chi^2/2}^{\infty} e^{-t} t^{\frac{N_f}{2}-1} dt. \quad (42)$$

This allows comparisons between fits of all 3 models to all 5 datasets despite the large range in dataset sizes (see Table 3-1). The Janssen, modified Janssen and OSL models



respectively have 1 ( $K$ ), 2 ( $K, H_{litho}$ ) and 2 ( $\eta, \mu$ ) adjustable parameters.  $Q_c$  measures the probability that the fit is not just by chance. Regressions with a quality coefficient larger than 0.001 are considered reliable. Quality coefficients near unity usually result from a large dispersion in the measurements.

The range of tested parameters was not strictly constrained *a priori* using theoretical bounds derived from stability criteria, such as the Rankine bounds for the parameter  $K$  (Le Dantec and Deane 2009) and equations (33-36) for the OSL parameters. These bounds require knowledge of the internal friction angle, which is not available here, to be adequately evaluated. The search range for the lithostatic height introduced in the modified Janssen model was limited by obvious constraints on the layer height,  $H_{litho}$  being required to be positive and not in excess of the maximum piling height.

## DISCUSSION OF MODELING RESULTS

### Comparison of apparent mass predictions

#### Free-surface pilings

The apparent mass of free-surface pilings is plotted against poured mass in Figs. 3-3A, 3-3B and 3-3C for dry, immersed and settled datasets, respectively, together with curves representing their Janssen (dash-dot), modified Janssen (dashed) and OSL (solid) model fits. Standard deviations for a selected data point are shown as a reference for the corrected measurement dispersion, and the trend of the lithostatic behavior is indicated in gray. The typical Janssen behavior is observed in the three datasets (Le Dantec and Deane 2009), i.e. a rapid departure from lithostatic behavior and a progressive shielding

until the free-surface apparent mass reaches an asymptotic value. A detailed description of the measurements can be found in (Le Dantec and Deane 2009).

Comparing dry and saturated datasets requires correcting for buoyancy effects because the apparent mass measurements of saturated pilings is obviously measured under reduced gravity. This correction reveals that the asymptotic apparent piling height increases when saturating the pilings. Decrease in packing ratio also increases the asymptotic apparent mass, as is observed when comparing Figs. 3-1B and 3-1C (see Table 3-3).

Here the focus is on the models fits to the free-surface data, using the distance  $E$  and the coefficient  $Q_c$ , reported in Table 3-3, to assess the quality of the adjustment between data and models. For reference, the measurement dispersion, corresponding to the model to data difference when  $E = 1$  (see section 3-4.3), is on the order of 20gr, ranging from 5gr to 50gr depending on the piling height and the dataset, and exceptionally reaching 70gr (Le Dantec and Deane 2009).

For dry and immersed pilings, all three models reproduce the gross features of the measurements, and fall well within the measurement dispersion. For settled piling, only the modified Janssen model is able to match the data reasonably well. The Janssen model systematically underestimates the apparent mass at small piling heights and overestimates the asymptotic apparent mass. These deficiencies are effectively corrected by the addition of a lithostatic layer in the modified Janssen model, especially for the immersed and settled pilings. The OSL model provides the same qualitative improvement over Janssen model. Yet, the Janssen and OSL model fits are quantitatively comparable to one another for dry and settled pilings, where their adjustment to the measurements for these two

piling types is good and poor, respectively. While the lesser quality of the fit of the OSL model compared to the modified Janssen model is due to the poor adjustment to the asymptotic mass in the dry case, it is caused by the oscillations in the OSL model in the settled case.

For both saturated pilings, the OSL model predicts oscillations of the apparent mass superposed on the typical Janssen behavior. It is interesting to observe that, while remaining well within measurement dispersion, the data show that the evolution of the apparent mass is not as smooth for both saturated pilings as for dry pilings.

Looking at the overall data range, the modified Janssen model always yields a better fit than the OSL model, noting that for immersed pilings both models are very close for all values of poured mass. However, the distance  $E$  gives more weight to the data points which have smaller measurement dispersion. Thus the quality of the model fit can best be assessed by considering only small piling heights, where the measurement dispersion is significantly smaller than for large piling heights (Le Dantec and Deane 2009). Then, the OSL model shows a slight improvement compared to the modified Janssen model, especially for dry pilings (see Appendix 6.1 for other regression functions).

**Table 3-3: Performance of Janssen, modified Janssen and OSL model fits to free-surface datasets: asymptotic mass, distance  $E$  and  $Q_c$**

Datasets	Models	$M_{asym}$ (kg)	$E$	$Q_c$
Free-Surface Dry	Janssen	0.8026	1.00	0.35
	Ad-hoc	0.8194	0.82	0.57
	OSL	0.7614	1.07	0.18
Free-Surface Immersed	Janssen	0.6241	1.30	0.05
	Ad-hoc	0.6097	0.50	0.97
	OSL	0.6155	0.57	0.94
Free-Surface Settled	Janssen	1.0373	4.65	$< 10^{-15}$
	Ad-hoc	0.9651	1.07	0.19
	OSL	1.008	3.46	$< 10^{-15}$

#### Overweight pilings

The apparent mass of overweight pilings is plotted against poured mass (triangles connected by dotted curve) in Figs. 3-4A and 3-4B for dry and immersed datasets, respectively, together with their OSL model fit (solid curve). In addition, curves representing the Janssen (dash-dot) and OSL (dashed) models predictions, obtained using parameters estimated from model fits to the corresponding free-surface pilings, are also displayed. The apparent mass varies non-monotonically with poured mass, showing an initial increase toward a maximum for small piling heights followed by a progressive decay, which is irregular for immersed pilings, toward approximately the same asymptotic regime as for free-surface pilings (Vanel *et al.* 2000; Ovarlez *et al.* 2003; Le Dantec and Deane 2009).

The OSL model fit to the overweight piling measurements (Table 3-4) is qualitatively adequate for small piling heights and inappropriate for large piling heights. The OSL model is able to reproduce the maximum, with a good adjustment to its width and small differences in its amplitude. However the OSL model shows oscillations after the initial maximum, with similar phase and comparable amplitude to that of the maximum. Such oscillations after the apparent mass initial maximum are not observed in the measurements, at least not with the same amplitude as in the model. It is still interesting to note that data for the immersed piling do show that the decay toward the asymptotic regime is non-monotonic. Notwithstanding the insufficient sampling density that prevents proper characterization of possible variability in the apparent mass for large piling heights, measurements suggest the presence of at least one oscillation of smaller amplitude than in the model fit, but similar wavelength and phase.

The OSL model predictions obtained using the estimated free-surface parameters show a maximum for small piling heights, followed by oscillations. The predicted maximum is much smaller than in the overweight piling measurements and actual OSL model fits, especially in the dry case. So are the oscillations, which even vanish with increasing poured mass for dry pilings. The wavelength of the oscillations is smaller in the OSL model predictions than in the fits. For immersed pilings, the amplitude of the oscillations predicted by the OSL model using free-surface parameters is comparable to the magnitude of the variations observed after the initial maximum in the data.

The apparent mass predicted by Janssen model is monotonic in poured mass, so that no attempt was made to fit Janssen model to the data for overweight pilings. The Janssen model predictions using the estimated free-surface parameter obviously fail to

reproduce the initial maximum. For dry pilings, they yield an asymptotic apparent mass that does not match the data. For immersed pilings, they show an overall trend comparable to the OSL predictions from free-surface parameters but without the initial maximum, nor the oscillations.

**Table 3-4: Performance of OSL model fits to all 5 datasets:  $E$  and  $Q_c$**

Datasets	$E$	$Q_c$
Free-Surface, Dry	1.07	0.18
Overweight, Dry	1.71	$3 \cdot 10^{-6}$
Free-Surface, Immersed	0.57	0.94
Overweight, Immersed	1.36	0.005
Free-Surface, Settled	3.46	$< 10^{-15}$

#### **Effect of saturation on overweight piling behavior**

##### *OSL model predictions for overweight pilings interchanging dry and immersed parameters*

Here the effect of saturation on the behavior of overweight pilings is considered by comparing dry and immersed pilings with an overweight. Dry, overweight (gray) and immersed, overweight (black) datasets that are plotted together in Fig. 3-5, which shows normalized apparent mass versus normalized poured mass. The figure displays the data points (symbols connected by dotted curves), the OSL model fits to the data (solid curves) and the OSL model predictions obtained using the parameters estimated by OSL model fit to the other overweight dataset (dashed curves). Measurements show that the initial maximum is wider and occurs for larger piling heights in the dry case than in the

immersed case. Such differences in the apparent mass maximum have been observed when changing the mass of the overweight applied at the top of otherwise similar pilings (Vanel *et al.* 2000), and are thus not necessarily related to piling saturation.

The difference in the normalized overweight masses is a complication for direct comparison of overweight piling behavior. Applying the reciprocal best fit to predict the apparent mass allows testing for changes to the overweight piling response only due to differences in piling type, without the influence of differences in the overweight mass. Yet, interchanging parameters between dry, overweight and immersed, overweight datasets yields completely erroneous predictions. In both cases, the predicted asymptotic value is quantitatively very different (by 30% to 50%) from the measurements and the small piling height behavior is not captured. The magnitude of the error on the asymptotic mass indicates that the adjustment to the asymptotic mass is the dominant criteria in the selection of the model parameters. The sensitivity of the asymptotic mass prediction to changes in the model parameters prevents from probing their effect on the overweight piling behavior at small piling heights. Since the latter depends on the ratio between the overweight and asymptotic masses (Vanel *et al.* 2000), the failure to reproduce the apparent mass initial maximum originates in the erroneous predicted asymptotic mass. In addition, the difference between data and model fits to data due to the presence of oscillations in the model fits now seems less dramatic in comparisons with the difference between data and model predictions from interchanged parameters.

*Shielding of overweight mass by granular pilings*

As described in the above section, the difference in asymptotic apparent mass hinders the examination of the effect of piling saturation on the overweight piling behavior at small piling heights. Put differently, the effect of piling mass shielding by the granular piling is the main component of the overweight piling behavior while the effect of overweight mass shielding by the granular piling is of lesser significance to the overall behavior of overweight pilings. To get around this, the free-surface piling apparent mass is subtracted from the overweight piling apparent mass in order to consider the overweight-induced contribution to the overweight piling apparent mass  $\hat{M}_{app}^{overweight}$ .

$$\hat{M}_{app}^{overweight} = (M_{app}^{overweight} - M_{app}^{free-surface}) \quad (43)$$

The asymptotic apparent mass is governed by the shielding of the piling mass. The decomposition allows isolating the effect of overweight shielding by the piling. Obviously the shielding of the piling mass will be different between the free-surface and overweight pilings, since placing the overweight affects the piling arrangement, at least slightly. The normalized  $\hat{M}_{app}^{overweight}$  is plotted against poured mass in Fig. 3-6A for the dry (circles) and immersed (squares) cases, together with the corresponding model fits that are reduced in the same manner as the data. As expected, the overweight mass is progressively shielded by the piling, as shown by the decrease in  $\hat{M}_{app}^{overweight} / M_{over}$  with poured mass. The decreasing trend is linear in both cases, consistent with Vanel *et al.* (2000). Differences between the dry and immersed cases combine differences between dry, free-surface and immersed free-surface piling behavior and differences between dry, overweight and immersed overweight piling behavior.



Finally, the same reduction method is used to obtain the overweight-induced contribution to the overweight piling behavior in terms of apparent piling height and piling height, which is plotted in Fig. 3-6B. The objective is to investigate the effect of piling saturation on the shielding of the overweight mass by the piling after correcting for buoyancy effects. Both the reduced data and the reduced model fits show a collapse of the dry and immersed cases. For small piling heights, the data collapse means the piling saturation has little to no impact on the shielding of the overweight mass, result which is all the more striking when recalling the increase in shielding length of free-surface pilings induced by piling saturation. For large piling heights, the model collapse is intriguing as it indicates that the relative amplitude, the wavelength and the phase of the oscillations, which originate in the model fit to the overweight data, are similar between dry and immersed pilings. Note the difference between the dry and immersed data points at 20cm piling height corresponding to a high in the oscillation pattern of the model curve.

### **Oscillations and influence of arching angle fluctuations**

#### $\sigma_{zz}$ and $\sigma_{rz}$ within simulated pilings

The oscillations are intrinsic to the OSL model (see section 3-3.2.3). Vertical cross-sections of the simulated stress fields are displayed in Fig. 3-7 for the model fits to all 5 datasets, confirming the presence of oscillations, depending on the model parameters. Obviously such well-defined oscillations and the associated features reminiscent of interference patterns are not expected in real pilings. Yet, the visual representation of the stress fields allows comparing the OSL model oscillations between

piling types. Consistent with the apparent mass predictions (Fig.1 and 2), oscillations are almost imperceptible in the dry, free-surface case, mild in both saturated, free-surface cases and significant in both overweight cases. In agreement with Fig 6B, oscillations in both overweight pilings are in phase and have the same wavelength, which can be read along the piling height scale of the vertical axis. Observation of the oscillations in both saturated, free-surface pilings suggests that a decrease in packing ratio is associated with an increase in the wavelength of the OSL oscillations, consistent with a decrease in shielding intensity (see section 3-5.1.1). In addition, note that the pressure field in the dry, free-surface case is larger near the wall than near the central axis of the piling, contrary to all other piling types, which indicates a significant difference in the simulated stress propagation. The dry, free-surface, simulated piling is characterized by outward stress deflection typical of active failure and other simulated pilings are rather in a situation of passive failure.

#### *Tentative mechanism for oscillation-damping*

An attempt has been made at damping the oscillations generated in the OSL model. This was done by allowing for random fluctuations in the arch direction  $\tau$ .

In practice, the arch direction was changed at every horizontal grid level by adding a small random perturbation to a weighed average of the arch direction in the cell immediately above and the initial arch direction, i.e.

$$\tau(r, z + \Delta z) = \alpha\tau(r, z) + (1 - \alpha)\tau_o + \tau_\epsilon \quad (44)$$

where  $\tau_\epsilon$  is a random number within  $[-\tau_\sigma, \tau_\sigma]$ ,  $\tau_\sigma$  setting the order of magnitude for the fluctuations in  $\tau$ . This procedure keeps the departure of the arch angle from its initial

value sufficiently small to avoid unphysical values, and introduces a correlation range associated with  $\alpha$ . The parameter  $\alpha$  renders the length over which an arch changes direction, i.e. the number of consecutive contacts having a similar orientation. The initial arch direction  $\tau_o$  is obtained for any given pair of OSL parameters  $(\eta, \mu)$  via the slopes  $c_{\pm}$  using equations (12, 45), where equations (45-46) below are derived from (6, 7, 12).

$$\tau = \text{atan}(c_+), \text{ and} \quad (45)$$

$$\psi = -\text{atan}(c_-) + \tau - \pi/2 \quad (46)$$

Then  $\tau$  is modified according to (44) and the updated OSL parameters  $(\eta, \mu)$  are derived from  $(\tau, \psi)$  using equations (6, 7).

The attempt was unsuccessful, which indicates that the oscillations are a robust feature of the OSL model. Two examples are shown in Figs. 3-8A and 3-8B, where the fluctuations parameters were respectively  $(\alpha = 0.9, \tau_{\sigma} = 0.02\tau_o)$ , i.e. long correlation range and small magnitude, and  $(\alpha = 0.3, \tau_{\sigma} = 0.05\tau_o)$ , i.e. short correlation range and large magnitude. Differences in the arch direction variability between the two pairs of fluctuation parameters can be observed comparing the insets of Figs. 3-8A and 3-8B. The initial OSL parameters  $(\eta, \mu)$  correspond to the best fit to the dry, free-surface data. With both scenarios and both model fits to the free-surface and overweight data, the ensemble average of 10 realizations simulating the apparent mass with random fluctuations in  $\tau$  shows almost no deviation from the simulation without fluctuations. Random fluctuations even cause an increase in the amplitude of the relatively small oscillations in the case of the model predictions for the overweight data using the estimated free-surface parameters. Note that increasing the correlation range  $\alpha$  is more effective at generating

variability in single realizations than increasing the allowed range  $\tau_\sigma$  of the incremental random perturbation  $\tau_\epsilon$ . Individual simulations for a single realization of the fluctuations show some deviation from the simulation without fluctuations but no decrease in the amplitude of the oscillations. Abrupt variations observed in Fig. 3-8B for larger piling heights arise from numerical instabilities that occur within a certain subset of the OSL parameter space (see Appendix 6.2).

### **Changes in piling behavior within the OSL framework**

#### *Physical signification of the OSL parameters*

The results from the regression analysis performed to adjust the OSL model to the data are shown in Table 3-5. The angles  $(\tau, \psi)$  are obtained from  $(\eta, \mu)$  using equations (12, 45, 46). The correspondence between the arching and effective internal friction angles and the OSL parameters relating the stress tensor components comes from the two-dimensional analysis of the OSL approach. Although in real systems the arch network has a three dimensional structure, the parameter correspondence can be applied here considering that the network is projected on a vertical plane. This is what is done in practice for the numerical implementation of the stress propagation, which is effectively two-dimensional due to the choice of the second OSL relation. The numerical solution is still that of a three-dimensional piling.

The physical signification of the parameters is recalled first, in order to interpret differences between datasets. Large values of  $\eta$  are associated with effective lateral stress redirection through arching effects, i.e. small screening lengths. The parameter  $\mu$

is related to shear stress within the piling. Positive values mean that the inward characteristic carries most of the stress, which could correspond to the occurrence of inward avalanches during the piling base descent. Negative  $\mu$  values correspond to an outward stress propagation associated with an increase in the stress supported by the column walls. A decrease in arching angle  $\tau$  means steeper, more vertical arches. Finally, positive (negative) values of  $\psi$  correspond to a situation of active (passive) failure where the tangential force along the arch is directed outward (inward).

*Interpretation of the changes in piling behavior*

Focusing on  $\eta$  and  $\tau$ , the deflection of normal stresses is more intense in dry than in immersed pilings, confirming that piling saturation reduces mass shielding efficacy. Similarly, a decrease in packing ratio is associated with a decrease in mass shielding intensity, as is observed by comparing the immersed, free-surface and settled, free-surface cases. This effect seems to be associated with steeper arches. The apparent contradiction in a more vertical orientation of force chains corresponding to an increased efficiency in lateral stress redirection may be explained as follows. Increasing the steepness of force lines augments their strength, i.e. allows intergranular forces of larger amplitudes along force lines. The same pattern is observed in response to the overweight. The parameters  $\eta$  and  $\tau$  are respectively larger and smaller in free-surface than in overweight pilings, which confirms that placing the overweight affects the internal structure of the piling, with a tendency to increase its stiffness.

Now looking at  $\mu$  and  $\psi$ , stress propagation is asymmetric within all pilings. The signs of these parameters show that an accentuated inward stress deflection, possibly

caused by small-scale avalanches away from the column walls during the piling base descent, is observed in all but the dry, free-surface pilings. This effect is more pronounced in free-surface, settled pilings than in free-surface, immersed pilings, a result which is consistent with a previous study (Vanel *et al.* 2000) where pilings with higher packing ratios showed a reduced sensitivity to the proposed mechanism of inward avalanches during piling base descent. In the dry, free surface case, the outward stress deflection may result from outward avalanches at the piling surface during its formation, the memory of which is not overprinted by the piling base descent. Again, the large packing ratio of dry pilings may be responsible for the limited role of the inward avalanches mechanism. In addition, the large sensitivity of both saturated pilings to this mechanism may be due to the piling preparation methods. Piling immersion may sufficiently affect the piling arrangement that the local asymmetry arising from the dry pouring formation is partially erased. Settled piling may also show near-local symmetry before the piling base descent, due to the reduced kinetic energy involved in the piling construction.

In addition,  $|\psi|$  increases with a decreasing efficacy of the mass shielding effect, consistent with a yield criterion along arches approaching the bulk yield criteria applying everywhere else within the granular system. This effect is most significant in settled, free-surface pilings where  $|\psi| = \phi$ . Lines of preferred stress propagation still exist but the difference in small-scale stress propagation behavior is not very marked with the rest of the assembly.

**Table 3-5: Estimated OSL parameters and derived arching angle and yield angle along arches for OSL model fits to all 5 datasets**

Datasets	$\eta$	$\mu$	$\tau$	$\psi$
Dry, FS	1.47	-0.9	40.1°	10.3°
Dry, OV	0.7	1.39	60.7°	-7.9°
Immersed, FS	0.7	0.52	48.6°	-9.7°
Immersed, OV	0.55	0.98	54.0°	-14.2°
Settled FS	0.31	1.21	55.0°	-22.8°

*Selectivity of the OSL model in its adjustable parameters*

The results from the OSL regression analysis are also displayed in parameter space in Fig. 3-9, in the form of pair-wise comparisons between datasets. The distance arrays are scaled by their respective minima and color-coded, with blue regions corresponding to the optimal parameters. Black lines represent the stability bounds. That optimal parameter regions (see Table 3-5) lie outside their stability domain, or at best along one bound, is an indication that using the repose angle in replacement for the internal friction angle is not appropriate for the granular systems considered here (see section 3-4.1.4). Differences in the parameter values between datasets can be better appreciated with the parameter space view. Except in Fig. 3-9D, the optimal parameter regions are well dissociated in all pair-wise comparisons. Hence placing the overweight does not dramatically affect the behavior of immersed pilings, while stress propagation within dry pilings is significantly altered by the presence of the overweight. In the dry case, the sensitivity of the piling to the inward avalanching effect could be enhanced

when placing the overweight, maybe through a reduction in the local asymmetry originating in the piling formation.

The scaling chosen to display the distance arrays allows the examination of the selectivity of the model adjustment, i.e. the sharpness of the minimum, to the expense of information on the goodness of fit which have already been reported (see Tables 3-3 and 3-4). Although  $\eta$  is rather well defined, the model fit is not very selective in  $\mu$ , especially for free-surface pilings. This confirms that the second term in the OSL relation (5) can be seen as a small correction to the closure equation of Janssen model. For free-surface pilings, only accounting for the first term in (5) yields a good approximation of the measurements, i.e. a good description of the mass shielding effect. Note that for overweight pilings, at least in the dry case (Fig. 3-9C), the minimum is more localized. The requirement to reproduce the initial maximum in the apparent mass of overweight pilings narrows the selection criteria for  $\mu$ , consistent with the second term in (5) being responsible for the ability of the OSL model to capture the small piling height behavior.

### **Correspondence between the Janssen and OSL model parameters**

Finally the estimated parameters are compared across models. The Janssen parameter  $K$  equivalent to a given pair  $(\eta, \mu)$  can be calculated using equation (26). Obviously this is done only as a reference, since the correspondence is based on the tall pilings approximation to the analytical OSL solution in two-dimensional geometry (see section 3-3.4.2). The reciprocal equivalence requires adding the following equation (Claudin 1999)



$$\eta = \eta_o (1 - \mu \tan \phi), \quad (47)$$

where  $\eta_o$  is obtained from equation (35). The underlying assumption is that the piling is at the sliding limit near the column walls. Although the piling base descent is aimed at obtaining full friction mobilization at the wall (Le Dantec and Deane 2009), equation (47) is not necessarily satisfied, thus the reciprocal equivalence should be used with caution. Equations (26, 47) yield

$$\mu = (K - \eta_o) / (\frac{1}{2} K \tan \theta - \eta_o \tan \phi). \quad (48)$$

Results are shown in Table 3-6, where parameters obtained from model fits are printed in bold font. The equivalent  $K$  parameters calculated from fitted OSL parameters are very close the  $K$  parameters estimated from the Janssen and modified Janssen model fits. The counterpart is only true for settled, free-surface pilings, while equivalent OSL parameters calculated from  $K$  are not consistent with fitted OSL parameters in the case of dry, free-surface and immersed, free-surface pilings. This could mean that the assumption required to obtain equation (47) is not verified, in particular in the dry case. In the immersed case, the error is mostly on the value of  $\mu$  and, despite the sign change, could be due to the low selectivity of the OSL model in  $\mu$ .

Table 3-6 also presents estimated parameters for the Janssen and modified Janssen models, and shielding lengths derived from  $K$ . The analysis of the piling behavior in the framework of Janssen model has been presented elsewhere (Le Dantec and Deane 2009). An increase in the shielding length is observed in response to saturation and decrease in packing ratios. Concerning the modified Janssen model fits to the three free-surface datasets, as expected,  $H_{litho}$  increases with increasing shielding length. A

reduction in mass shielding is naturally associated with an increase in the lithostatic height. Note that the screening lengths are similar between the Janssen and modified Janssen model fits.

**Table 3-6: Summary of estimated (bold) and derived (regular, see section 3-5.5) parameters for Janssen, modified Janssen and OSL model fits to free-surface datasets**

Datasets	Models	$\eta$	$\mu$	$K$	$\lambda$ (cm)	$H_{litho}$ (mm)
Free-Surface Dry	Janssen	1.99	-4	1.15	<b>6.1</b>	0
	Ad-hoc	1.79	-3.39	1.11	<b>6.3</b>	<b>0.5</b>
	OSL	<b>1.47</b>	<b>-0.9</b>	1.26	5.6	N/A
Free-Surface Immersed	Janssen	0.84	-0.35	0.79	<b>8.2</b>	0
	Ad-hoc	0.89	-0.49	0.81	<b>8.0</b>	<b>8.3</b>
	OSL	<b>0.70</b>	<b>0.52</b>	0.77	8.4	N/A
Free-Surface Settled	Janssen	0.34	1.28	0.45	<b>14.5</b>	0
	Ad-hoc	0.37	1.17	0.48	<b>13.5</b>	<b>31.1</b>
	OSL	<b>0.31</b>	<b>1.21</b>	0.41	15.8	N/A

## CONCLUDING REMARKS

### Summary of main results

Solutions for the stress propagation in quasistatic granular pilings confined in a cylindrical column have been obtained by numerical implementation of the OSL model. Predictions were fitted to experimental measurements of the apparent mass at the base of dry and saturated pilings, without and with an overweight. The main objective was to

interpret the effect of saturation of granular pilings on arching mechanisms, which are quantified in a very simple manner by the two adjustable parameters of the OSL model. The piling saturation-induced decrease in the efficiency of the mass shielding behavior observed in measurements is associated with the following effects: 1- decrease in the lateral deflection of normal stresses, 2- decrease in the steepness of the force chains or granular arches, 3- increase in the sensitivity to a mechanism of inward avalanches arising from wall friction mobilization during piling base descent, and 4- decrease in the difference between the internal friction angle and the absolute value of the effective internal friction angle. In addition, the collapse of dry and immersed, reduced data defining the overweight-induced contribution to the apparent piling height of overweight pilings indicates that piling saturation has little impact on the shielding of the overweight mass by the piling. Finally, although the OSL model provides significant improvements over Janssen model, it is weakly selective in the adjustable parameter associated with the vertical shear stress when fitted to measurements of apparent mass at the base of granular pilings.

### **Comments on the oscillations**

Despite its deficiencies in other respects, the OSL model was also selected for its ability to qualitatively capture the small piling height behavior of overweight pilings. This strength comes at the expense of the prediction of the large piling height behavior of overweight pilings, where multiple oscillations arise from the intrinsic resonant behavior of the OSL model. Although it is interesting to note that the measurements for immersed and settled pilings do suggest the possibility of small oscillations, consistent with a recent

study where the data sampling was sufficient to lend reliability to the observed oscillations (Liu *et al.* 2009), the large oscillations predicted in the OSL model constitute a major weakness of the OSL approach.

Data regressions show that placing the overweight changes the arching behavior of the piling, insofar as it is characterized by the OSL parameters. The measurements of the apparent mass at the base of overweight pilings seem to show differences in piling behavior between small and large piling heights. If a small amplitude resonant behavior exists in real pilings, there is undoubtedly a change in the amplitude and possibly the wavelength of the apparent mass oscillations between small and large piling heights. In any case, the shielding of the overweight mass by the piling is different from the shielding of the piling mass by the piling. In its current form, the OSL model is unable to capture such change in the arching properties of the piling. Aside from introducing vertical variability in the OSL parameters, a decomposition of the piling in two layers (Ovarlez and Clement 2005), which would be consistent with an overweight-induced modification of the internal structure of the piling limited to a certain depth, may yield an adequate solution.

### **Lubrication effects and relevance of dry granular theories to saturated granular systems**

The piling saturation-induced changes in the arching mechanisms quantified by the OSL parameters (see section 3-6.1) are all consistent with the expected effects of lubrication on the microscopic physics at the scale of intergranular contacts. That the OSL model describes equally well and with quantitative differences in the adjustable

parameters the behavior of dry and saturated pilings extends the commonality of behavior between dry and saturated assemblies observed experimentally to the applicability of the theoretical concepts underlying the OSL model, such as that of fragile matter and local stress propagation rules for example. This is consistent with the idea that lubrication does not prevent intergranular contact and thus does not prevent saturated materials from supporting shear stress, therefore granting them solid-like properties (Cates *et al.* 1998b).

Additional experimental data acquired with different interstitial fluids spanning a range of lubrication properties would allow further examination of the role of the fluid in defining the intergranular contact properties and thus the characteristics of stress propagation and arching mechanisms. For example, such data would likely provide decisive evidence on the possibility that lubrication may increase the homogeneity of intergranular contacts throughout the piling, i.e. the uniformity in the direction and shear strength of the arching granular structures which are proposed to propagate stresses, thus favoring the occurrence of resonance effects. This would constitute a good test for the OSL model and other candidate theories for granular matter mechanics.

### **Accounting for random fluctuations of the piling texture**

The tentative mechanism for oscillation-damping was unsuccessful because the fluctuations in the arching angle that were introduced did not affect the mean arching angle, which determines the wavelength of the oscillations. Fluctuations in the effective internal friction angle may achieve a reduction in the amplitude of the oscillations, provided a different expression for the incremental change in angle is chosen so that the mean value differs from the initial value. In addition, the dependence of the arching angle

at a given grid cell on the arching angle at the grid cell directly above is inconsistent with arching mechanisms. Using the two grid cells on the level directly above but in diagonal would be more adequate. In any case, proper numerical implementation requires adjusting the height of each grid cell to the new OSL parameters, since they set the slope of the characteristics along which stress is propagated (Claudin 1999). This generates irregularities in the discretization grid, which constitutes a significant technical difficulty if the numerical simulations are to be used in data regression procedures.

### **About the OSL approach**

A desirable elaboration on the OSL model would consist in using the OSL framework to define failure criteria and changes in the arching properties between pre- and post- failure granular assemblies. This would most likely require the definition of the displacements and their description in relation to the failure events, hence to the stress. Such an extended OSL model would be applicable to dynamic situations and would then obviously have the potential for valuable industrial and geophysical applications.

## **APPENDIX**

### **Alternate regression methods**

The effect of the choice of the cost function  $E$  is illustrated here using two other examples of possible distances to fit the three models to the dry, free-surface data. In order to account for the irregular data sampling in poured mass, with a large point density

for small piling heights and very few data points for large piling heights, a normalized Euclidian distance  $E_w$  is introduced.

$$E_w = \sqrt{\frac{1}{N_d} \sum_{i=1}^{N_d} H_w^i \left( \frac{M_{app}^i - M_{pred}^i}{\Delta M_{app}^i} \right)^2}, \quad (49)$$

where  $H_w^i$  is a measure of the distance between data points, which applies a weighing inversely proportional to the data points density.

$$H_w^i = (H^{i+1} - H^{i-1})/2 \quad \text{for } 1 < i < N_d, \text{ and} \quad (50)$$

$$H_w^1 = (H^2 - H^1)/2 \quad \text{and} \quad H_w^{N_d} = (H^{N_d} - H^{N_d-1})/2$$

The second alternate distance is the least mean square fit  $E_{rms}$ , which is the root mean square (rms) error in the model fit compared to the data.

$$E_{rms} = \sqrt{\frac{1}{N_d} \sum_{i=1}^{N_d} (M_{app}^i - M_{pred}^i)^2} \quad (51)$$

The results are shown in Figs. 3-10A and 3-10B, respectively, which should be compared with Fig. 3-3A. Since both  $E_w$  and  $E_{rms}$  bypass the issue of increased weight given to the data points in the small piling height region (see section 3-5.1.1), the quality of model fits to the data can be evaluated over the entire curve. The improvement of the OSL model over the other two models is visually discernable. The modified Janssen model fit is close to the OSL model fit when using the distance  $E_{rms}$ .

### Numerical instabilities

Numerical instabilities arise in a region of the parameter space that can be roughly identified as  $\mu < -1$ . The problem was resolved by smoothing the horizontal profiles of the stress tensor components every 100 vertical grid levels using a fourth-order polynomial. Note that the stress profiles were also smoothed before evaluating the apparent mass at the required piling heights, which was done outside the incremental stress propagation algorithm to avoid perturbations to the regularity at which smoothing is done.

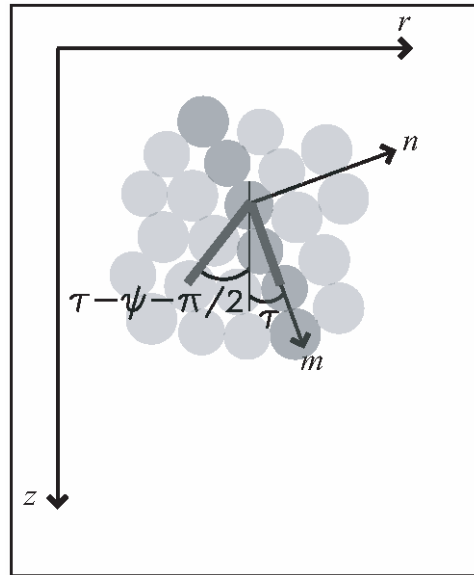
Several attempts were made to choose the frequency at which smoothing was applied. Correcting the stress profiles too often induces deviations from the stable, non-smoothed apparent mass prediction. This is illustrated in Fig. 3-11A. In addition, another strategy was pursued, consisting in coarsening the discretization grid. Results are shown in Fig. 11B. The apparent mass prediction is affected by the grid cell size, as advertised earlier (see section 3-4.1.4), while numerical instabilities may still be present, for example when doubling the grid cell size in the case displayed in Fig. 3-11B. This approach was abandoned.

The stress fields from two simulation scenarios are shown in Fig. 3-12. The top panel displays the case of the parameters corresponding to the model fit to the dry, free-surface data obtained by smoothing numerical instabilities. The bottom panel shows the case of nearby parameters that are outside of the parameter space subset where numerical instabilities occur but still yield a similar goodness of fit due to the extension of the optimal parameter region (see section 3-5.4.3). Differences are very minor, indicating that the stress fields are not significantly impacted by the smoothing procedure.

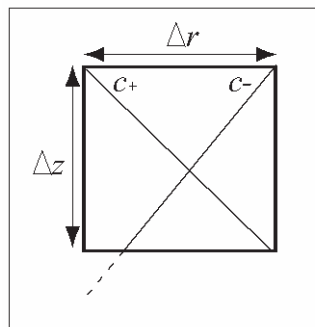


This algorithm was applied to all the OSL numerical simulations for the dry, free-surface dataset, including the entire data regression for this case. No smoothing was applied for the other four datasets since their optimal parameters were outside of the region where numerical instabilities occur.

**Acknowledgements:** Financial support was provided by the U.S National Science Foundation.

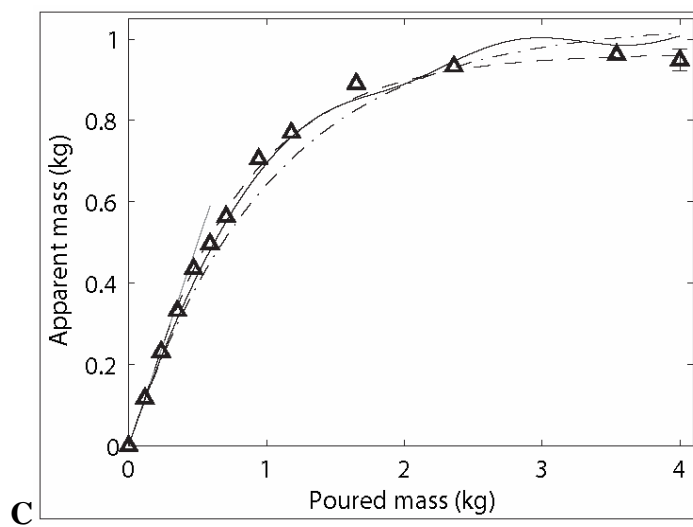
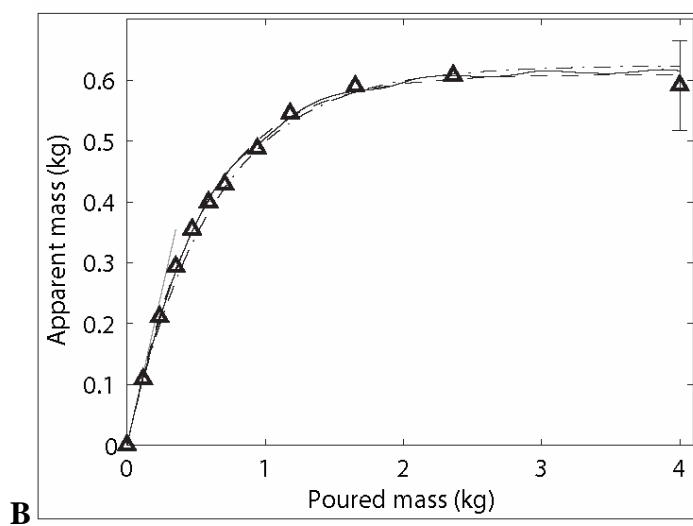
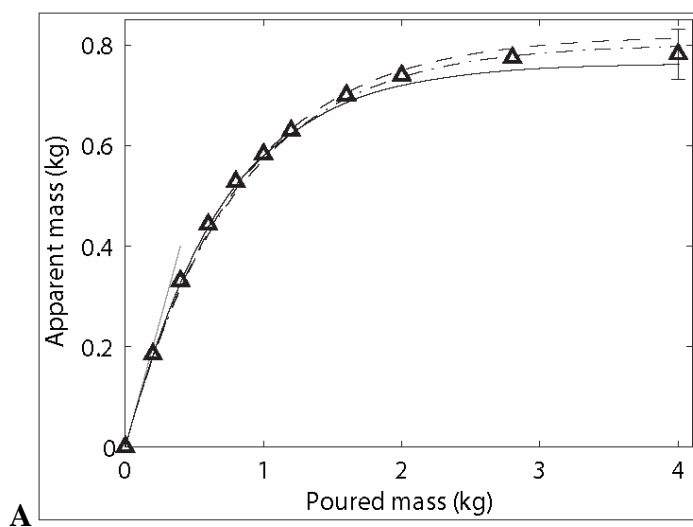


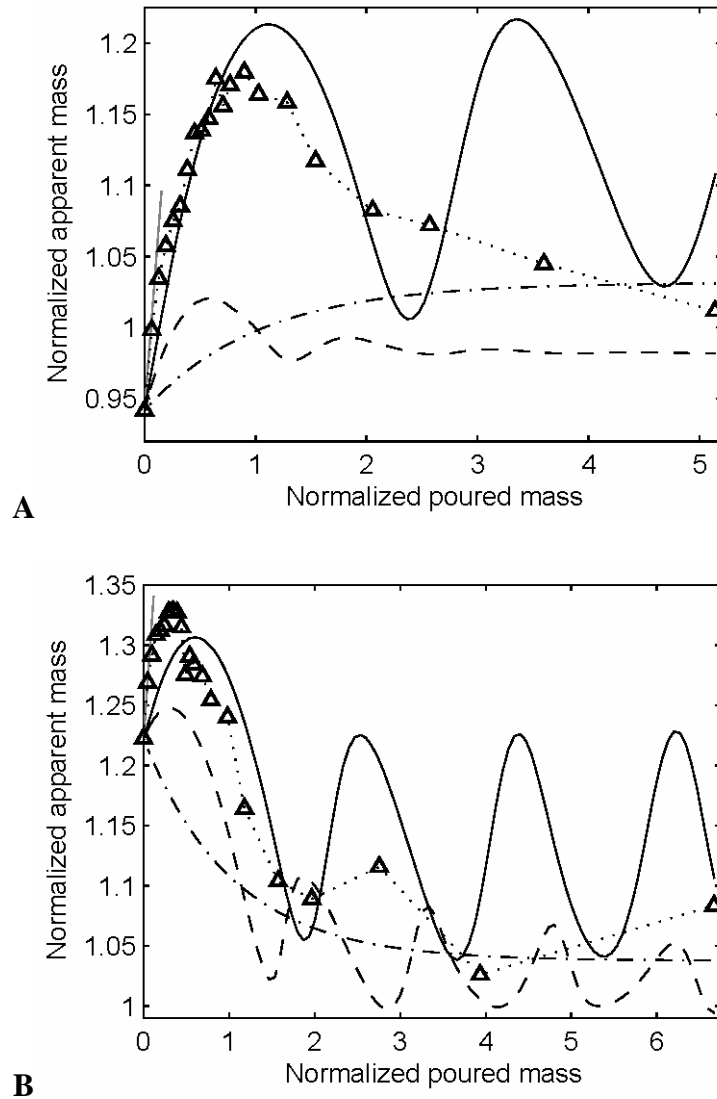
**Figure 3-1: Schematic of the small-scale stress propagation rule. Granular packing in a vertical plane  $(r, z)$ , showing the arching angle  $\tau$ , i.e. the major principal axis of the texture tensor at a point within the granular assembly. The thick, gray lines represent the characteristics along which stress is propagated. The darker grains symbolize a force line**



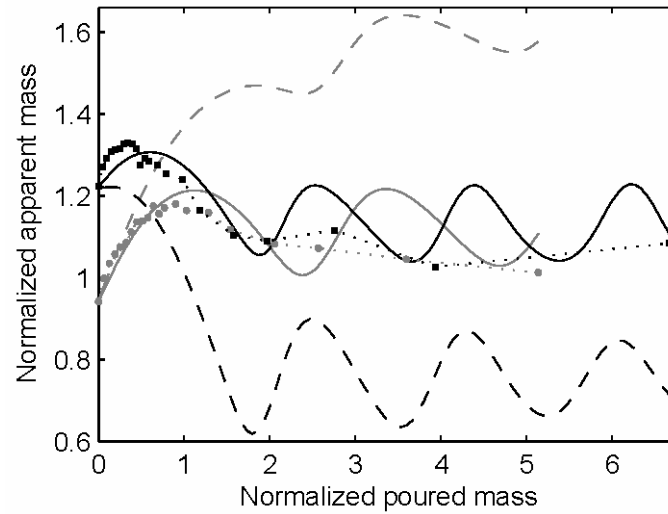
**Figure 3-2: Schematic illustrating the aspect ratio of a computational grid cell. For a given radial step  $\Delta r$ , the vertical step  $\Delta z$  is set by the largest of the two slopes  $c_{\pm}$  of the characteristics, which is  $c_+$  in this example.**

**Figure 3-3: Model fits for free-surface datasets. Apparent mass versus poured mass. Each data point, represented by a triangle, corresponds to the ensemble mean of all the repeated runs for a fixed piling height. The dash-dot, dashed and solid curves show model fits to the data (see section 3-4.3 for a description of the regression method used to estimate the model parameters), respectively with the Janssen, modified Janssen and OSL models. The oblique gray line represents the lithostatic behavior. The vertical line corresponds to the standard deviation of one point representative of the asymptotic regime. A. Dry dataset. B. Immersed dataset. C. Settled dataset**

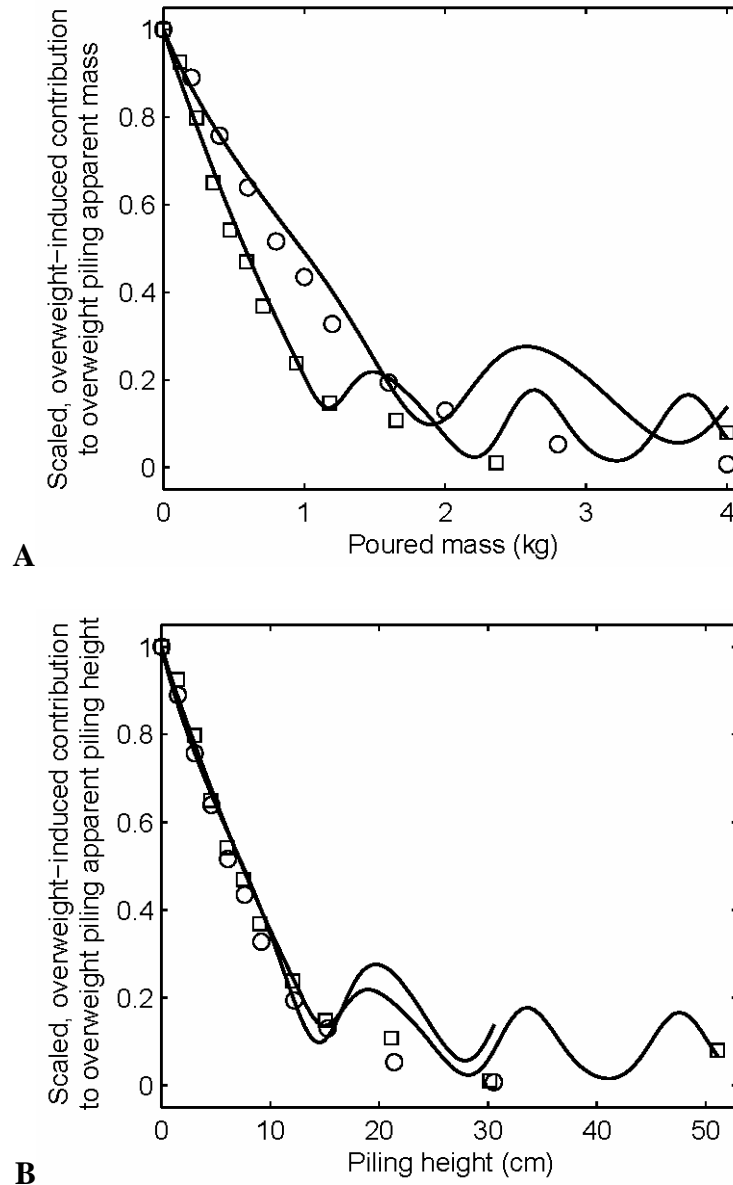




**Figure 3-4: Model fits for overweight datasets. Apparent mass versus poured mass, both normalized by the asymptotic mass. Triangles connected by a dotted line represent data, each point corresponding to the ensemble mean of all the repeated runs for a fixed piling height. The dash-dot and solid curves show model fits to the data (see section 3-4.3 for a description of the regression method used to estimate the model parameters), respectively with the Janssen and OSL models. The dashed curve shows the OSL model prediction using the parameters estimated from a fit to the free-surface data. The oblique gray line represents the lithostatic behavior. A. Dry dataset. B. Immersed dataset**



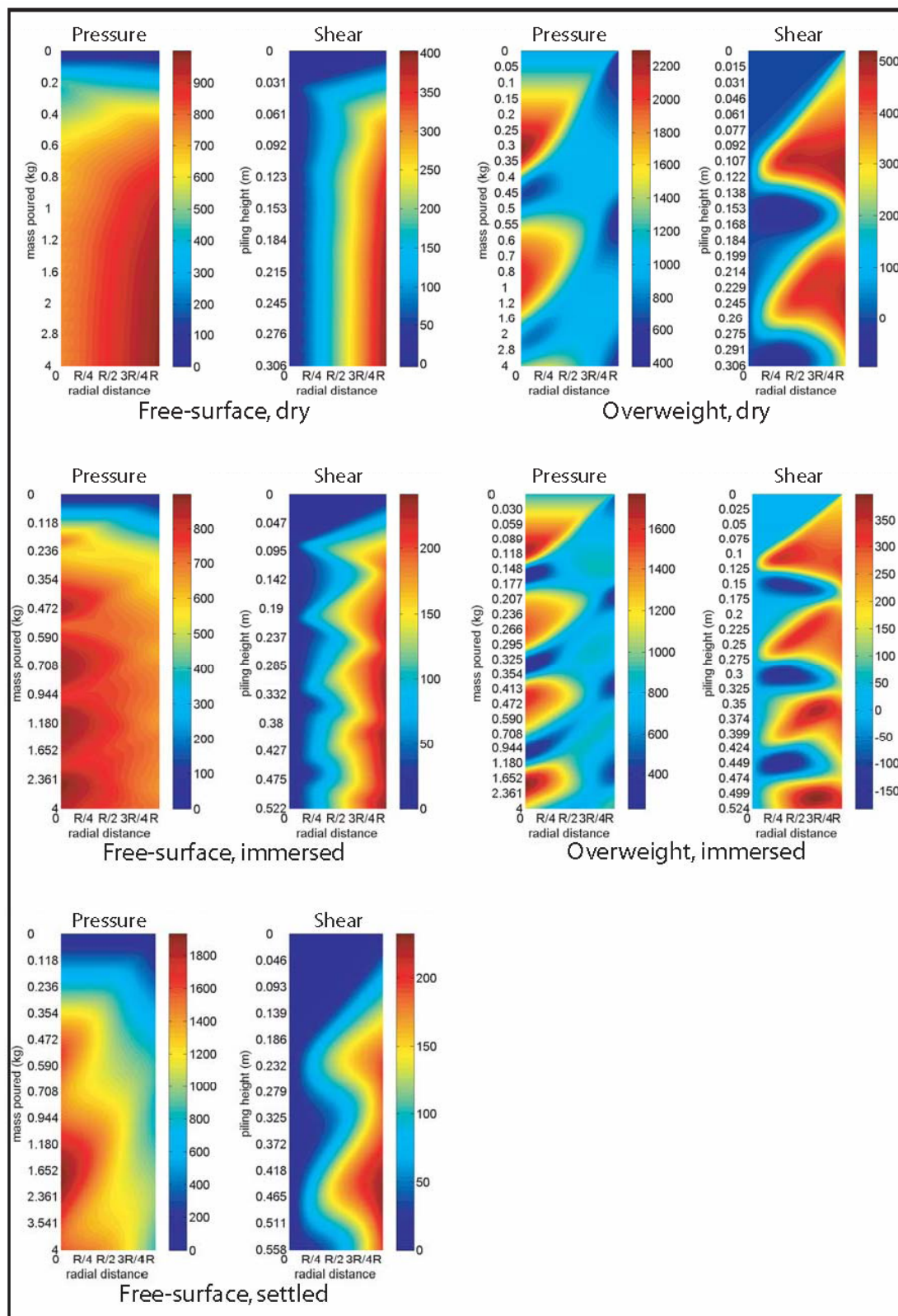
**Figure 3-5: OSL model predictions. Apparent mass versus poured mass, both normalized by the asymptotic mass. Filled symbols connected by dotted lines are data points. Gray and black are used respectively for the dry and immersed cases. Solid curves show the OSL model fits to the data. Dashed curves show the OSL model prediction using the parameters estimated from a fit to the other overweight dataset (i.e., for example, the gray, dashed curve is the model prediction for the dry, overweight case when using the OSL parameters estimated from a fit to the immersed, overweight dataset)**



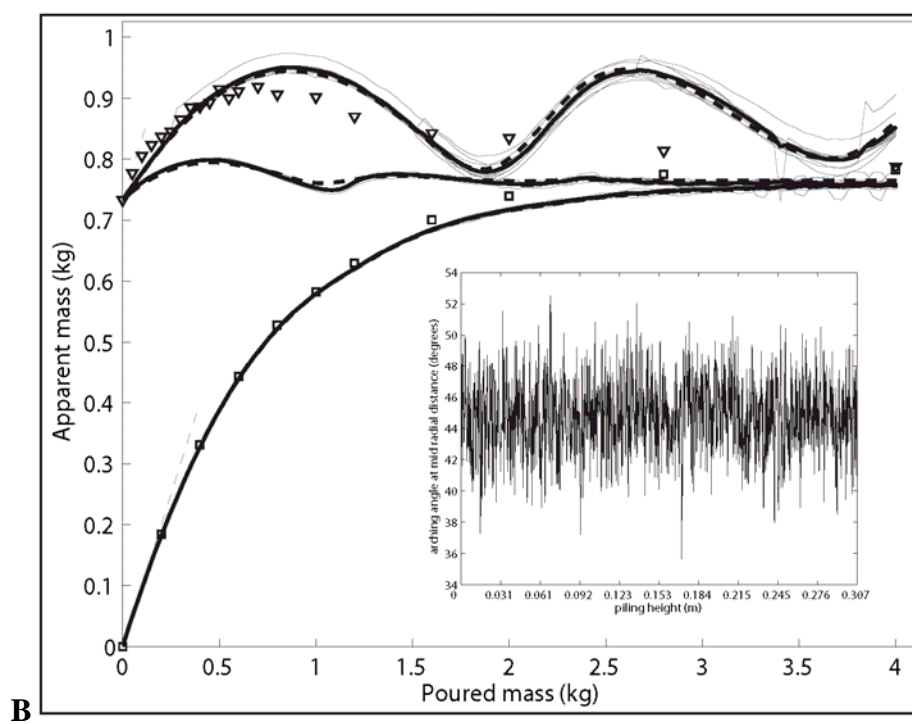
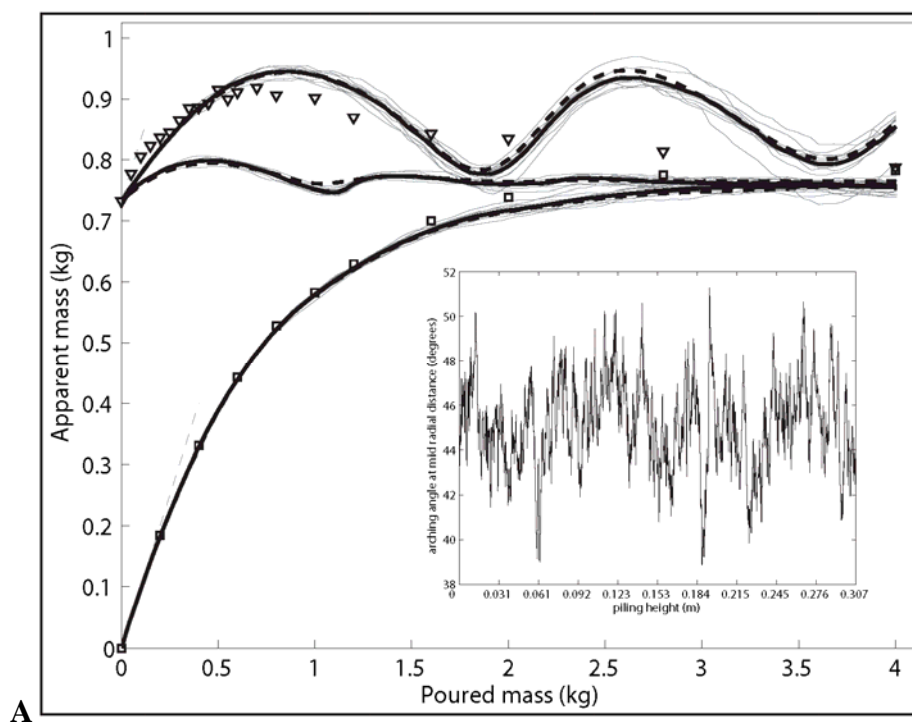
**Figure 3-6: Overweight datasets collapse. Contribution to the apparent mass of overweight pilings induced by the overweight, normalized by the overweight mass  $\left(\frac{(M_{app}^{overweight} - M_{app}^{free-surface})}{M_{over}}\right)$ . Symbols are obtained from free-surface and overweight data points. Circles and squares respectively correspond to the dry and immersed cases. Curves are derived from OSL model fits to the data (shown in Figs. 3-3 and 3-4). A. Plotted against poured mass. B. Plotted against piling height**

**Figure 3-7: Simulated stresses within pilings. Vertical cross-section of the color-coded stress intensity (in Pa) extending from the piling central axis to the wall. Pressure and shear stress obtained from the same simulation are shown respectively in the left and right panels in each subplot, with vertical axis labeled respectively as poured mass and piling height. Simulations correspond to the parameters estimated from model fits to each of the 5 datasets, as labeled on figure**





**Figure 3-8: Model predictions with fluctuations of the arching angle. Apparent mass versus poured mass for the dry datasets. Squares and triangles correspond respectively to the free-surface and overweight data points. There are three series of curves, each consisting of 10 thin, gray and 2 thick, black curves. Gray curves show OSL model predictions with random fluctuations of the arching angle. Black curves show respectively the ensemble average of the ten realizations (solid) and the model prediction without noise (dashed). The series of curves correspond to the free-surface (lower) and overweight (upper) cases, and to the scenario of model predictions for overweight pilings using free-surface model parameters (middle). Random noise is added to the mean arching angle derived using the OSL parameters determined from model fit to data (see section 3-5.3.2). The gray, dashed lines represent the lithostatic behavior. A. Long correlation range ( $\alpha = 0.9$ ) and small magnitude ( $\tau_\sigma = 0.02\tau_o$ ) of the arching angle fluctuations. B. Short correlation range ( $\alpha = 0.3$ ) and large magnitude ( $\tau_\sigma = 0.05\tau_o$ ) of the arching angle fluctuations. Insets for Figures 8A and 8B. Vertical profile of the arching angle  $\tau$ , taken half a radius away from the piling center and plotted in degrees, versus piling height**



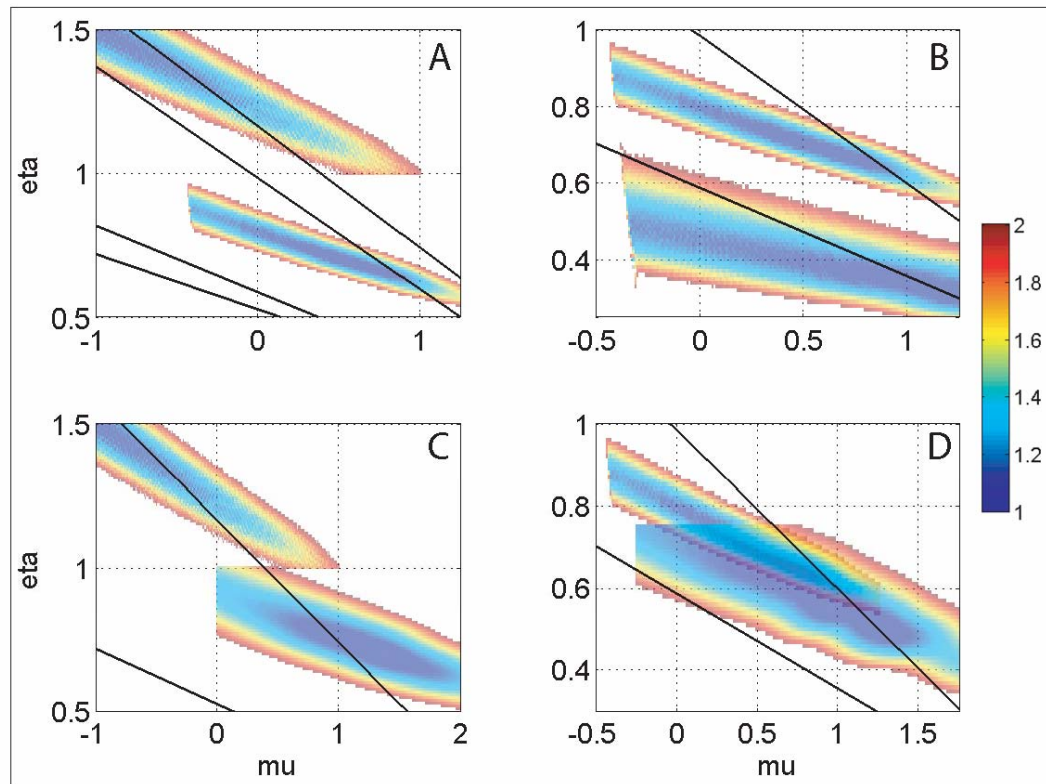


**Figure 3-9: Pair-wise comparisons of the OSL parameters estimated by fitting the data. Color-coded quadratic error arrays plotted in the  $(\eta, \mu)$  parameter space. Each array is scaled by its minimum value and masked at twice its minimum value, so the unique color scale is relative to each error array, even within the same subplot. Black solid lines represent the bounds of the stability cone determined from the Mohr-Coulomb criteria and evaluated using the appropriate (i.e. dry or immersed) repose and wall friction angles. The compared arrays correspond to the following datasets: A. Free-surface, dry (upper) and free-surface, immersed (lower). The widest stability cone represents dry conditions. B. Free-surface, immersed (upper) and free-surface, settled (lower). C. Free-surface, dry (upper) and overweight, dry (lower). D. Free-surface, immersed (upper) and overweight, immersed (lower)**

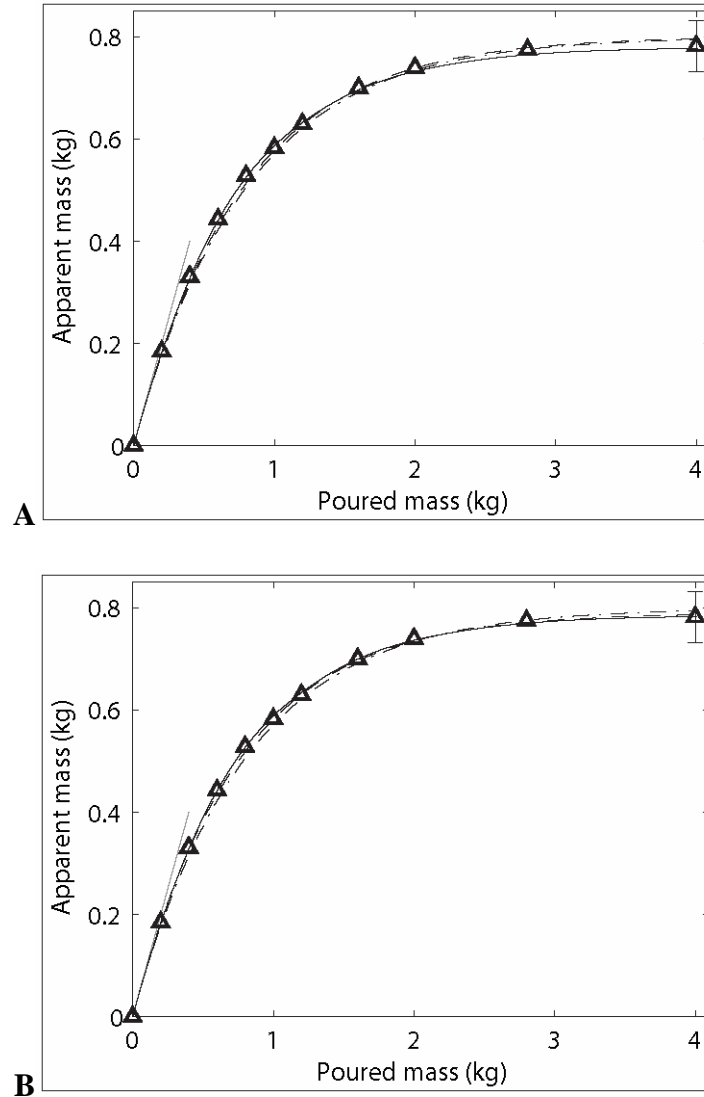


**Figure 3-10: Different regression methods for OSL model fit to the free-surface, dry dataset. Apparent mass versus poured mass. Triangles are data points. The dash-dot, dashed and solid curves show model fits to the data, respectively with the Janssen, modified Janssen and OSL models. The oblique gray line represents the lithostatic behavior. The vertical line corresponds to the standard deviation of one point representative of the asymptotic regime. A. Regression method using a normalized Euclidian distance weighed with inverse data points density (see Appendix A.1). B. Regression method using a least mean square fit.**

**Figure 3-11: Suppression of numerical instabilities. Apparent mass versus poured mass for dry datasets. Squares and circles correspond respectively to the free-surface and overweight data points. The 2 gray curves show respectively OSL model fit to the free-surface data and OSL model prediction for overweight pilings using free-surface model parameters, both realized with a discretization of the piling consisting of 200 bins in the radial direction. The black curves are OSL model predictions obtained for the same OSL parameters as the gray curves but modifying the numerical simulations. A. By smoothing the horizontal stress profiles (see Appendix A.2) every 100 (solid), 10 (dashed) or at each (dash-dot) vertical bin(s). B. By coarsening the radial grid size to 100 (solid), 50 (dashed) and 25 (dash-dot) bins**

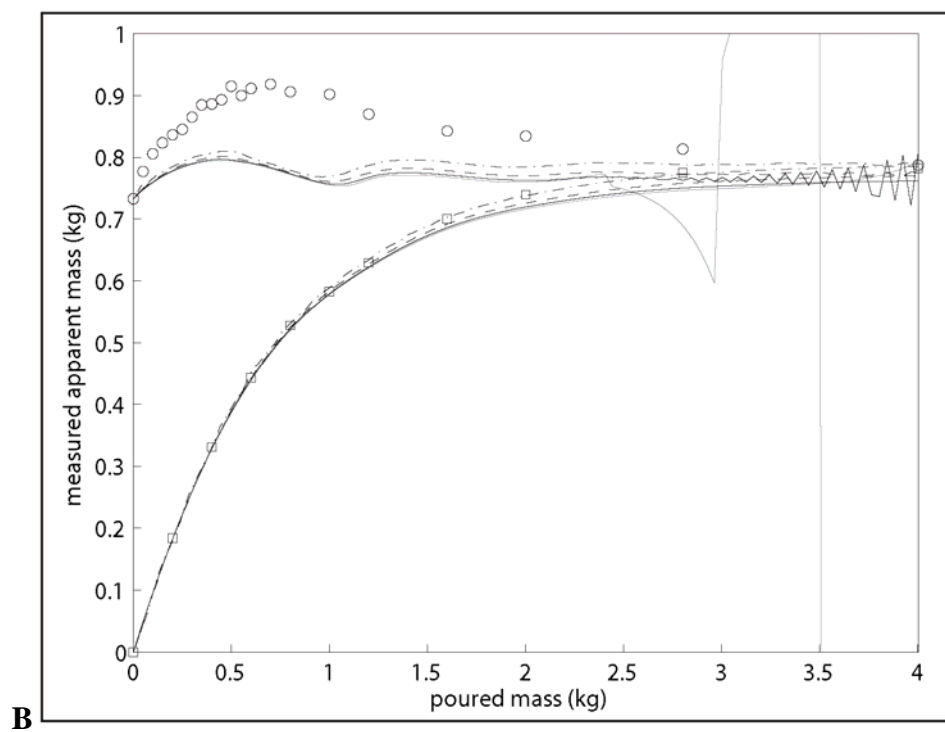
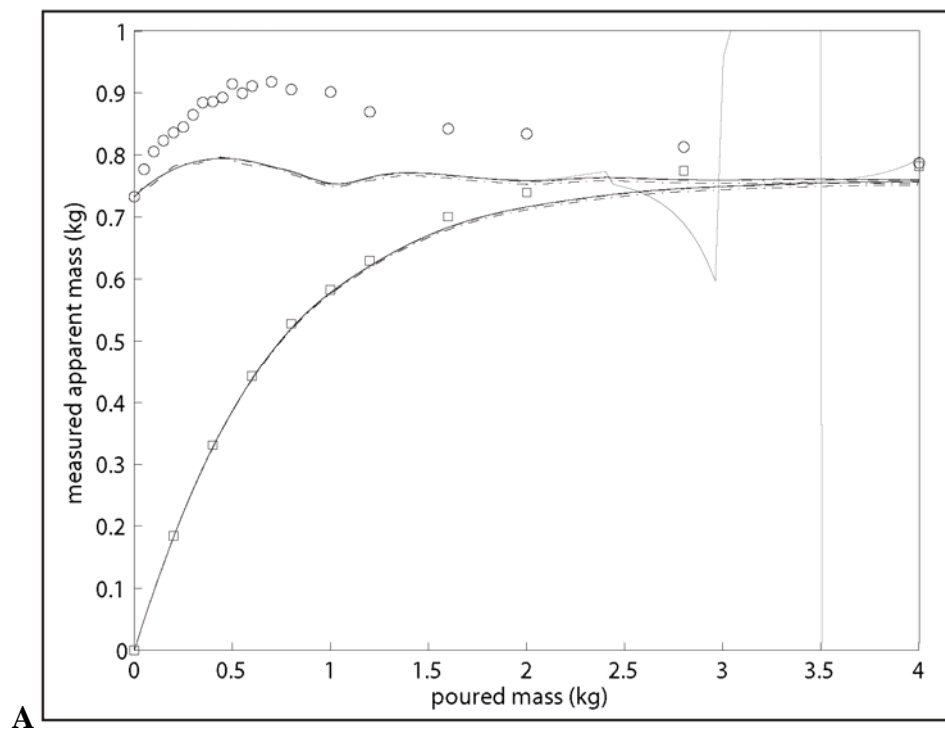
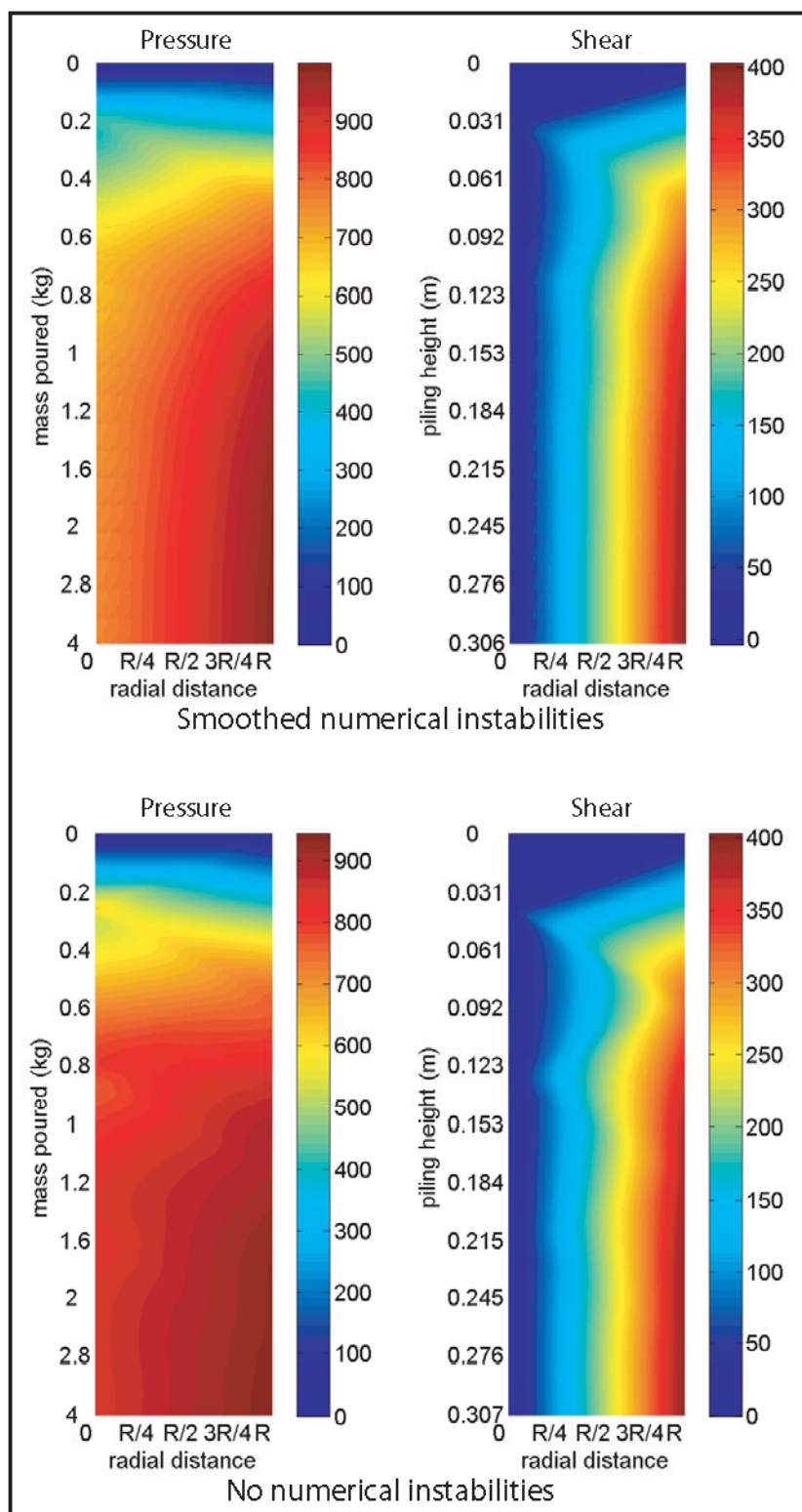


**Figure 3-12: Simulated stresses within pilings with numerical instabilities (see Fig. 3-7 for details on cross-sectional views of stress fields). Simulations correspond to the parameters estimated from the model fit to the free-surface, dry dataset ( $\eta = 1.47$ ,  $\mu = -0.9$ ) with smoothing of horizontal stress profiles every 100 vertical (upper subplot) bins and a sub-optimal pair of OSL parameters ( $\eta = 1.30$ ,  $\mu = -0.3$ ) close to the estimated parameters from the fit to the free-surface, dry dataset but that do not cause numerical instabilities (lower subplot)**





## References

- Bagster D, Nedderman R (1985) A note on the application of the Coulomb method to the calculation of wall stresses in cylindrical silos. *Powder technology* 42:193-197
- Bouchaud JP, Cates ME, Claudin P (1995) Stress-Distribution in Granular Media and Nonlinear-Wave Equation. *Journal De Physique I* 5:639-656
- Brauer K, Pfitzner M, Krimer DO, Mayer M, Jiang YM, Liu M (2006) Granular elasticity: Stress distributions in silos and under point loads. *Physical Review E* 74
- Brown R, Richards J (1970) principles of powder mechanics. Pergamon Press, Oxford
- Cates ME, Wittmer JP, Bouchaud JP, Claudin P (1998a) Development of stresses in cohesionless poured sand:2535-2560
- Cates ME, Wittmer JP, Bouchaud JP, Claudin P (1998b) Jamming, force chains, and fragile matter. *Physical Review Letters* 81:1841-1844
- Claudin P (1999) Sandpile physics - A phenomenological description of stress propagation in granular materials. EDP sciences
- Claudin P, Bouchaud JP (1997) Static avalanches and giant stress fluctuations in silos. *Physical Review Letters* 78:231-234
- Dauchot O, Marty G, Biroli G (2005) Dynamical heterogeneity close to the jamming transition in a sheared granular material. *Physical Review Letters* 95
- de Gennes PG (1999) Granular matter: a tentative view. *Reviews of Modern Physics* 71:S374-S382
- Didwania AK, Cantelaube F, Goddard JD (2000) Static multiplicity of stress states in granular heaps. *Proceedings of the Royal Society a-Mathematical Physical and Engineering Sciences* 456:2569-2588
- Duran J (2000) Sand, powders, and grains: An introduction to the physics of granular materials. Springer-Verlag, New York
- Evesque P, de Gennes PG (1998) On the statics of silos. *Comptes Rendus De L Academie Des Sciences Serie Ii Fascicule B-Mecanique Physique Astronomie* 326:761-766
- Fortin J, Millet O, De Saxcé G (2005) Numerical simulation of granular materials by an improved discrete element method. *Int J Numer Meth Engng* 62:639-663

Geng JF, Behringer RR (2005) Slow drag in two-dimensional granular media. *Physical Review E* 71

Horne R, Nedderman R (1976) Analysis of the stress distribution in two-dimensional bins by the method of characteristics. *Powder Technology* 14:93-102

Jaeger HM, Nagel SR, Behringer RP (1996) Granular solids, liquids, and gases. *Reviews of Modern Physics* 68:1259-1273

Kolymbas D (2000) *Introduction to hypoplasticity*. AA Balkema

Kuwano R, Jardine RJ (2002) On measuring creep behaviour in granular materials through triaxial testing. *Canadian Geotechnical Journal* 39:1061-1074

Landry JW, Grest GS, Silbert LE, Plimpton SJ (2003) Confined granular packings: Structure, stress, and forces. *Physical Review E* 67

Le Dantec N, Deane G (2009) Measurements of the Apparent Mass at the Base of Water-Saturated Granular Pilings. In preparation

Liu J, Shi QF, Liang XW, Yang L, Sun G (2009) Size dependence of effective mass in granular columns. *Physica a-Statistical Mechanics and Its Applications* 388:379-384

Lubarda V (2002) *Elastoplasticity theory*. CRC Press, Boca Raton

Luding S (2005) Granular media - Information propagation. *Nature* 435:159-160

Majmudar T, Behringer R (2005) Contact force measurements and stress-induced anisotropy in granular materials. *Nature* 435:1079-1082

Mehta A (2007) *Granular physics*. Cambridge University Press

Morrison D (1967) *Multivariate statistical methods*. McGraw-Hill New York

Nedderman R (1992) *Statics and kinematics of granular materials*. Cambridge University Press

Ovarlez G, Clement E (2005) Elastic medium confined in a column versus the Janssen experiment. *European Physical Journal E* 16:421-438

Ovarlez G, Fond C, Clement E (2003) Overshoot effect in the Janssen granular column: A crucial test for granular mechanics. *Physical Review E* 67

Peters J, Muthuswamy M, Wibowo J, Tordesillas A (2005) Characterization of force chains in granular material. *PHYSICAL REVIEW E Phys Rev E* 72:041307

Rao K, Nott P, Sundaresan S (2008) *An Introduction to Granular Flow*. Cambridge University Press

Reynolds O (1885) On the dilatancy of media composed of rigid particles in contact. *Philosophical Magazine* 20:469-481

Rotter J, Holst J, Ooi J, Sanad A (1998) Silo pressure predictions using discrete-element and finite-element analyses. *Philosophical Transactions: Mathematical, Physical and Engineering Sciences*:2685-2712

Sanfratello L, Fukushima E, Behringer R (2009) Using MR elastography to image the 3D force chain structure of a quasi-static granular assembly. *Granular Matter* 11:1-6

Savage S (1997) Problems in the statics and dynamics of granular materials. In: Behringer R, Jenkins J (eds) *Powders and Grains*. Balkema, Rotterdam, pp185--194

Savage S (1998) Modeling and granular material boundary value problems. In: Herrmann H, Hovi J, Luding S (eds) *Physics of dry granular media*. Kluwer Academic Publishers, Dordrecht, pp25-96

Socular J, Schaeffer D, Claudin P (2002) Directed force chain networks and stress response in static granular materials. *The European Physical Journal E* 7:353-370

Sperl M (2006) Experiments on corn pressure in silo cells - translation and comment of Janssen's paper from 1895. *Granular Matter* 8:59-65

Tejchman J (1998) Numerical simulation of filling in silos with a polar hypoplastic constitutive model. *Powder Technol* 96:227-239

Tejchman J, Wu W (2008) FE-calculations of stress distribution under prismatic and conical sandpiles within hypoplasticity. *Granular Matter* 10:399-405

Terzaghi K, Peck R, Mesri G (1996) *Soil mechanics in engineering practice*. Wiley and Sons, New York

Tordesillas A, Shi J, Muhlhaus H (2009) Noncoaxiality and force chain evolution. *International Journal of Engineering Science*

Vanel L, Clement E (1999) Pressure screening and fluctuations at the bottom of a granular column. *European Physical Journal B* 11:525-533

Vanel L, Clement E, Lanuza J, Duran J (1998) Pressure fluctuations in a granular column *Physics of Dry Granular Media*. Kluwer Academic Publishers, pp249-254

Vanel L, Claudin P, Bouchaud JP, Cates ME, Clement E, Wittmer JP (2000) Stresses in silos: Comparison between theoretical models and new experiments. *Physical Review Letters* 84:1439-1442

Wittmer JP, Cates ME, Claudin P (1997) Stress propagation and arching in static sandpiles. *Journal De Physique I* 7:39-80

Wittmer JP, Claudin P, Cates ME, Bouchaud JP (1996) An explanation for the central stress minimum in sand piles. *Nature* 382:336-338

Chapter 3, in part is currently being prepared for submission for publication as: Le Dantec, Nicolas; Deane, Grant B. “Modeling stress in saturated granular pilings using the OSL approach to quantify arching”. The dissertation author was the primary investigator and author of this paper.

**CHAPTER 4: Tectonic Controls on Nearshore Sediment  
Accumulation and Submarine Canyon  
Morphology Offshore La Jolla, Southern  
California**

## ABSTRACT

CHIRP seismic and high-resolution swath bathymetry data recently acquired offshore La Jolla, California provide an unprecedented three-dimensional depiction of the La Jolla and Scripps submarine canyons. Uplift and subsidence associated with constraining and releasing bends along the right lateral Rose Canyon fault system impart a shore-parallel pattern of deformation that controls nearshore sediment accumulation and canyon morphology. Because of the orthogonal geometry, it is possible to assess the impact of local tectonic deformation versus eustatic sea level fluctuations on nearshore processes. Based on stratal geometry and acoustic character, I identify three sedimentary sequences overlying a prominent angular unconformity inferred to be the transgressive surface: an acoustically laminated estuarine unit, an infilling unit formed during the so-called “healing-phase,” and an upper Holocene transparent unit. Beneath the transgressive surface, steeply dipping beds are observed with several dip reversals that record the faulting and folding along the Rose Canyon fault system. In addition to the dip reversals, relief along the transgressive surface, being shallow in the north with its depth systematically increasing toward the south near the canyon heads, records the tectonic wrenching in the region. Furthermore, the small-scale roughness observed on the transgressive surface decreases in water depths  $\leq 25$  m, which may reflect the diminished rate of sea level rise and thus longer exposure to wave-base erosion at these water depths. Isopach and structure contour maps for the region reveal the close interplay between spatial distribution and thickness of these units and tectonic deformation. For example, the estuarine units are predominantly deposited along the edges of the canyons that may

have been inlets along barrier beaches during the sea level rise. The distribution of the infilling unit is controlled by a structural low seaward of an erosional notch and most likely represents a transgressive lag. The thickness and distribution of the Holocene transparent unit is controlled by the long wavelength relief on the transgressive surface and by hydrodynamics. Finally, I refine the relationship between the development of the Scripps and La Jolla canyons and tectonic deformation in the region. The Scripps Canyon is located at the crest of an antiform, where the rocks are faulted and more susceptible to erosion. The asymmetric morphology of the La Jolla canyon is linked to folding and back-tilting along the Rose Canyon fault. Such a detailed understanding of the geologic framework is critical when investigating nearshore sediment accumulation and morphology along a tectonically active margin.



## INTRODUCTION

The importance of underlying structures in controlling the formation and evolution of morphological features and sediment accumulation has long been appreciated (Emery 1958; Shepard and Emery 1941). Several studies illustrate the influence of tectonic deformation on geomorphology, such as continental slope morphology on tectonically active margins (Pratson and Haxby 1996) or drainage patterns and formation of fluvial terraces (Peters and van Balen 2007). Tectonics also plays a role in secondary morphological characteristics, for instance the orientation of fissure-ridge travertines (Altunel and Hancock 1993) or pockmark formation and distribution in shallow water estuaries (Rogers *et al.* 2006). Long-term retreat of modern beaches (Honeycutt and Krantz 2003) and the preservation and evolution of barrier-island system (Belknap and Kraft 1985; Harris *et al.* 2005; Schwab *et al.* 2000; Thieler *et al.* 2001) as well as short-term dynamic processes such as the position and stability of sandbars in the nearshore (McNinch 2004) are also affected by underlying structures. Here I present new geophysical and geological data that show the importance of tectonic deformation in controlling canyon location and morphology as well as on the distribution of modern sediment offshore La Jolla, California.

The sedimentary and morphological evolution of continental margins depends on many factors, three of which are eustasy, sediment supply, and tectonic deformation (Christie-Blick and Driscoll 1995; Posamentier and Allen 1999). On active margins tectonics plays a large role in controlling the nearshore physiography. Discerning how these parameters affect sediment accumulation is often difficult even when the factors are

operating at different spatial scales (Sommerfield and Lee 2003, 2004). In our study site, transpression and transtension associated with the dextral Rose Canyon fault create deformation that is shore parallel and thus can be isolated from the regional tectonic uplift and eustatic fluctuations that impart base level changes with a cross-shore orientation. Our work examines how local deformation affects the relief on the transgressive surface, which in turn, plays an important role in controlling regions of sediment bypass and accumulation. I also focus on the role of faulting and folding in submarine canyon development. Research on active processes in submarine canyons indicates that their formation is usually a combination of several factors. In many instances, both erosional mechanisms and tectonic processes are proposed to explain submarine canyon formation, through preferential erosion of a weaker substrate associated with tectonic deformation (e.g., Cirac *et al.* 2001). However, most research has focused on erosional mechanisms including gravitational slides, undercutting, retrogressive failures, axial incision, breaching, sapping, downslope-eroding sediment flows, overpressure build-up, and earthquake-induced failures (Baztan *et al.* 2005; Chamberlain 1964; Dill 1969; Driscoll and Uchupi 1997; Marshall 1978; Mastbergen and van den Berg 2003; Pratson *et al.* 1994; Wolinsky and Pratson 2007).

The La Jolla Canyon and the surrounding continental margin (Fig. 4-1) is one of the most studied sites of its nature worldwide (Brueggeman 2008). The geological setting consists of Cretaceous mudstones, sandstones, and conglomerates overlain by Eocene and younger shales, siltstones, sandstones, and conglomerates with several unconformities (Kennedy 1975; Lomar *et al.* 1979). The Rose Canyon Fault Zone (RCFZ; Moore 1972; Treiman 1993), a right-lateral, strike-slip fault system in the California Borderlands, is a

major tectonic feature in the area. Wave-cut notches are observed along the shelf at various water depths and appear to record still-stands during the last sea level transgression (Byrd *et al.* 1975; Darigo and Osbourne 1986; Emery 1958; Henry 1976; Waggoner 1979). La Jolla Bay is located at the southern end of the Oceanside littoral cell with dominant sediment transport to the south (Inman and Chamberlain 1960). Multiple studies have examined the Holocene sediment distribution (Henry 1976; Waggoner 1979), origin, age, transport mechanisms, and transport pathways (Everts and Dill 1988; Haas 2005; Young and Ashford 2006), particularly in relation to the dynamics of littoral cell (Inman and Masters 1991a, 1991b). Research on the Quaternary sediment cover on the shelf off San Diego County has also focused on coastal management, protection of marine habitats and resource inventory for mining purposes (Darigo and Osbourne 1986). The sediment thickness exhibits a wedge-shaped cross-shore profile with a mid-shelf depocenter (Byrd *et al.* 1975; Henry 1976; Hogarth *et al.* 2007). Sediment input mostly consists of sand and silt derived from river discharge to the north and cliff erosion (Haas 2005; Stow and Chang 1987; Young and Ashford 2006). The relative importance of the past and present contributions of these sources is not well constrained. This is partly due to the episodic nature of these inputs, which depend on climate forcing and watershed alteration (Inman and Jenkins 1999; Warrick and Rubin. 2007). Knowledge of the overall patterns observed in modern sediment transport and distribution over the inner shelf provides a regional context for our study.

Multiple aspects of the La Jolla Canyon, including its physiography, geology, physical oceanography, and biology have been investigated. The close proximity to Scripps Institution of Oceanography allowed a diverse research community easy access

to the submarine canyon. This canyon was the site of the earliest scuba diving and submersible explorations (Shepard 1972), which increased our understanding of these and other underwater valleys (Shepard 1981). This work has yielded fundamental scientific advances in the understanding of canyon morphology and architecture (Buffington 1964; Shepard and Dill 1966), the role of canyons for transport between deep oceans and shallow waters, submarine fan stratigraphy (Covault *et al.* 2007), turbidity flows and bottom canyon currents (Inman *et al.* 1976), erosive processes accompanying the formation and persistence of canyons (Shepard 1981), sedimentation and erosion at canyon heads (Chamberlain 1964; Dill 1964), and interactions between canyons and biota (Vetter 1994). The upper course of the La Jolla submarine canyon is predominantly controlled by the RCFZ (Buffington 1964; Moore 1972). The canyon has two branches, the Scripps Branch and the La Jolla Branch. Because the entire canyon has been termed the La Jolla Canyon, for clarity purposes, I will refer to the entire canyon as the La Jolla Canyon System. The La Jolla and the Scripps canyon heads extend into shallow water (~8-10 m) and as such they modify nearshore circulation, surface wave patterns, and littoral sediment transport (Shepard and Inman 1950; Thomson *et al.* 2005). In addition, currents measured along the floor of the canyons show a strong tidal signal (Inman *et al.* 1976; Shepard *et al.* 1977). The La Jolla and Scripps canyons are large morphologic features and are dynamic pathways for sediment transport to the deep sea. To date much of the research focus has been on canyon morphology and active sediment transport (Chamberlain 1964; Dill 1964; Marshall 1978). Nevertheless, tectonic deformation also plays an important role in controlling canyon morphology and the long-term sediment accumulation in the region (e.g., Hogarth *et al.* 2007).

In this study, high-resolution seismic and bathymetric data acquired offshore La Jolla between the surf zone and the shelf break (Fig. 4-2A) allow the examination of the tectonic control on the formation of and evolution of the La Jolla and Scripps submarine canyons as well as the impact of tectonics on Holocene sedimentation on the inner shelf offshore La Jolla.

## **METHODOLOGY**

### **Data acquisition**

In 2002 and 2003, high-resolution swath bathymetry and seismic data were acquired offshore La Jolla, Southern California during three successive cruises. The surveys covered the narrow shelf from Point La Jolla north to Penasquitos Lagoon. The survey tracks mostly consist of strike lines with about 150 m line spacing, augmented with four dip lines (Fig. 4-2A). I used a SwathPlus-L (formerly Submetrix) interferometric swath bathymetric sonar by Sea Ltd (<http://www.sea.co.uk>) and the Scripps subbottom reflection sonar system (SUBSCAN), which is a modified EdgeTech (<http://www.edgetech.com/>) system and includes a dual transducer X-Star sonar with an ADSL link from the fish to the topside computers.

The SwathPlus-L sonar, which operates at 117 kHz and has a nominal cross-track resolution up to 15 cm, yielded better than 50 cm horizontal resolution even over the steep topographic features of the survey area, up to at least 75 m depth. The SUBSCAN sonar uses a 50 ms swept pulse across a 1.5 – 5 kHz range with 24° beam width, yielding sub-meter vertical resolution to sub-seafloor depths of approximately 50 m. During the

nearshore surveys in 2002 onboard the RV Saikhon, the SwathPlus-L system was attached to a side-mount while the SUBSCAN system was ‘floated’ on a surface tow frame. The deployment configuration was complemented with an on-board motion sensor and a global positioning system (GPS) receiver to measure attitude and position. A second GPS receiver was attached to the surface tow frame to minimize navigation error for the CHIRP data. During the offshore survey in 2003 onboard the R/V Sproul, only seismic data were collected and the SUBSCAN system was towed at approximately 10 m above the seafloor. Winch cable payout records allowed for the correction of layback error. Data were acquired at a ship speed of approximately 4–5 knots for both surveys.

In December 2007 and January 2008, a survey was performed with a Light Detection and Ranging (LIDAR; Hsieh *et al.* 2007) system to map the sea cliffs between La Jolla Cove and the southern portion of La Jolla Shores beach. Faulting and folding are observed along the sea cliffs in this region as a result of deformation along RCFZ (Figs. 4-1 and 4-2). LIDAR is an optical remote sensing technology yielding a high-resolution spatial record of a target surface in the form of a point cloud representation. I used the I-site 4400-LR (<http://www.isite3d.com/>) terrestrial LIDAR system, a diode laser operating at 905 nm wavelength, with 360° of field of view and 80° of angular range in the vertical. By scanning the cliffs orthogonally at approximately 100 m spacing and with a target distance of 100 m, we obtain a point density of 5-10 cm with 5 cm resolution in range. In addition to range and intensity, a panoramic high-resolution digital camera was used to simultaneously map color information to each scan point.

Finally, a short push core was acquired during a scuba dive on Dec 14<sup>th</sup> 2007 from a layer that outcrops along a ridge at 23 meters water depth near the head of the La

Jolla Canyon (Figs. 4-2A and 4-3). The site was selected to ground-truth one of the stratigraphic packages identified in the seismic data, which has a laminated acoustic signature and outcrops in this area. A 2-inch diameter clear plastic tube with a tapered extremity was pushed into the seafloor and capped before pulling it out to create suction and improve sediment recovery. The lower end of the core was capped underwater so that the sample was well preserved. The core was split, described and photographed.

### **Data Processing**

Processing the raw bathymetry data involved numerous steps. First, several corrections were applied using the proprietary SwathPlus software developed by SEA, Ltd. The soundings were corrected incorporating the acquisition parameters - attitude and position - as well as water level fluctuations due to tidal elevations using observations from the NOAA tide gauge installed at the Scripps Pier in La Jolla. The vertical datum was shifted from MLLW to NAVD 88. The sound speed was adjusted using profiles measured during the survey in order to account for the variability between nearshore, shelf and deeper waters within the submarine canyons. Uncertainties in the exact positions of the CTD casts were corrected by using the measured profiles to match cast depth with water depth. Other artifacts, including errors due to low-frequency vessel motion poorly captured by the motion sensor, were removed by filtering each sounding using SwathPlus software options. Then, remaining outliers were discarded and the data volume was gridded at 50 cm resolution with a continuous curvature spline in tension. Finally, the data were smoothed using a linear convolution filter of 11.5 meters averaging window size in both horizontal directions. Because the bathymetry is rather devoid of

bedforms in the 2 – 10 m wavelength range and I am interested in the larger scale morphology, these filters, designed to remove artifacts from the data, did not alias features of interest.

After converting the seismic data from the original X-Star format into standard SEG-Y, the seismic data were heave-corrected, processed, and plotted using SIOSEIS (Henkart 2003) and SeismicUnix (Cohen and Stockwell 2002) seismic processing software packages. In addition, depths to various acoustic reflectors identified in each profile were digitized. The corresponding horizons were then gridded at 10 meter resolution and used to generate isopach maps of the stratigraphic packages. In order to convert travel time to sediment thickness, a velocity of 1720 m/s was used for non-silty sediments and a velocity of 1520 m/s was used for water and mud-dominated sediments (Jackson *et al.* 1996; Buckingham and Richardson 2002; Williams *et al.* 2002). I used the Interactive Visualization Systems (IVS, Fledermaus, <http://www.ivs3d.com>) software to merge all graphic elements into three-dimensional perspective views.

The LIDAR point clouds were merged from multiple scans using differential global positioning satellites (DGPS) coordinates in combination with common features that can be identified within the data sets. Using the I-site Studio software as well as an improved merging software (Olsen, M.J., Personal software 2008), the error due to alignment of overlapping areas of the scans is reduced to 10 cm. Additionally, undesirable returns such as tall vegetation were removed.

## RESULTS



## **Bathymetry**

Our survey provides very detailed bathymetry of the shallow section of the prominent La Jolla submarine canyon, inboard of the confluence of the two branches (Fig. 4-2B). Our dataset extends north of the submarine canyon system where the relief diminishes. The offshore pop-up structure characterized by a marked seaward deflection of the isobaths (Fig. 4-1; Hogarth *et al.* 2007) is north of our high-resolution bathymetry dataset (Fig. 4-2). The prominent northward shoaling of the transgressive surface (Hogarth *et al.* 2007) is not manifested in the inner shelf bathymetry as the isobaths parallel the coastline in this area. Note that, out of the three heads of the Scripps Canyon, only the largest one, North Branch, is well imaged (Figs. 4-2B and 4-3). The Sumner and South branches of the Scripps Canyon (Rindell 1991) were not well sampled as a result of the orientation of the survey and the lack of soundings over the narrow branches. I will first present the results for the canyon morphology and then I will discuss the stratigraphic packages observed along the margin from oldest to youngest based on the first comprehensive maps of their aerial distribution offshore La Jolla.

### *Canyon Morphology*

The two canyons, as revealed by our new high-resolution bathymetry, exhibit very different morphologies (Fig. 4-2B). The La Jolla Canyon is much wider than the Scripps Canyon, especially near its head (Fig. 4-3). At 75 m, the Scripps Canyon is ~150 m wide and narrows to ~30 m wide near its head. In contrast, the width of the La Jolla Canyon oscillates between 200 m and 250 m along its length, being widest at its head. In addition, the Scripps Canyon is very linear, whereas the La Jolla Canyon gently curves to

the north with a  $30^\circ$  change in its azimuth from the canyon head to where it intersects the Scripps canyon. The Scripps Canyon head is narrow and steep-walled. Conversely, the La Jolla Canyon head is characterized by a concave upwards morphology with moderate slopes. Furthermore, the La Jolla Canyon heads are more rounded as they widen upwards. The upper reaches of the La Jolla Canyon are dissected by a number of ridges and gullies (Fig. 4-3). Some of these ridges extend quite far into the canyon acting as promontories separating the bowl-shaped canyon heads. The La Jolla Canyon appears to be the dominant branch with the Scripps Canyon being subordinate and intersecting the La Jolla Canyon System at a high angle (Fig. 4-1).

#### Secondary incisions

The morphology of the secondary incisions along the walls of the two canyons is also dissimilar. For example, the La Jolla Canyon has just a few large and deep side channels incised into the consolidated basement rock. Near or within the head of the canyon, these channels are long and remarkably tortuous, with one in particular taking two well defined and opposite turns (“S”; Fig. 4-2B). The incision located closest to the intersection with the Scripps Canyon is wide and rounded, resembling the scalloping on the east wall of the La Jolla Canyon System north of the intersection (Fig. 4-1). One of these incisions on the east wall of the La Jolla Canyon System is suggested in our dataset by the shoreward inflexion of the 75 m isobaths causing an apparent depression in the bathymetry just north of the intersection of the branches (northernmost “I”; Fig. 4-2B). In contrast with the La Jolla Canyon, the secondary side canyons of the Scripps Canyon have smoother walls and are shallower, being mostly restricted to the upper

unconsolidated sediments. Despite their gentle slopes, some secondary canyons extend far away from the canyon axis (~ 500 m, Figs. 4-2 and 4-3; and up to 1 km, Fig. 4-6A). More secondary channels are observed along the Scripps Canyon than in the La Jolla Canyon, with a wide range in size and separation. As a consequence, the slope of the upper walls along the Scripps Canyon is highly variable (Fig. 4-3). Secondary channel orientation is in general not perpendicular to the main channel but is predominantly oblique to the axis of the Scripps Canyon. Farther north along the margin, a notch is observed in the bathymetry that defines the southeast corner of the pop-up structure and is where the Rose Canyon Fault takes a westerly jog (Fig. 4-1).

*Asymmetry between the north and south walls*

The canyon walls exhibit marked asymmetry (Figs. 4-2 and 4-3). For example, most of the ridges and secondary channels of the La Jolla Canyon occur on its north wall. Conversely, the south wall has little or no secondary incisions, especially in the shallow section near the canyon head. In the Scripps Canyon, the north and south walls exhibit differences in size, shape, and number of secondary incisions, which are larger, deeper and more frequent along the south side. The 20 meter isobath north of the Scripps Canyon is deflected towards the east exhibiting a north-east trend as it wraps around the shore-parallel North Branch at the head of the canyon. The resulting terrace along the north rim of the canyon is about 15 m deeper than other along-shore locations at the same cross-shore distance from the coastline ("T"; Fig. 4-2B). The contours on the south side of the canyon do not exhibit this deflection near the canyon. Consequently, in this nearshore section of the Scripps Canyon, the greatest relief is along the southern rim.

Despite these many differences in morphology, the canyons do share some morphologic features. One similarity is the northward orientation of their heads. As the canyons come close to the shoreline after crossing the entire shelf, their shallow extensions are preferentially developed towards the north. Another common trait is that, except for the head of the La Jolla Canyon, the slopes of the walls are very steep in both canyons.

### **Transgressive surface structure**

The transgressive surface is identified in seismic profiles by marked truncation of underlying bedding. The transgressive surface is generally quite flat and exhibits high acoustic reflectivity. As reported by Hogarth *et al.* (2007), a constraining bend in the Rose Canyon Fault in the north of the study area creates a structural high in the transgressive surface. Beyond this first order effect, our analysis brings to light several other features of the transgressive surface in this region.

The transgressive surface shows much variability in the along-shore and cross-shore directions. It is relatively high on either side and in the immediate proximity of the La Jolla and Scripps canyons (Fig. 4-4). To the south of the La Jolla Canyon, Cretaceous mudstones outcrop on the seafloor. Between the two canyons the transgressive surface is relatively flat, uniformly slopes to the northwest, and is overlain by up to 20 m of sediments. The high in the transgressive surface near the Scripps Canyon is more pronounced to the north of the canyon (Fig. 4-4). Farther to the north of the Scripps Canyon, a saddle along the transgressive surface is observed between the high coincident with the Scripps Canyon and the high associated with the pop-up structure described by

Hogarth *et al.* (2007). Within this low, strike profiles show a localized high offshore with an along- and cross-shore extent of  $\sim 1$  km and moderate vertical relief of a few meters (Figs. 4-4 and 4-5). In dip lines we observe several notches or wave cut terraces that create relief in the transgressive surface (Fig. 4-6B). These notches have relief on the order of several meters.

A notable decrease in roughness along the transgressive surface is observed from offshore to onshore. Seismic profiles show variation in roughness offshore with less variation nearshore (Fig. 4-5). The onshore trend of the Carmel Valley Fault appears to be aligned with the deformation observed in water depths  $> \sim 45$  m (Figs. 4-2A and 4-4). At shallower depths the expression of the fault on the transgressive surface is subtle and only delineated by changes in bedding orientation below the transgressive surface. Furthermore, notches observed in dip lines are confined to deeper water depths ( $> 20$ -30 m) and, their relief increases with water depth (Fig. 4-6B).

Three areas exhibit reversals in the regional southern dip of bedding beneath the transgressive surface (Fig. 4-7H). Bedding dips to the north in the following locations: 1) directly north of the La Jolla Canyon, 2) directly north of the Scripps Canyon (Fig. 4-4), and 3) in the localized offshore high aligned with the Carmel Valley fault (Fig. 4-4). Reversal of dip on beds below the transgressive surface north of the La Jolla Canyon extends approximately 500 m towards Scripps Canyon. This dip reversal spans the area on the northern side of the westward-stepping constraining bend of the Rose Canyon Fault that controls uplift of Mt. Soledad to the south. The reversal of dip north of the Scripps Canyon corresponds to the northern extent of the high in the transgressive surface. In addition, the east-west strikes of the bedding offshore follow the orientation of

the Rose Canyon Fault similar to the northwest-southeast strikes of bedding measured on land to the east by Kennedy (1975). Nevertheless, where the reversal of dip is observed the offshore units dip more steeply to the north ( $\sim 15\text{-}20^\circ$ ) than those onshore ( $\sim 5\text{-}10^\circ$ ).

### **Tectonic expressions on-land**

Observations from the sea cliffs in our survey area, offer an ideal opportunity to examine the along-shore variability of the tectonic landscape, which complements our offshore observations. In the northern part of our study area, Legg and Kennedy identified a system of east-west trending oblique faults (1979), including the Carmel Valley and Salk faults. Sea cliffs between the south extremity of La Jolla Shores beach and Point La Jolla are of particular significance because they lie within the RCFZ, where trench studies suggest Holocene deformation (Lindvall and Rockwell 1995). Visual observations at this location are augmented by analysis of LIDAR data (Fig. 4-8). Along the seacliffs, we observe three strike-slip faults, namely the Country Club, Mount Soledad, and Rose Canyon faults from south to north (Figs. 4-2A and 4-8; Treiman 1993), as well as a number of more diffuse fault splays. The change in coastal relief from the low-lying La Jolla Shores to the sea cliffs parallels the change in seabed type from sandy bottom to the kelp-bearing rocky substrate observed around Point La Jolla. This transition from mobile sands to hardgrounds is associated with the Rose Canyon Fault, which lines up with the La Jolla Canyon, and delineates the northern extent of the uplift of Mount Soledad. In turn, the Country Club Fault correlates with a zone of increased seafloor roughness that occurs immediately south of the La Jolla Canyon. The Country Club Fault is also associated with differences in erosion patterns along the sea cliffs.

South of the Country Club Fault and north of the Mount Soledad Fault, rocks are sand-dominated while in between these two faults they are mud-dominated. The southernmost sand-dominated cliffs have eroded into small caves, which provide habitat for a large bird population. Finally, we observe another expression of this deformation in the tide pool rocks in front of a narrow cobble beach backed by the faulted cliffs. Outcropping rocks are tilted at least  $25^\circ$  to the south to form a regular pattern of cuestas with a short horizontal wavelength of 5 m to 10 m (Fig. 4-8).

### **Sedimentary Units Offshore La Jolla**

#### *Estuarine unit*

Near the canyons, a unit characterized by parallel, highly reflective horizons interbedded with acoustically transparent sediments is observed beneath the transgressive surface (Figs. 4-4, 4-6A, and 4-9A). Furthermore, these layers tend to attenuate the acoustic signature of underlying bedding quite effectively. Push cores obtained by divers at  $\sim 23$  m depth in the head of the La Jolla Canyon recovered fine-grained muds interbedded with sands (Figs. 4-2A, 4-3 and 4-9C). An isopach map of these acoustically laminated sediments shows that they occur at the canyon edges (Fig. 4-7G). These sediments have a large spatial extent at the head of the La Jolla Canyon, whereas they are confined to the edges of the Scripps Canyon. Furthermore, the sediments of this unit are thicker near the La Jolla Canyon ( $> 10$  m thick) than in the Scripps Canyon.

#### *Healing-phase deposits*

Within the sediments overlying the transgressive surface, a basal unit exhibiting distinct lamination is observed (Fig. 4-6). The acoustic character of these sediments is different from the unit observed near the canyons: these have sub-parallel, highly reflective horizons inter-bedded with unevenly reflective layers. The unit is spatially limited to the lows in the transgressive surface between the two canyons and to the north of the Scripps Canyon (Figs. 4-4 and 4-6). These laminated sediments are thickest, up to 12 m thick, seaward of the 30 m isobath. Moreover, these deposits infill lows or notches in the transgressive surface (Figs. 4-5 and 4-6B). Moving shoreward, similar units are observed upsection that onlap the transgressive surface and also downlap onto older deposits of the same nature.

An isopach map detailing the thickness and distribution of these basal acoustically-reflective deposits shows marked variability (Fig. 4-7E), with a depocenter just to the north of the Scripps Canyon infilling a structural low along the transgressive surface (Fig. 4-7B). The landward limit of this unit is delineated by the 20 m contour (Fig. 4-7E) with a marked increase in along-shore variability with depth. For example, at ~60 m water depth, the wavelength of variability is ~500 m, whereas at 40 m water depth the wavelength increases to ~1 km. Although there is thickness variability in the entire sediment package above the transgressive surface (Fig. 4-7D), most of the observed variability is associated with thickness variations of this basal reflective unit (Fig. 4-7E).

#### Holocene sands

The uppermost unit is acoustically transparent, exhibits cross-shelf thickness variability with a mid-shelf depocenter, and makes up the majority of sediment overlying



the transgressive surface (Figs. 4-4 and 4-6). The unit is described as fine-grained to very fine-grained, homogenous sands based on cores acquired in the area (Fig. 4-2A; Darigo and Osbourne 1986; Hogarth *et al.* 2007). Despite being acoustically homogenous, the transparent unit does contain several subtle, oblique or occasionally curved reflectors (Fig. 4-10). These features appear in strike lines at the canyon edges, as the seabed slope increases. They dip towards the canyon axis and, where curved, they are generally concave upwards. They are usually acoustically faint and often disappear within the transparent sediment package before intersecting or joining other acoustic reflectors at depth. In general, they originate at or near the seabed, and sometimes occur in groups of two or three sub-parallel reflectors. The geometry of these features is similar to seafloor slopes observed along the modern canyon edges. Where the above-mentioned reflectors intercept the basal highly-reflective package near the canyon edges, they appear to truncate the underlying reflectors and also exhibit a change in trend from concave up to concave down (Fig. 4-10B). Several profiles exhibit an apparent increase in thickness of the transparent sediment unit in close proximity to the canyon due to the oblique orientation of secondary channels (Fig. 4-6). This creates a concave up geometry of the seabed in strike profiles crossing the canyon, reflecting the three-dimensionality of these tributaries. By revealing the wide and shallow incisions not readily observable in the bathymetry, our seismic data improves our characterization of these features.

An isopach map of the Holocene sediments (Fig. 4-7D), which consists of both the reflective package that onlaps the transgressive surface (Fig. 4-7E) and the overlying transparent sands (Fig. 4-7F), illustrates the infilling of relief observed along the transgressive surface (Fig. 4-7B). In the isopach map (Fig. 4-7D), from south to north, we

observe the following: 1) Holocene sediment is absent on top of the hard grounds south of the La Jolla Canyon, 2) over 20 m of sediment overlies the erosional surface between the two branches of the canyon, 3) there is a depocenter north of the Scripps Canyon, and 4) sediment thickness thins to ~5 m in a region between Scripps Canyon and the pop-up structure to the north.

As previously mentioned, much of the variability in the thickness of the Holocene unit (Fig. 4-7D) corresponds to variability in the basal, reflective package (Fig. 4-7E). This basal unit makes up most of the depocenter north of the Scripps Canyon (Fig. 4-7E), while the upper transparent unit accounts for the majority of sediment in the depocenter between the two canyons (Fig. 4-7F). In addition, to the north of the Scripps Canyon only, the overlying acoustically transparent unit (Fig. 4-7F) reveals a mid-shelf depocenter. Note the slight seaward deflection of the mid-shelf depocenter toward the north offshore Torrey Pines State Park reflecting deformation on the constraining bend and uplifted pop-up structure (Hogarth *et al.* 2007).

## DISCUSSION

Except for the La Jolla and Scripps Canyons, the transgressive surface offshore La Jolla shows much more relief than the bathymetry because its structure is obscured by modern sediment accumulation. Our observations of stratigraphic architecture, structural variability, and detailed bathymetric features highlight the role of tectonics in canyon location and morphology as well as Holocene sediment distribution and thickness.

### Structural controls on canyon location

Although researchers have long known that the Rose Canyon Fault controls the location of the La Jolla Canyon, our data emphasize the offshore expression of the constraining bend on the fault, which has a large influence on the structure of the shelf to the north. The widespread dip reversal on bedding to the north of the La Jolla Canyon (Fig. 4-7H) is similar to structures observed in other regions where compression results in folding and back-tilting of bedding (e.g., Gulick and Meltzer 2002). The relatively steep dip of these units is the expression of the compressional component of this tranpressional strain regime, whereas the more shallowly inclined bedding mapped by Kennedy (1975) onshore occurs where the fault is translational. The dipping beds and consequent cuestas observed at the base of the cliffs and in shallow-water near the head of the La Jolla Canyon further illustrate this deformation in the proximity of the RCFZ (Figs. 4-8 and 4-11C).

The transgressive surface is not just a simple monocline with uplift by the northern pop-up structure (Hogarth *et al.* 2007). In fact, from south to north, the transgressive surface deepens from the La Jolla Canyon until just north of the Scripps Canyon (Fig. 4-11) at which point the transgressive surface shoals northward. This localized northward deepening of the transgressive surface may indicate that the influence of the southern constraining bend on the Rose Canyon Fault extends up to  $\sim 1$  km to the north of the fault.

The seismic and bathymetric data suggest that the Scripps Canyon formed at the apex of a structural antiform. While many other rectilinear canyons extending close to the coastline appear to be fault controlled (e.g., the Redondo Canyon; Gardner *et al.* 2002),

none of the en-echelon oblique faults observed in the sea cliffs onshore of the Scripps Canyon correlate with its orientation (Fig. 4-2A). Instead, our new data image an anticline that would explain the formation of the Scripps Canyon. We see expression of this antiform most distinctly to the north of the Scripps Canyon in the reversal of the regional southern dip on bedding beneath the transgressive surface (Figs. 4-4 and 4-7H). Furthermore, although there is a subtle topographic high observed in the Submetrix bathymetry, the high is clearly observed in the depth to the transgressive surface on the north side of the Scripps Canyon (Figs. 4-4, 4-6A and 4-7B). I propose that erosion at the apex of this antiform would be enhanced due to the faulted and structurally weakened nature of the rock (Davis and Reynolds 1996) and that this antiform plays a significant role in the location of the Scripps Canyon. Because of the linear morphology of the Scripps Canyon, other researchers also invoked a tectonic control (Rindell 1991; Webb 1988). In their conceptual models joints related to the Torrey Pines Fault have been proposed to exert a structural control on the orientation of the shallow water branches at the head of the canyon. However, there is no evidence in seismic profiles of faults intersecting the heads of the Scripps Canyon. In our scenario, these joints are not fault-controlled, but are rather associated with tension along the crest of an antiform.

### **Morphology of the La Jolla Canyon**

Tectonically induced structure governs the characteristics of secondary incisions that link up with the La Jolla Canyon. The marked asymmetry exhibited by these tributary channels, being much larger on the northern side, is likely controlled by lithologic differences across the Rose Canyon Fault. Short, arcuate cuts in the south wall

of the La Jolla Canyon (Figs. 4-3 and 4-11) occur due to the highly resistive nature of the Cretaceous hard rock uplifted to the south of the Rose Canyon Fault. The secondary channels on the northern wall of the La Jolla Canyon (Figs. 4-3 and 4-11) cut much deeper into the adjacent shelf due to the less indurated substrate. The geometry of these incisions appears to be controlled by faults and dipping bedding associated with the RCFZ as well as Scripps Fault (Fig. 4-2A). For example, the largest secondary canyon of ~500 m length trends northeasterly, but takes an abrupt curve to the north at its head. This sinuous morphology is coincident with Scripps Fault and back-tilted bedding (Fig. 4-11).

Similarly, tectonic framework may also play a role in the large width of the bowl-shaped head of the La Jolla Canyon, as opposed to the narrow heads of the Scripps Canyon (Fig. 4-3). I propose the La Jolla Canyon has grown asymmetrically with most of the lateral development to the north where erosion can exploit the weaker, less indurated Eocene rocks. Conversely, the south wall, which is incised into Cretaceous rocks, is eroding at a much slower rate. Differential uplift across the Rose Canyon Fault as evidenced by uplift of Mount Soledad and deformation of the transgressive surface might also explain the northward deflection of the thalweg of the La Jolla Canyon (Fig. 4-11).

Complementary observations on the locations of the three main faults on land and of their offshore extensions imaged in the seismic data refine our understanding of the structural control on the formation of the La Jolla Canyon and on the morphology of the surrounding inner shelf and coastline (Fig. 4-8). The thalweg of the La Jolla Canyon occurs in a region of compression associated with the left-lateral jog along the Rose Canyon Fault. South of this fault, outcrops of Cretaceous indurated mudstones and sandstones influence kelp forest location (Hogarth et al 2007; Shepard and Emery 1941).

The Country Club Fault, despite having large horizontal offset on land, has little influence on the location of the La Jolla submarine canyon. This fault appears to correlate with asperities in the transgressive surface observed directly northwest of Point La Jolla that may be indicative of fault-induced displacement. The difference in erosional patterns on the cliffs due to the change in lithology across this fault also influences the spatial distribution of nesting habitats.

### **Morphology of the Scripps Canyon**

The unlithified nature of the Holocene sediments affects the erosion, deposition, and stability of the upper walls of the Scripps Canyon, which are incised by shallow secondary channels. Some of the secondary canyon tributaries are active as evidenced by continuous sediment fluxes and catastrophic slump events (Dill 1964; Marshall 1978). The oblique intersection of these secondary incisions to the thalweg of the Scripps Canyon suggests that they are not formed by gravitational failure alone, which would yield a more orthogonal geometry (Farre *et al.* 1983). Nevertheless, erosion and overprinting from bottom-up mechanisms driven by gravity are likely. Downslope-eroding sediment flows, which could explain the oblique geometry of the secondary incisions, may trigger retrogressive failures (Pratson and Coakley 1996). In addition, Mastbergen and van den Berg (2003) recently proposed a breaching model based on negative pore pressure build-up and tested it on a well-documented slide in the south wall of the Scripps Canyon (Marshall 1978). The role of slope failure in forming these channels is apparent in the shape of the canyon edges. The steep upper walls appear to be formed by failure of the unlithified Holocene deposits. In addition, there is no observed

down-lap in the strike lines across the Scripps Canyon that would be indicative of the non-deposition and sediment bypass associated with strong axial canyon currents. Faint reflectors within the unconsolidated sediment facies may be evidence of ancient failure events (Fig. 4-10).

The large morphological variability of the tributary channels of the Scripps Canyon, (Figs. 4-2 and 4-3) may be explained by several factors including the spatial heterogeneity of hydrodynamic forcing, sediment supply by the southward littoral drift, and the structural framework. The transport and sorting of shelf sediments by surface gravity waves is depth-dependant (Nielsen 1992). Divergence and convergence phenomena due the effect of the canyon topography on wave propagation generate extreme wave heights in localized zones and intense rip currents in other areas (Shepard and Inman 1950). The southward orientation of sediment transport in the littoral cell (Inman and Chamberlain 1960; Inman and Frautschy 1965; Inman and Masters 1991b), being intercepted by the Scripps Canyon, may induce asymmetry in sediment supply between the north and south walls. Differences in structure may also play a role in the slope variability of the upper walls on the canyon. On the north side of the Scripps Canyon, the pronounced northward dip of the bedrock along the antiform (Fig. 4-7H) may enhance the stability of deposits. The wide range of morphologic features observed in the canyon likely reflects different evolutionary histories of the side canyons. For example, some side canyons may be young and more linear, whereas others are wider and have been overprinted and reshaped by other processes. Understanding the evolution of this morphology and asymmetry requires a more detailed spatial and temporal study. In addition, the hypothesis of a young age for the Scripps Canyon could explain some of

these features as well as its overall narrow shape. Indeed, younger age translates into narrower canyons with less developed heads and side canyons (Farre *et al.* 1983).

### **Topographic effect**

The distance away from the canyon over which the bathymetry is affected by the presence of the canyon appears to be much larger than one may predict from basic principles of mechanical stability. This distance is characterized by the average value of the actual slope, which is related to the stability or erodability of the unconsolidated sediments. For the upper walls of the Scripps Canyon and of the north side of the La Jolla Canyon, the slopes cannot exceed the repose angle of saturated sands as they are eroded into unconsolidated sediments. Small average slopes are associated with large areas where the bathymetry is modified due to the canyon. Topographic effects of the Scripps Canyon are observed as far as 1 km from the thalweg, despite the steepness of the lower walls. This distance, which can be interpreted as a boundary layer length, is highly variable along the Scripps Canyon and between the north and south walls (Figs. 4-2B and 4-3). The influence of local forcing parameters subject to small scale fluctuations could partially account for this variability. For example, the terrace to the north of the Scripps Canyon may be formed by localized larger waves that could result in enhanced sediment resuspension and transport shoreward into the North Branch. As waves travel faster in deeper water, the Scripps Canyon modifies the velocity and the direction of propagation of incident waves. Refraction and reflection of gravity and infragravity waves can locally engender an increase of wave height and of the associated energy flux just north of the Scripps Canyon (Magne *et al.* 2007; Munk and Traylor 1947; Thomson *et al.* 2007). This



sediment resuspension and transport into the thalweg of the North Branch of the canyon is consistent with the deflection of the 20 m isobath to the east (Fig. 4-2B). Alternatively, the orientation of the North Branch of the canyon head might affect the interplay between along and across shore sediment transport and play an important role in the capture of sediment transported between the surf zone and the shelf.

### **Erosive processes at the canyon edges**

A systematic investigation of the slopes versus rock type of canyons walls could shed light on the relationships between lithology and submarine erosion processes. For example, this would allow one to study the role of cohesion in erosion rate. At shallow depths where sediment deposits are affected by wave and current, substrate along the La Jolla and Scripps canyon walls range from unconsolidated sand to estuarine mud (Figs. 4-4 and 4-9). Similarly, in some seismic profiles across the Scripps Canyon, the healing-phase deposits could continue laterally towards the canyon, in which case the healing-phase deposits would outcrop at the canyon walls. Although little is known about seafloor instabilities (Pratson 2001), differences in consolidation of the sediments along the canyon edges likely affect their stability. The change in facies may explain some morphological aspects of the canyon edges, such as their variable slopes.

A better understanding of the failures observed along the edges of the canyons could improve our knowledge of mechanisms and triggering factors for submarine slumps, as well as the preservation of these events in the geologic record. The concave-up horizons observed within the unconsolidated Holocene deposits (Fig. 4-10B) could be ancient failures, possibly associated with storm events or earthquakes. Mapping the

distribution of these failures within the Holocene layer may reveal correlation with overlying sediment thickness or with water depth along the canyon edges. Alternatively, preferred slump locations may be identified, with a possibly heterogeneous concentration on either side of the canyons. A comparison of slopes between contemporary exposed lagoonal substrate in the head of the La Jolla Canyon and ancient canyon edges covered by recent sediment deposits could improve our understanding of canyon edge morphology or provide information on the depositional environment of these relict features. In addition, developing a method to estimate the age of failure events could lead to examining timing relationships with triggering mechanisms such as earthquakes (Dill 1969; Marshall 1978; Shepard and Dill 1966).

### **Tectonic control on sediment distribution and thickness during the transgression**

Three sedimentary units have been identified in the seismic data based on stratal geometry, acoustic character, and analyses of sediment samples where available. I interpret the highly reflective unit observed near the canyons and sampled by push cores as an estuarine or lagoonal deposit, consistent with previous reports of estuarine sediments within the head of the La Jolla Canyon (Holden 1968; Judy 1987; Shepard and Dill 1966). To the best of our knowledge, the occurrence of this estuarine unit along the edges of the Scripps Canyon has not reported. I identify the basal sediments infilling lows or notches in the transgressive surface (Figs. 4-4, 4-5, and 4-6) as a healing-phase wedge, while Darigo and Osbourne (1986) had considered this unit as Pleistocene sediments. Healing-phase deposits have been referred to as transgressive backfill or transgressive lag (e.g., Cattaneo and Steel 2003 and references therein). The overlying, acoustically

transparent unit is interpreted to be Holocene unconsolidated sands, consistent with Hogarth *et al.* (2007).

The geometries and locations of the three sedimentary units in the area reflect the interplay of tectonics, eustacy, and sediment supply. The spatial distribution of the three facies is controlled chiefly by eustacy and tectonics. We are able to distinguish the influences of eustacy and transpressional tectonics because of the geometry; transpression on the RCFZ imparts a shore parallel trend while effects due to sea level change and long-term, regional tectonic deformation engender a cross-shore signal. As sea level rises and a shoreline transgresses, areas of the coastal plain landward of the shoreline become potential areas of aggradation. In the case where sediment supply out paces upper shoreface erosion, estuarine deposits can be preserved. As sea level continues to rise, erosion of the upper shoreface provides sediments to infill, or “heal,” the lows in the lower shoreface and on the shelf (Catuneanu 2006; Posamentier and Allen 1999). These lows usually occur seaward of notches (Fig. 4-6B) that are the consequence of relative sea level still stands and erosion of incised platforms, or terraces (Fig. 4-6B). In some cases, the location of these notches is also influenced by the presence of back-tilted blocks, which allowed for differential erosion (Fig. 4-6B). The lows are subsequently backfilled as the shoreline migrates landward, eroding the coastline, with the consequent coarse-grained lag deposited offshore. As the transgression continues, so-called healing-phase deposits overlie the preserved estuarine sediments, as observed in strike lines (> 20 m) around the Scripps Canyon (Fig. 4-6A).

As the Scripps and La Jolla submarine canyons cut across the entire shelf into the nearshore, the upper reaches of these prominent bathymetric features constitute

embayments favorable to the deposition of estuarine sediments. In the case of the La Jolla Canyon (Figs. 4-9A and 4-7G), estuarine deposits found at shallow depths (~10-15 m) correspond to a later period of lagoonal development. The occurrence of the thickest estuarine deposits around the head of the La Jolla Canyon is likely related to the local physiographic and tectonic setting. A lagoon still occupied this site only 100 years ago (Moriarty 1964), over the low-lying inland area extending ~ 1 mile to the east of the current La Jolla Shores beach. These thick estuarine deposits outcrop in some areas, in particular along isolated ridges within the head of the La Jolla Canyon (Fig. 4-9). Most likely, wave-base energy is efficiently reworking sediments or preventing the deposition of modern sands over the mud-dominated units that outcrop at shallow water depths.

Beyond the primary features controlled by eustasy and long-term tectonic deformation, we observe tectonically induced secondary relief in the transgressive surface. The pop-up structure associated with the constraining bend on the Rose Canyon Fault generates a local northward shoaling trend on the transgressive surface (Hogarth *et al.* 2007). The antiform through which the Scripps Canyon is incised is an influential secondary structure as well. Operating at smaller wavelengths, east-west trending faults and associated deformation offset bedding, create along shore variability, and influence the pattern of modern sediment deposition. The most significant example of this deformation is the localized structural high north of the Scripps Canyon associated with the Carmel Valley and Salk faults on land (Figs. 4-7B and 4-7H). The area between these two oblique faults appears to be uplifted relative to the surrounding area (Fig. 4-2A) Both the large wavelength uplift associated with the pop-up structure and the short wavelength

deformation associated with these oblique faults create along-shore relief in the transgressive surface (Figs. 4-4, 4-5, 4-6, and 4-7B).

The healing-phase wedge is confined to the saddle region away from the canyons. Similar infilling of lows in the antecedent topography during transgression has been observed elsewhere (e.g., on the northern California shelf, Sommerfield and Wheatcroft 2007). In addition, onlap of the healing-phase wedge onto the transgressive surface indicates that its deposition occurred after deformation. North of the Scripps Canyon, the northern Holocene depocenter and much of the along-shore thickness variability observed in the Holocene sequence corresponds to variations in the basal healing-phase unit (Figs. 4-7D and 4-7E). Such a correlation is not observed in the inter-canyon shelf where the transparent upper sands appear to account for the majority of the sediment thickness in the depocenter (Figs. 4-7D, 4-7E, and 4-7F). The depression in the transgressive surface is more pronounced north of the Scripps Canyon than in the inter-canyon shelf (Fig. 4-7B). This is likely due to the positive uplift associated with the pop-up structure to the north and the shoaling of the transgressive surface towards the RCFZ in the south. The reflectors observed in the healing-phase deposits of the main depocenter are horizontal and on-lap the transgressive surface (Figs. 4-4 and 4-6A). This indicates that offset on the Carmel Valley and Salk faults, and more importantly, uplift of the pop-up structure pre-date deposition of the healing-phase.

Some of the relief in the transgressive surface is modified by wave erosion in the nearshore, which enhances the smoothness of the seafloor as coarse-grained sediments eroded from the shore-face are transported to the low areas offshore (Fig. 4-7E). For example, fault-induced roughness in the transgressive surface is mostly observed in

deeper water because these areas were rapidly transgressed. I interpret the overall decrease in the relief of transgressive surface from offshore to onshore, which greatly influences the location of healing-phase deposits, as a consequence of the varying rates of sea level rise during the last transgression (Fig. 4-5; Fairbanks 1989). With decreasing rate of sea level rise, the shallower part of the shelf was exposed to wave-based erosion over a longer period and existing structures were more effectively leveled. Another example of this decrease in relief is that the most landward of the terrace notches is observed at ~35 m depth.

### **Hydrodynamic control on modern sediment accumulation during the highstand**

The distribution of the upper Holocene sediment package in the along-shore direction is mostly affected by hydrodynamic factors such as the wave climate. Based on stratal geometry, the onset of deposition of these acoustically transparent sediments corresponds to a decrease in the rate of sea level rise. This sets the upper age limit of the transparent Holocene deposits to approximately 6-8 ka, at the beginning of the current sea level highstand. The map showing the depth to the top of the healing-phase (Fig. 4-7C) indicates that by this time much of the transgressive surface relief had been infilled by the healing-phase wedge, leaving a relatively smooth inner shelf profile with a seaward dip with little along-shore variability. North of the Scripps Canyon, the thickness of unconsolidated sediments exhibits a wedge cross-shore profile (See discussion by Hogarth *et al.* 2007; Figs. 4-6B, 4-7D and 4-7F), which corresponds to the mid-shelf high typical of Californian margins (Sommerfield and Nittrouer 1999). This wedge develops inshore of the depth where incipient velocities at the seabed are large enough to

resuspend, rework, sort, and transport sediments, and offshore of the depth where impinging waves cause rapid transport of unconsolidated sediments and prevent accumulation (Harris and Wiberg 2001; Henry 1976; Zhang *et al.* 1999).

The tectonic setting still influences the accumulation of the upper Holocene unit. In the northern part of our survey area, offshore Torrey Pines State Park, very little modern sedimentation deposition occurs at shallow water depths as the mid-shelf high is deflected seaward due the shoaling of the transgressive surface (Figs. 4-7D and 4-7F). The marked thinning of this overlying unit in the deeper area of our survey corresponds to the deformation associated with oblique faults as little sediment has accumulated over the transgressive surface high (Fig. 4-5). Because the healing-phase infilled and obscured the relief along the transgressive surface offshore, little to no thickness variation in the overlying Holocene package is observed in this region (Figs. 4-7C and 4-7F).

Our work questions the efficiency of Scripps Canyon in capturing and transporting sediment offshore during the most recent sea level rise and challenges the existing view on Holocene sediment transport and deposition offshore La Jolla. Observation of sediment wasting events in the Scripps Canyon heads (Chamberlain 1964; Dill 1964) and related studies involving mass balance estimates for littoral cell sediment budgets (Inman and Chamberlain 1960; Inman and Masters 1991b) have led the research community to conclude that the majority of sediment is captured and transported offshore by the La Jolla Submarine Canyon System. However, our data shows that modern sediment accumulation offshore La Jolla may be more complex. The well-defined thickness maximum in the Holocene layer, which corresponds to the inter-canyon Holocene depocenter, requires a net influx of sediment to the inter-canyon shelf within

the last approximately 6-8 ka. In addition, the beach and shoreface sands at the base of the cliffs and filling the Scripps Canyon head are thought to be a consistent feature throughout the present sea level highstand. Under present conditions there is a persistent mobile sand cover sloping up towards the beach along the shoreward extent of the canyon even after major flushing events that expose the wall and floor substrate (Peter Brueggeman, Personal communication 2008; Chamberlain 1964). This observation suggests that sediment from longshore drift may have bypassed the Scripps Canyon head despite the reported capture of large quantities of sediments, the very narrow pathway between the canyon head and the beach, and the head of the Scripps Canyon still being within wave base (Covault *et al.* 2007; Sommerfield and Lee 2004). An inhomogeneous incident wave field can drive significant alongshore currents at shallow depths, via wave setup-induced pressure gradients (Apotsos *et al.* 2008). Such currents engendered by the large along-shore variation in wave heights observed near Scripps Canyon are a mechanism for enhanced sediment transport within the surf zone onshore of the Scripps Canyon head. Thus, we need to reassess the role of the La Jolla Canyon System on sediment accumulation on the inner shelf offshore La Jolla and evaluate the proportion of sand captured by canyons versus that shunted out to the depocenter.

Observations of modern sediment accumulation on the San Diego County shelf, which provide a perspective on the regional pattern, confirm that the inner shelf offshore La Jolla is generally a depocenter of modern sediments. Regional studies reveal that exposed bedrock is common between the mid-shelf wedge and the beach, except at river mouths (Henry 1976). Excepting the two areas of uplift due to the RCFZ, offshore La Jolla there is no bedrock exposed between the mid-shelf wedge and the beach. Our study



area appears to be characterized by an atypically large accumulation of young sediment. The westward step of the coastline at the southern extremity of the Oceanside littoral cell may act as a jetty and promote sediment accumulation. The well-developed rip currents consistently observed south of the Scripps Pier at La Jolla Shores beach (Shepard and Inman 1950) and also immediately north of the Scripps Pier (Smith and Largier 1995) are likely contributing to this net accumulation. They redistribute modern sediments seaward on the inter-canyon shelf (Inman 1952; Inman 1953) to form the constructional feature observed in isopach maps.

Unfortunately, the present evolution of this depocenter is not very well constrained. Repeated sounding surveys performed between 1949 and 1950 (Inman 1952; Inman 1953; Shepard and Inman 1951) and seismic surveys conducted in 1976 and 1979 with a 3.5 kHz seismic profiler (Henry 1976; Waggoner 1979) indicate that sand levels are fairly stable on short time scales, respectively 1 and 3 years, at the location where I have identified the upper Holocene depocenter in the inter-canyon shelf. However, both accretion and erosion dynamics have been reported (Dayton *et al.* 1989; Inman 1953; Marshall 1978). This would imply that the Holocene sediment depocenter is currently in near equilibrium, with no net influx or outflux over the last few decades. Note the well-defined scour mark due to dredging observed in 20 m water depth to the north of our study area (Fig. 4-1). The preservation of this feature over a decade after the dredging occurred indicates that longshore drift is currently limited to the nearshore region. Sediment transport in the littoral cell may be episodic with high sediment transport periods during abnormally wet climatic regimes. A high sediment supply during a wetter

climate could be one mechanism to supply large amounts of sediment to the inter-canyon over a short time period.

## CONCLUSION

High-resolution three-dimensional coverage of the shelf in the vicinity of the La Jolla and Scripps submarine canyons, obtained from CHIRP seismic data and swath bathymetry, highlights the control of the structural framework on the observed stratigraphy and morphology. The faulted and folded tectonic landscape associated with constraining bends in the Rose Canyon Fault plays a critical role in canyon location and morphology as well as in the distribution of modern facies offshore La Jolla, California. Beyond the northward shoaling of the transgressive surface, our high-resolution seismics show much cross-shore and along-shore structural variability. We observe a widespread dip reversal in the bedrock and an increased dip of offshore units compared to those onshore due to deformation. I propose that the observed structural deformation offshore La Jolla is the expression of the compressional component of the transpressional strain regime associated with the RCFZ. I also propose that an antiform controls the location of the Scripps Canyon, contrary to the previous hypothesis of fault control. Furthermore, the action of wave-based erosion is reflected in leveling and smoothing of bedrock highs and subsequent infilling of lows with reworked shelf materials. There is also an overall decrease of relief and small-scale roughness in the transgressive surface landward of ~ 25 m water depth due to a decrease in the rate of sea level rise and longer exposure to wave-base erosion.

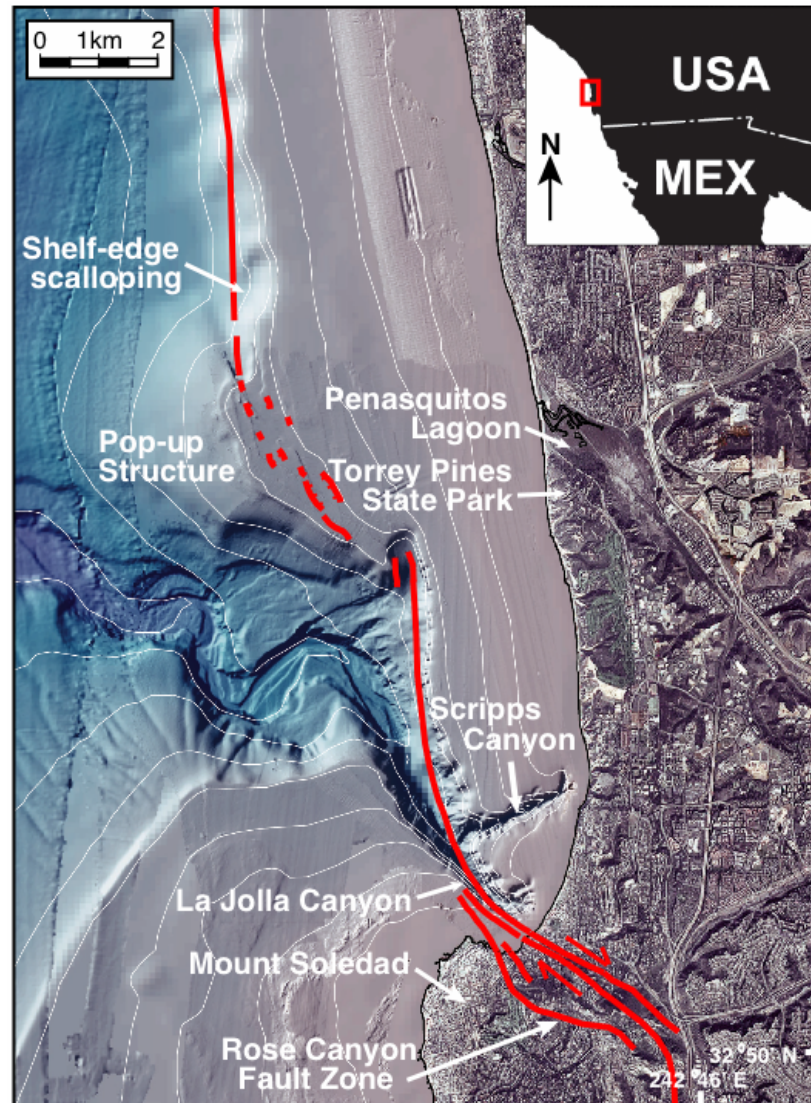
The detailed bathymetry exposes morphological differences between the La Jolla Canyon and the Scripps Canyon at various scales, from overall canyon shape to morphology of secondary incisions. The asymmetric development and deep secondary channels of the La Jolla Canyon are indicative of differential erosion due to deformation near the RCFZ. The longitudinal variability of the unconsolidated modern sediment cover on the upper walls of the Scripps Canyon appears to result from erosion of shallow gullies by failure processes. Ancient failures or sliding planes within the upper Holocene unit record the evolutionary history of the canyon edges.

I identify 3 stratigraphic sequences overlying the bedrock offshore La Jolla: estuarine deposits, a healing-phase wedge, and homogeneous sands. I interpret the spatial distribution of these modern stratigraphic units in the light of the complex interaction between sea level rise, tectonics, and sediment supply. The primarily along shore variation in the local tectonic structure allows to distinguish the influences of eustasy and transpressional tectonics. The deposition pattern of the two older packages is structurally controlled, with lagoonal deposits limited to the shallow upper reaches of the canyons and the healing-phase deposits infilling the lows seaward of notches and the saddle away from uplifted areas. The accumulation of the younger sand unit, which is controlled by local hydrodynamics, contrary to the two older packages, exhibits a typical mid-shelf wedge north of the Scripps Canyon and a depocenter on the inter-canyon shelf. This depocenter questions the efficiency of canyons in capturing sediments and refines our conceptual model for the Holocene sediment transport and deposition offshore La Jolla.

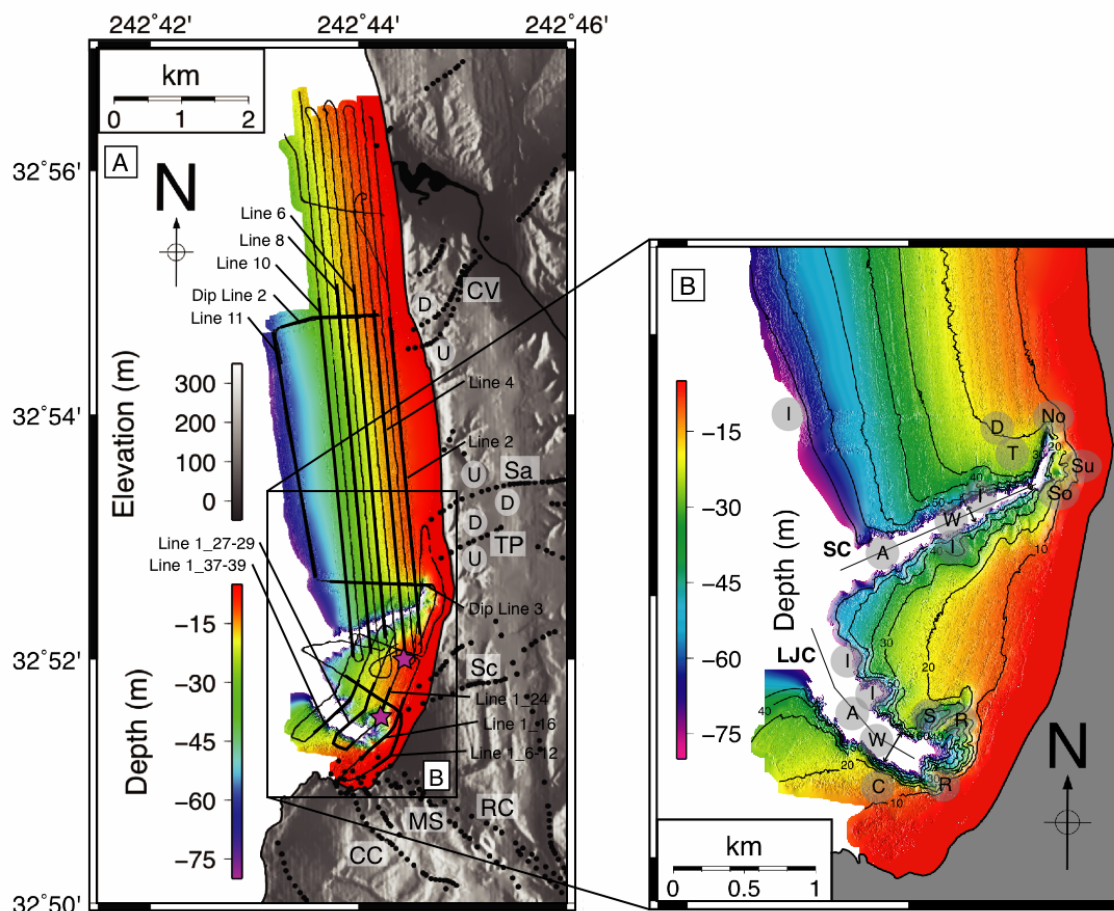
Detailed understanding of the processes that shape continental margins that affect long-term sediment accumulation is critical to predict the response of the inner shelf

environment to sea level change and to climate change. Canyons may play a major role in linking the coastal and deep ocean. Knowledge of geologic framework is also critical when investigating short-term sediment transport problems including beach evolution, sediment slides, coastal sediment budget, and the fate of sediments in the littoral zone.

**Acknowledgements:** This research was funded by the Office of Naval Research, the Southern California Coastal Ocean Observing System (SCCOOS), and an Achievement Rewards for College Scientists fellowship. I thank William W. Danforth for his help processing the Submetrix data, Warren L. Smith for his assistance in analyzing cores, Captain Eddy Kisfaludy for operating the R/V Saihkon, the crew of the R/V Sproul, and Elizabeth A. Johnstone for collecting the LIDAR data. The authors also acknowledge the use of software packages for data processing. The Generic Mapping Tools (GMT, Smith and Wessel 1990; Wessel and Smith 1998; <http://gmt.soest.hawaii.edu>) and Mirone (Luis 2007; <http://w3.ualg.pt/~jluis/mirone>) are available online free of charge. Kindgom Suite (<http://www.seismicmicro.com>) is commercial software made available for educational use at no charge.



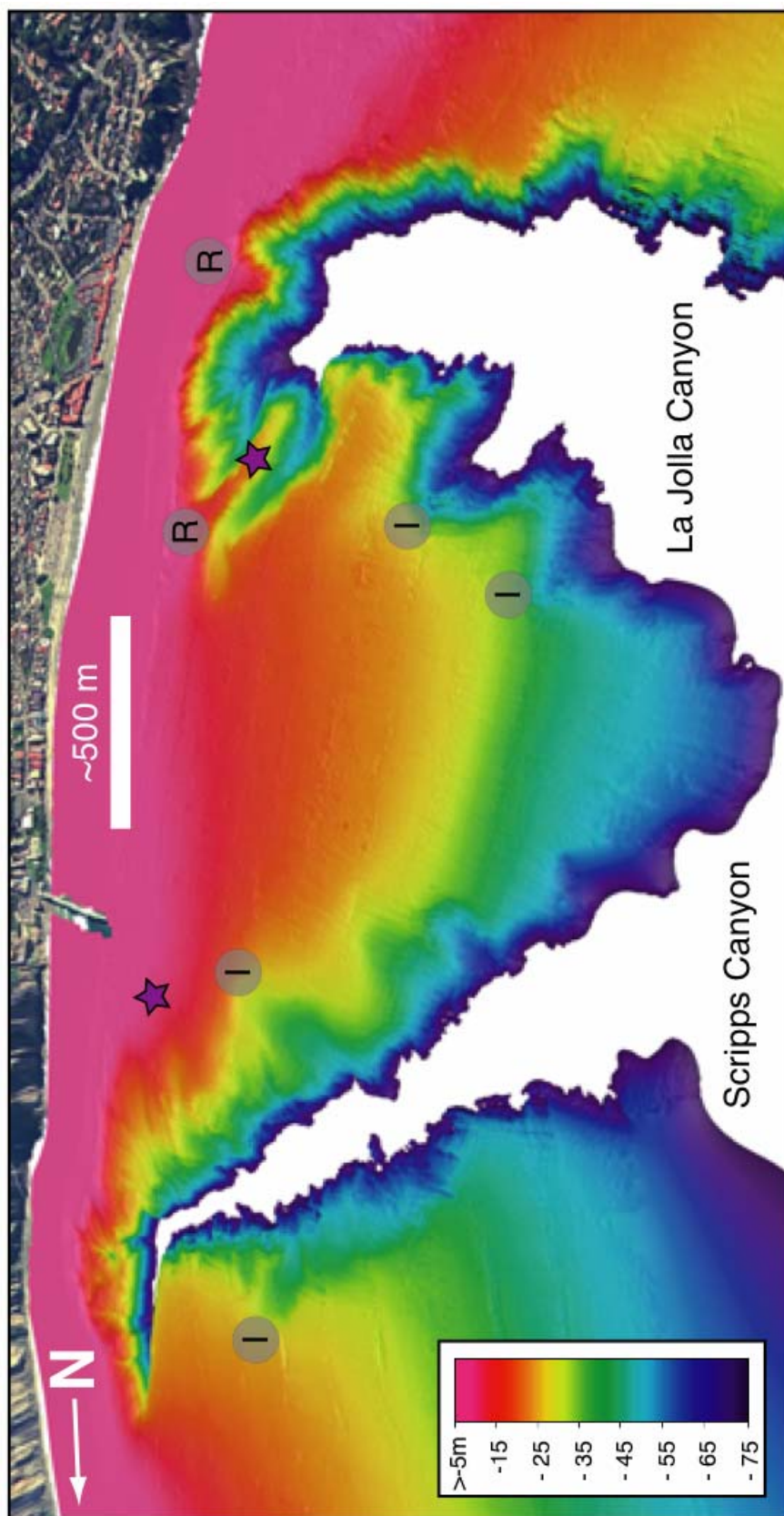
**Figure 4-1:** Location map showing expression of the structural high on the shelf, the left-lateral jogs on the right-lateral Rose Canyon Fault (arrows indicate sense of strike-slip motion), and the fault-induced scalloping where the Rose Canyon Fault coincides with the shelf edge north and south of the pop-up structure. Bathymetry modified from Dartnell *et al.* (2007)



**Figure 4-2: Survey coverage and bathymetry. A.** Survey ship tracks shown in black lines and superimposed on high-resolution Submetrix bathymetry show data coverage as well as core locations with purple stars (push core near the La Jolla Canyon head and vibracore near the Scripps Pier south of the Scripps Canyon). Local faults shown in dotted black lines are based on Kennedy (1975). D and U for downthrown and upthrown sides. CC=Country Club, MS=Mount Soledad, RC=Rose Canyon, Sc=Scripps, TP=Torrey Pines, Sa=Salk and CV=Carmel Valley faults. **B.** View of high-resolution bathymetry near La Jolla and Scripps canyons. SC=The Scripps Canyon, LJC=The La Jolla Canyon, A=Axis of canyon thalweg, W=Width of canyon thalweg, I=Incision into canyon wall (side channel), S=Sinuous secondary channel, C=Cretaceous hard grounds, R=Ridge within La Jolla Canyon head, D=Deflection of isobath shoreward, T='Terrace', So=South Branch of Scripps Canyon, Su=Sumner Branch of Scripps Canyon, No=North Branch of Scripps Canyon

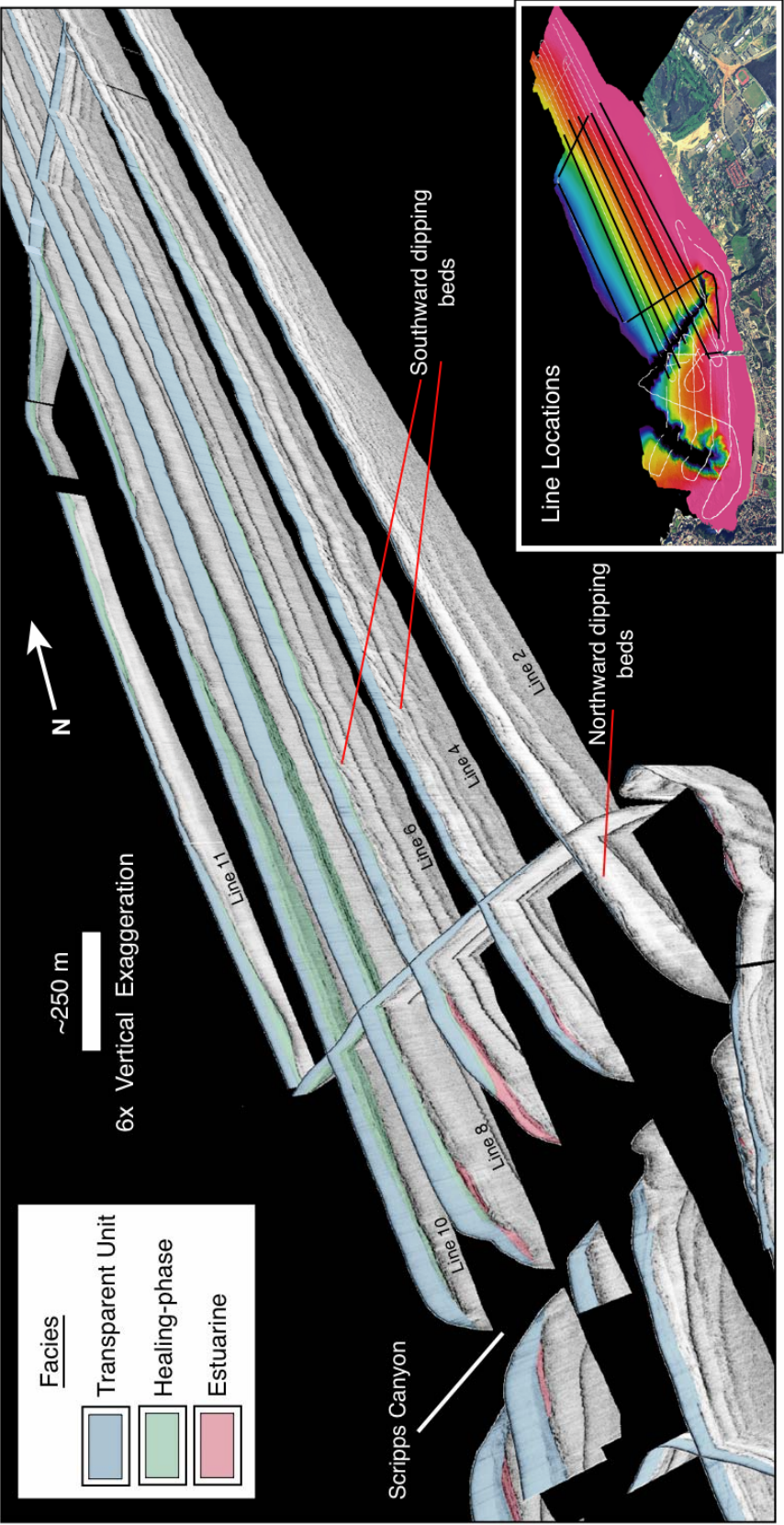
**Figure 4-3: Perspective view of the submarine canyon heads. Submetrix bathymetry has a vertical exaggeration of 6:1 while land topography has none. Note the asymmetry in the canyon heads and in secondary canyon development and the longitudinal variability of the canyon edges. Features labeled as in Figure 4-2**



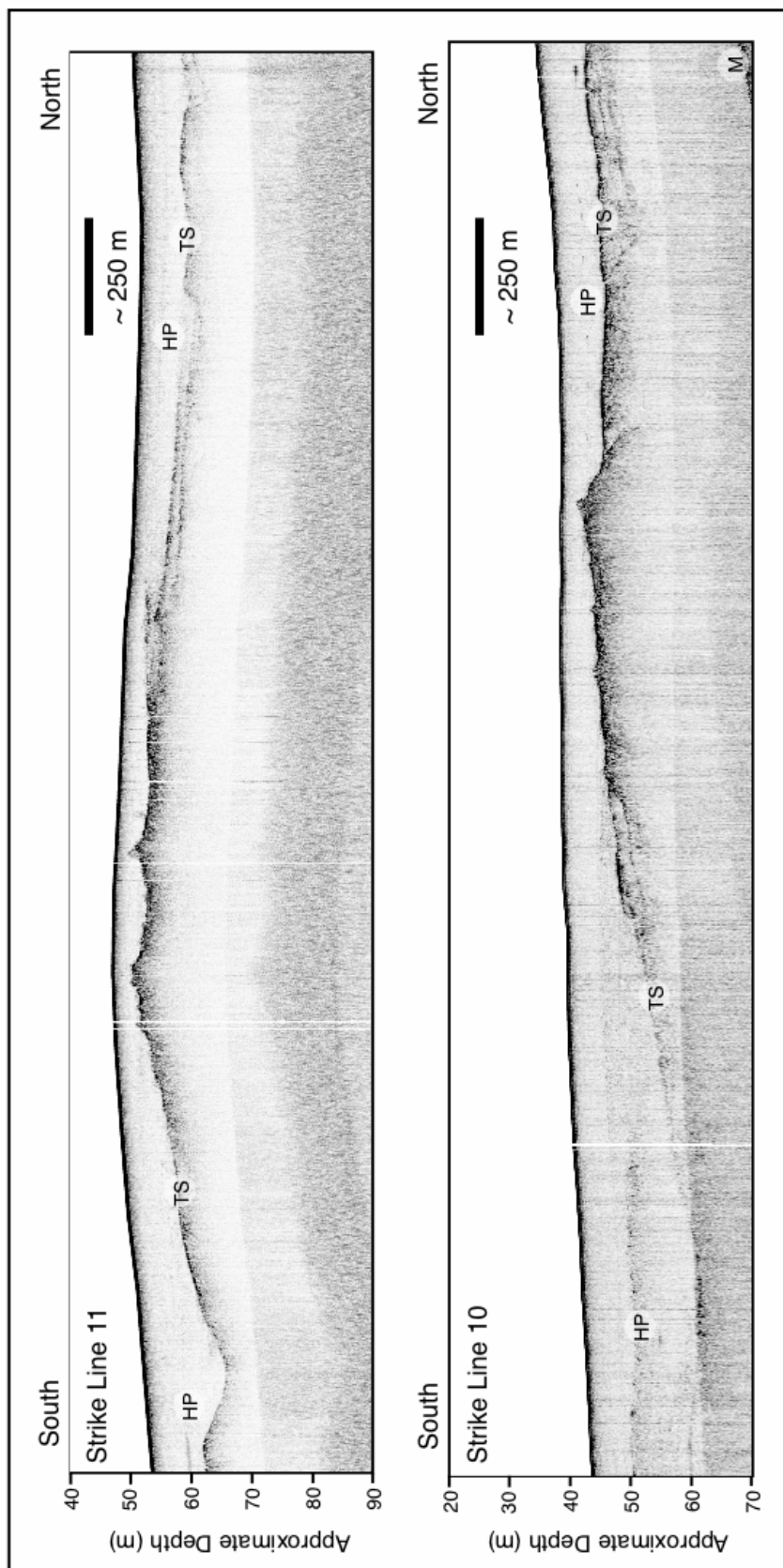


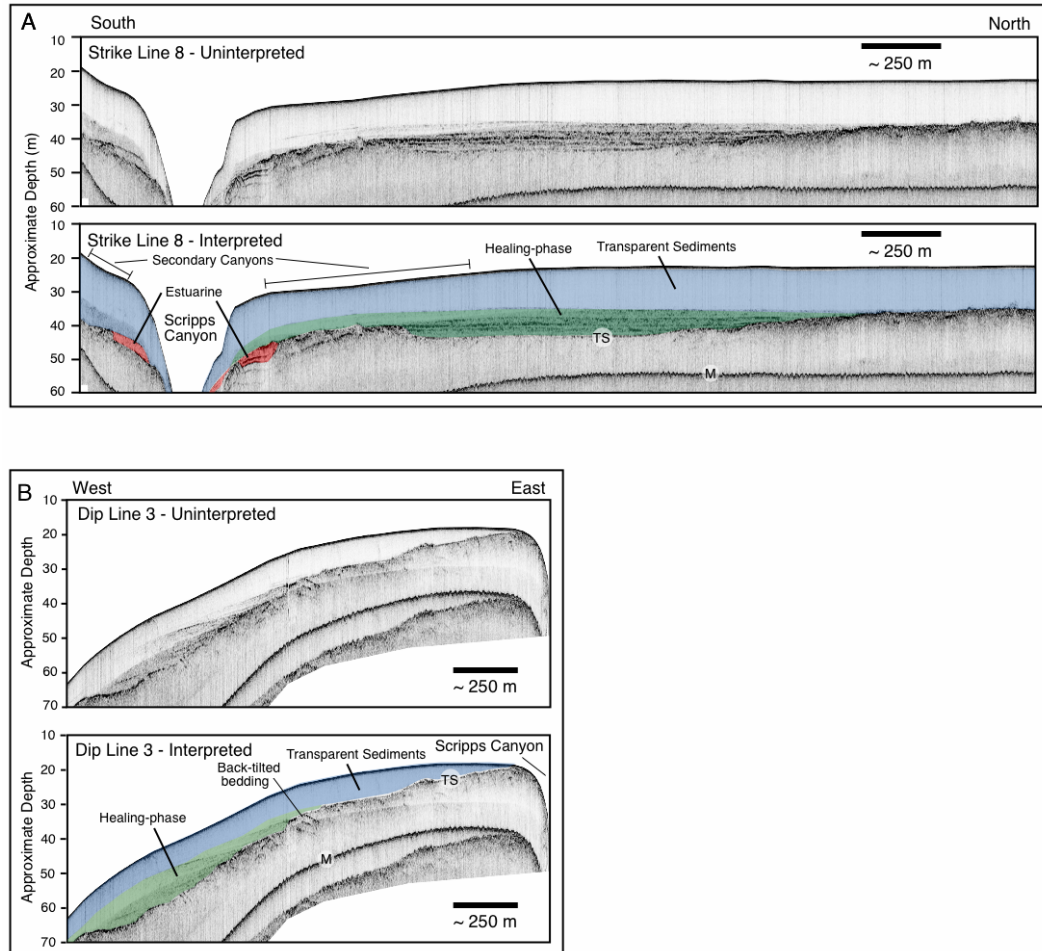


**Figure 4-4: Perspective view of the seismic dataset. Selected seismic profiles showing the estuarine, healing-phase, and upper Holocene sand units are displayed with a vertical exaggeration of 6:1. Beds dip regionally to the south, but dip to the north just north of the Scripps Canyon. Note the thinning of the Holocene sands towards the north due to the pop-up structure. In addition, a structural high is observed on either side of the canyon. Inset shows line locations and figure orientation. For deformation related to the Carmel Valley and Salk faults see Figure 4-5**



**Figure 4-5: Transgressive surface roughness increases with water depth. A. The most offshore line, strike line 11, exhibits more roughness on the transgressive surface due to deformation on the Carmel Valley and Salk faults. B. Strike line 10 is slightly shallower and exhibits significant smoothing of the transgressive surface (M=multiple, TS=Transgressive surface, HP=Healing-phase deposits)**

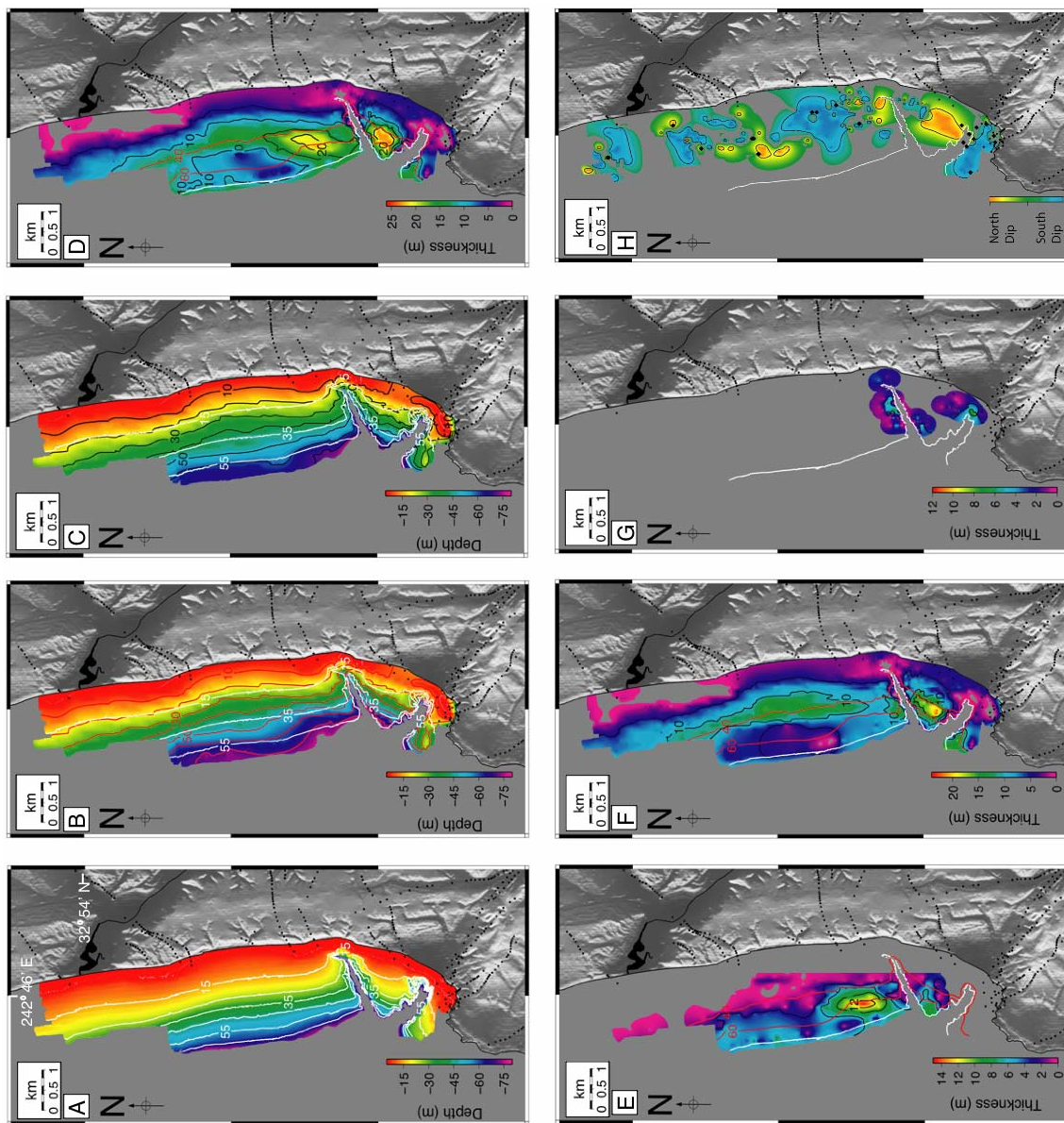


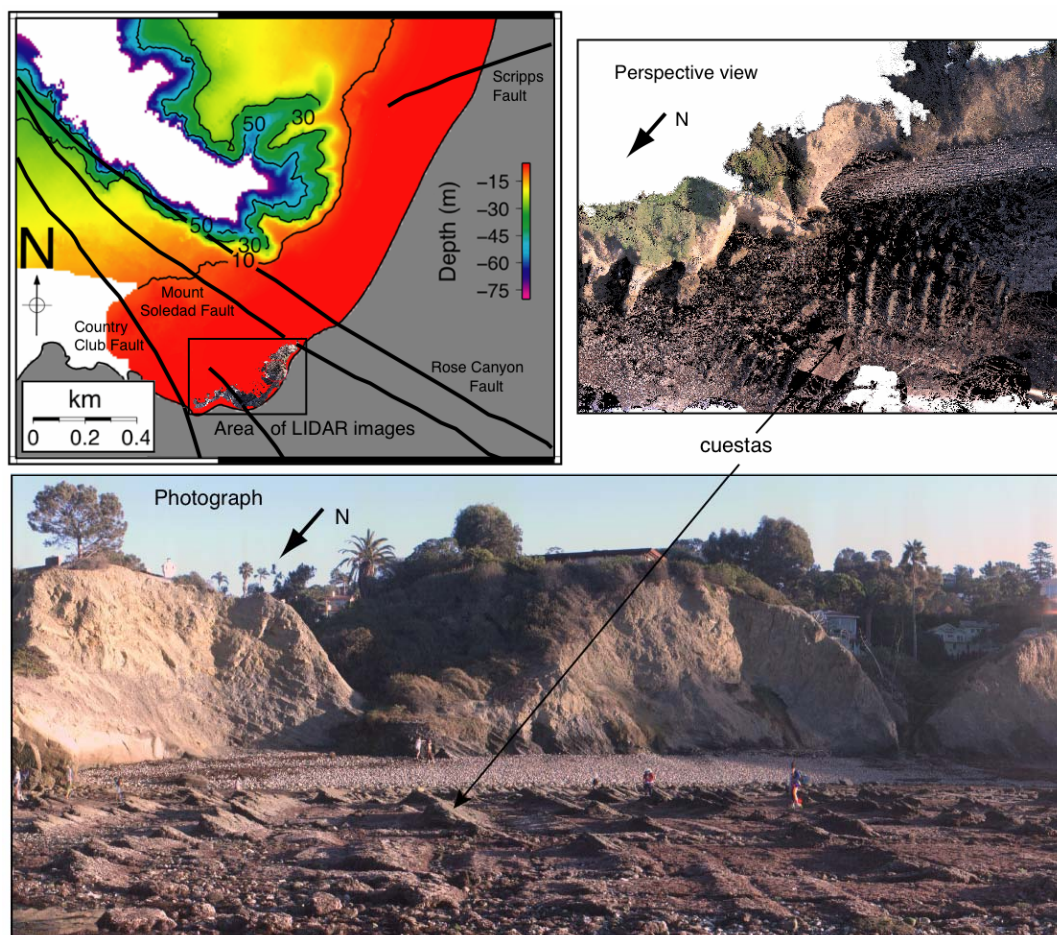


**Figure 4-6: Chirp profiles. A. Strike line 8 uninterpreted (top) and interpreted (bottom) shows estuarine, healing-phase, and Holocene sand units. Note that the Scripps Canyon is located within a high in the transgressive surface. B. Dip line 3 uninterpreted (top) and interpreted (bottom) shows healing-phase and upper Holocene sand units. The terraces formed during relative sea level still stands are more prominent at greater depths. (M=Multiple, TS=Transgressive surface). Color code is as follows: red = estuarine unit, green = healing-phase unit, and blue = upper Holocene sand unit. See Figure 4-2 for line locations**

**Figure 4-7: A. Bathymetry. B. Depth to the transgressive surface. C. Depth to the top of the healing-phase. D. Healing-phase and Holocene sand units cumulative isopach map. E. Healing-phase isopach map. F. Holocene sands isopach map. G. Estuarine sediments isopach map. H. Local bedding dips showing reversal with faults identified on seismic profiles. Note that the healing-phase wedge makes up most of the northern Holocene depocenter, whereas the upper Holocene sand unit constitutes most of the inter-canyon Holocene depocenter. All maps have superimposed bathymetric contours in white, reduced to the 65 m isobath in maps D to H. Maps D to F have superimposed contours of the transgressive surface structure in red**



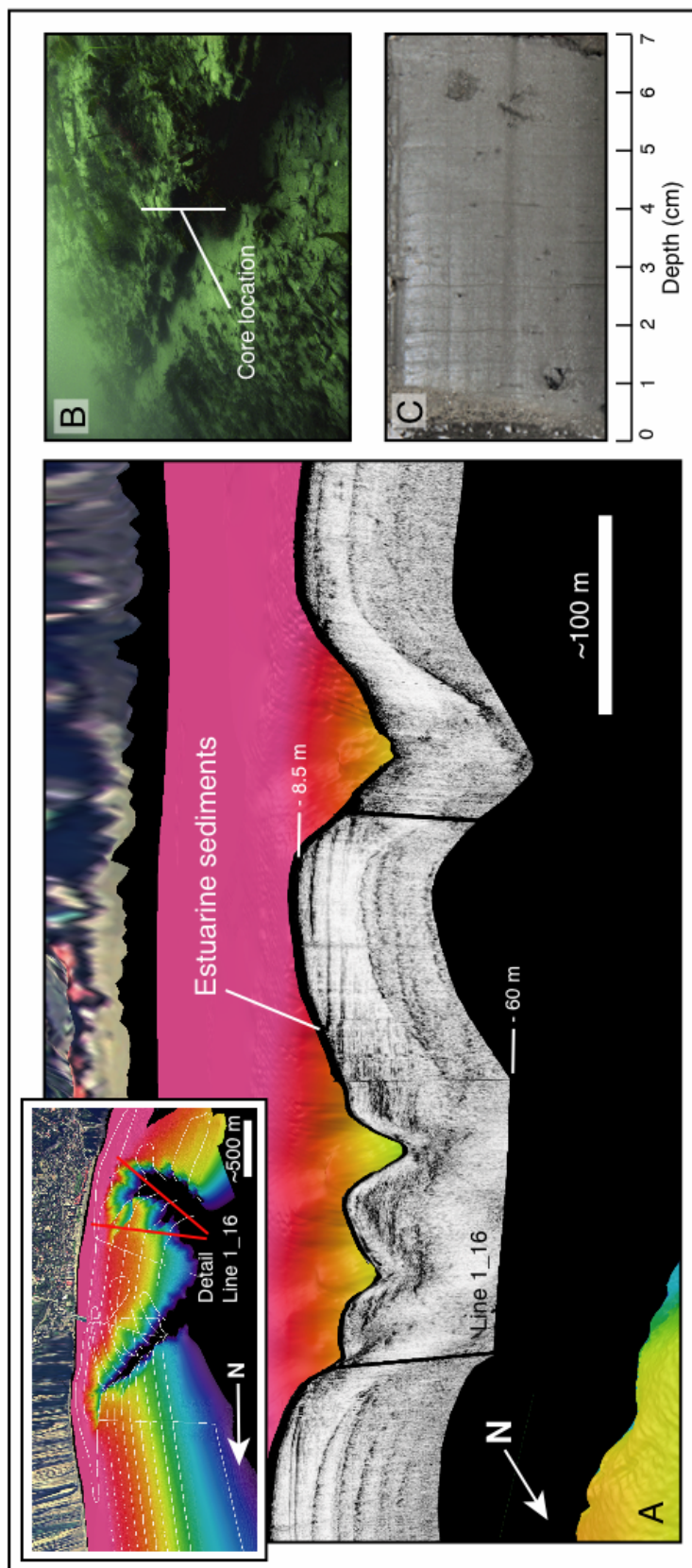




**Figure 4-8: Bathymetry with superimposed faults. Perspective view and photograph of the sea cliffs between La Jolla Shores and La Jolla Cove looking southeast and showing cuestas in the intertidal reefs as well as details of dipping beds**



**Figure 4-9: A. Perspective view that shows estuarine sediments outcropping at the seafloor. Bathymetry and seismic profile have vertical exaggeration of 6:1 while land topography has none. Inset shows line location and figure orientation. B. Dive picture showing estuarine sediments at seafloor along slope of canyon ridge. Push core collected was from the same lithographic unit. C. Push core of estuarine sediments. See Figure 4-2 for core location**



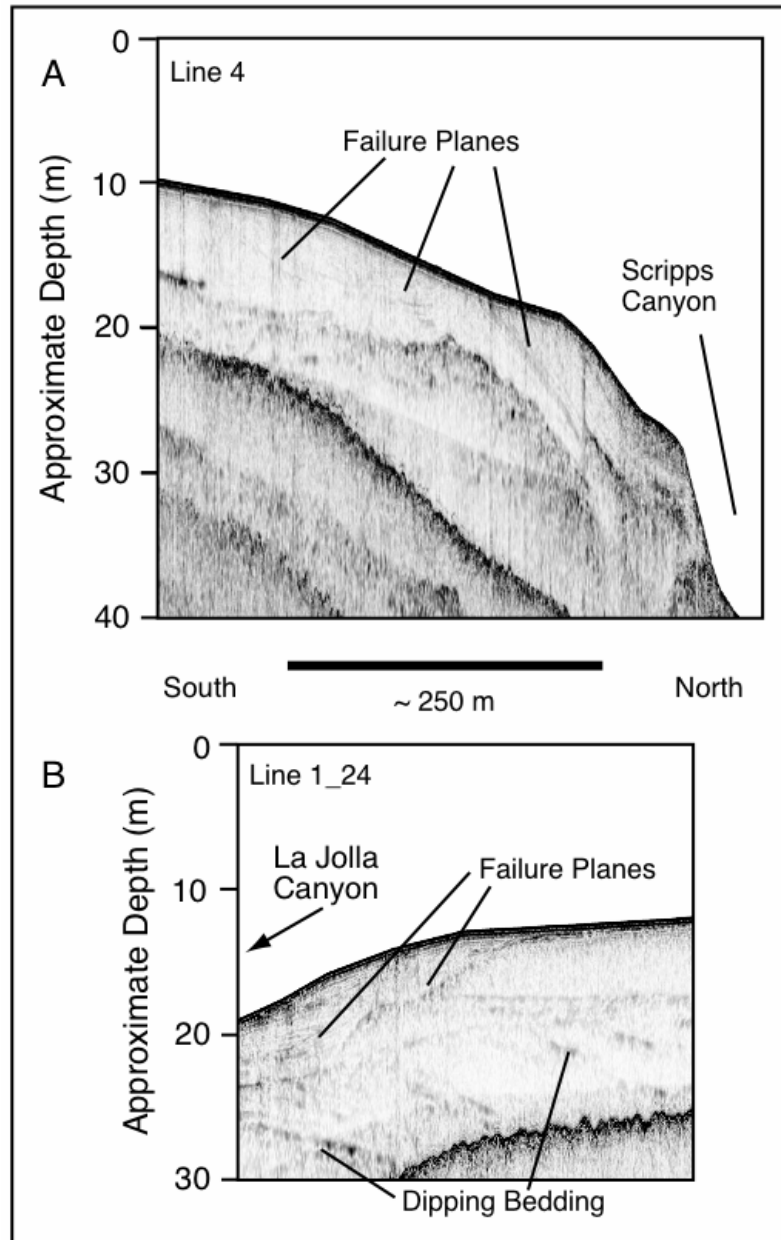
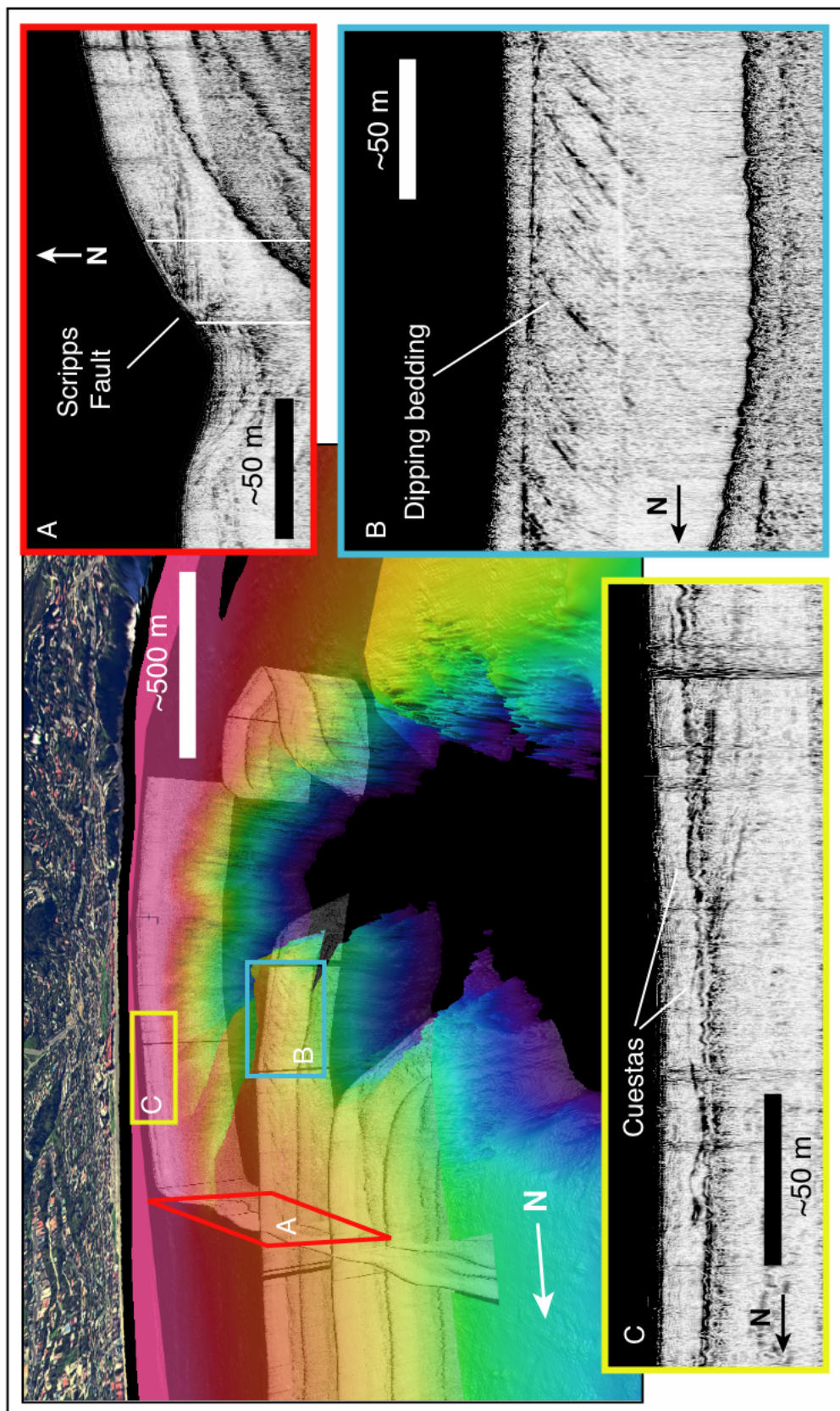


**Figure 4-10: A. Line 4 shows failure planes near the Scripps Canyon seen as faint, dipping reflectors within the transparent Holocene sand unit. The concave character of some of these reflectors is similar to the concave up features on the seafloor corresponding to secondary canyons in Figure 4-6A. B. Line 1\_24 shows failure planes and convex reflector observed near the La Jolla Canyon**

**Figure 4-11: Perspective view of the head of the La Jolla Canyon looking southeast, with insets of selected seismic profiles, illustrating bedrock deformation in the RCFZ. A. Possible expression of the Scripps Fault. B. Submarine cuestas. C. Dipping bedding. Submetrix bathymetry and inset CHIRP seismic profiles have a vertical exaggeration of 4:1 while land topography has none**



## References

- Altunel, E., Hancock, P.L., 1993. Morphology and structural setting of Quaternary travertines at Pamukkale, Turkey. *Geological Journal*, 28 (3-4), 335-346.
- Apotsos, A., Raubenheimer B., Elgar S., Guza, R.T., 2008. Wave-driven setup and alongshore flows observed onshore of a submarine canyon. *Journal of Geophysical Research*, 113, C07025.
- Baztan, J., Berné, S., Olivet, J.-L., Rabineau, M., Aslanian, D., Gaudin, M., Réhault, J.-P., Canals, M., 2005. Axial incision: the key to understand submarine canyon evolution (in the western Gulf of Lion). *Marine and Petroleum Geology*, 22, 805–826.
- Belknap, D.F., Kraft, J.C., 1985. Influence of antecedent geology on stratigraphic preservation potential and evolution of Delaware's barrier systems. *Marine Geology*, 63, 235-262.
- Brueggeman P., 2008. La Jolla Canyon and Scripps Canyon bibliography. Scripps Institution of Oceanography Library, Bibliography, Paper 12, <http://repositories.cdlib.org/sio/lib/bibliography/12>.
- Buckingham, M.J., Richardson, M.D., 2002. On tone-burst measurements of sound speed and attenuation in sandy marine sediments. *IEEE Journal of Oceanic Engineering*, 27 (3), 429-453.
- Buffington, E.C., 1964. Structural control and precision bathymetry of La Jolla submarine canyon, California. *Marine Geology*, 11, 44-58.
- Byrd, R.E., Berry, R.W., Fischer, P.J., 1975. Quaternary geology of the San Diego - La Jolla underwater park. IN: *Studies of the geology of Camp Pendelton and Western San Diego County, CA*. San Diego Association of Geologists, 77-79.
- Catuneanu, O., 2006. *Principles of Sequence Stratigraphy*. Amsterdam, Elsevier, 375 p.
- Cattaneo, A., Steel, R.J., 2003. Transgressive deposits: a review of their variability. *Earth-Science Reviews*, 62 (3-4), 187.
- Chamberlain, T.K., 1964. Mass transport of sediment in the heads of Scripps submarine canyon, California. IN: *Papers in Marine Geology, Shepard Commemorative Volume*. R.L. Miller, New York, Macmillan Company, 42-64.
- Christie-Blick, N., Driscoll, N.W., 1995. Sequence stratigraphy. *Annual Review of Earth and Planetary Sciences*, 23, 451-478.

- Cirac, P., Bourillet, J.F., Gribouard, R., Normand, A., Mulder, T., 2001. Le canyon de Capbreton: nouvelles approches morphostructurales et morphosédimentaires, premiers résultats de la campagne Itsas. *Earth and Planetary Sciences*, 332, 447-455.
- Cohen, J.K., Stockwell, Jr. J.W., 2002. CWP/SU: Seismic Unix release 36, a free package for seismic research and processing. Center for Wave Phenomena, Colorado School of Mines, Golden, Colorado, [www.cwp.mines.edu/cwpcodes](http://www.cwp.mines.edu/cwpcodes).
- Covault, J.A., Normark, W.R., Romans, B.W., Graham, S.A., 2007. Highstand fans in the California borderland: the overlooked deep-water depositional systems. *Geology*, 35, 783-786.
- Darigo, N.J., Osbourne, R.H., 1986. Quaternary stratigraphy and sedimentation of the inner continental shelf, San Diego County, California. IN: Knight, R.J., McLean, J.R., eds., *Shelf sands and sandstones*. Canadian Society of Petroleum Geologists Memoir II, 73-98.
- Dartnell, P., Normark, W.R., Driscoll, N.W., Babcock, Gardner, J.M., Kvitek, J.V., Rikk, G., Iampietro, P.J., 2007. Multibeam bathymetry and selected perspective views offshore San Diego, California. U.S. Geological Survey Scientific Investigations Map 2959, 2 sheets, version 1.0, June 14, 2007, <http://pubs.usgs.gov/sim/2007/2959/>.
- Davis, G.H., Reynolds, S.J. 1996. *Structural Geology of Rocks and Regions*. New York, Wiley and Sons, 776 p.
- Dayton, P.K., Seymour, R.J., Parnell, P.E., Tegner, M.J., 1989. Unusual marine erosion in San Diego County from a single storm. *Estuarine, Coastal and Shelf Science*, 29 (2), 151-160.
- Dill, R.F., 1964. Sedimentation and erosion in Scripps submarine canyon head. IN: *Papers in Marine Geology, Shepard Commemorative Volume*. R.L. Miller, New York, Macmillan Company, 23-41.
- Dill, R.F., 1969. Earthquake effects on fill of Scripps submarine canyon. *Geological Society of America Bulletin*, 80, 321-328.
- Driscoll, N.W., Uchupi E., 1997. The importance of water motion and gas/fluid expulsion in landscape and seascape evolution: application to continental margin evolution. *Thalassas*, research article, invited manuscript, 13, 32-46.
- Emery, K.O., 1958. Shallow submerged marine terraces of Southern California. *Geological Society of America Bulletin*, 69 (1), 39-60.



Everts, C.H., Dill, R.F., 1988. Sedimentation in submarine canyons, San Diego County, California, 1984-1987. US Army Corps of Engineers, Coastal Engineering Research Center, Waterways Experiment Station, Reference No. CSTWS 88-2.

Fairbanks, R.G., 1989. A 17,000-year glacio-eustatic sea level record: influence of glacial melting rates on the Younger Dryas event and deep-ocean circulation. *Nature*, 342, 637-642.

Farre, J.A., McGregor, B.A., Ryan, W.B.F., Robb, J.M., 1983. Breaching the shelf break: passage from youthful to mature phase in canyon evolution. IN: *The shelfbreak: critical interface on continental margins*. Society of Economic Paleontologists and Mineralogists (SEPM) Special Publication No. 33, edited by Stanley, D.J., and Moore, G.T., Tulsa, Oklahoma, 25-40.

Gardner, J.B., Dartnell, P., Stone, C.J., Mayer, L.A., Hughes Clarke, J.E., 2002. Bathymetry and selected perspective views offshore greater Los Angeles, California. USGS - Water Resource Investigations Report 02-4126, 1 map sheet, <http://walrus.wr.usgs.gov/pacmaps/pubs.html>.

Gulick, S.P.S., Meltzer, A.S., 2002. Effect of the northward-migrating Mendocino triple junction on the Eel River forearc basin, California: structural evolution. *Geological Society of America Bulletin*, 114 (12), 1505-1519.

Harris, C.K., Wiberg, P.L., 2001. A two-dimensional, time-dependent model of suspended sediment transport and bed reworking for continental shelves. *Computers & Geosciences*, 27 (6), 675-690.

Harris, M.S., Gayes, P.T., Kindinger, J.L., Flocks, J.G., Krantz, D.E., Donovan, P., 2005. Quaternary geomorphology and modern coastal development in response to an inherent geologic framework: an example from Charleston, South Carolina. *Journal of Coastal Research*, 21 (1), 49-64.

Hass, J.K., 2005. Grain size and mineralogical characteristics of beach sand in the Oceanside Littoral Cell, Southern California: implications for sediment provenance. Thesis (M. S.)-University of California, San Diego.

Henkart, P., 2003. SIOSEIS software. Scripps Institution of Oceanography, La Jolla, California, <http://sioseis.ucsd.edu>.

Henry, M.J., 1976. The unconsolidated sediment distribution on the San Diego County mainland shelf, California. Masters thesis, San Diego State University.

Hogarth, L.J., Babcock, J., Driscoll, N.W., Le Dantec, N., Hass, J.K., Inman, D.L., Masters, P.M., 2007. Long-term tectonic control on Holocene shelf sedimentation offshore La Jolla, California. *Geology*, 35 (3), 275-278.



Holden, J.C., 1968. Brackish water ostracods from La Jolla submarine canyon 7200 (plus/minus) 500 years before present. *Paleobios*, No. 5, University of California, Berkeley, Museum of Paleontology.

Honeycutt, M.C., Krantz, D.E., 2003. Influence of the geologic framework on spatial variability in long-term shoreline change, Cape Henlopen to Rehoboth Beach, Delaware. *Journal of Coastal Research*, Special Issue No. 38, 147-167.

Hsieh, T.J., Olsen, M.J., Johnstone, E.A., Young, A.P., Driscoll, N.W., Ashford, S.A., Kuester, F., 2007. VR-based visual analytics of LIDAR data for cliff erosion assessment. *VRST '07, Proceedings of the 2007 ACM symposium on Virtual reality software and technology*, 249 – 250.

Inman, D.L., 1952. Areal and seasonal variations in beach and nearshore sediments at La Jolla, California. Ph. D. Thesis, University of California, Los Angeles.

Inman, D.L., 1953. Areal and seasonal variations in beach and nearshore sediments at La Jolla, California. US Dept of the Army, Corps of Engineers, Office of the Chief of Engineers, Beach Erosion Board, Technical Memorandum No. 39.

Inman, D. L., Chamberlain, T. K., 1960. Littoral sand budget along the southern California coast. Volume of Abstracts, Report of the 21st International Geological Congress, Copenhagen, Denmark, 245-246.

Inman, D.L., Frautschy, J.D., 1965. Littoral processes and the development of shorelines. IN: *Coastal Engineering*, Santa Barbara Specialty Conference, ASCE, New York, 511-536.

Inman, D.L., Nordstrom, C.E., Flick, R.E., 1976. Currents in submarine canyons; an air-sea-land interaction. *Annual Review of Fluid Mechanics*, 8, 275-310.

Inman, D.L., Masters, P.M., 1991a. Coastal sediment transport concepts and mechanisms. IN: *Coast of California Storm and Tidal Waves Study*, State of the Coast Report, Los Angeles, U.S. Army Corps of Engineers.

Inman, D. L., Masters, P. M., 1991b. Budget of sediment and prediction of the future state of the coast. IN: *State of the Coast Report*, San Diego Region, Coast of California Storm and Tidal Waves Study, U. S. Army Corps of Engineers, 5, 43.

Inman, D.L., Jenkins, S.A., 1999. Climate change and the episodicity of sediment flux in small California Rivers. *The Journal of Geology*, 107, 251-270.

Jackson, D.R., Briggs, K.B., Williams, K.L., Richardson, M.D., 1996. Tests of models for high-frequency seafloor backscatter. *IEEE Journal of Oceanic Engineering*, 21 (4), 458 – 470.

- Judy, T.C., 1987. Reconnaissance geology of the Holocene lagoonal deposits in the La Jolla submarine canyon and their relationship to the Rose Canyon Fault. Undergraduate Research Report, San Diego State University.
- Kennedy, M.P., 1975. Western San Diego metropolitan area: Del Mar, La Jolla, and Point Loma, 7 1/2 minute quadrangles. Bulletin, California, Division of Mines and Geology, Volume 200, 9–39.
- Legg, M.R., Kennedy, M.P., 1979. Faulting offshore San Diego and Northern Baja, California. IN: Abbott, P.L., Elliott, W.J., eds., Earthquakes and other perils, San Diego region, San Diego, California, United States. San Diego Association of Geologists, 29–46.
- Lindvall, S.C., Rockwell, T.K., 1995. Holocene activity of the Rose Canyon Fault zone in San Diego, California. Journal of Geophysical Research, B, Solid Earth and Planets, 100, 24121–24132.
- Lomar, J.M., May, J.A., Boyer, J.E., Warme, J.E., 1979. Shelf edge deposits of the San Diego embayment. IN: Shelf-edge depositional systems, San Diego, California, P.L. Abbot.
- Luis, J.F., 2007. Mirone: a multi-purpose tool for exploring grid data. Computers & Geosciences, 33, 31-41.
- Magne, R., Belibassakis, K.A., Herbers, T.H.C., Ardhuin, F., O'Reilly, W.C., Rey, V., 2007. Evolution of surface gravity waves over a submarine canyon. Journal of Geophysical Research - Oceans, 112 (C1), C01002.
- Marshall, N.F., 1978. Large storm-induced sediment slump reopens an unknown Scripps submarine canyon tributary. IN: Sedimentation in submarine canyons, fans, and trenches. Stanley, D.J., Gilbert, K., Stroudsburg, Pa, Dowden, Hutchinson and Ross, 73-84.
- Mastbergen, D.R., van den Berg, J.H., 2003. Breaching in fine sands and the generation of sustained turbidity currents in submarine canyons. Sedimentology, 50 (4), 625-637.
- McNinch, J.E., 2004. Geologic control in the nearshore: shore-oblique sandbars and shoreline erosional hotspots, Mid-Atlantic Bight, USA. Marine Geology, 221, 121-141.
- Moore, G.W., 1972. Offshore extent of the Rose Canyon Fault, San Diego, California. U.S. Geological Survey Professional Paper P 0800-D, 113-116.
- Moriarty, J.R., 1964. The use of oceanography in the solution of problems in a submarine archaeological site. IN: Papers in Marine Geology. R.L. Miller, New York, Macmillan, 511-522.

- Munk, W.H., Traylor, M.A., 1947. Refraction of ocean waves: a process linking underwater topography to beach erosion. *Journal of Geology*, 55 (1), 1-26.
- Nielsen, P., 1992. Coastal bottom boundary layers and sediment transport. World Scientific, Advanced Series on Ocean Engineering, Volume 4.
- Peters, G., van Balen, R.T., 2007. Tectonic geomorphology of the northern Upper Rhine Graben, Germany. *Global and Planetary Change*, 58, 310-334.
- Posamentier, H.W., Allen, G.P., 1999. Siliciclastic sequence stratigraphy: concepts and applications. *SEPM, Concepts in Sedimentology and Paleontology*, Volume 7, 210 p.
- Pratson, L.F., Ryan, W.B.F., Mountain, G.S., Twichell, D.C., 1994. Submarine canyon initiation by downslope-eroding sediment flows: evidence in late Cenozoic strata on the New Jersey continental slope. *Geological Society of America Bulletin*, 106, 395-412.
- Pratson, L.F., Coakley, B.J., 1996. A model for the headward erosion of submarine canyons induced by downslope-eroding sediment flows. *Geological Society of America Bulletin*, 108 (2), 225-234.
- Pratson L.F., Haxby W.F., 1996. What is the slope of the U.S. continental slope? *Geology*, 24, 3-6.
- Pratson, L.F., 2001. A perspective on what is known about seafloor instability in the context of continental margin evolution. *Marine and Petroleum Geology*, 18 (4), 499-501.
- Rindell, A.K., 1991. An investigation of Scripps submarine canyon: its geology, sedimentary regime, and bubbling gases. Masters Thesis, San Diego State University.
- Rogers, J.N., Kelley, J.T., Belknap, D.F., Gontz, A., Barnhardt, W.A., 2006. Shallow-water pockmark formation in temperate estuaries: a consideration of origins in the western gulf of Maine with special focus on Belfast Bay. *Marine Geology*, 225 (1-4), 45-62.
- Schwab, W.C., Thieler, E.R., Allen, J.R., Foster, D.S., Swift, B.A., Denny, J.F., 2000. Influence of inner-continental shelf geologic framework on the evolution and behavior of the barrier-island system between Fire Island Inlet and Shinnecock Inlet, Long Island, New York. *Journal of Coastal Research*, 16 (2), 408-422.
- Shepard, F.P., Emery, K.O., 1941. Submarine topography off the California coast: canyons and tectonic interpretation. Baltimore MD, Waverly Press.

Shepard, F.P., Inman, D.L., 1950. Nearshore water circulation related to bottom topography and wave refraction. *Transactions of the American Geophysical Union*, 31 (2), 196-212.

Shepard, F.P., Inman D.L., 1951. Sand movement on the shallow inter-canyon shelf at La Jolla, California. US Dept of the Army, Corps of Engineers, Office of the Chief of Engineers, Beach Erosion Board, Technical Memorandum No. 26.

Shepard, F.P., Dill, R.F., 1966. Submarine canyons and other sea valleys. Chicago, Rand McNally.

Shepard, F.P., 1972. Submarine canyons. *Earth-Science Reviews*, 8, 1-12.

Shepard, F.P., McLoughlin, P.A., Marshall, N.F., Sullivan, G.G., 1977. Current-meter recordings of low-speed turbidity currents. *Geology*, 5 (5), 297-301.

Shepard, F.P. 1981. Submarine canyons: multiple causes and long-time persistence. *American Association of Petroleum Geologists Bulletin* 65 (6), 1062-1077.

Smith, J.A., Largier, J.L., 1995. Observations of nearshore circulation - rip currents. *Journal of Geophysical Research - Oceans*, 100 (6), 10967-10975.

Smith, W. H. F., P. Wessel, 1990. Gridding with continuous curvature splines in tension. *Geophysics*, 55 (3), 293-305.

Sommerfield, C.K., Nittrouer, C.A., 1999. Modern accumulation rates and a sediment budget for the Eel shelf: a flood-dominated depositional environment. *Marine Geology*, 154 (1-4), 227-241.

Sommerfield, C.K., Lee, H.J., 2003. Magnitude and variability of Holocene sediment accumulation in Santa Monica Bay, California. *Marine Environmental Research*, 56, 151-176.

Sommerfield, C.K., Lee, H.J., 2004. Across-shelf sediment transport since the Last Glacial Maximum, southern California margin. *Geology*, 32 (4), 345-348.

Sommerfield C.K., Wheatcroft, R.A., 2007. Late Holocene sediment accumulation on the northern California shelf: oceanic, fluvial, and anthropogenic influences. *Geological Society of America Bulletin*, 119 (9-10), 1120-1134.

Stow, D.A., Chang, H.H., 1987. Coarse sediment delivery by coastal streams to the Oceanside Littoral Cell, California. *Shore & Beach*, 55 (1), 30-40.

Thieler, E.R., Pilkey, O.H.J., Cleary, W.J., Schwab, W.C., 2001. Modern sedimentation

of the shoreface and inner continental shelf at Wrightsville beach, North Carolina, USA. *Journal of Sedimentary Research*, 71 (6), 958-970.

Thomson, J., Elgar, S., Herbers, T.H.C., 2005. Reflection and tunneling of ocean waves observed at a submarine canyon. *Geophysical Research Letters*, 32 (10), L10602.

Thomson, J., Elgar, S., Herbers, T.H.C., Raubenheimer, B., Guza R.T., 2007. Refraction and reflection of infragravity waves near submarine canyons. *Journal of Geophysical Research*, 112, C10009.

Treiman, J.A., 1993. The Rose Canyon Fault Zone, southern California. California Division of Mines and Geology, Open File Report 93-02, 45 p.

Vetter, E.W., 1994. Hotspots of benthic production. *Nature*, 372, 47.

Waggoner, J.A., 1979. Unconsolidated shelf sediments in the area of Scripps and La Jolla submarine canyons. Masters of Science in Geology, San Diego State University.

Warrick, J., Rubin D., 2007. Suspended-sediment rating curve response to urbanization and wildfire, Santa Ana River, California. *Journal of Geophysical Research*, Volume 112 (f2), F02018.

Webb, D.A., 1988. A structural interpretation of Scripps submarine canyon. *Advances in Underwater Science, Proceedings of the American Academy of Underwater Sciences*, 8th Annual Scientific Diving Symposium, La Jolla, CA, American Academy of Underwater Sciences, 213-220.

Wessel, P., W. H. F. Smith, 1998. New, improved version of Generic Mapping Tools released. *EOS Transactions of the American Geophysical Union*, 79 (47), 579.

Williams K.L, Jackson D.R., Thorsos E.I., Tang D., Schock S.G., 2002. Comparison of sound speed and attenuation measured in a sandy sediment to predictions based on the Biot theory of porous media. *IEEE Journal of Oceanic Engineering*, 27 (3), 413.

Wolinsky, M.A., Pratson, L.F., 2007. Overpressure and slope stability in prograding clinoforms: implications for marine morphodynamics. *Journal of Geophysical Research*, 112, F04011.

Young, A.P., Ashford, S.A., 2006. Application of airborne LIDAR for seacliff volumetric change and beach-sediment budget contributions. *Journal of Coastal Research*, 22 (2), 307-318.

Zhang, Y., Swift, D., Fan, S., Nedoroda A., Reed, C., 1999. Two-dimensional numerical modeling of storm deposition on the northern California shelf. *Marine Geology*, 154 (1-4), 155-167.

Chapter 4 was submitted for publication in Marine Geology, 2009 as: Le Dantec Nicolas; Hogarth Leah J.; Driscoll, Neal W.; Babcock Jeff. “Tectonic controls on nearshore sediment accumulation and submarine canyon morphology offshore La Jolla, Southern California”. The dissertation author was the primary investigator and author of this paper.

**APPENDIX: LONG-TERM TECTONIC CONTROL ON HOLOCENE SHELF  
SEDIMENTATION OFFSHORE LA JOLLA, CALIFORNIA**

# Long-term tectonic control on Holocene shelf sedimentation offshore La Jolla, California

Leah J. Hogarth\*  
 Jeffrey Babcock  
 Neal W. Driscoll  
 Nicolas Le Dantec  
 Jennifer K. Haas  
 Douglas L. Inman  
 Patricia M. Masters

Scripps Institution of Oceanography, University of California–San Diego, La Jolla, California 92093, USA

## ABSTRACT

A high-resolution Compressed High-Intensity Radar Pulse (CHIRP) survey reveals shore-parallel variations in the Holocene sediment thickness offshore La Jolla, California. Sediment thicknesses decrease from >20 m in the south near Scripps Canyon to zero in the north approaching Torrey Pines. In addition to the south-to-north variation in sediment thickness, the transgressive surface observed in seismic lines shoals from Scripps Canyon to the north. Despite these dramatic shore-parallel subsurface changes, the nearshore bathymetry exhibits little to no change along strike. A left jog (i.e., a constraining bend) along the Rose Canyon fault causes local uplift in the region and appears to explain the northward shoaling of the transgressive surface, the decrease in relief on the transgressive surface away from the left jog, and the Holocene sediment thickness variation. This tectonic deformation is shore parallel, and thus the accommodation can be separated into its tectonic and eustatic components.

**Keywords:** tectonic deformation, accommodation, transgressive surface, transpression.

## INTRODUCTION

Many investigators have recognized the important role of tectonics in the preservation of sediments on active margin shelves (e.g., Orange, 1999; Driscoll and Hogg, 1995). In most locations, tectonic uplift or subsidence offsets the coastline vertically and causes base-level changes that are difficult to distinguish from sea-level changes; a common manifestation of tectonic uplift is subaerial terraces parallel to the coastline. Eustatic sea level has risen ~125 m in the past 20 k.y. (e.g., Fairbanks, 1989). Consequently, in seismic images and in outcrop, it is often difficult to separate sea-level changes from tectonic changes acting in the same plane during this time period. In the San Diego, California, area, regional uplift and sea-level change have created terraces (e.g., Bay Point Formation), but due to the geometry of the Rose Canyon fault zone, much tectonic deformation occurs shore parallel or orthogonal to eustatic sea-level changes and regional tectonic uplift (Kennedy, 1975). Thus, we can use the stratigraphic variability parallel to shore to discern the tectonic signal associated with the Rose Canyon fault from glacial-eustatic fluctuations or regional tectonic uplift. Furthermore, this will aid us in understanding how tectonic processes govern the preservation of sediments on the shelf. Such

an understanding will allow us to define sand resources offshore as well as the distribution of hardgrounds on the seafloor, which may play an important role in biohabitats.

The San Diego area is west of the San Andreas fault zone and is characterized by a series of subparallel, en echelon faults including, from east to west, the San Jacinto, Elsinore, and Newport–Inglewood–Rose Canyon fault zones. In the La Jolla region, the Rose Canyon fault zone is a dextral strike-slip fault zone with complex surface expression (Treiman, 1993). The fault zone passes through La Jolla, forming Mount Soledad, a pop-up structure with a maximum uplift of ~150 m (Fig. 1); pop-up structures are areas of local uplift due to transpression or compression created when lateral motion on a strike-slip fault is interrupted by a bend or a jog in that fault. In the case of Mount Soledad, a left-stepping jog on the right-lateral Rose Canyon fault creates compression and uplift (Kennedy, 1975; Kennedy et al., 1979). Seismic surveys reveal that the Rose Canyon fault zone extends northwest 60 km offshore (Moore, 1972). Evidence of Holocene activity on the Rose Canyon fault zone comes from both offshore seismic data (Moore, 1972) and onshore trenches (Lindvall and Rockwell, 1995). Lindvall and Rockwell (1995) estimated that the total horizontal component of slip ranges from 1 to 2 mm/yr during the Holocene. In addition to the Rose Canyon

fault system, Kennedy (1975) identified several other inactive northeast-southwest-trending oblique faults with vertical offset of ~10 m in the cliffs of Torrey Pines Beach (Fig. 1).

Our objective is to image the transgressive surface, overlying sands, and fault structures to better understand the processes influencing sediment accumulation and preservation on the shelf near La Jolla. Here we describe the observed morphology of the transgressive surface. We propose that our observation of a pop-up structure offshore, created by a constraining bend along the right-lateral Rose Canyon fault zone, controls the long-term accumulation of sediment in this region of the nearshore.

## METHODS

In 2002, ~300 km of Compressed High-Intensity Radar Pulse (CHIRP) seismic data were acquired offshore from La Jolla Cove north to Del Mar (Fig. 1). We used a CHIRP sonar (Edgetech) with a swept frequency of 1–5.5 kHz yielding submeter vertical resolution. During the nearshore survey, the CHIRP seismic system was mounted on a surface tow frame with an attached global positioning system receiver, thus minimizing navigation error. We generated an isopach map by tracing the transgressive surface and differencing it from the seafloor throughout the seismic grid. A nominal velocity of 1500 m/s was used to convert travel-

\*E-mail: lhogarth@ucsd.edu.

time to sediment thickness. Bathymetric data were acquired, processed, archived, and distributed by the Seafloor Mapping Lab of California State University Monterey Bay (<http://seafloor.csUMB.edu/SFMLwebDATA.htm>).

## RESULTS

Layers in the units below the transgressive surface generally exhibit distinct dips to the south (Fig. 2) that are consistent with the local dips of the Ardat Shale, Torrey Sandstone, and Del Mar Formation on land (Kennedy, 1975). The transgressive surface is identified in the profiles by marked truncation (Figs. 2 and 3), which was formed by wave-base erosion during the sea-level rise, and is mantled by a basal unit and an overlying acoustically transparent layer. This part of the shelf has been subaerially exposed during many sea-level lowstands during the Pleistocene; the erosion and truncation on this surface probably reflect multiple sea-level cycles, not just the last sea-level rise. The poorly laminated basal unit is only observed in the mid- to outer-shelf region and appears to record the early transgression in the region. The overlying transparent unit might reflect the early stage of the highstand systems tract, which exhibits cross-shelf thinning with a maximum depocenter in the mid-shelf. The acoustically transparent character, however, precludes identification of a downlap surface, and thus our ability to confidently discern whether this package is part of the late transgressive systems tract or the early highstand systems tract.

Seismic images from our survey show that the transgressive surface exhibits an overall southward dip, and the overlying sediment thickness decreases along strike to the north of Scripps Canyon (Figs. 2 and 4). A local reversal of dip also exhibits a change in acoustic reflectivity that might imply a more resistive hardground and may be fault controlled (Fig. 2A). It is difficult, however, to trace the fault laterally shoreward from line S10 to adjacent lines because of the limited acoustic penetration beneath the transgressive surface (Fig. 2A). The dip lines show that the maximum sediment thickness above the transgressive surface is located on the mid-shelf and systematically diminishes both landward and seaward (Fig. 3). The extent of the isopach map is limited by data density; it captures the edge of the mid-shelf depocenter and delineates the south-to-north thinning.

The isopach map of sediment thickness shows a depocenter between the La Jolla and Scripps canyons, as well as to the north of Scripps Canyon (Fig. 4). Sediment thickness systematically decreases along strike to the north from ~20 m just north of Scripps Canyon to zero offshore Torrey Pines (Figs. 2 and 4). Perpendicular to shore, sediment thickness ranges from ~0–5 m nearshore to maximum thicknesses of 10–20 m

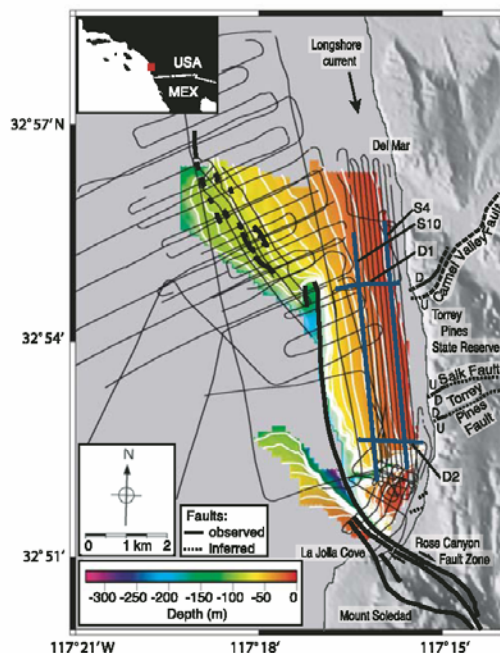


Figure 1. Survey ship track (black lines) superimposed on 2 m gridded bathymetry (data used in this study were acquired, processed, archived, and distributed by Seafloor Mapping Lab of California State University Monterey Bay: <http://seafloor.csUMB.edu/SFMLwebDATA.htm>). White lines on bathymetry are contours (10 m intervals) to 100 m. Faults are shown in bold black: dashed for inferred location, D and U for downthrown and upthrown side, and right-lateral sense of strike-slip motion is shown with arrows. Left-stepping bond in Rose Canyon fault zone creates uplift of Mount Soledad. S4, S10, D1, and D2 (bold blue lines) indicate locations of strike lines shown in Figure 2 and dip lines shown in Figure 3. Local faults shown are based on Kennedy (1975).

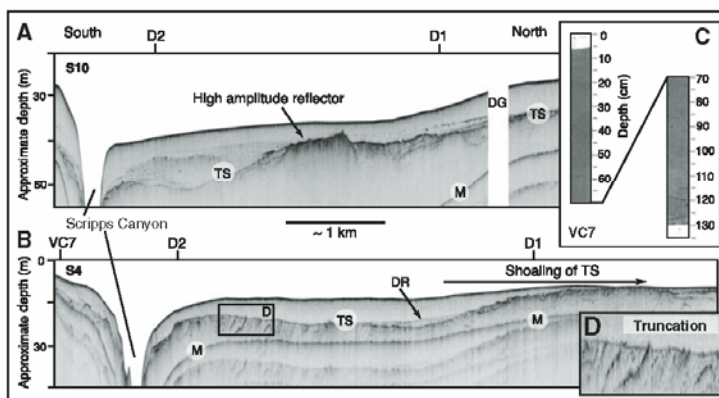


Figure 2. CHIRP along-shelf strike lines. A: Profile S10 from offshore shows shoaling of transgressive surface (TS) to north of Scripps Canyon. At this depth, Holocene sediments mantle transgressive surface. B: Nearshore profile S4 shows truncation of underlying layers as consequence of wavebase erosion, which is interpreted to occur during sea-level transgression. TS is exposed at seafloor to north. Vibracore VC7 is projected onto line S4 south of Scripps Canyon. D1 and D2 are locations of crossing dip lines. See Figure 1 for locations (M—multiple, DG—data gap, DR—dipping reflector). C: Inset shows Vibracore VC7, which recovered fine-grained to very fine grained, olive-green, homogeneous sands. In upper 135 cm of Holocene sediment there is no evidence for event beds associated with storms or floods. See Figure 4 for core location. D: Inset shows detail of TS and associated truncation.



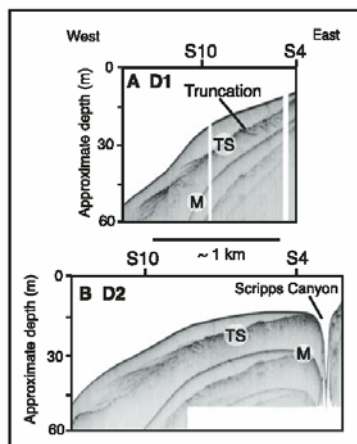


Figure 3. CHIRP cross-shelf dip lines. A: Profile D1 shows truncation along interpreted transgressive surface. Basal reflective package is interpreted as part of early transgression, and thickness of overlying acoustically transparent unit is greatest in mid-shelf, thinning both landward and seaward. B: Profile D2, farther to south, also shows mid-shelf depocenter of acoustically transparent unit. S4 and S10 are locations of crossing strike lines. TS—transgressive surface; M—multiple. See Figure 1 for locations.

in the mid-shelf region before thinning again as water depth increases (Figs. 3 and 4).

The area where hardgrounds crop out to the north correlates with the deflection of bathymetric contours offshore at water depths >60 m (Fig. 4). Note that the nearshore contours do not exhibit this deflection, even though the slope of the isobath surface changes in this area from west dipping to southwest dipping.

A 135-cm-long Vibracore acquired in 2005 (Figs. 2 and 4) recovered fine-grained to very fine grained, olive-green, homogeneous sands consistent with the sediment recovered in longer Vibracores from the region (Darigo and Osbourne, 1986; Fig. 4). Mud horizons or coarse layers indicative of flood or storm events are not observed in this homogeneous upper layer. Beneath the sand is a slightly coarser unit that is not as well sorted, and includes larger clasts and more abundant shell fragments (units II and III of Darigo and Osbourne, 1986), which may be a transgressive lag deposit. The major fluvial input to this littoral cell is by the Santa Margarita and San Luis Rey rivers to the north, with predominant southern longshore transport (Inman and Jenkins, 1999). Wave reworking and longshore transport winnow out the fine-grained particles, resulting in a homogeneous nearshore deposit, consistent with the transparent acoustic character observed in the seismic data. Early Holo-

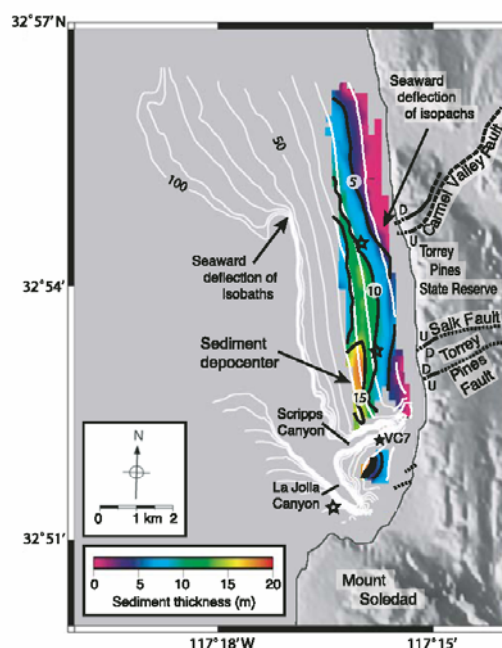


Figure 4. Holocene sediment thickness above transgressive surface (contour interval = 5 m) superimposed on bathymetric contours (contour interval = 10 m). Extent of isobath map is limited to mid-shelf and shoreward by data density shown in Figure 1. Isobaths show depocenter of Holocene sediments directly north of Scripps Canyon, where sediments are nearly 20 m thick. Along strike to the north, sediments thin to zero, whereas bathymetry does not change. Note spatial correlation between the step off-shore of isobaths >60 m and that of isobaths. Stars represent locations of Vibracores; solid for this study (2005) and unfilled for previous study (Darigo and Osbourne, 1986).

cene floods may have contributed coarser material, but fine-grained to very fine grained sand likely resulted from the past 5 k.y. of enhanced El Niño-driven wave energy and consequent southern sand transport (Masters, 2006).

## DISCUSSION

Several faulting trends in the La Jolla area could potentially explain the observed sea-floor structure and sediment distribution. For example, one possible scenario is that the relief on the transgressive surface is only controlled by steeply dipping northeast-southwest-trending normal faults, such as those observed onshore at the southern end of Torrey Pines State Reserve (e.g., Carmel Valley fault, Fig. 1). On the basis of terrace offsets, these faults are older than 120 ka (Treiman, 1993). If such a fault caused uplift of the more resistant Del Mar Formation to the north with respect to the less resistant Scripps Formation to the south, we would expect a jog of isobaths seaward as the more resistant Del Mar Formation formed a promontory. If this scenario were correct, it would not predict that the isobaths should return shoreward north of the fault (Fig. 5A), and the faults would cause a marked local thickness change across the fault from the downdropped to the upthrown block (e.g., Fig. 2A). The lateral extent of the depocenter exhibits a wavelength longer than that

of the onshore downdropped block bounded by the Salk and Torrey Pines faults (Figs. 1 and 4). Furthermore, the Carmel Valley fault onshore is down to the north; i.e., the sense of motion across the fault is opposite to that predicted by the observed sediment thickness. Alternatively, in a pop-up or constraining bend scenario, a left jog in a right-lateral fault zone would cause the thickness of the transgressive deposits to thin systematically from the depocenter toward the structural high without a sharp local thickness change (Fig. 5B). Such a constraining bend would predict that the isobaths shift seaward at the south end and return shoreward at the north end of the pop-up structure, which is consistent with the isobaths deeper than ~60 m (Fig. 4; see also the regional National Oceanic and Atmospheric Administration (NOAA) National Geophysical Data Center 3-arc-second coastal relief model [http://www.ngdc.noaa.gov/mgg/coastal/grddas06/grddas06.html]). A gentle, long-wavelength uplift of the transgressive surface is observed in the seismic images, consistent with a left jog along the Rose Canyon fault zone. The relief on the transgressive surface is largest in the west near the jog in the Rose Canyon fault (e.g., 26.5 m; Fig. 2A) and diminishes eastward away from the jog (e.g., 21.5 m; Fig. 2B), as would be predicted by the pop-up hypothesis (Fig. 5). Seismic data recently acquired (2005 R/V *New*

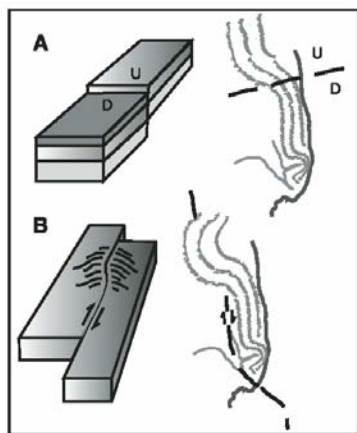


**Figure 5.** Two models of possible faulting mechanisms and expected bathymetry. **A:** Offset with more resistant Del Mar Formation exposed on upthrown block, along predominantly strike-slip fault, would cause bathymetry to step offshore. **B:** In case of left step on dextral strike-slip fault (e.g., Rose Canyon fault), we would expect bathymetric contours to deviate seaward on south end of fault and return landward on north end of fault, which we observe in both local bathymetry (California State University Monterey Bay 2 m) and regional bathymetry (National Oceanographic and Atmospheric Administration 3-arc-second model: <http://www.ngdc.noaa.gov/mgg/coastal/grddas06/grddas06.htm>). Black lines indicate fault trace; sense of motion is illustrated by arrows or D and U for downthrown and upthrown blocks.

Horizon cruise, unpublished data) to the north of the pop-up structure, where the isobaths shift shoreward, reveal that the transgressive surface has a northward dip, which is also consistent with the pop-up model. The relief on this surface may be augmented by the differential erodibility of the Eocene subsurface rocks, more indurated in the north than in the south (Kennedy, 1975).

The thickness of sediments between the canyons and directly north of Scripps Canyon, along with the near absence of sediments on the structural high to the north, suggest that uplift along constraining bends of the Rose Canyon fault plays an important role in long-term sediment accumulation in the region. The relief on the transgressive surface that predates sea-level incursion is difficult to constrain, and thus prevents reliable estimates for the deformation rate after sea-level incursion. Any relict

relief would have created promontories and embayments. The dip of the reflector (DR) overlying the transgressive surface observed in line S4 can be explained by either post-transgression tilting or as backfill associated with erosion of the relict promontory (Fig. 2B). If we assume that all the relief postdates the sea-level rise, the estimated uplift rate will be biased toward a maximum. For example, if this differential relief is the consequence of tectonic uplift and tilting since inundation (ca. 10 ka), it yields deformation rates an order of magnitude larger than previous estimates of uplift rate in the region (0.13–0.14 mm/yr; Legg and Kennedy, 1979). Given that it is difficult to determine what portion of the relief is pre-incursion or post-incursion, long cores are required to place further constraints on the local tectonic uplift rates.

## CONCLUSIONS

High-resolution geophysical data suggest that uplift offshore La Jolla, California, results from a left jog along the Rose Canyon right-lateral fault system, similar to the process responsible for forming Mount Soledad onshore. CHIRP seismic profiles show a shoaling of the transgressive surface from south to north. The seaward deflection of isobaths in the bathymetric data correlates with the change in slope of the transgressive surface and the change in overlying sediment thickness observed in the isopach map. Seismic profiles reveal that the sediments thin to zero above the uplifted bedrock, while the thickest sediments occur to the south of the pop-up structure. The observed sediment thicknesses suggest that tectonics control long-term sediment accumulation in the region, and hydrodynamics control sediment dispersion. Strain accommodation between right-lateral fault segments offshore Southern California results in marked thickness variability of the Holocene sediments. This new insight into controls on sediment accumulation and preservation may advance the understanding of our offshore sand resources and exposure of hardgrounds in the California Borderlands.

## ACKNOWLEDGMENTS

This research was funded by the Office of Naval Research and the Kavli Institute. Reviews from Paul Liu, Dan Orange, and Glen Spinelli improved the manuscript.

## REFERENCES CITED

Darigo, N.J., and Osbourne, R.H., 1986, Quaternary stratigraphy and sedimentation of the inner continental shelf, San Diego County, California, in Knight, R.J., and McLean, J.R., eds.,

- Shelf sands and sandstones: Canadian Society of Petroleum Geologists Memoir II, p. 73–98.
- Driscoll, N.W., and Hogg, J.R., 1995, Stratigraphic response to basin formation; Jeanne d'Arc Basin, offshore Newfoundland, in Lambiase, J.J., ed., Hydrocarbon habitat in rift basins: Geological Society of London Special Publication 80, p. 145–163.
- Fairbanks, R.G., 1989, A 17,000-year glacio-eustatic sea level record: Influence of glacial melting rates on the Younger Dryas event and deep-ocean circulation: *Nature*, v. 342, p. 637–642, doi: 10.1038/342637a0.
- Inman, D.L., and Jenkins, S.A., 1999, Climate change and the episodicity of sediment flux of small California rivers: *Journal of Geology*, v. 107, p. 251–270, doi: 10.1086/314346.
- Kennedy, M.P., 1975, Western San Diego metropolitan area; Del Mar, La Jolla, and Point Loma 7 1/2 minute quadrangles: California Division of Mines and Geology Bulletin, v. 200, p. 9–39.
- Kennedy, M.P., Clarke, S.H., Greene, H.G., and Legg, M.R., 1979, Recency and character of faulting offshore from metropolitan San Diego, California: California Division of Mines and Geology, 37 p.
- Legg, M.R., and Kennedy, M.P., 1979, Faulting offshore San Diego and northern Baja, California, in Abbott, P.L., and Elliott, W.J., eds., Earthquakes and other perils, San Diego region: San Diego, California, San Diego Association of Geologists, p. 29–46.
- Lindvall, S.C., and Rockwell, T.K., 1995, Holocene activity of the Rose Canyon fault zone in San Diego, California: *Journal of Geophysical Research B, Solid Earth and Planets*, v. 100, p. 24,121–24,132, doi: 10.1029/95JB02627.
- Masters, P.M., 2006, Holocene sand beaches of southern California: ENSO forcing and coastal processes on millennial scales: *Palaeogeography, Palaeoclimatology, Palaeoecology*, v. 232, p. 73–95, doi: 10.1016/j.palaeo.2005.08.010.
- Moore, G.W., 1972, Offshore extension of the Rose Canyon fault, San Diego, California: U.S. Geological Survey Professional Paper P 0800-C, p. 113–116.
- National Oceanic and Atmospheric Administration (NOAA) National Geophysical Data Center (NGDC) 3-arc-second coastal relief model: <http://www.ngdc.noaa.gov/mgg/coastal/grddas06/grddas06.htm> (July 2006).
- Orange, D.L., 1999, Tectonics, sedimentation, and erosion in northern California: Submarine geomorphology and sediment preservation potential as a result of three competing processes: The formation of continental-margin strata: *Marine Geology*, v. 154, p. 369–382, doi: 10.1016/S0025-3227(98)00124-8.
- Treiman, J.A., 1993, The Rose Canyon fault zone, southern California: California Division of Mines and Geology Open File Report 93–02, 45 p.

Manuscript received 25 July 2006

Revised manuscript received 21 October 2006

Manuscript accepted 29 October 2006

Printed in USA

The appendix to Chapter 4, in full, is a reprint of the material as it appears in: Geology, 2007, Hogarth Leah J.; Babcock Jeff; Driscoll, Neal W.; Le Dantec Nicolas; Hass, Jennifer K.; Inman, Douglas L.; Masters, Patricia M. “Long-term tectonic control on Holocene shelf sedimentation offshore La Jolla, California”. The dissertation author was a co-author on this paper.

## **CHAPTER 5: Sediment dynamics below the seabed**

## FOREWORD

This chapter is a report of field observations suggestive of a dynamical behavior of sand grains at depths of 100 to 1000 grains below the water-sediments interface. The measurements were acquired in the surf zone, near the Scripps Pier, as the culmination of an extensive experimental project. Observations included the deformation of a small (200 by 120 grain diameters), horizontal, compliant sheet embedded in the sediments below the seabed. Such deformation was caused by local, horizontal displacements of sediments integrated over the cross sectional area of the compliant sheet. Measurements indicate that the deformation was discrete in time and depth-dependant, with creep at shallower depths (200 grain diameters) and episodic yield events at greater depths (600 grain diameters).

The observation of dynamic features at such depth is interesting because the usual view when studying coastal sediment transport is that the bedload layer is approximately 20 to 50 grain diameters, below which the medium is taken as immobile (Fredsoe and Deigaard 1992; Nielsen 1992). Admittedly, the field data presented here may only be considered as indications of granular motions at depths well below the bedload layer thickness. Several factors prevent a definitive analysis of the field measurements, including the lack of a complete understanding of the interactions between the sensors and the sediments, the absence of a more thorough characterization of the mechanical response of the sediments to environmental forcing and the need for a comprehensive theoretical framework adapted to the examination of small scale granular mechanics.

The field observations are still presented here because they are relevant to the dissertation on at least two major accounts. The laboratory studies on liquid-saturated granular piling were motivated by the preliminary results from the sediment dynamics project. In addition, the arching mechanism and the large stress fluctuations characterized in the experiments on saturated granular piling are likely to have implications for the small scale mechanics of marine sediments.

The project on seabed sediment dynamics involved the design of multiple sensors, preliminary tests and calibration in the laboratory, the adaptation of a video system tracking individual grains for use in laboratory and field experiments, and the outfitting and deployment of the sensor package. In this chapter I will describe the operation of the sensors and the deployment configuration, show preliminary results from the first of two deployments and discuss the significance of the observations.

## INSTRUMENTATION

### **Development, operation and performance characteristics of three sensors built for the project**

#### *Differential pressure sensor*

The differential pressure sensor (Fig. 5-1) measures the overburden pressure from sediments above the sensor's diaphragm, thanks to a vent tube (Fig. 5-9). The sensor's diaphragm is directly in contact with grains so that it does not only monitor surface wave-induced pore pressure fluctuations but also the actual sediment pressure, i.e. the overburden pressure transmitted through the granular skeleton and measured as the pressure exerted by grains in contact with the diaphragm. Assuming a lithostatic behavior

for unconsolidated marine sediments, seabed elevation fluctuations can be derived from the output of the sensor if the sediment density is known. The resolution of the differential pressure sensor is approximately 10 Pa, which corresponds to a few millimeters of sediment height. The sensor output can be related to the sensor depth below the seabed level using the following equation. The signification of the variables is indicated on Table 5-1.

$$\Delta P = \int_{\zeta_{sensor}}^{\eta_{seafloor}} (\rho_s(z) - \rho_w(z)) \cdot g \cdot dz + P_d^{sed}(\zeta, \zeta_{sensor}, h) - P_d^{vent tube}(\zeta, \zeta_{sensor}, h)$$

**Table 5-1: List of the variables involved in the mathematical model for the analysis of the differential pressure sensor output**

$\Delta P$	Differential pressure measured across the sensor diaphragm
$\rho_s$	Sediment density
$\rho_w$	Water density
$\eta_{seafloor}$	Seabed level
$\zeta_{sensor}$	Depth of pressure sensor
$g$	Acceleration of gravity
$\zeta$	Water surface level
$h$	Average water column height
$P_d^{sed}$	Surface wave-induced dynamic pressure transmitted through sediments
$P_d^{vent tube}$	Surface wave-induced dynamic pressure transmitted through the vent tube

#### Displacement sensor

The displacement sensor (Fig. 5-2) consists of two wire strain gauges bonded on the base of a deformable plastic sheet (approximately 5 cm tall and 3 cm wide) made of a

compliant material (0.5 mm thick reinforced nylon) and wired into a bridge configuration. The sensor output corresponds to the displacement of the sediment particles located in the immediate neighborhood of the compliant sheet. The sheet deforms at the same time and in the same fashion as the granular assembly around it, therefore causing resistance changes in the strain gauge as it is elongated or compressed. The flexibility of the sheet allows it to keep a deformed configuration governed by the local grain dynamics, so that the displacement sensor's output displays DC shifts that record grain motion. Time series of grain displacement can be extrapolated to obtain estimates of fluxes in the shallow upper seabed. Note that using two strain gauges, one on either side of the base of the compliant sheet and with opposite polarities, reduces temperature effects to a level compatible with the required sensor performance. The resolution of the displacement sensor is on the order of 50 microns, approximately one fifth of a grain diameter for sand at La Jolla Shores beach. The displacement sensor is meant to be deployed on a vertical plane to measure horizontal displacements. The sensor output can be related to sediment flux using the following equations. The signification of the variables is indicated on Table 5-2.

$$\Delta m = \Delta x \cdot A \cdot \rho_s$$

$$\phi = \Delta m \cdot \frac{\Delta x}{\Delta t}$$

$$\Phi = \frac{\phi}{A} = \frac{\Delta x^2 \cdot \rho_s}{\Delta t}$$

$$\overline{\Phi} = \frac{1}{\eta - \xi} \int_{\xi}^{\eta} \Phi(\zeta) d\zeta$$



**Table 5-2: List of the variables involved in the mathematical model for the analysis of the displacement sensor output**

$\Delta m$	Mass of sediment displaced
$\Delta x$	Displacement of the compliant sheet
$\rho_s$	Sediment density
$\Delta t$	Time interval
$A$	Cross-sectional area of the compliant sheet
$\phi$	Sediment flux
$\Phi$	Sediment flux per area
$\eta$	Seabed level
$\xi$	Reference depth below which sediment motion is neglected
$\zeta$	Depth of displacement sensor

#### Force sensor

The force sensor (Fig. 5-3) operates according to the same principle as the displacement sensor except that the deformable material is a much stiffer beam, so that it does not comply with local deformations of the granular assembly. Hence, the sensor measures the stress exerted by grains in contact with the bending beam. The force sensor is meant to be deployed on a vertical plane to measure changes in the horizontal principal component of stress. The resolution of the force sensor is approximately 10 Pa.

#### Sensor outfitting

The three sensor types are designed to be deployed within the upper shallow seabed. The lower end of each sensor is encapsulated in epoxy along with the bridge

excitation and instrumentation amplifier electronics. The sensing parts, i.e. the strain gauges and diaphragm, are coated with a compliant, waterproofing compound.

The sensor outputs are connected to differential line drivers (i.e. two complementary signals coming from the sensor bridge are carried by two separate wires) which provide a measure for noise immunity in the cable connection between the sensors and the data acquisition system when they are rather large distances away. Since both wires are connected to identical impedances at source and load, electromagnetic interference-induced voltages are balanced between each line and thus cancel out when the output is obtained as the difference in voltage between the two signal lines.

### **Calibration and laboratory tests**

Preliminary calibrations were performed for the differential pressure and displacements sensors. Some calibration results are displayed for the particular case of the displacement sensor (Fig. 5-4), showing the range of linear behavior, the symmetry in the bidirectional response, the temperature sensitivity and the homogeneity of behavior between sensors. Other properties were also examined to check the repeatability of measurements recorded by the displacement sensors, including drift and memory effects, i.e. dependence on the history of previous deformation states of the compliant sheet.

All three sensors have been tested in the laboratory during controlled experiments in a tank filled with sand from La Jolla Shores beach (Fig. 5-5). First the sensors were buried within the sediments in the tank and left operating in a medium at rest to obtain a reference measurement. Then a series of experiments was conducted with controlled constraints on the environment, mostly applying surface disturbances such as bedform

displacement over the sensor's burial location and positioning of a point load (in practice a lead weight) on the sediment surface, and also driving a wedge into the sediment.

Some experimental results are shown in Figs. 5-6 and 5-7 to illustrate certain features of the sensors behavior. The differential pressure sensor adequately captures the changes in seabed elevation. The displacement sensor indicates that granular motions are well correlated with changes in the external constraints. Events are driven by bedform migration steps and are often followed by a relaxation phase. The synchronization of the stress sensor response to the external conditions is not as systematic as in the case of the force sensor. Interestingly, large stress changes always consist in an increase in stress, while the bedform displacement is bidirectional. The increase in stress could be due to compaction which probably increases regardless of the surface bedform migration direction. The sensitivity to packing ratio is clearly observed in the case where a wedge is temporarily inserted through the sediments. Under such forcing conditions, the stress within the upper shallow sediment layer shows large fluctuations, with transient variations of amplitude 3 to 5 times the average signal.

### **Field deployments**

The field measurements were collected in the surf zone, with waves breaking over the location where the sensor package is buried. For deployments, the sensors are mounted on a plate (Figs. 5-8 and 5-9). A hole is created in the seabed by fluidizing the sediments to suspend them. The plate is slipped on a pipe jetted vertically in the seabed. Then sediments are allowed to redeposit from suspension, settle over the sensor package (Fig. 5-10) and bury it. To avoid generating significant horizontal stress and displacement

during burial, the sediments surrounding the sensors are gently fluidized as the sensors get buried. In addition, the field experiments are sufficiently long, respectively 7 and 10 days, to allow relaxation of residual deformation stemming from the initial burial conditions. Consequently the measurements cannot be reduced to artifacts caused by the sediments response to the disturbance from the deployment of the instruments. In some cases the sensors are even uncovered and reburied by the sole action of hydrodynamics (see Fig. 5-15), thus eliminating deployment-induced perturbation of the sediments in the vicinity of the sensors.

Both deployments were conducted by the Scripps Pier (Fig. 5-11), which served as a platform for the computer acquisition system (Inset of Fig. 5-11). For the first deployment, the instrumented plate, with the configuration shown in Fig. 5-8, was installed underneath the Scripps Pier between pilings 15 and 16. For the second deployment, the configuration was modified (Fig. 5-9), in particular with the addition of a video system (see section 5-2.4), and the instrumented plate location was 40 meters north of the pier at the level of piling 18. Complementary data from the Scripps Pier weather station, such as significant wave height, are available to augment the dataset and help in its interpretation.

### **Video system to track individual granular displacements**

A video system consisting of a high speed and high resolution camera behind a transparent optical face plate (Fig. 5-12) was added in the objective of investigating individual grain displacements below the seabed. While the displacement sensor measures motion of sediments integrated over the area of the compliant sheet (Fig. 5-2D),

the purpose of the video system is to study the motion of individual grains within the seabed corresponding to rearrangements of the granular skeleton.

The camera can capture as many as 30 frames per second and provides images of approximately  $6 \text{ cm}^2$  with a resolution of  $40 \mu\text{m}^2$ , i.e. approximately one sixth of the mean grain diameter of local sediments. It is augmented with a light head that provides an illumination source in the otherwise dark seabed. Grains constituting local surf zone sediments have a dual reflectivity spectrum. The grains against the face plate appear either darker or lighter. This contrast property is exploited to track the motions of individual grains in a plane parallel to the face plate of the video system.

The video data can be analyzed with a piece of software developed to rapidly detect grains displacements. The procedure is illustrated in Fig. 5-13 using images collected in the laboratory. The color-coded difference image between two successive frames is non-zero where contrasting grains have moved. If a vector represents the linear displacement over a certain time interval of a grain appearing as darker, the difference between the corresponding images will show a dark region centered at the end-point extremity of the translation vector and a light region centered at the origin of the translation vector. This dual or stripped pattern is reversed if the displaced grain or aggregate appears lighter. The color of the translated grain can be obtained by looking at the corresponding raw images at the identified location of grain displacements. Events of mass grain motion can be extracted by setting a threshold based on the number of pixels corresponding to individual displacements in a single difference image, for instance.

A complication arises from the fact that when a grain rotates, its apparent color, or reflectivity, is very likely to change, so that color variation of a pixel between two

successive images does not always indicate net displacement. Note that rotations are also indicative of rearrangements of the internal structure of the granular assembly. Besides, rotations can still be distinguished from translations because they don't have the typical stripped pattern. In addition, the absence of color change does not necessarily mean that there was no grain motion. It can also mean that there was no contrasting grain to be used as a marker in the area considered.

The analysis of laboratory data, acquired with the camera focusing on the sediments against the side wall of the tank (Fig. 5-12), shows that granular motion is episodic but can be very significant. Granular displacements are non-uniform and exhibit localization, with a stripe pattern reminiscent of arch-like features (Fig. 5-14). Such heterogeneous behavior may indicate the existence of preferred directions of displacement, which is consistent with the role of force chains in the small-scale response of granular materials to variations in the external forcing. Compiling successive events definitely suggests the existence a net flux, rather than an oscillatory pattern, which could be associated with overlying bedforms migration.

## **PRELIMINARY FIELD OBSERVATIONS**

### **Dataset overview**

Here preliminary results from the first deployment are presented. The goal was to prove the design of the sensors and to test whether they were able to detect any dynamic features within the upper shallow seabed. The sensor package was deployed in an energetic location to increase the probability that the sensors would capture interesting

phenomena. The deployment location, which was in approximately 1.5m water depth, was under breaking waves with energetic swell conditions for most of the trial (Fig. 5-15). One of the displacement sensors failed during a period of large wave heights, presumably because the sensor became exposed and the compliant sheet was subject to a strong oscillatory flow in the bottom boundary layer. Overall, the instruments operated successfully and acquired measurements of displacements and stress fluctuations within the seabed, such as the time series of selected sensors shown in Figs. 5-16 and 5-17.

A period of approximately 22 hours is shown in Fig. 5-16. The time series data during the period annotated by the red bar in the middle plot is shown in an expanded view in Fig. 5-17. The top plot shows the output from the differential pressure sensor. The middle plot shows the output from a displacement sensor buried approximately 6cm below the differential pressure sensor and the bottom plot corresponds to a displacement sensor buried at approximately the same depth as the pressure sensor. The rapid variations in signal that are annotated by the broken line in the bottom plot correspond to time periods when the shallow displacement sensor was exposed to the water. The large steps in signal annotated by the solid lines in the top and middle plots correspond to time periods when the sediment depth was sufficiently so that the differential pressure sensor output overloaded the data acquisition card, resulting in channel cross-talk. No data for the force sensors is shown here because they failed early on during the field experiment.

### **Preliminary analysis of selected features**

The output signal from the differential pressure sensor consists of two components. The mean trend characterized by slower variations is due to the overburden

pressure from the grains and depends on the depth-integrated density of the overlying sediments and the stress propagation from the seabed to the sensor diaphragm. The dynamic pressure characterized by short time-scale variations is caused by surface gravity waves shoaling or breaking over the location of the instrument, with oscillations of larger amplitude when swell conditions are more energetic.

Field measurements from the displacement sensor are consistent with results from controlled laboratory experiments. The output signal of the displacement sensor shows discrete step features that may be regarded as evidence of sediment motion, particularly the output of deep sensor during the 800-900 minutes interval (Fig. 5-16). Note that the correlation between the displacement events and seabed level changes is not obvious in the field data.

As illustrated in Fig. 5-17, the granular displacements are depth dependent by their nature and rate, with a creeping process in the shallowest part and an episodic process a little deeper in our shallow upper layer of interest. The creep event measured by the shallower sensor has amplitude of 3 mm over a little less than an hour while the single event measured by the deeper sensor has amplitude of a little more than 1 mm over a few minutes.

The creeping mode may be comparable to a boundary layer flow where the momentum originated in the overlying hydrodynamics and transmitted through the sediments is damped with depth from the seabed. The discrete motion deeper below the seabed may correspond to a different rheology. Yet, the dataset does not preclude a continuous regime transition between a steady creeping mode observed at intermediate depth and the episodic process.



### **Measurement strategy for the second deployment**

The results from the first deployment have actually motivated the development of the video system (see section 5-2.4) to confirm the occurrence and nature of grain motions. The video system was used in the second deployment, the sensor configuration of which was motivated by a number of specific objectives. A displacement sensor was positioned right in front of the camera, with the compliant sheet perpendicular to the face plate and only a few grain diameters away, in order to obtain a visual characterization of the grain motions associated with the output signal of the displacement sensor. Two differential pressure sensors were placed side-by-side to study arching effects and stress heterogeneities by comparing the vertical stress at the same depth and with similar overlying sediment geometries. A pair of almost collocated displacement and force sensors was meant to identify stick-slip dynamics. The dataset of the second deployment has not yet been analyzed.

## **COMMENTS**

### **Other examples of dynamical behavior in the bulk of granular assemblies from laboratory studies**

The displacement patterns observed in the field measurements at depths of 400 grain diameters are consistent with the behavior of granular systems (Jaeger and Nagel 1992; Jaeger *et al.* 1996). In particular, they are reminiscent of results from recent work by several research groups, including studies on shear bands and stick-slip processes. Experiments on gravity-driven granular flows involving long-term monitoring suggest

that particles below the surface exhibit very slow flow that can be detected at arbitrary depths and thus question the existence of a depth below which grains are immobile (Komatsu *et al.* 2001). Studies on dense slow flows driven by boundary shear indicate that wide fluidized layers can exist away from the boundary (Fenistein *et al.* 2003). Such flows can show complex time-dependent rheology associated with internal reorganization of the granular skeleton and changes in compaction (Tsai and Gollub 2005). In addition, work on granular drag exerted on a rod driven horizontally through by a granular layer shows evidence of stick-slip processes (Albert *et al.* 2000).

Only few such studies have been conducted on saturated granular assemblies (Geminard *et al.* 1999; Divoux and Geminard 2007; Tsai and Gollub 2005). To ensure that the results mentioned in the above paragraph constitute an appropriate context to examine and appreciate the field observations within marine sediments, a natural question was to verify the commonality of behavior between dry and saturated granular matter. That saturating granular assemblies does not fundamentally modify their mechanical properties may be *a priori* anticipated (Tsai and Gollub 2005; Geminard *et al.* 1999). Granular matter mechanics is governed by the physical properties of intergranular contacts, in particular the frictional properties. Thus the presence of interstitial fluid is not expected to alter the main characteristics of the mechanics of granular systems provided that grains are still in contact. Controlled laboratory studies are in order to provide conclusive experimental evidence of this point. One such study is reported in Chapter 2.

### **Experiments by Bagnold**

Bagnold conducted experiments (Bagnold 1966) on the shearing and dilatation, also referred to as dilatancy, of a layer of dry sand. The experimental set-up, with which some of my laboratory work (involving the manual displacement of a bedform over the buried sensors with a push-plate) bears similarities (see Fig. 5-5), consisted in pushing the granular assembly in a bull-dozer fashion by means of a plate that applied a controlled force. Bagnold analyzed the displacement of the overburden heap in relationship with the dilatation of the layer at successive shearing planes along which the pushed grains pass-over underlying grains.

Following his previous experiments on the state of stress within dispersions of solid spheres under shear (Bagnold 1954), the granular assembly is in the grain-inertia regime (Bagnold had understood that the shearing of dense granular systems generates a normal, dispersive stress related to dilatation and that the ratio of the shear to normal stresses  $T/P$  defines a dynamic friction coefficient  $\tan \phi'$  for a sheared dispersion of granular solids, with  $\phi'$  the effective friction angle characterizing the resistance due to solid to solid friction; see also Hunt *et al.* (2002) for a critical review of Bagnold's 1954 study). Then, on the basis of considerations relative to the frictional properties and the geometry of the granular system, motion is expected to occur as forward, constant-velocity jumps associated with the hysteresis in the friction angle along the shearing plane (i.e. the difference between the static friction angle and the residual angle).

The results for displacement versus velocity of the push-plate showed a continuous transition between step motions and more regular patterns of creep occurring when increasing the velocity of the push-plate. The data confirmed that the primary steps have a constant velocity independent of the mean push-plate velocity. It is interesting that

the measurements from buried sensors presented here show resemblance with the behavior observed in the insightful experiments by Bagnold. In particular, the change in the nature of granular displacements could follow from the decrease in the mean velocity with depth.

### **Limitations to the interpretation of the dataset**

The current lack of a theory adapted to the study of the small-scale mechanics and rheology of dense, unconsolidated marine sediments is a severe obstacle to the analysis of the data. Beyond the examples cited in the previous section, a large body of work shows that, at least at a scale of 10 to 1000 grain diameters, the response of granular materials to external forcing is largely influenced by collective behaviors arising from structural heterogeneities. A comprehensive theoretical framework for granular matter that would allow interpreting the field measurements is not available at present.

In addition, there are limitations specific to the dataset. First, a more detailed calibration of the sensors output, in particular for the force sensor, is required for a definitive interpretation of the field measurements. Then, although wave height is known from a nearby pressure gauge, complementary data providing a detailed record of the environmental factors, i.e. current at the seabed interface, seabed elevation and bedforms, are lacking. A more complete field experiment is required to provide accurate estimates of sediment fluxes over a sufficiently long time period and adequately characterize the nature and depth-dependence of sediment motion within the seabed and their relation to forcing conditions.

## Implications

Despite such limitations, the field measurements presented here constitute an encouraging attempt at a novel approach to study small-scale sediment dynamics. Given the difficulty in acquiring reproducible datasets, which is inherent to granular systems even in the laboratory, the observations are a significant achievement. The preliminary analysis of the data suggests that, quantitatively, the displacements below the seabed only contribute to a negligible part of the total flux of sediment transport. Yet there are indications of interesting behavior that deserve further investigation.

The results from the laboratory work presented in Chapter 2, and which was motivated by the field measurements, can be applied to the study of small-scale marine sediments mechanics. The observed episodic displacements below the seabed can be analyzed in terms of the jamming phenomenon associated with long-range force chains in granular materials. Such jamming behavior is likely involved in the apparent mass fluctuations reported in the saturated granular pilings experiments (Le Dantec and Deane 2009). Event-driven granular motion may be associated with failure of granular arches caused by changes in the stress applied to the overlying sediments. The observed steps in granular displacements may also arise from dilatation along a shearing plane, following the analysis by Bagnold mentioned above. In any case, the laboratory experiments on granular pilings outline the importance of characterizing the (effective) internal friction of unconsolidated marine sediments to describe their rheology.

More generally, the phenomena associated with the spatial and temporal heterogeneity intrinsic to granular assemblies, such as the emergence of force chains, are pertinent to the response of seabed sediments to the stress exerted by the overlying fluid.

Internal rearrangements at shallow depths below the seabed and coupling effects between the interstitial flow and the granular skeleton, in particular in the presence of surface bedforms, may turn out to play a significant role in certain beach and shelf sedimentary processes.

**Acknowledgments:** I thank James Uyloan and Cary Humphries for technical assistance and contribution to the success of the field deployments. Financial support was provided by the U.S National Science Foundation and the Office of Naval Research.

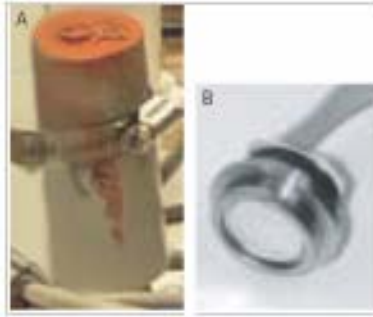


**Figure 5-1: Differential pressure sensor. A. Waterproofed sensor potted in epoxy with accompanying circuit board and clamped to a deployment mount. B. Sensor alone showing diaphragm**

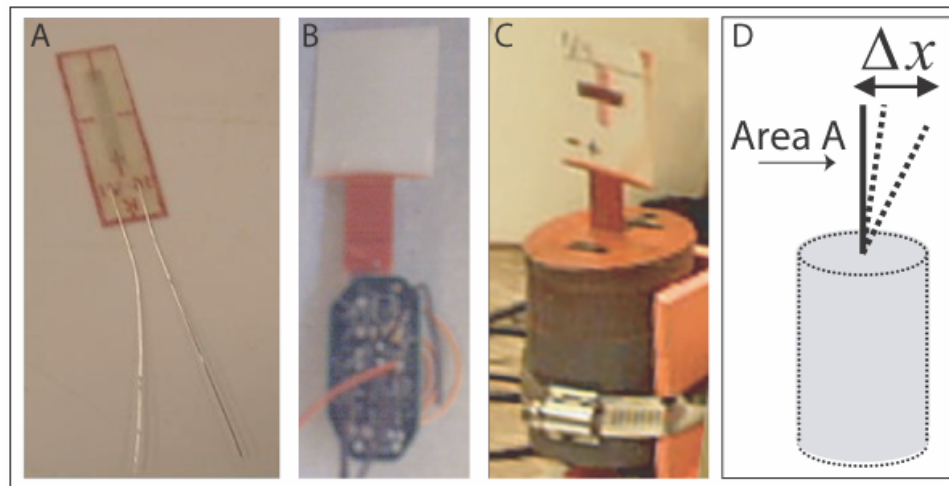


**Figure 5-2: Displacement sensor. A. Strain gauge alone. B. Compliant plastic sheet with waterproofed strain gauges at the base of the sheet and circuit board. C. Sensor potted in epoxy with accompanying circuit board and clamped to a deployment mount. D. Schematic of the deformation of the compliant sheet of area A. The deformation is measured as the displacement  $\Delta x$  of the extremity of the sheet**



**Figure 5-3: Force sensor. A. Sensor alone showing the notch in the bending beam and wires attached to the strain gauge that is bonded on the back side. B. Waterproofed sensor potted in epoxy with accompanying circuit board and clamped to a deployment mount. The strain gauge and notch are covered with a protective jacket**



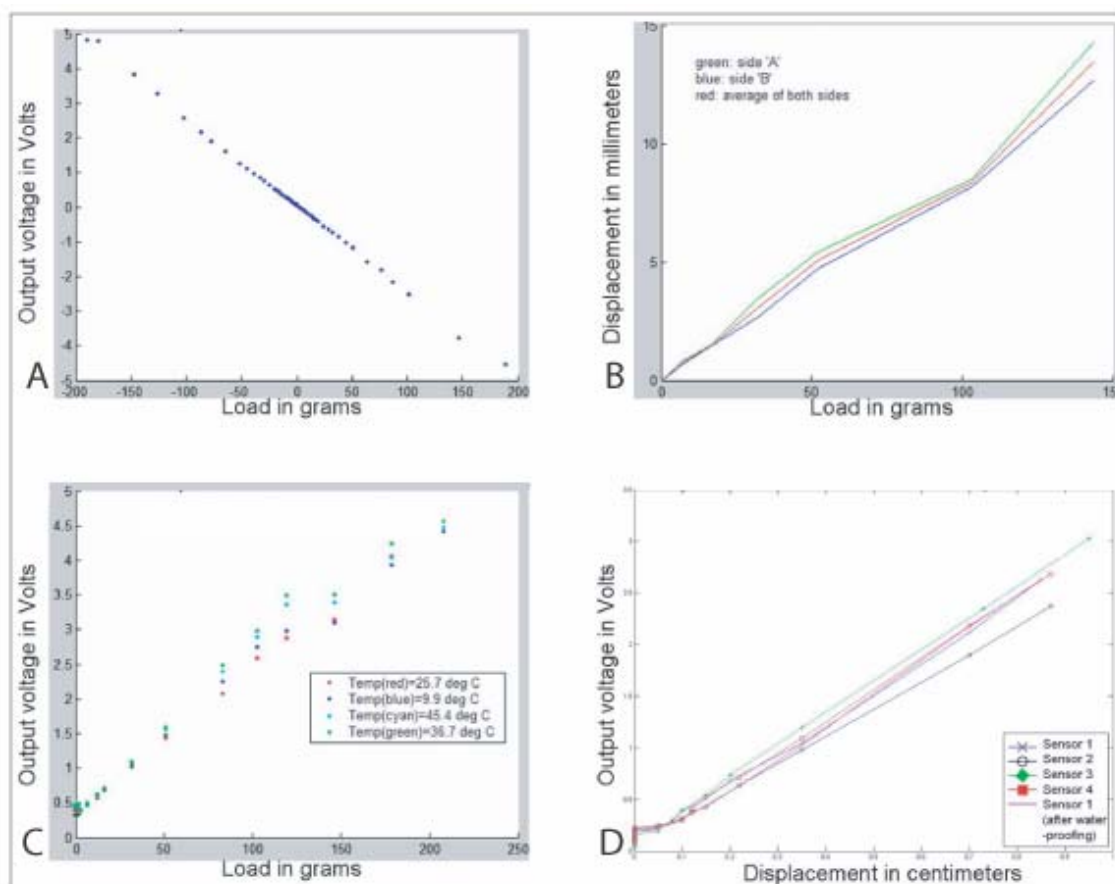


**Figure 5-4: Calibration of the displacement sensors. A. Linearity.** Sensor output in Volts plotted against load in grams. Each point represents one measurement. **B. Symmetry.** Measured deformation in millimeters of displacement of the extremity of the compliant sheet plotted against load in grams. The blue and green curves correspond to both directions of deformation and the red curve to their average. **C. Temperature sensitivity.** Sensor output in Volts plotted against load in grams for 4 different temperatures (9.9, 25.7, 36.7 and 45.4 degrees C). Each point represents one measurement. **D. Homogeneity of behavior between sensors.** Sensor output in Volts plotted against the measured deformation. Measurements from four displacement sensors are compared, each represented by a curve connecting data points, together with a fifth line corresponding to the measurements for one of the sensors after applying the waterproofing treatment.

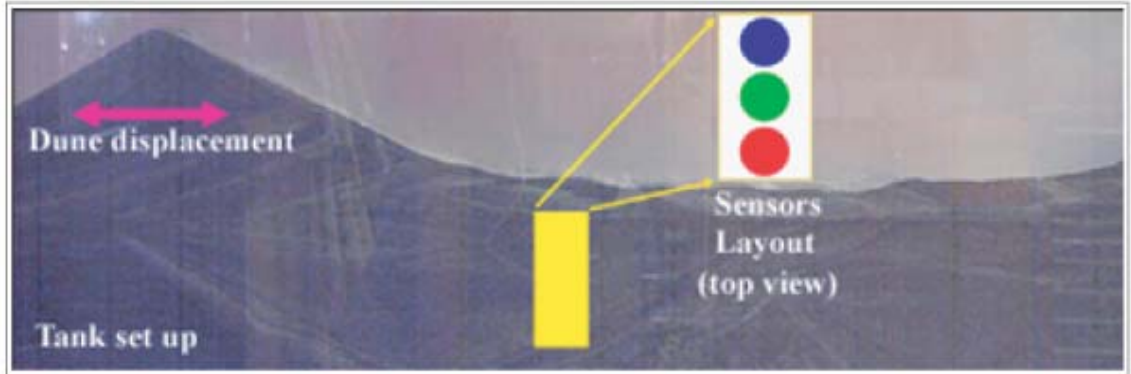


**Figure 5-5: Geometry of the tank set-up for preliminary laboratory experiments. Three sensors are simultaneously used to measure differential pressure (blue), displacement (green) and force (red). The colored dots represent a top view of the sensor layout. The photograph shows an example of controlled modification of the environment conditions where a bedform is laterally pushed across the tank to pass over the sensors**

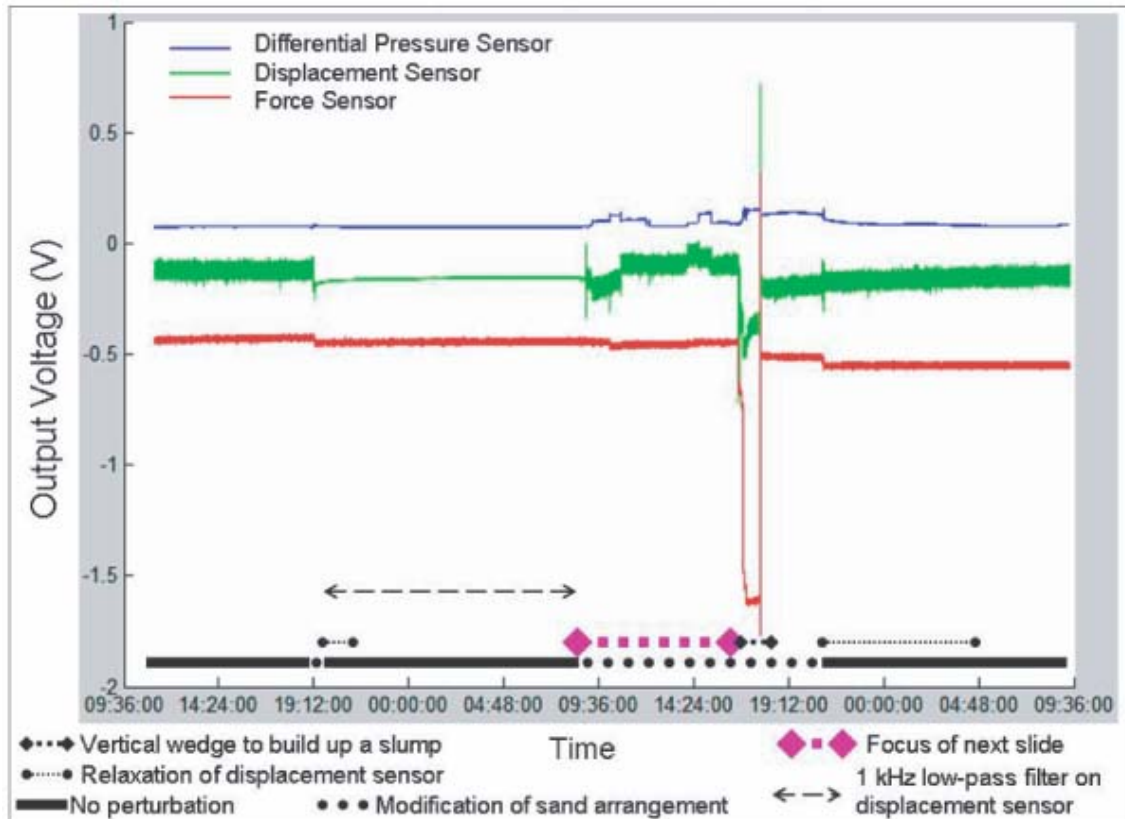


**Figure 5-6: Time series of sensor outputs for measurements acquired in the configuration shown in Fig. 5-5. Steps in the experimental procedure are indicated below the plots, together with the identified phases of relaxation of the displacement sensor and relevant data filtering information. For the differential pressure sensor, 5 mV correspond to 1 cm of overlying sediment thickness and for the displacement sensor 250 mV correspond to 1 mm of deformation of the compliant sheet**

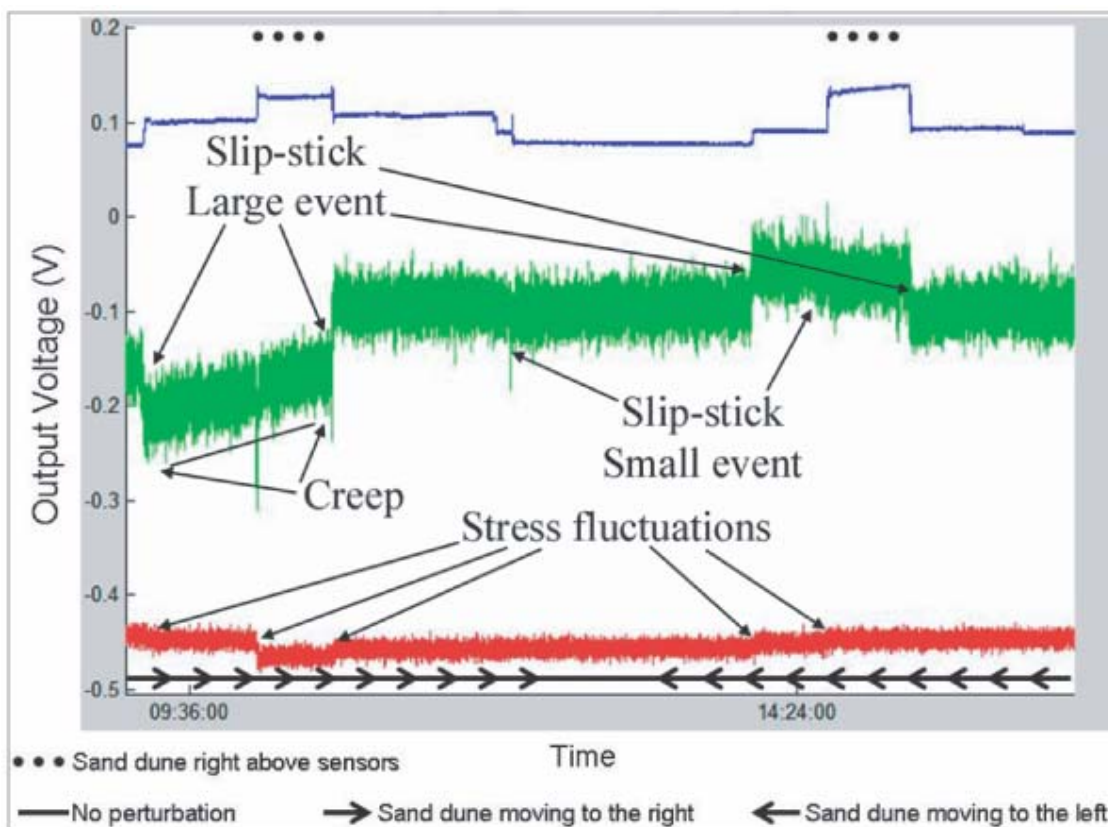


**Figure 5-7: Enlarged view of a portion of the time series shown in Fig.6. The same correspondences between the voltage output of the sensors and the associated physical variables apply**

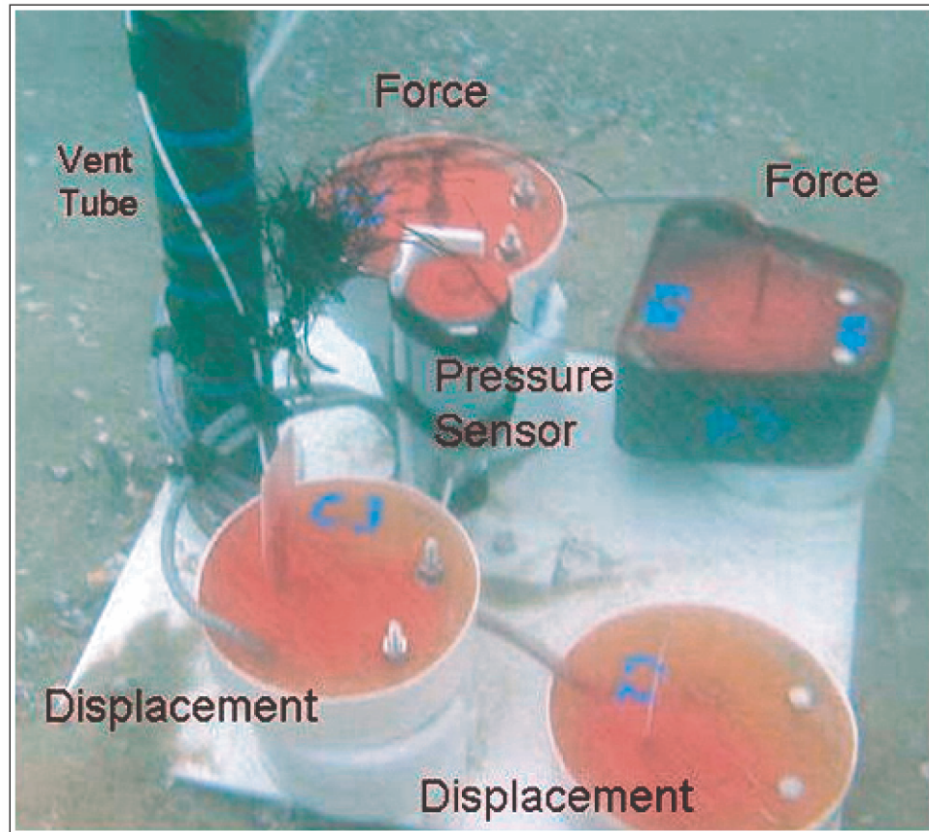


**Figure 5-8: First deployment. The sensor package is shown before burial to illustrate the sensor configuration, with two displacement sensors in the foreground, one differential pressure sensor in the middle and two force sensors in the background. Note that the two right-most sensors are lower than the pair of left-most sensors. All sensors are attached to a base plate that is slipped on a vertical pipe. The water-filled vent tube connects a chamber located against the lower face of the pressure sensor diaphragm to the water column. The top extremity of the vent tube is well above the level reached by the seabed is after sediments deposit over the sensor package and bury it**

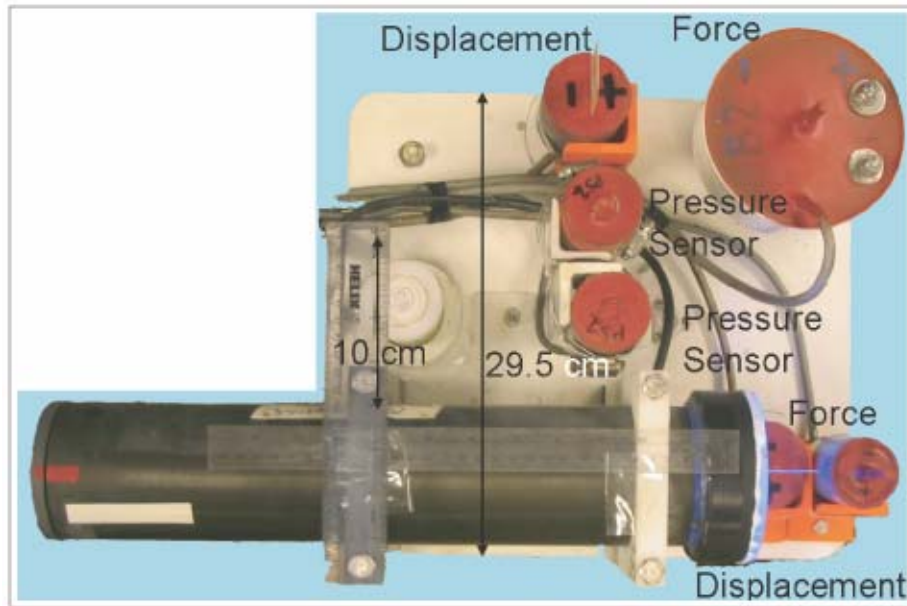


**Figure 5-9: Second deployment configuration. Note the pair of nearby differential pressure sensors in the middle aimed at investigating arching effects and stress heterogeneities, the almost collocated displacement and force sensors meant to identify stick-slip dynamics and the video system in the black housing, with a displacement sensor right in front of the face plate to image granular motion in the immediate vicinity of the compliant sheet. Rulers serve to survey the set-up geometry**



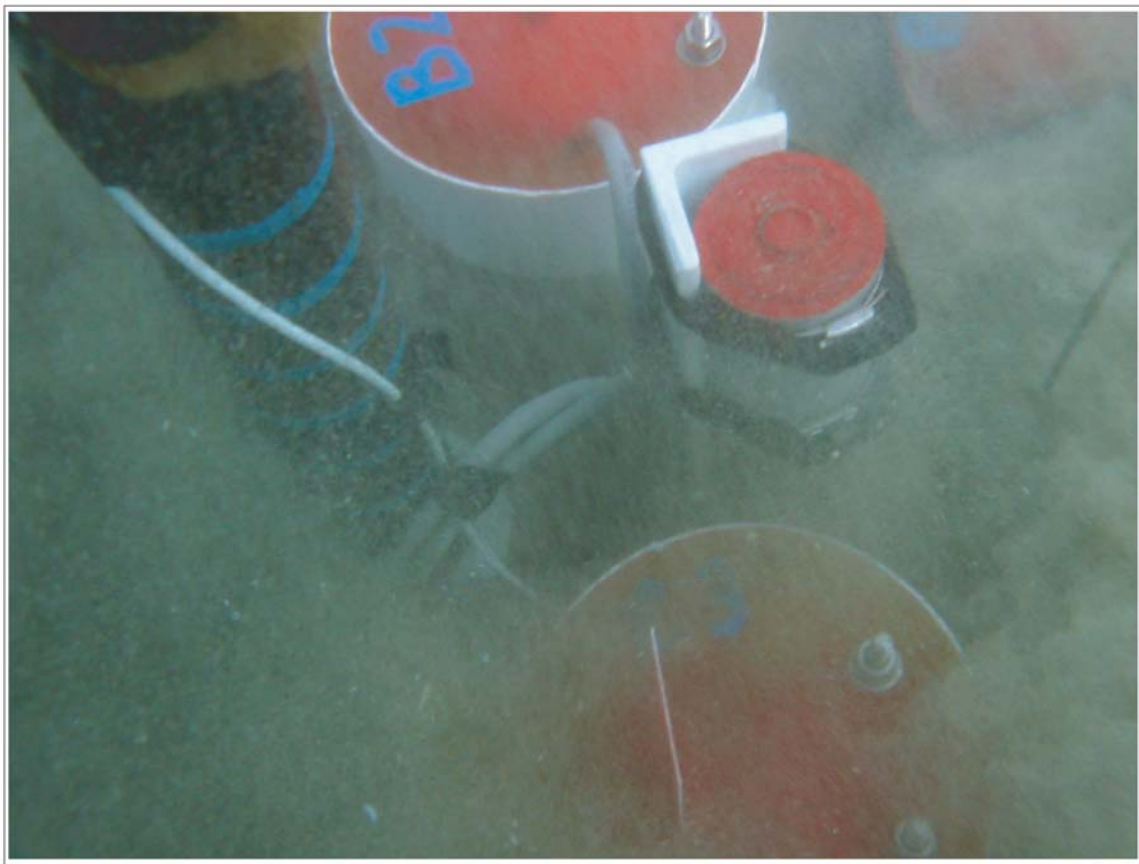


**Figure 5-10: Burial of the sensor package. The photograph shows suspended sediments settling over the instruments**



**Figure 5-11: Deployment location. For both measurements campaigns, the sensor package was set-up in the surf zone by the Scripps Pier, which is shown in the photograph. The inset is a photograph of the computer set-up on the Scripps Pier**





**Figure 5-12: Video system. A. Front view of the high speed and high resolution camera in its waterproof housing used for deployment, showing the transparent optical face plate and the light head. In the photograph a force sensor is set-up right in front of camera. The monitor displays the image of two orthogonal rulers indicating the size of the field of view. B. Photograph of the camera without the housing in front of the laboratory tank**

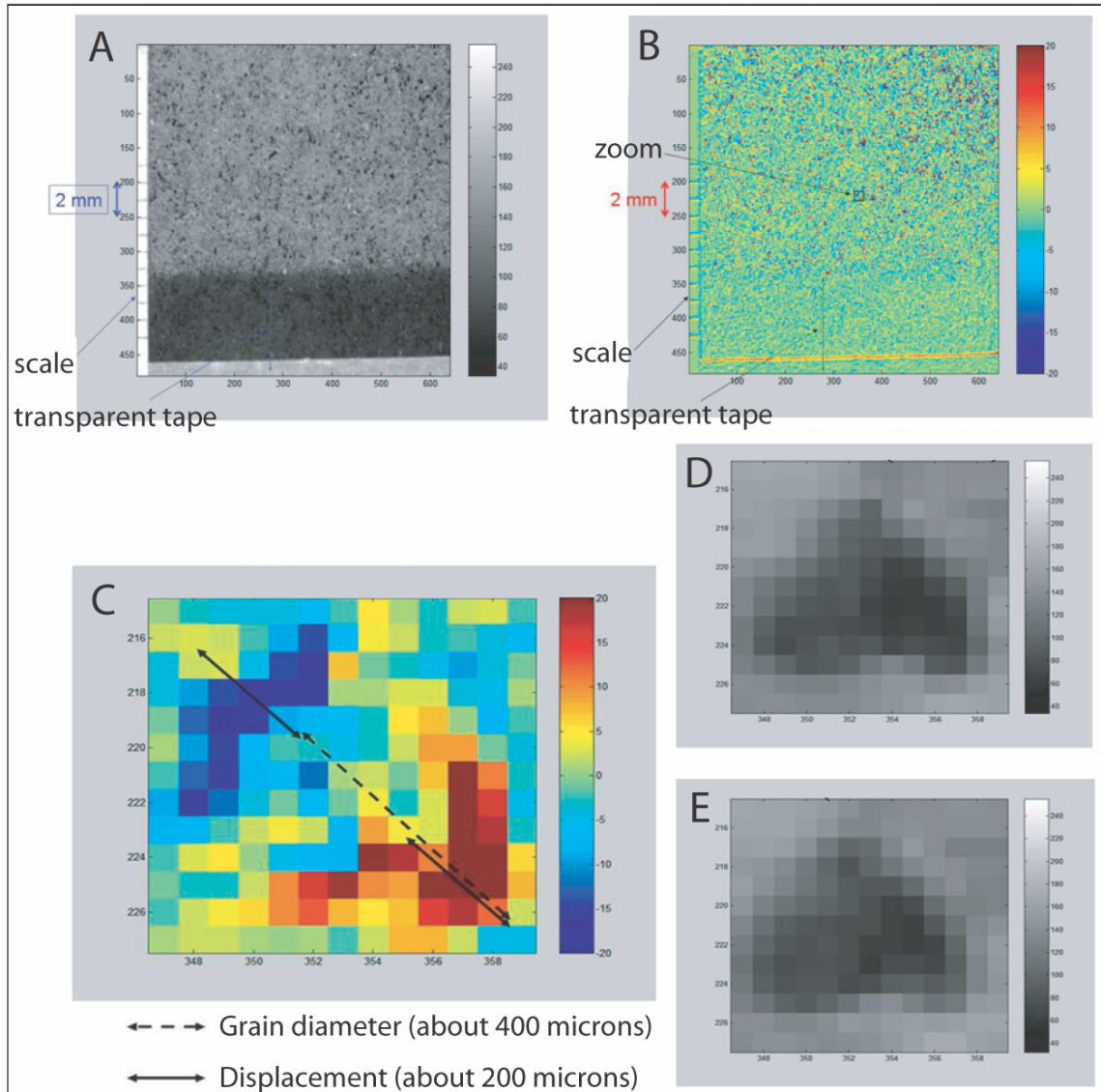


**Figure 5-13: Analysis of images from the video system used to track individual grain displacements. All axes are labeled in pixels (1 pixel = 40 microns) A. Grayscale image from the video system. B. Color-coded difference between two images taken 3 seconds apart. The color scale is chosen to obtain a convenient contrast and has no quantitative significance. C. Enlarged portion of B showing the displacement of a grain. D and E. Same enlarged portion as in C, respectively at time T and T+3 sec, showing that the moving grain appears dark**

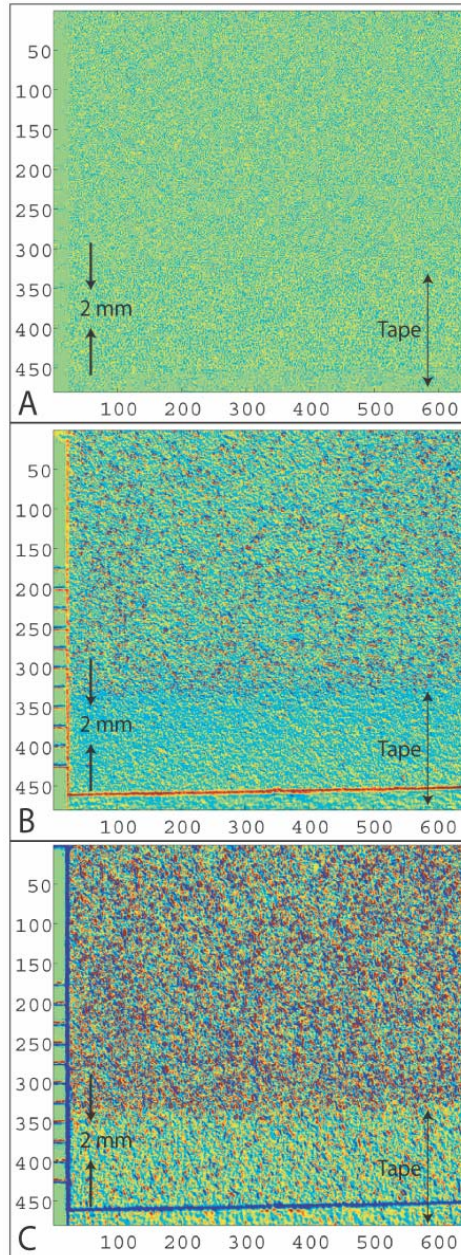


**Figure 5-14: Heterogeneity and localization of granular motion.** Three difference images from laboratory experiments on bedform displacement with a push-plate (see Fig. 5-5). The images are color-coded with arbitrary scales and each image was obtained from still frames 3 seconds apart (see the caption of Fig. 5-13). Panels A, B and C correspond to selected times during the displacement of a heap of sand over the field of view of the camera, with increasing overall granular motion as the bedform passes directly above the imaged area. Axes labels, scales and indications for the transparent tape are as in Fig. 5-13

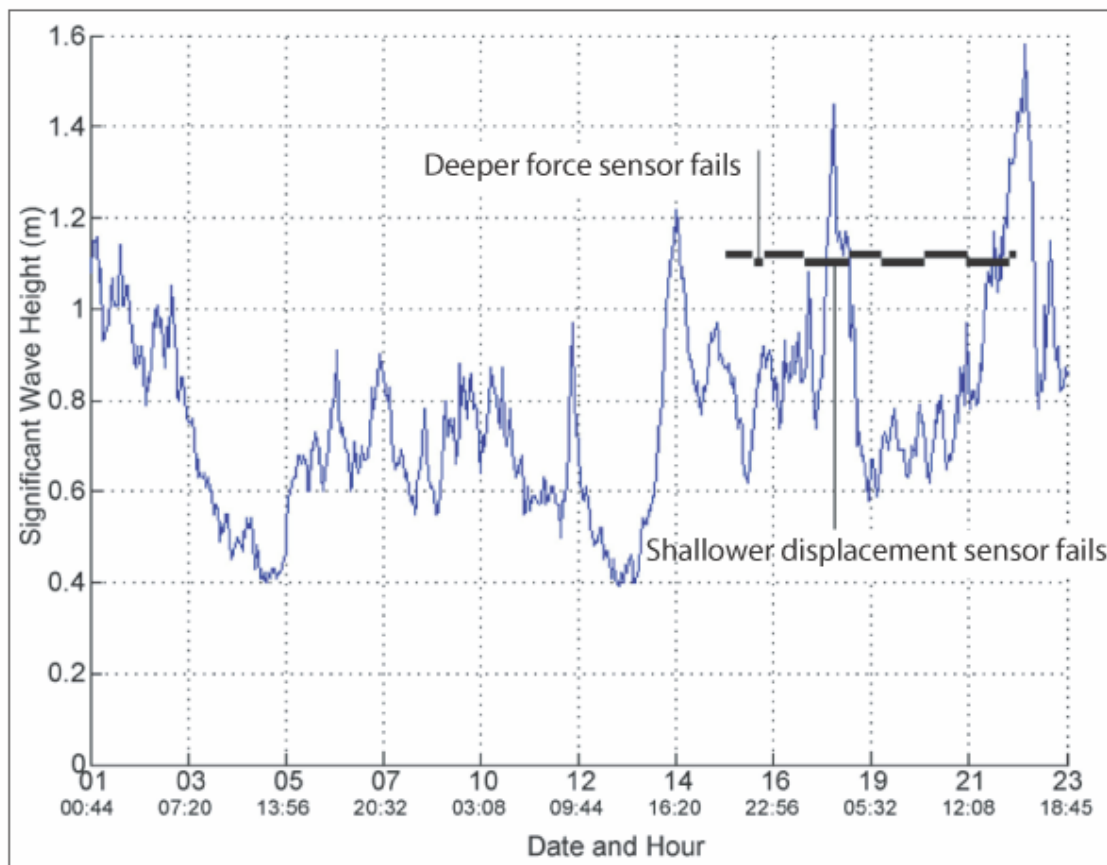


**Figure 5-15: Experiment overview. Plot of the significant wave height at the Scripps Pier at the time of the first deployment. One of the displacement sensors failed during a large wave event where the compliant sheet was exposed**

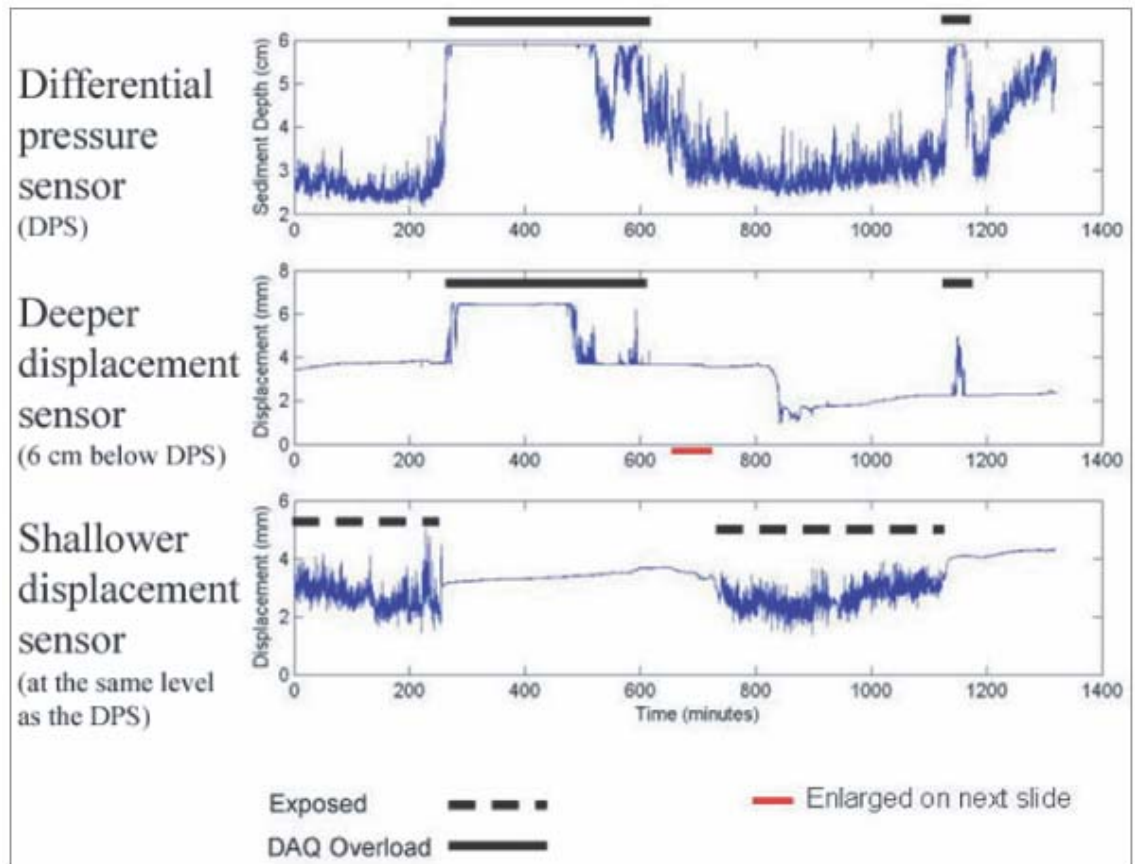


**Figure 5-16: A 22 hour summary time series from the differential pressure sensor (top plot) and the deeper and shallower displacement sensors (middle and bottom plot respectively). Annotations provide information on the sensors operation. Note the 3 mm displacement measured at approximately 9 cm depth at around 850 minutes on the middle plot**



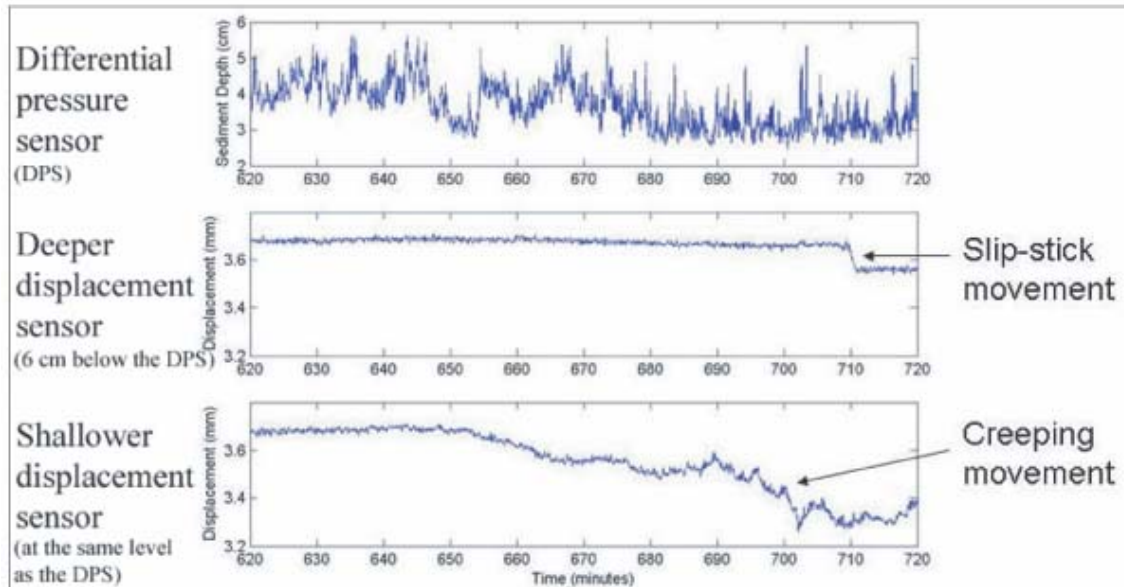


**Figure 5-17: Expanded view of 100 minutes of data taken from Fig. 5-15. Note the difference in the nature of motion between both sensors, with single event displacements at a depth of approximately 9 cm below the seabed (middle plot) and creep at approximately 3 cm below the seabed (lower plot)**

## References

- Albert I, Tegzes P, Kahng B, Albert R, Sample JG, Pfeifer M, Barabasi AL, Vicsek T, Schiffer P (2000) Jamming and fluctuations in granular drag. *Physical Review Letters* 84:5122-5125
- Bagnold R (1954) Experiments on a gravity-free dispersion of large solid spheres in a Newtonian fluid under shear. *Proceedings of the Royal Society of London Series A, Mathematical and Physical Sciences*:49-63
- Bagnold R (1966) The shearing and dilatation of dry sand and the 'singing' mechanism. *Proceedings of the Royal Society of London Series A, Mathematical and Physical Sciences*:219-232
- Divoux T, Geminard JC (2007) Friction and dilatancy in immersed granular matter. *Physical Review Letters* 99
- Fenistein D, van de Meent JW, van Hecke M (2004) Universal and wide shear zones in granular bulk flow. *Physical Review Letters* 92
- Fredsøe J, Deigaard R (1992) *Mechanics of coastal sediment transport*. World Scientific
- Geminard JC, Losert W, Gollub JP (1999) Frictional mechanics of wet granular material. *Physical Review E* 59:5881-5890
- Hunt M, Zenit R, Campbell C, Brennen C (2002) Revisiting the 1954 suspension experiments of RA Bagnold. *Journal of Fluid Mechanics* 452:1-24
- Jaeger HM, Nagel SR (1992) Physics of the Granular State. *Science* 255:1523-1531
- Jaeger HM, Nagel SR, Behringer RP (1996) Granular solids, liquids, and gases. *Reviews of Modern Physics* 68:1259-1273
- Komatsu T, Inagaki S, Nakagawa N, Nasuno S (2001) Creep motion in a granular pile exhibiting steady surface flow. *Physical Review Letters* 86:1757-1760
- Nielsen P (1992) *Coastal bottom boundary layers and sediment transport*. World Scientific
- Tsai JC, Gollub JP (2005) Granular packings sheared in an annular channel: Flow localization and grain size dependence. *Physical Review E* 72:10